Investigation of Seismic Excitation as a Method for Flow Enhancement in Porous Media

by

James Leigh Davis

A thesis
presented to the University of Waterloo
in fulfillment of the
thesis requirement for the degree of
Master of Applied Science
in
Civil Engineering

Waterloo, Ontario, Canada, 2008

AUTHOR'S DECLARATION

I hereby declare that I am the sole author of this thesis. This is a true copy of the thesis, including any required final revisions, as accepted by my examiners.

I understand that my thesis may be made electronically available to the public.

ABSTRACT

The concept of using dynamic excitation to enhance fluid flow in a porous medium began to arise in the mid-twentieth century. The initial spark of interest in the subject spurred numerous laboratory investigations throughout the latter half of the twentieth century to identify the mechanisms at work, and to develop field techniques for practical application of the technology. Several prominent laboratory and field studies have been published; however, there are some deficiencies that facilitate the need for further investigation. Groundwater flow and soil dynamics are two distinct areas of research. There is little in common between the two subjects and there is no consideration of soil dynamic properties in any of the reviewed papers. This study will attempt to bridge the gap between these two areas of research.

The objective of this research is to attempt to determine how dynamic excitation of a soil matrix affects saturated single-phase fluid flow. This question is investigated through an extensive literature review of previous studies conducted on this topic, as well as through experimentation designed to replicate the mechanisms responsible for this phenomenon. Experimentation on coarse soil samples is conducted using a modified Stokoe-type resonant column device that allows a quantification of the effects of torsional and axial excitation, frequency of vibration, and strain level. This type of testing in the both the torsional and axial mode has never been conducted before using a resonant column; the Poisson ratios computed using the complimentary data has never been published in the literature.

The flow test results are inconclusive, likely because the input signal amplitudes utilized are simply not large enough to cause a measurable increase in fluid flow rates. Also, increased flow rates observed in previous studies may be the result of local increases in fluid pressure that increase the fluid flow rate, rather than an added inertial component or porosity dilation.

From the additional data obtained during this study, it appears there are some general conclusions that can be drawn regarding the dynamic properties of sands with varying degrees of saturation. The damping ratio of the unsaturated sand increases 270 % in torsional mode and 74 % in axial mode with a 133 % increase in grain diameter. In general, damping is minimal at the partially saturated and saturated conditions and much higher in the dry condition. The damping ratio at dry condition is 243 % more than in the partially saturated

condition in torsional mode and 37 % in axial mode for the Barco sand, and 1170 % more in torsional mode and 59 % in axial mode for the Indusmin sand.

Calculation of the Poisson ratio using the shear and longitudinal wave velocities yields some interesting results. For the dry and saturated conditions, the computed values are within the range of a loose to medium-dense sand specimen; however, the values computed for the partially saturated condition in both sands are an order of magnitude lower and are quite close to the reported value for the mineral quartz. In general, the Poisson ratio increases for high strains; 7.4 % for the Barco sand and 6.3 % for the Indusmin sand.

Future study must be able to characterize the dynamic properties of the soil specimen and NAPL droplets, in addition to quantifying the observed increase in flow. Therefore, the main recommendation of this study is the design of equipment which is capable of not only measuring the response of a soil specimen to dynamic stimuli, but is also capable of accurately measuring flow through the specimen. The optimal design will probably be based on the design of the resonant column. However, effort must be made to ensure the device does not impede flow through the matrix, and it is recommended that all flow connections be located on the exterior of the confinement chamber to minimize the potential for gas leaks into the specimen. Thought should be put into the type of NAPL to be utilized and the degree of sorption to organics. Membranes and plastic tubing should be selected to minimize NAPL loss due to sorption.

ACKNOWLEDGEMENTS

A great deal of thought and effort went into the creation of this document and it would not have been possible without the help and support of a small army of people.

First, thanks to Professor G. Cascante for guidance with theoretical background of soil dynamics and laboratory experimentation. The expertise of K. Bowman and the other Civil Engineering support staff proved invaluable with finicky lab equipment. Thanks to my lab-mates for their insight with laboratory procedures and equipment.

Second, thanks to the many great graduate students in the department for their support as well as making this experience an unforgettable one. In particular, A. Arnold, P. O'Neill, M. O'Connell, P. Javor and A. Rauf, thanks for the countless hilarious lunchtime conversations. Your friendship means very much to me and I could not have survived here without it. Thanks to the past and present members of the great MC Hammers basketball team, whose tales of glory shall be passed on through many generations, no doubt.

Finally, and most importantly, to my family and loved ones outside of university life and far away from this place, thank you for your support and encouragement through the most difficult times. You know who you are; I couldn't possibly have done it without you.

Cheers!

TABLE OF CONTENTS

LIST OF TABLES viii

LIST OF FIGURES x

1.0 FOREWORD 1

1.1 Motivation 1
1.2 Research Objective 2

2.0 LITERATURE REVIEW 4

2.1 Effect of Pore Fluid Viscosity on Dynamic Soil Properties 4
2.2 Response of Fluid Flow in an Aquifer to Seismic Waves 12
2.3 Response of Oil Recovery to Seismic Waves 16
2.4 Laboratory Studies of the Effects of Seismic Stimulation on Fluid Flow 23
2.5 Field Applications of Seismic Stimulation on Fluid Flow 30
2.6 Summary 32

3.0 THEORETICAL BACKGROUND 36

3.1 Pore-Scale Phenomena 36
3.1.1 Unsaturated Soil 36
3.1.2 Vadose Behaviour 41
3.1.3 Fully-Saturated Soil 46
3.1.4 Immiscible Phase Behaviour 50
3.2 Heterogeneity and Scale 61
3.3 Macroscopic Behaviour 67
3.3.1 Wave Propagation 67
3.3.2 Fluid Flow 73

4.0 EXPERIMENTAL SETUP AND METHODOLOGY 76

4.1 Equipment Setup 76
4.1.1 Physical Setup 76
4.1.2 Signal Processing Schematic 80
4.2 Experimental Methodology 82

5.0 EXPERIMENTAL RESULTS AND DISCUSSION 85

5.1 Results 85
5.1.1 Wave Velocity Degradation Curves 85
5.1.2 Specimen 1 88
5.1.3 Specimen 2 94
5.1.4 Specimen 3 99
5.1.5 Specimen 4 111
5.1.6 Specimen 5 124
5.1.7 Specimen 6 131
5.1.8 Specimen 7 140

5.2 Summary 150
6.0 CONCLUSIONS 154
6.1 Enhanced Fluid Flow 154
6.2 Axial and Torsional RC Tests 155
7.0 RECOMMENDATIONS 157
REFERENCES 158

APPENDICES

APPENDIX A 163
APPENDIX B 165
APPENDIX C 169
APPENDIX D 176
APPENDIX E 202
APPENDIX F 210

LIST OF TABLES

Table 2-1 - Constant values in Biot wave propagation model 5
Table 2-2 - Recovery values for different pore fluids at various frequencies of excitation 23
Table 3-1 - Published Poisson ratio values for various materials 40
Table 3-2 - Fluid wettability classification 44
Table 4-1 - Sand parameters 83
Table 5-1 - Summary of hyperbolic model parameters 87
Table 5-2 - Summary of maximum degradation 88
Table 5-3 - Specimen 1, physical properties 89
Table 5-4 - Specimen 1, dynamic properties 89
Table 5-5 - Specimen 1, flow test dynamic properties 90
Table 5-6 - Specimen 2, physical properties 94
Table 5-7 - Specimen 2, dynamic properties 94
Table 5-8 - Specimen 2, flow test dynamic properties 96
Table 5-9 - Specimen 3, physical properties 99
Table 5-10 - Specimen 3, dry dynamic properties 102
Table 5-11 - Specimen 3, partially saturated dynamic properties 104
Table 5-12 - Specimen 3, flow test dynamic properties 108
Table 5-13 - Specimen 4, physical properties 111
Table 5-14 - Specimen 4, dry dynamic properties 114
Table 5-15 - Specimen 4, partially saturated dynamic properties 118
Table 5-16 - Specimen 4, flow test dynamic properties 121
Table 5-17 - Specimen 5, physical properties 124
Table 5-18 - Specimen 5, dry dynamic properties 126
Table 5-19 - Specimen 5, partially saturated physical properties 127
Table 5-20 - Specimen 5, partially saturated dynamic properties 129
Table 5-21 - Specimen 6, physical properties 131
Table 5-22 - Specimen 6, saturated dynamic properties 133
Table 5-23 - Specimen 6, flow test dynamic properties 136
Table 5-24 - Specimen 6, partially saturated dynamic properties 138
Table 5-25 - Specimen 7, physical properties 141

Table 5-26 - Specimen 7, saturated dynamic properties 143
Table 5-27 - Specimen 7, flow test dynamic properties 145
Table 5-28 - Specimen 7, partially saturated dynamic properties 148
Table 5-29 - Summary of strain ratios 151
Table 5-30 - Summary of soil properties 152
Table 5-31 - Calculation of shear modulus 152
Table 5-32 - Calculation of Young's modulus 152
Table 5-33 - Summary of resonant frequency ratio 153

LIST OF FIGURES

Figure 2.1 - Relationship between Biot parameters and soil porosity 7
Figure 2.2 - Theoretical relationship between damping ratio and frequency 10
Figure 2.3 - Cross-section of ridge geology and hydrogeology..... 13
Figure 2.4 - Amplification of well pressure head fluctuation..... 15
Figure 2.5 - Entrapped droplet with pinned contact 20
Figure 2.6 - Residual NAPL droplet resonant frequency as a function of grain size diameter . 21
Figure 2.7 - Comparison of residual droplet resonant frequency predicted by Alvarellos and Hilpert 25
Figure 3.1 - Conceptual diagram of SC packing..... 36
Figure 3.2 - Simple harmonic motion..... 38
Figure 3.3 - Deformation caused by (a) compression and (b) shear waves..... 39
Figure 3.4 - Liquid droplet at equilibrium in an inclined capillary tube..... 43
Figure 3.5 - Capillary force versus (a) water content, and (b) hydraulic conductivity in unsaturated soils..... 45
Figure 3.6 - Entrapped water droplet (a) conceptual diagram and (b) force balance 46
Figure 3.7 - Tortuosity in a pore matrix..... 48
Figure 3.8 - Drag forces on a soil grain undergoing dynamic excitation 49
Figure 3.9 - NAPL contamination conceptual diagram..... 51
Figure 3.10 - Conceptual diagram of capillary entry pressure..... 52
Figure 3.11 - Conceptual diagram of drag forces on an immiscible fluid droplet..... 56
Figure 3.12 - Conceptual diagram of viscous fingering in a porous matrix 58
Figure 3.13 - Conceptual diagram of pinch-off mechanism..... 59
Figure 3.14 - Conceptual diagram of bypass mechanism..... 60
Figure 3.15 - Conceptual diagram of sand and clay grains..... 62
Figure 3.16 - Relative grain size comparison 63
Figure 3.17 - Conceptual drawing of soil matrices with differing grain size, shape, angularity and orientation 64
Figure 3.18 - Schematic of macroscopic uniformity..... 65
Figure 3.19 - SDOF system (a) analogy and (b) force diagram..... 68
Figure 3.20 - Thin disk undergoing applied acceleration 70
Figure 4.1 - Physical equipment setup..... 76

Figure 4.2 - Resonant column in torsional mode 77
Figure 4.3 - Resonant column in axial mode 78
Figure 4.4 - Base plate plan view (from top plate) 78
Figure 4.5 - Top plate plan view (from bottom plate) 79
Figure 4.6 - Modified RC end plates 80
Figure 4.7 - Signal processing schematic diagram 81
Figure 5.1 - Barco sand torsional wave velocity degradation curve 85
Figure 5.2 - Barco sand compression wave velocity degradation curve 86
Figure 5.3 - Indusmin sand torsion wave velocity degradation curve 86
Figure 5.4 - Indusmin sand compression wave velocity degradation curve 87
Figure 5.5 - Specimen 1 partially saturated, RC test, torsional mode 89
Figure 5.6 - Specimen 1, flow test measured time intervals 91
Figure 5.7 - Specimen 1, flow test computed hydraulic conductivities 92
Figure 5.8 - Barco sand pore pressure coefficient B measurement results 93
Figure 5.9 - Specimen 2 partially saturated, RC test, torsional mode 95
Figure 5.10 - Specimen 2 partially saturated, NR test, torsional mode 96
Figure 5.11 - Specimen 2, flow test measured time intervals 97
Figure 5.12 - Specimen 2, flow test computed hydraulic conductivities 98
Figure 5.13 - Wideband frequency sweep of specimen 3 dry 100
Figure 5.14 - Axial wideband frequency sweep of specimen 3 dry at varying confinement 101
Figure 5.15 - Specimen 3 dry, RC test, torsional mode 102
Figure 5.16 - Specimen 3 dry, RC test, axial mode 103
Figure 5.17 - Specimen 3 dry, NR test, torsional mode 103
Figure 5.18 - Specimen 3 dry, NR test, axial mode 104
Figure 5.19 - Wideband frequency sweep of specimen 3 partially saturated 105
Figure 5.20 - Difference between partially saturated and dry specimen 3 normalized transfer functions 106
Figure 5.21 - Specimen 3 partially saturated, RC test, torsional mode 106
Figure 5.22 - Specimen 3 partially saturated, RC test, axial mode 107
Figure 5.23 - Specimen 3 partially saturated, NR test, torsional mode 107
Figure 5.24 - Specimen 3 partially saturated, NR test, axial mode 108
Figure 5.25 - Specimen 3, flow test measured time intervals 109
Figure 5.26 - Specimen 3, flow test computed hydraulic conductivities 110

Figure 5.27 - Wideband frequency sweep of specimen 4 dry 112
Figure 5.28 - Axial wideband frequency sweep of specimen 4 dry at varying confinement 113
Figure 5.29 - Specimen 4 dry, RC test, torsional mode 114
Figure 5.30 - Specimen 4 dry, RC test, axial mode 115
Figure 5.31 - Specimen 4 dry, NR test, torsional mode 115
Figure 5.32 - Specimen 4 dry, NR test, axial mode 116
Figure 5.33 - Wideband frequency sweep of specimen 4 partially saturated 117
Figure 5.34 - Difference between partially saturated and dry specimen 4 normalized transfer functions 117
Figure 5.35 - Indusmin sand pore pressure coefficient B measurement results 118
Figure 5.36 - Specimen 4 partially saturated, RC test, torsional mode 119
Figure 5.37 - Specimen 4 partially saturated, RC test, axial mode 120
Figure 5.38 - Specimen 4 partially saturated, NR test, torsional mode 120
Figure 5.39 - Specimen 4 partially saturated, NR test, axial mode 121
Figure 5.40 - Specimen 4, flow test measured time intervals 122
Figure 5.41 - Specimen 4, flow test computed hydraulic conductivities 123
Figure 5.42 - Wideband frequency sweep of specimen 5 dry 125
Figure 5.43 - Specimen 5 dry, RC test, torsional mode 126
Figure 5.44 - Specimen 5 dry, NR test, torsional mode 127
Figure 5.45 - Wideband frequency sweep of specimen 5 partially saturated 128
Figure 5.46 - Difference between partially saturated and dry specimen 5 normalized transfer function 129
Figure 5.47 - Specimen 5 partially saturated, RC test, torsional mode 130
Figure 5.48 - Specimen 5 partially saturated, NR test, torsional mode 130
Figure 5.49 - Wideband frequency sweep of specimen 6 saturated 132
Figure 5.50 - Indusmin sand pore pressure coefficient B measurement results 133
Figure 5.51 - Specimen 6 saturated, RC test, axial mode 134
Figure 5.52 - Specimen 6 saturated, RC test, torsional mode 134
Figure 5.53 - Specimen 6 saturated, NR test, axial mode 135
Figure 5.54 - Specimen 6 saturated, NR test, torsional mode 135
Figure 5.55 - Specimen 6, flow test measured time intervals 136
Figure 5.56 - Specimen 6, flow test computed hydraulic conductivities 137
Figure 5.57 - Wideband frequency sweep of specimen 6 partially saturated 138

Figure 5.58 - Specimen 6 partially saturated, RC test, axial mode 139
Figure 5.59 - Specimen 6 partially saturated, RC test, torsional mode 139
Figure 5.60 - Specimen 6 partially saturated, NR test, axial mode 140
Figure 5.61 - Specimen 6 partially saturated, NR test, torsional mode 140
Figure 5.62 - Wideband frequency sweep of specimen 7 saturated 142
Figure 5.63 - Barco sand pore pressure coefficient *B* measurement results 142
Figure 5.64 - Specimen 7 saturated, RC test, axial mode 143
Figure 5.65 - Specimen 7 saturated, RC test, torsional mode 144
Figure 5.66 - Specimen 7 saturated, NR test, axial mode 144
Figure 5.67 - Specimen 7 saturated, NR test, torsional mode 145
Figure 5.68 - Specimen 7, flow test measured time intervals 146
Figure 5.69 - Specimen 7, flow test computed hydraulic conductivities 146
Figure 5.70 - Wideband frequency sweep of specimen 7 partially saturated 147
Figure 5.71 - Specimen 7 partially saturated, RC test, axial mode 148
Figure 5.72 - Specimen 7 partially saturated, RC test, torsional mode 149
Figure 5.73 - Specimen 7 partially saturated, NR test, axial mode 149
Figure 5.74 - Specimen 7 partially saturated, NR test, torsional mode 150

1.0 FOREWORD

The concept of using dynamic excitation to enhance fluid flow in a porous medium began to arise in the mid-twentieth century. Anecdotal evidence of well water level changes and increased oil recovery rates in existing reservoirs exposed to vibrations caused by earthquakes and passing trains started to infiltrate literature on the subject. This evidence motivated Russian scientists to attempt to increase oil recovery rates using field equipment capable of simulating seismic waves on crude oil reservoirs without fully understanding the mechanisms behind the observed phenomena. Not surprisingly, these blind efforts produced mixed results.

The initial spark of interest in the subject spurred numerous laboratory investigations throughout the latter half of the twentieth century to identify the mechanisms at work, and to develop field techniques for practical application of the technology. Although general understanding of the physical mechanisms leading to the observed fluid flow rate increases has improved with each new study, to date no complete theory has been proposed and limited field applications have occurred. The purpose of this research is to investigate the use of applied dynamic excitation to enhance fluid flow in a porous matrix.

1.1 Motivation

The primary motivation behind this research is to develop the application of seismic excitation as an enhancement to existing groundwater remediation technology including validation of a published mathematical model using experimental data. Proposed dynamic excitation models recently published in the literature are incomplete. Additionally, no study in the literature has specifically investigated the effects of pore fluid viscosity on wave propagation in soil. The model must be completed and validated before a working field application technique can be developed.

It is important to remember that the technique must be non-invasive. What is the point of using dynamic excitation to speed up groundwater remediation if the aquifer properties are altered by the applied dynamic forces to such a degree that it no longer produces water at a useable rate? Permanent deformations in the aquifer must be avoided.

The mechanisms behind enhanced flow are known, at least in theory. In addition, there appears to be two separate phenomena occurring during single-phase flow as opposed to multi-phase flow (including the vadose zone). Several prominent laboratory and field studies have been published; however, there are some deficiencies that facilitate the need for further investigation. First, many studies published in the literature are vague and don't include concise, detailed specifications of experimental parameters and equipment (i.e. it is impossible to replicate results because important information about the experimental setup is missing). Second, no study attempts to link a mathematical model of capillary trapping to experimental data. Model development appears to be nearly complete, and there are a few good sets of experimental results, yet no elegant link between the two exists. Third, the vast majority of the research into enhanced fluid flow has been focused on enhanced oil recovery with groundwater remediation included as an afterthought in the published work. And finally, groundwater flow and soil dynamics are two distinct areas of research. There is little in common between the two subjects and there is no consideration of soil dynamic properties in any of the reviewed papers. This study will attempt to bridge the gap between these two areas of research.

1.2 Research Objective

The objective of this research is to attempt to determine how dynamic excitation of a soil matrix affects saturated single-phase fluid flow. This question is investigated through an extensive literature review of previous studies conducted on this topic, as well as through experimentation designed to replicate the mechanisms responsible for this phenomenon.

Experimentation on coarse soil samples is conducted using a modified Stokoe-type resonant column device that allows a quantification of the effects of torsional and axial excitation, frequency of vibration, and strain level. Currently, there are no other resonant column devices in operation that can apply both torsional and axial excitation to the same specimen under unsaturated and saturated conditions. Therefore, the results of this study include several additional conclusions which have not yet been published in available literature. The shear and compression wave velocities and damping ratios are measured in both unsaturated and saturated conditions for two different sands. These measurements allow the comparison of the poisson ratio between drained and undrained soils. This ratio is often used

for the detection and delineation of oil deposits and may also serve as a tool for delineating NAPL contaminant plumes.

2.0 LITERATURE REVIEW

This section outlines previous studies of the effect of pore fluid viscosity on dynamic soil properties, the effects of seismic events on fluid flow in groundwater aquifers and oil extraction, as well as laboratory and field testing that applies these basic concepts to increased fluid flow in soil samples.

2.1 Effect of Pore Fluid Viscosity on Dynamic Soil Properties

There are two prominent methodologies in the literature for developing mathematical expressions for the damping ratio in soils proposed by Wilson (1988) and Gajo et al. (1996); however, both essentially arrive at the same conclusion. Excluding geometric effects, damping in soils is comprised of two components: skeleton damping ξ_s, and viscous damping ξ_v.

Following Biot's theory (Biot, 1956), Gajo et al. (1996) described wave propagation in a linear elastic porous medium by

$$\begin{bmatrix} \rho_{11} & \rho_{12} \\ \rho_{12} & \rho_{22} \end{bmatrix} \cdot \begin{bmatrix} u_{tt} \\ U_{tt} \end{bmatrix} + \begin{bmatrix} b & -b \\ -b & b \end{bmatrix} \cdot \begin{bmatrix} u_t \\ U_t \end{bmatrix} = \begin{bmatrix} c_{11} & c_{12} \\ c_{12} & c_{22} \end{bmatrix} \cdot \begin{bmatrix} u_{xx} \\ U_{xx} \end{bmatrix} \text{.....[2.1]}$$

where u and U are the absolute solid skeleton and pore fluid displacements, respectively (differentiated with respect to time t and distance x as indicated), and the constants ρ, b and c differ for the case of longitudinal waves versus torsional waves as defined in Table 2.1. The constants, ρ_s and ρ_f are the solid grain and pore fluid densities, respectively, τ is the tortuosity of the specimen which is related to the porosity of the specimen n, γ_f is the pore fluid specific weight, K_D is the hydraulic conductivity of the specimen, and the constrained modulus M, the coefficient α, quality factor Q and shear modulus G are determined using Equations [2.2] through [2.5].

Table 2-1 - Constant values in Biot wave propagation model

Constant	Longitudinal Wave	Torsional Wave
ρ_{11}	$(1-n)\rho_s + (\tau-1)n\rho_f$	
ρ_{12}	$-(\tau-1)n\rho_f$	
ρ_{22}	$n\rho_f + (\tau-1)n\rho_f$	
b	$\frac{n^2\gamma_f}{K_D}$	
c_{11}	$M + (\alpha-n)^2 Q$	G
c_{12}	$n(\alpha-n)Q$	0
c_{22}	$n^2 Q$	0

$$M = \frac{E(1-\nu)}{[(1-2\nu)(1+\nu)]} \quad \text{.....[2.2]}$$

$$\alpha = 1 - \frac{K}{K_s} \quad \text{.....[2.3]}$$

$$\frac{1}{Q} = \frac{n}{K_f} + \frac{(\alpha-n)}{K_s} \quad \text{.....[2.4]}$$

$$G = \frac{E}{[2(1+\nu)]} \quad \text{.....[2.5]}$$

In Equations [2.2] through [2.5], ν is Poisson's ratio, E is Young's modulus, K is the bulk modulus of the solid skeleton ($K = E/[3(1-2\nu)]$), K_s is the bulk modulus of the solid grains, and K_f is the bulk modulus of the pore fluid.

In Equation [2.1], all of the non-diagonal coefficients are non-zero, meaning the equations are coupled in three ways:

- inertial coupling due to inertial forces (ρ_{12}),
- viscous coupling due to interaction between pore fluid and solid skeleton (b), and

- mechanical coupling related to bulk compressibility's of the skeleton, grains and pore fluid (c_{12})

Inertial coupling is more pronounced when the relative motion between the skeleton and pore fluid is large (i.e. when viscous coupling is low). Higher inertial coupling leads to a decrease in wave velocity and amplitude variation. Viscous coupling complicates the dynamic interaction between the skeleton and pore fluid because it makes wave propagation dispersive (high frequency components travel faster, but are also more attenuated). An input excitation changes shape and apparent velocity when it travels through a specimen with a high degree of viscous coupling, therefore the propagation velocity is a function of the specimen hydraulic conductivity and the frequency content of the input wave.

There are two distinct cases involving viscous coupling: low viscous coupling and high viscous coupling. The transition from low to high viscous coupling occurs over a single order of magnitude of the specimen hydraulic conductivity, if input wave frequency content and specimen height remain constant. For example, if a specimen with a hydraulic conductivity of 10^{-2} *cm/s*, 10 *cm* height, and an input excitation frequency of 1 *MHz* were approximated as low viscous coupling, then a specimen with a 1 cm height, subjected to an input excitation frequency of 100 *kHz* would have to possess a hydraulic conductivity of 10^{-3} *cm/s* to also be considered a low viscous coupling system (all variables reduced an order of magnitude).

The inertial and viscous coupling parameters ρ_{12} and b are plotted for a uniform rounded coarse sand (see Appendix A for grain size distribution), shown as Figure 2.1.

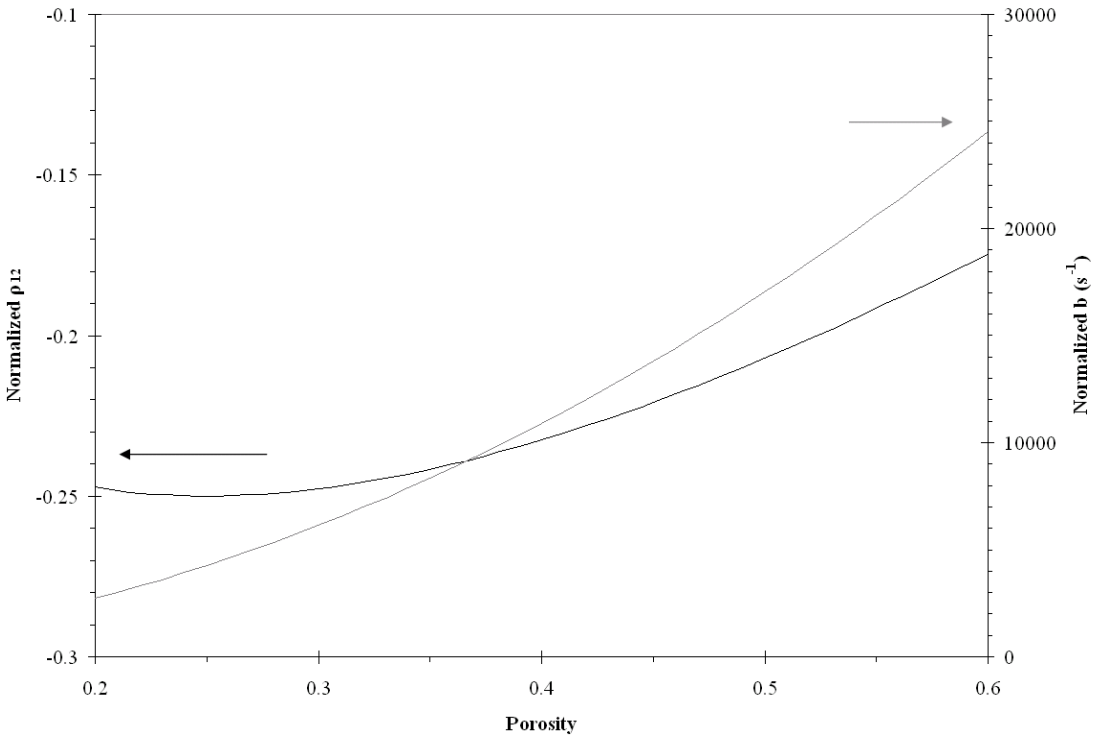

Figure 2.1 - Relationship between Biot parameters and soil porosity

The degree of viscous coupling depends on the relative motion between the soil grains and the fluid. Depending on the viscosity of the pore fluid, there exists a frequency threshold which represents the barrier between low- and high-relative motion between grains and pore fluid. For a soil-water system, low frequency excitation (less than 100 Hz) produces high relative motion (i.e. high viscous coupling); relative motion between phases begins to drop off at excitation frequencies higher than this threshold (Dusseault, 2007). In the case of low viscous coupling, the porous medium behaves like a single-phase medium where $b = \infty$ ($K_D \approx 0$). This case is typical in specimens with low hydraulic conductivity, or when the input excitation is composed of high frequencies (above the frequency threshold). On the other hand, high viscous coupling makes the porous medium behave as a two-phase medium where $b = 0$ ($K_D \approx \infty$) and a large degree of viscous damping is observed. This case is typical in specimens with high hydraulic conductivity, or when the input excitation is composed of low frequencies (below the frequency threshold).

Wilson (1988) tested three sand samples (unsaturated, water-saturated, and oil-saturated) using a Stokoe-type resonant column. Using the experimental results, the author

proposed that damping is a combination of energy dissipation in the soil skeleton and pore fluid. The total damping ratio ξ may be written as a sum of the viscous and skeleton damping components, as

$$\xi = \xi_s + \mu \cdot \chi(\gamma, \omega, d, L, m) \quad \text{.....[2.6]}$$

where ξ_s is the skeleton damping component, μ is the pore fluid viscosity, and χ is a function of shear strain γ, excitation angular frequency ω, specimen diameter *d*, height *L* and mass *m*.

If the viscosity of the pore fluid were changed from μ_1 to μ_2 and the other test parameters were held constant, the change in damping ratio ξ as a function of frequency *f* is given as

$$\Delta\xi \propto (\mu_1 - \mu_2) \cdot f \quad \text{.....[2.7]}$$

Therefore, the change in damping ratio is proportional to the change in pore fluid viscosity.

Bolton and Wilson (1990) derive a relationship for the viscous damping component ξ_v of material damping. Using the drag forces created as a particle moves through a fluid-filled tube, a relationship between ξ_v and pore fluid viscosity μ is developed, as

$$\xi_v = F_v\left(\frac{\mu\omega}{G}\right) \quad \text{.....[2.8]}$$

where ω is the angular frequency of excitation and *G* is the shear modulus of the soil matrix. The constant $F_v = 0.5 \cdot 10^3 \cdot \lambda^2$, where λ is a dimensionless parameter to describe the average void constriction of the sample.

In a completely dry soil sample, material damping is due to the skeleton damping ξ_s alone (the authors refer to it as hysteretic damping). Wilson (1988) found that the addition of water (μ = 1.0 centipoise (*cP*)) as a pore fluid produced a negligible addition to the material

damping ratio. The introduction of silicon oil (μ = 97.2 *cP*, an increase of two orders of magnitude) doubled the viscous damping component when compared to dry or water-saturated samples.

Shibuya et al. (1995) separated the relationship between load frequency *f* and damping ratio ξ for fine soils into the following three phases:

- creep, at frequencies up to 0.1 *Hz*,
- hysteretic, at frequencies between 0.1 *Hz* and 10 *Hz* (seismic loadings), and
- rheological, at frequencies above 10 *Hz*

During the creep phase, the damping ratio decreases as loading frequency increases. This phenomenon is attributed to the dependency of the stress-strain relationship on shear strain rate. During the hysteretic phase, the damping ratio remains constant for all load frequencies. This is attributed to the non-linear visco-elastic nature of the soil, and its ability to both store and dissipate the torsional wave energy in the seismic frequency range. Finally, during the rheological phase, the damping ratio increases with frequency. This is attributed to an increasing contribution of pore fluid viscosity (viscous coupling).

Figure 2.2 illustrates a conceptual diagram of damping ratio as a function of load frequency. Ellis et al. (2000) experimentally verified this relationship. Although the relationship is developed for a fine soil, it is expected that a coarse soil would mimic the behaviour of a fine soil as pore fluid viscosity is increased.

Ellis et al. (2000) used a resonant column to test three different types of sand of varying sizes. In total, four samples were prepared, one dry sample, and three samples saturated with water (μ = 1.0 *cP*), light silicon oil (μ = 29.2 *cP*), and silicon oil (μ = 97.2 *cP*). Essentially, the authors tried to fill in the data gap between water and silicon oil viscous damping coefficients originally determined by Wilson (1988).

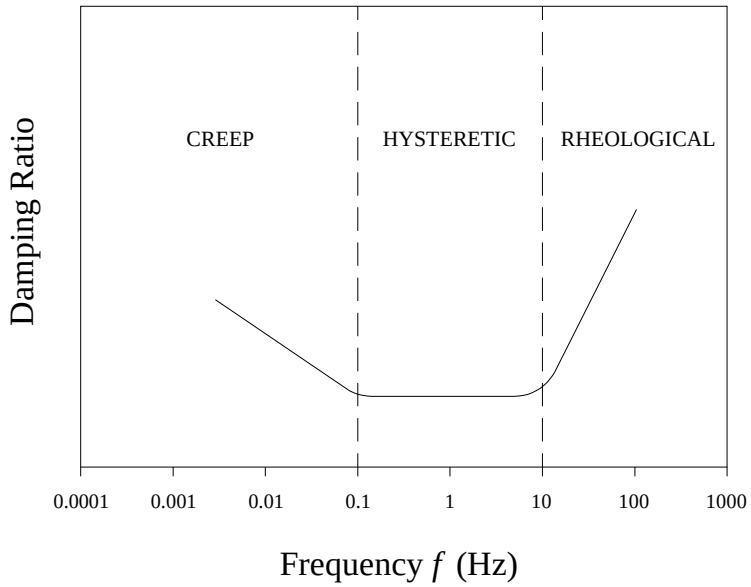

Figure 2.2 - Theoretical relationship between damping ratio and frequency (after Shibuya et al., 1995)

Several conclusions were reached as a result of the study:

- Shear modulus and excess pore pressure generation are practically independent of pore fluid viscosity
- Viscosity of water does not play a significant role in increasing viscous damping at resonant frequencies
- Viscous damping increases when:
  - shear strain γ is increased
  - sand particle size is decreased
  - viscosity of pore fluid is increased
- At large shear strains, small increases in damping ratio due to viscous damping are masked by a large increase of skeleton damping

More recently, Khan et al. (2007) achieved damping ratios of up to 12 % in a sand sample saturated with a bentonite mud at resonance, much higher than the 7 % damping ratio achieved in the dry sand sample.

Khan et al. (2007a) used a resonant column to excite sand samples with varying degrees of saturation of a viscous pore fluid (μ = 1135 *cP*). Assuming that the damping ratio in a soil

has a component due to skeleton damping and viscous damping, two sets of tests were designed to validate that theory.

In the first set of tests, the confinement pressure was varied at a constant shear strain. The results of the tests show that shear modulus remains virtually constant for all degrees of saturation, while the damping ratio increases dramatically at elevated saturation levels, indicating the addition of viscous pore fluid has little effect on the damping component due to the soil skeleton and a large effect on viscous damping. Using a micromechanical model of a simple cubic packing structure, the degree of saturation was related to the surface area of contact between the pore mixture and soil particles, with good correlation of the data.

In the second set of tests, the shear strain was varied at a constant confinement pressure. The results of the tests show a proportional increase in damping ratio as the degree of saturation of pore fluid is increased for strain levels up to approximately 5.0×10^{-2} %, indicating that viscous damping is strain-independent.

2.2 Response of Fluid Flow in an Aquifer to Seismic Waves

Hydrograph data has been recorded and published for many seismic events from as early as 1928; however, the magnitude 9.2 earthquake near Anchorage, Alaska, on March 27, 1964, was the most documented earthquake in history to that point in time. Changes in groundwater well levels were recorded in over 700 wells in the United States alone and many more world-wide (Vorhis, 1967). Since that time there has been a great deal of study on the effect of seismic waves on aquifer water levels.

In the majority of cases, increased fluid flow is the result of a change in hydraulic conductivity of the regional aquifer due to fracturing or re-settling of material.

The Pymatuning earthquake of September 25, 1998, near Jamestown, Pennsylvania, changed the groundwater flow system in the vicinity of the epicenter causing approximately 120 domestic water supply wells to go dry, while others reportedly experienced an increased yield – some even turning into flowing artesian wells. In addition, local streams with a significant contribution of baseflow due to groundwater seepage experienced an increase in flow, and local ponds fed by groundwater springs also experienced elevated water levels. The quality of water in the production wells was also affected; well owners reported changes in turbidity and colour, as well as a sulfuric odour. Some of the effects occurred almost immediately after the quake (within 24 hours), and lasted 10 months after the seismic event.

Most of the production wells which went dry were located at the top of a local ridge, while most of the wells which experienced an increase in yield were located at the base of the ridge. A cross section of the ridge geology and hydrogeology is shown in Figure 2.3.

The ridge acts like a hydrologic island, where groundwater is perched on top of the underlying shale bedrock and flows down to the surrounding valleys vertically through fractures in the shale layer and horizontally between formation layers. The rate of vertical flow depends on the hydraulic conductivity of the shale, which is generally quite low.

Fleeger (1999) concluded that the most plausible explanation is the earthquake increased the vertical hydraulic conductivity of the shale layers within the ridge either by increasing the number of fractures in the rock, or increasing the size of existing fractures. The increased hydraulic conductivity allowed groundwater to flow more rapidly from the top of the ridge to the surrounding valleys. This explains the rapid decrease in water levels in production

wells at the top of the ridge, and the rapid increase in water levels in production wells and ponds in the valleys, as well as the increased flow experienced by local streams fed by groundwater seepage.

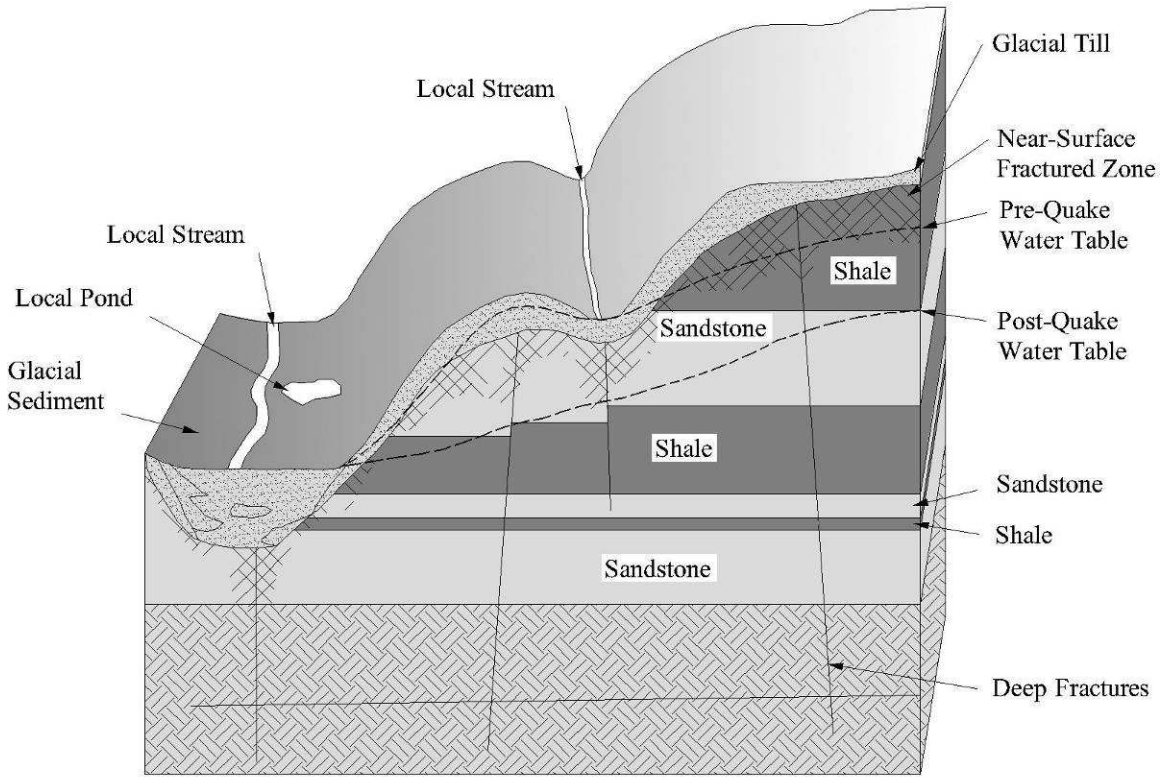

Figure 2.3 - Cross-section of ridge geology and hydrogeology
(after Fleeger, 1999)

A hydrologic model of the ridge groundwater system was created to simulate the hydrologic effects of the earthquake on the bedrock layer. By simulating the change in water levels before and after the earthquake, the vertical hydraulic conductivity in the shale layers is estimated to have increased between 10 and 60 times the initial values.

Manga (2001) analyzed streamflow data for five streams at varying distance from the epicenter of earthquake events which reported an increase in baseflow to the stream from groundwater sources. The data suggest that for these particular cases, increased streamflow was not caused by an increase in the hydraulic conductivity of the surrounding aquifer, but rather an increase in fluid pressure (i.e. increased hydraulic gradient) caused by liquefaction due to the dynamic strain induced by the earthquake.

These types of cases represent destructive events, where the properties of the aquifer are altered permanently. During a post-seismic response, the water level in a well or stream increases or decreases over a period of time until a new equilibrium is reached. Manga (2001) suggests that a temporary hydraulic gradient increase causes an initial step in the water level which dissipates over a period of time proportional to the initial hydraulic conductivity of the surrounding geological formation.

In terms of nondestructive mechanisms, Vorhis (1967) used the term hydroseism to describe all seismically-induced water-level fluctuations (not including tsunamis). A hydroseism may occur during the event (co-seismic) or following the event (post-seismic). During a co-seismic response, the water level in the well appears to oscillate at a seismic frequency. The mechanism behind this phenomenon is believed to be the expansion and contraction of the groundwater aquifer hydraulically connected to the well, causing an oscillatory pressure wave (Sneed, 2003).

Cooper et al. (1965) derived an analytic equation for the oscillation of the water level in a groundwater well due to seismic waves which compress and expand the aquifer and produce oscillatory pressure waves. For a groundwater well that is open to atmospheric pressure, non-flowing and screened across the entire thickness of a confined, homogeneous, isotropic aquifer, subjected to a steady-state oscillating pressure p_T, given by

$$p_T = \rho_w g(H + z) + p_0 \cdot \mathbf{sin}(\omega t - \varphi) \quad \text{.....[2.9]}$$

the ratio A of the maximum water level fluctuation x_0 to the static pressure head h_0 in the well bore is given as

$$A = \left[\left(1 - \frac{\omega r^2}{2\tau_r} \cdot \mathbf{Im}(\alpha(\omega)) - \frac{\omega^2 H_e}{g} \right)^2 + \left(\frac{\omega r^2}{2\tau_r} \cdot \mathbf{Re}(\alpha(\omega)) \right)^2 \right]^{-\frac{1}{2}} \quad \text{.....[2.10]}$$

where ρ_w is the density of water, $g = 9.81$ *N/kg*, H is the height of the water column in the well, z is the reference datum for the well, p_0 is the amplitude of the pressure head fluctuations, ω and φ are the angular frequency and phase angle of the wave, respectively, r is the well

radius, τ_r, S and d are the aquifer transmissivity, storativity and thickness, respectively, and $H_e = H + 3/8d$ is the effective height of the column of water in the well. The coefficient α is computed by

$$\alpha(\omega) = r \cdot \sqrt{\frac{\omega \cdot S}{\tau_r}} \quad \text{.....[2.11]}$$

As the period of the seismic wave decreases below the apparent well resonant frequency, the amplification *A* decreases rapidly, as shown in Figure 2.4.

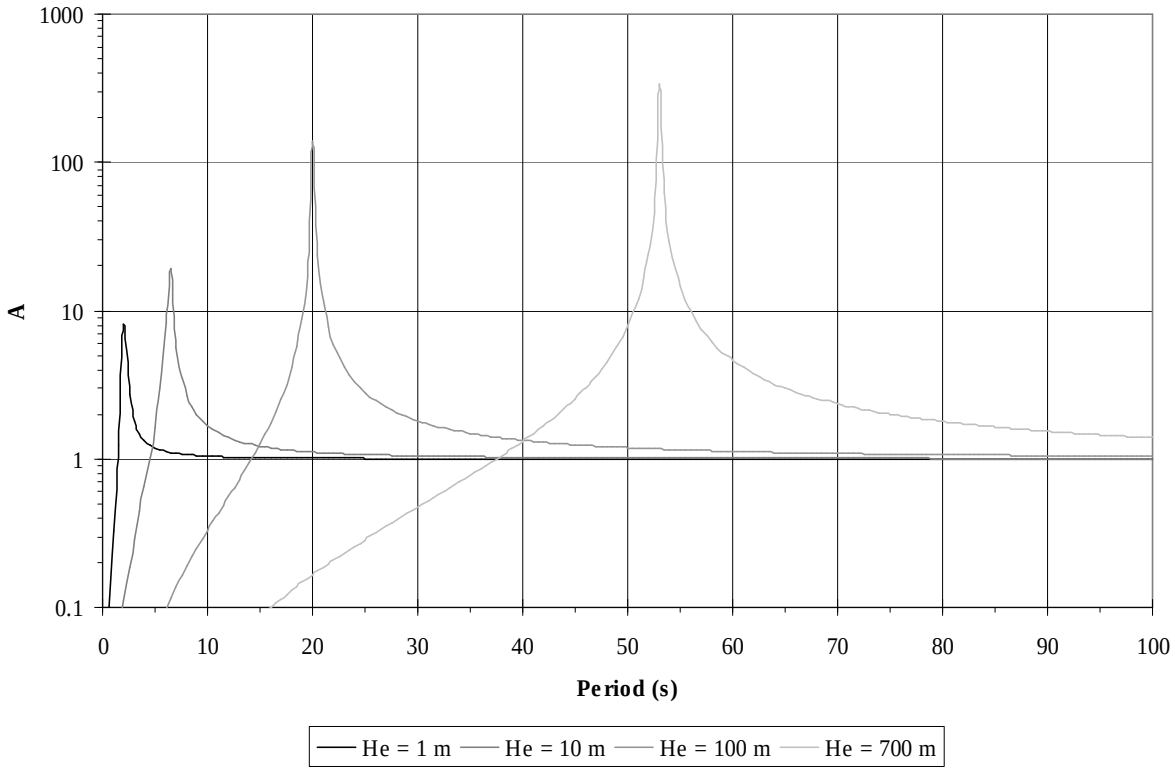

Figure 2.4 - Amplification of well pressure head fluctuation
(after Cooper et al. (1965))

For a confined sandstone aquifer (n = 0.30, d = 60 *m*, S = 0.0001, d_{10} = 0.06 *mm*) which is screened along the entire formation (r = 0.076 *m*), the resonant peaks of the well pressure head fluctuations are shown as a function of the period *T* of the oscillating pressure wave created by

compression of the aquifer during an earthquake event. For aquifers with large transmissivity τ_r (thick, highly permeable aquifers), resonant peaks occur at frequencies which are highly dependent on the effective water column height H_e.

2.3 Response of Oil Recovery to Seismic Waves

Changes in oil well production following earthquake events have been reported in literature for 70 years (Beresnev and Johnson, 1994). On January 7, 1938, an earthquake near the present-day country of Georgia caused a 45 % increase in oil production, however, no detailed quantitative analysis was provided. On July 21, 1952, an earthquake in Kern County in Southern California increased the pressure in several oil production wells, decreased the pressure in atleast one production well, and had no effect on others. Yet another earthquake on May 14, 1970, in Daghestan caused abandoned production wells to resume flow. Other production wells experienced a co-seismic increase in production, and then gradually returned to initial production levels over several months.

The limited data provided in the literature makes it nearly impossible to determine the actual mechanisms at work during oil production increases. Beresnev and Johnson (1994) state that it is "unclear whether [the oil production increases are] caused by the actual elastic wave effect or by rupture within the reservoir." Since oil production rate data is generally sparsely collected, there is no way to determine if production increases occur during the actual wave stimulation. It is likely that, similar to the changes in water well levels experienced after the Pymatuming earthquake of 1998, most reports of increased oil production in the literature are due to permanent deformation of local geological formations (Fleeger et al, 1999).

In terms of non-destructive mechanisms, capillary and gravitational forces are suspected to be the primary factors controlling the rate of migration (Beresnev and Johnson, 1994). Gravitational forces act on the density difference between the oil and surrounding pore fluid to form immiscible droplets which disperse in the groundwater. Capillary forces (due to surface tension) restrict the flow of immiscible droplets which become entrapped within pore spaces.

Flow of an immiscible fluid in a saturated matrix is restricted to continuous streams; thus, when the degree of saturation of oil S_0 in a reservoir falls below a threshold value, the oil

becomes immobile and the residual droplets are held in place by capillary forces (Odeh, 1987). Elastic wave stimulation reduces the surface tension of the immiscible fluid. In addition, elastic wave stimulation may reduce the viscosity of the oil due to a thermal energy increase in the medium from the absorption of wave energy.

Aarts and Ooms et al (1999) suggest that seismic stimulation creates dynamic transverse waves which travel along the pore throat walls in a soil matrix and induce higher pore fluid velocities; however, the results of their own experimental study into the phenomenon seem to disprove their theory. The proposed mechanism is analogous to peristaltic transport, commonly employed by organs in living organisms, where wave-like muscular contractions advance a fluid mass through a cavity. The peristaltic transport mechanism predicts higher velocities with increased intensity (amplitude of input waves) and decreased pore wall shear modulus. A simple experiment was carried out to assess the plausibility of peristaltic transport as a mechanism for enhancing fluid flow in a porous medium. A hole was drilled in a rubber stopper to simulate a pore throat, and the stopper was fitted in a chamber filled with water. The total head in the chamber was kept constant (similar to a constant head test), and a manometer tube was installed at the effluent port to measure hydraulic head (indirect measurement of fluid velocity). The head levels were monitored before, during, and after seismic pressure waves ($f = 20\ Hz$) were induced in the water. The experiment was repeated with three different rubber stoppers of varying shear moduli, and three different intensity levels.

The results of the experiment show that fluid velocity through the pore throat increased with intensity as the peristaltic transport model predicts; however, the fluid velocity is virtually independent of the pore throat shear modulus. The author concedes that the plausibility of the peristaltic transport model as the mechanism for increased fluid flow in a porous medium is cast in doubt as a result of this study. It is suggested that a higher pressure differential in the water induced by the low frequency waves may be responsible for the observed increase in flow rates, which is more congruent with conclusions in the literature of the response of fluid flow in aquifers to seismic waves. It is further suggested that experimentation should be repeated with pore throats of varying diameter; although the recommendation was never carried out, the results may have shown that the simple Darcy flow equation may explain the

increased pore fluid velocities as hydraulic gradient increased due to the induced pressure waves.

Beresnev and Iassonov (2003) propose that two main mechanisms are responsible for increased NAPL flow using seismic stimulation – non-Newtonian fluid rheology and capillary trapping. A non-Newtonian fluid is considered to be a viscous fluid that requires a minimum applied stress before it deforms. In a reservoir, crude oil often exhibits the properties of a non-Newtonian fluid, where a yield stress must be applied before it can be set in motion. The authors develop a yield-stress model for an elongated spherical droplet in order to predict the minimum pressure gradient ΔP_{crit} required to set the droplet in motion, given as

$$\Delta P_{crit} = \frac{2\tau_0}{R} \quad \text{.....[2.12]}$$

where τ_0 is the yield stress of the pore fluid and R is the pore throat radius. The required intensity I_c (W/m^2) of the applied wave is

$$I_c = \frac{\rho V}{2\omega^2 \rho_f{}^2} \Delta P_{crit}^2 \quad \text{.....[2.13]}$$

where ρ and V are the average density and sound velocity in the saturated porous medium respectively, ω is the angular frequency of input wave motion and ρ_f is the pore fluid density. Equation [2.13] is only applicable for frequencies in the seismic bandwidth ($f < 100$ *Hz*). The authors point out that for systems where a large pressure gradient already exists, the addition of seismic stimulation does not affect the fluid flow rate in the medium.

Capillary trapping has a similar effect on isolated immiscible droplets in a soil matrix. A critical pressure gradient ΔP_{crit} is required before the meniscus failure and droplet mobility, given as

$$\Delta P_{crit} = \frac{2(p_c)_{crit}}{L} \quad \text{.....[2.14]}$$

$$(p_c)_{crit} \leq \frac{2\sigma}{R} \quad \text{.....[2.15]}$$

where $(p_c)_{crit}$ is the critical capillary pressure, L is the length of the immiscible fluid droplet, σ is the surface tension of the droplet and R is the pore throat radius. Using this model, for small droplets (i.e. low residual oil saturation) the critical pressure gradient required to mobilize the droplets is large ($(p_c)_{crit} \leq 400\ Pa$); hence, mobilization may be virtually impossible if capillary trapping is the mechanism at work.

Hilpert et al. (2000) develop a model for NAPL droplet resonance in a capillary tube and propose that droplet resonance can be used as a mechanism for inducing entrapped droplet mobilization. In a multi-phase system of capillary tubes and two immiscible pore fluids, the non-wetting fluid forms menisci at the contact area between the two fluids. The droplet of non-wetting fluid is referred to as a residual, as it cannot flow under a pressure gradient due to the capillary forces holding it in place. At the microscopic level, soil particle surfaces are rough and sometimes composed of varying chemical compounds. Both of these factors pin the contact lines of a residual droplet, allowing it to resonate. Under dynamic excitation of the capillary tube walls, droplet resonance occurs due to pinned contact lines that force the menisci to resonate. The angular resonant frequency ω_0 of a pinned droplet in a capillary tube is

$$\omega_0 = \sqrt{\frac{4\sigma \sin\theta_0 (1+\sin\theta_0)^2}{\rho_f R_0^2 L}} \quad \text{.....[2.16]}$$

where σ is the surface tension at the immiscible fluid interface, ρ_f is the non-wetting droplet fluid density, R_0 is the capillary tube radius, L is the droplet length and θ_0 is the contact angle formed at the meniscus.

Assuming a simple cubic packing of spherical soil particles, and further assuming an average cylindrical droplet occupies 5 contiguous pore spaces (Hilpert et al., 2000), R_0 and L can be approximated by

$$R_0 = 0.287D \quad \text{.....[2.17]}$$

$$L = 3.66D \quad \text{.....[2.18]}$$

where D is the average diameter of the soil grains, as shown in Figure 2.5. Thus, Equation [2.16] reduces to

$$\omega_0 = \sqrt{\frac{13.268\sigma \sin\theta_0 (1+\sin\theta_0)^2}{\rho_f D^3}} \quad \text{.....[2.19]}$$

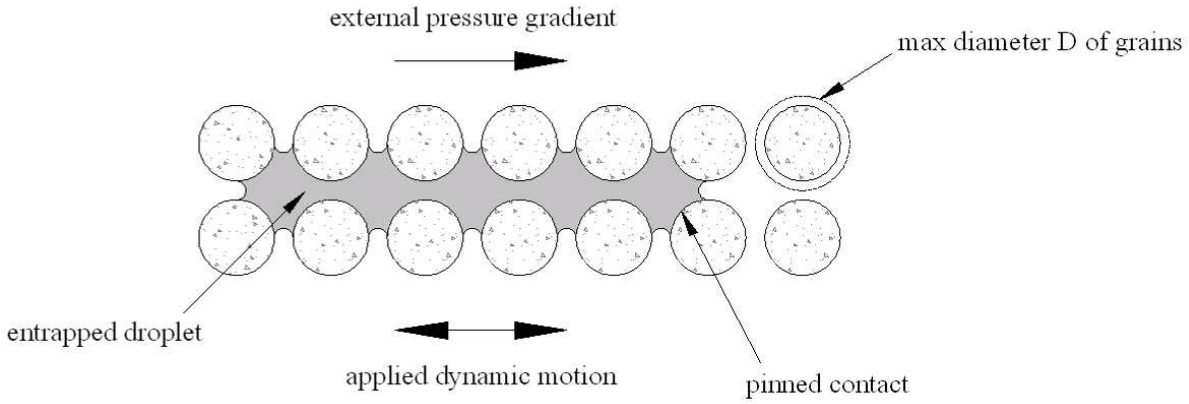

Figure 2.5 - Entrapped droplet with pinned contact

To determine the response of residual NAPL droplets in a water-saturated soil matrix, the properties of trichloroethylene (TCE), a common dense NAPL, are used (ρ_f = 1460 *kg/m*^{3}, σ = 30 *mN/m*). Figure 2.6 illustrates droplet resonant frequency as a function of soil grain diameter using contact angles of 20º and 90º.

Beresnev (2006) further develops the yield-stress model to describe the mobilization of residual NAPL droplets in a porous media using a methodology similar to Hilpert et al. (2000); however, the pore size considered is dramatically smaller to simulate pore space in a typical oil reservoir sandstone, and a more detailed look at required accelerations (energy input) of the soil matrix is undertaken.

Residual NAPL droplets act as a yield-stress fluid, a certain amount of excess external force is required (either through an external pressure gradient or an inertial force provided by the oscillation of the pore walls) before the capillary force holding the droplet in place is

overcome, and the droplet is free to move. When a soil matrix is subjected to seismic excitation, both the pore walls and the residual droplet oscillate. Unless the pore walls are oscillating at the same frequency as the droplet, the superposition principle applies, and destructive/constructive interference complicates the process of mobilization.

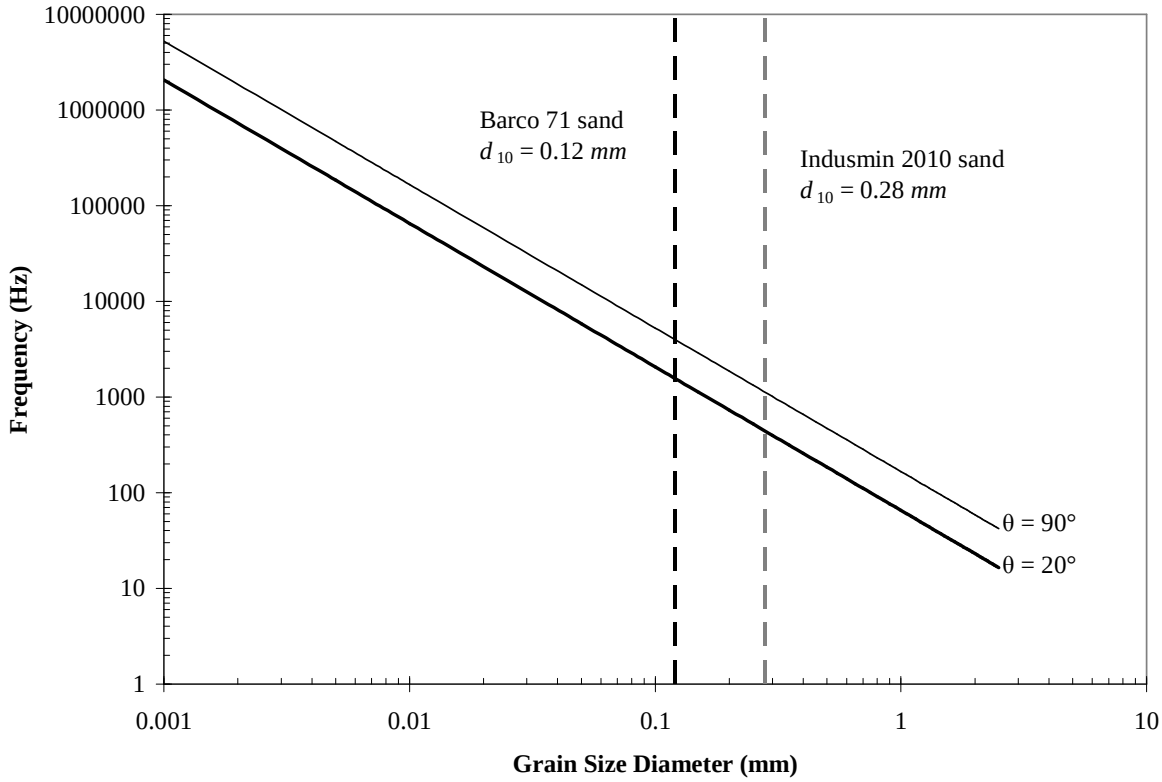

Figure 2.6 - Residual NAPL droplet resonant frequency as a function of grain size diameter

Beresnev (2006) also notes that at very high frequencies, mobilization by dynamic excitation is difficult, as the destructive interference caused by the pore wall vibration and the motion of the residual droplet restrict the available external force to values much lower than required to overcome the capillary force holding the droplet in place. This effect may be compensated for by increasing the amplitude of the applied dynamic excitation. Several numerical simulations were run to predict the required acceleration of soil particles to induce mobilization of residual droplets. In the first set of simulations, the maximum pore radius considered was 0.1 *mm*, and the external pressure gradients were set at two levels: nearly at the required gradient for mobilization, and half of the required gradient for mobilization. The

results indicate that when the external pressure gradient is nearly enough to mobilize the droplet, an acceleration of over 3*g* is required at a frequency of 100 *Hz*; this value increases to over 23*g* when the external pressure gradient is halved. The cutoff frequency for each test run was 100 *Hz* and 200 *Hz*, respectively.

Two additional iterations were performed, the first used a much wider pore space, with a maximum pore radius of 1 *mm* and the second used a pore space with smoother walls (lower capillary force holding the droplet in place). For both iterations, the external pressure gradient applied was nearly at the required value to mobilize the droplet. For the first iteration, an acceleration of 0.4*g* is required at a frequency of 1 *Hz* to mobilize the droplet, with a cutoff frequency of 25 *Hz*. For the second iteration, the required acceleration was negligible at a frequency of 1 *Hz*, with a cutoff frequency of 0.5 *Hz*.

While current technological limitations prevent the creation of in-situ dynamic excitations of the required acceleration amplitudes for mobilization of residual oil droplets in sandstone typical of oil reservoirs, the application of in-situ dynamic excitations by surface shakers may be a viable groundwater remediation technology.

2.4 Laboratory Studies of the Effects of Seismic Stimulation on Fluid Flow

The earliest known laboratory study into the effects of dynamic excitation on fluid flow was conducted by Duhon (1964) who used high-frequency vibration (1 – 5.5 *MHz*) to investigate the displacement of oil by water in sandstone.

A sandstone core (r = 0.203 *m*, h = 0.046 *m*, n = 0.214) was used to test the effect of ultrasonic stimulation on the displacement of various immiscible pore fluids by water. Three different fluids (diesel oil, μ = 76.2 *cP*; core test fluid, viscosity not reported; SAE 10 oil, μ = 65 *cP*) were subjected to ultrasonic frequencies of 1.0, 3.1, and 5.5 *MHz*. The intensity of the wave stimulation is not specified. The total recovery of fluid, as a percentage of initial mass, was recorded for each test and compared with the base recovery value (from water displacement under no ultrasonic stimulation). The results are summarized in Table 2-2.

Table 2-2 - Recovery values for different pore fluids at various frequencies of excitation (after Duhon, 1969)

Frequency (MHz)	**Measured Recovery (%)**					
	Diesel Oil		Core Test Fluid		SAE 10 Oil	
1.0	60.1	+9.5	61.4	+14.7	40.5	+7.5
3.1	56.5	+5.9	53.9	+7.2	38.6	+5.6
5.5	53.1	+2.5	53.1	+6.4	38.3	+5.3
Base Recovery	50.6	--	46.7	--	33.0	--

High-frequency vibration increases the recovery of immiscible pore fluids during displacement by water by up to 15 %. Maximum recovery occurred at a stimulation frequency of 1 *MHz* for all three pore fluids. From these results, it is also possible to conclude that recovery values depend on the viscosity of the pore fluid. Higher viscosity fluids (i.e. SAE 10 oil) have much lower recovery values than lower viscosity fluids (i.e. core test fluid), even in the case of base displacement with no stimulation.

The water-oil ratio (WOR) during displacement of the pore fluid was also measured for each frequency and compared with the base displacement test (under no ultrasonic stimulation). The results indicate that ultrasonic stimulation during water displacement of pore fluids reduces the WOR (i.e. increased pore fluid mass in effluent) during the initial phase of

the test. Eventually, the WOR reaches values obtained from the base displacement test as the total mass of recovered pore fluid reaches a plateau.

At the time of study, equipment was not available to produce ultrasonic stimulation at frequencies less than 1 *MHz*. The author speculated it was likely a higher recovery value could be obtained by stimulating the sample at frequencies less than 1 *MHz*. The maximum recovery values of any pore fluid appear to occur at one frequency of excitation, insinuating recovery is dependent on some type of resonance phenomenon. Duhon (1964) suggests the main mechanisms behind increased oil recovery and reduced WOR are pore throat expansion caused by induced pressure waves as well as an increase in extraction energy caused by cavitation within the pore space due to the dynamic excitation.

Beresnev and Johnson (1994) report a Russian study conducted using an electromagnetic shaker to produce vibrations in a saturated, unconsolidated sand (the frequency of excitation is not reported). The author uses the term sono-capillary effect to describe the accelerated movement of fluids through pore spaces when subjected to dynamic excitation. Oil displacement occurred more rapidly (one-third the duration) and with greater efficiency (up to 15%) in vibrating the soil compared with the stationary sample.

Several studies have investigated the effects of dynamic excitation on viscosity and surface tension of fluids (reported by Beresnev and Johnson; 1994). One study measured oil viscosity after exposing it to dynamic excitation and found a decrease of 25% compared to initial values. Another applied dynamic excitation to a sample of transformer oil and found that surface tension of the fluid is a function of frequency of vibration. A later study investigated the influence of dynamic excitation on polymer viscosity by exposing a sample of the fluid to continuous vibration at 880 *kHz* for a duration of 20 minutes, which reduced the polymer viscosity by six-fold.

Alvarellos (2003) conducted a study of the effect of dynamic excitation of a droplet in a capillary tube. For this study, a simplified form of Equation [2.19] (originally developed by Hilpert et al. (2000)) to describe the resonant frequency of a residual droplet with pinned contact lines is used:

$$\omega_0 = \sqrt{\frac{16\pi\sigma}{\rho_f V_0}} \quad \text{.....[2.20]}$$

where σ is the surface tension of the pore fluid, ρ_f is the droplet fluid density and V_0 is the volume of the residual droplet. Assuming simple cubic packing, Equation [2.20] can be reduced to

$$\omega_0 = \sqrt{\frac{99.931\sigma}{\rho_f D^3}} \quad \text{.....[2.21]}$$

To compare the values of resonant frequency predicted by Equation [2.21] with those of Equation [2.19], the properties of TCE are utilized again. The resonant frequency of a residual droplet as a function of soil grain size diameter is shown as Figure 2.7. Alvarellos' model predicts higher resonant frequencies in comparison to Hilpert's model.

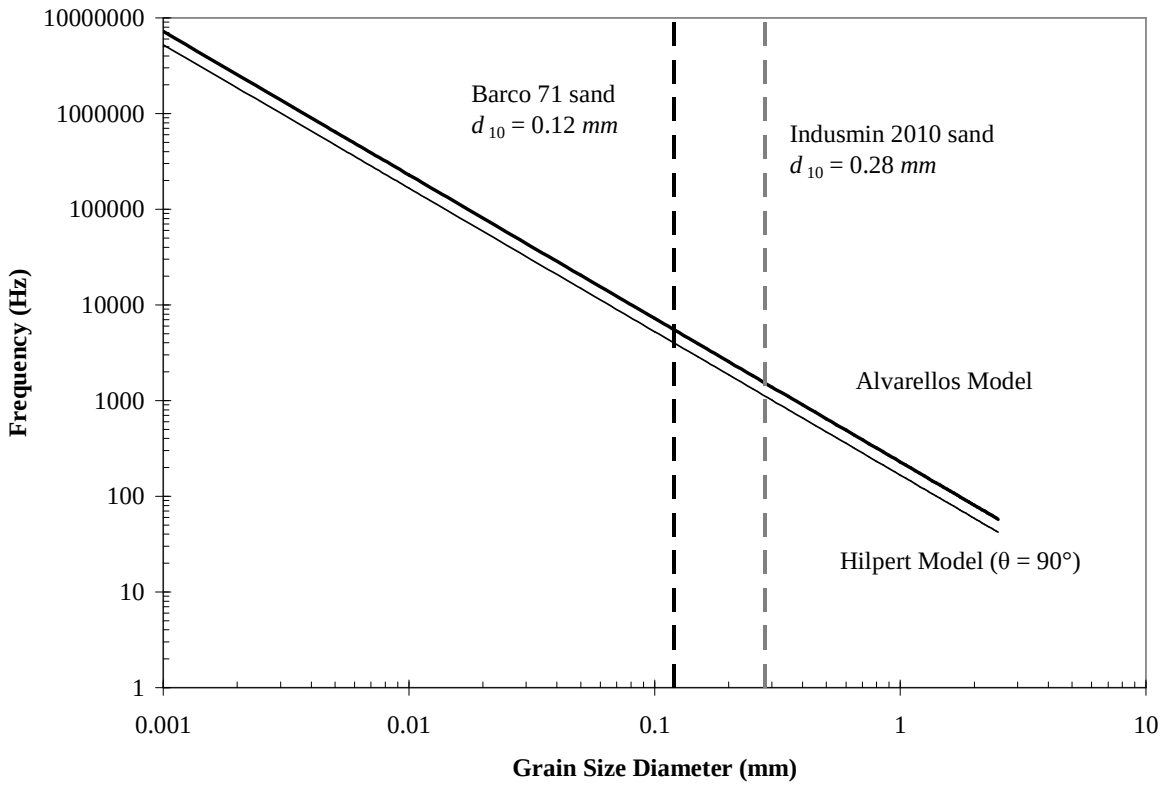

Figure 2.7 - Comparison of residual droplet resonant frequency predicted by Alvarellos and Hilpert

Alvarellos (2003) conducted three sets of experiments. In the first set, water droplets of varying wetted length (i.e. varying volume) from 0.018 *m* to 0.05 *m* are placed in a glass capillary tube, and the tube is subjected to axial dynamic excitation (f = 30 *Hz*). The inclination angle of the tube is increased until droplet mobility due to gravitational force is observed. For all droplet volumes, the inclination angle at droplet mobilization was up to 40 % lower compared to the case of no applied dynamic excitation.

In the second set of experiments, the weight component of the droplet was varied by changing the capillary tube radius and angle of inclination, as well as the droplet volume. The capillary tube was subjected to axial dynamic excitation at frequencies between 10 and 200 *Hz*. Initially, the amplitude of vibration was set at low levels (initial capillary tube axial velocity of 0.1 cm/s) and then increased until droplet mobilization was observed. The results show that a 10 % decrease in droplet weight requires an excitation amplitude increase of nearly 300 % to cause droplet mobility.

In the third set of experiments, both water (σ = 72.75 *mN/m*) and isopropyl alcohol (σ = 23.70 *mN/m*) droplets are placed in a capillary tube filled with air. Dynamic pressure differential excitation is induced by an oscillating air pump attached to the capillary tube ends. At initial conditions, both menisci of a water droplet are convex outward. As the pressure wave approaches, the meniscus facing toward the wave turns from convex to concave, while the meniscus facing away from the wave becomes even more convex. If the wave direction is inverted, the opposite effect occurs. As long as the droplet is stationary, any exterior pressure gradients force the menisci of the water droplet to change shape (redistribution of capillary forces) to counteract the added pressure force. In effect, the droplet undergoes resonance of meniscus curvature. In the experiments using an alcohol droplet, the meniscus curvature does not change; however, the contact lines change position as oscillation occurs. The alcohol droplet does not experience resonance, but rather relaxation, as the meniscus curvature does not change.

The main conclusions of this study are that an immobile droplet in a capillary tube acts as a single degree-of-freedom system which resonates at a natural frequency given by Equation [2.21]. The droplet is analogous to a mass-spring-dashpot system; the droplet is the mass, surface tension is the spring stiffness and viscous forces along the wetted perimeter of the droplet cause damping. In order for droplet mobilization to occur, the sum of the forces acting

to displace the droplet (gravity, pressure and inertia) must overcome the sum of the forces holding the droplet in place (surface tension and viscosity).

Chrysikopoulos and Vogler (2002) studied the effect of acoustic fluid pressure waves on both dispersion of aqueous phase contaminants and dissolution of immiscible contaminants. A glass column was packed with glass beads and held in place with Teflon screens and end caps. A microprocessor pump maintained a constant flow of degassed water through the column, while a pressure transducer provided dynamic fluid pressure excitations in a reservoir attached to the influent end of the column. Ports near the influent and effluent ends of the column allowed contaminant injection and effluent extraction, respectively.

In the first experiment, a pulse of bromide tracer was injected at the influent end of the column, while a pore fluid flow rate of 1.48 *mL/min* (2.4×10^{-8} m^3/s) was maintained in the column, and dynamic fluid pressure waves were generated with constant maximum amplitude of 565 *Pa* over a frequency range of 60 *Hz* to 245 *Hz* using a specially designed pressure transducer. The tracer breakthrough curves for each frequency were compared with the breakthrough curve where no dynamic excitations were applied. The results show that tracer velocity increased by a maximum of 12 % at an excitation frequency of 60 *Hz*, compared to the base case of no excitation, with diminishing velocity increases at higher frequencies. The authors also noted an increase in the dispersion coefficient *D*; however, they acknowledge that this increase is solely due to the increased velocity of the tracer dye in the column. It was impossible to interpret any changes in material longitudinal dispersivity α_L, tortuosity τ, or the tracer diffusion coefficient D_m.

In the second experiment, a small mass of TCE was injected at the middle of the column and allowed to equilibrate before a pore fluid flow rate of 3.25 *mL/min* (5.4×10^{-8} m^3/s) was applied. Dynamic fluid pressure waves were generated both at a constant amplitude of 812 *Pa* over a frequency range of 60 *Hz* to 245 *Hz*, and over an amplitude range of 500 to 1625 *Pa* and a frequency of 245 *Hz*. This experiment was repeated using two different diameter glass beads (1 *mm* and 2 *mm*). The effluent concentrations during dynamic excitation were compared with effluent concentrations obtained where no excitation was applied to determine the effects of the dynamic fluid pressure waves on the DNAPL mobility. When pressure amplitude was held constant over the entire frequency range tested, significant increases in

effluent DNAPL concentration occurred at some frequencies, while no increase was observed for others.

The effluent pressure was monitored and although the inlet pressure amplitude remained constant at 812 *Pa* throughout the experiment, effluent pressure varied over the frequency range tested, with peaks as high as 3500 *Pa*. While the authors offer no explanation for this phenomenon, it may be due to resonant frequencies of the bead column. When excitation frequency was held constant, the effluent DNAPL concentration increased linearly as pressure amplitude increased. The different glass bead sizes appeared to have little effect on either set of results.

Roberts et al. (2001) performed a series of laboratory studies to determine the effects of seismic wave excitation on mobilization of DNAPL in a sandy saturated aquifer. A column of sand was packed into a horizontal triaxial chamber under an effective confinement pressure of 415 *kPa* and saturated with deionized, degassed water. Water flow through the column was controlled with a constant-flow rate pump at varying rates between 5 *mL/min* ($8x10^{-8}$ m^3/s) and 65 *mL/min* ($1x10^{-6}$ m^3/s), while axial dynamic excitations were generated with a magnetostrictive actuator by producing sinusoidal waves between 25 *Hz* and 100 *Hz*, at strain levels between $1.3x10^{-5}$ % and $1x10^{-4}$ %. The sand column was injected with 7 *mL* of reagent-grade TCE near the inlet of the column and allowed to equilibrate with the pore water for several minutes before experimentation began.

In the first experiment, flow was initiated at 5 *mL/min* and continued until the TCE concentration in the effluent reached a steady-state value near the theoretical saturation limit in water (dissolution of free-phase TCE to dissolved phase). The flow rate was later doubled, with no increase in TCE concentration. In a later experiment, the flow rate was incrementally increased up to 65 *mL/min* (approximately one pore volume per minute) with no noticeable increase in TCE concentration, and in fact, the authors noticed a decrease in concentration most likely caused by a shorter time interval for the free-phase TCE to dissolve in the fast-moving pore water. One major conclusion of the study is that pore water flow rates have little to no effect on the removal rate of DNAPL in a soil matrix, which is consistent with observations from most pump-and-treat groundwater remediation projects. Mobilization of the entrapped NAPL droplets occurs when the ratio of viscous forces (acting on the droplet by passing fluid) to capillary forces (acting to hold the droplet in place) is high; this ratio is known as the

capillary number N_c. For each NAPL/porous matrix combination, there is a unique capillary number which specifies the condition for mobilization; simply increasing the flow rate alone will not reduce the capillary number of an entrapped droplet.

After the TCE concentration had reached steady-state in the first experiment, seismic waves at frequencies of 25 *Hz*, 50 *Hz*, 75 *Hz* and 100 *Hz* were applied to the sample for durations of 7 minutes each at a constant strain level of 1.2×10^{-2}%. For excitation at 25 *Hz*, 50 *Hz*, 75 *Hz* and 100 *Hz*, the concentration of TCE in the effluent surpassed the theoretical saturation limit by 109 %, 127 %, 155 % and 64 %, respectively, due to the presence of free-phase TCE in the effluent. The increase was noticeably lower for the 100 Hz stimulation, and the authors concluded that frequencies above this value would have a diminishing effect on DNAPL mobility.

In the second experiment, the effluent TCE concentration had noticeably decreased due to the removal of TCE mass in the first experiment; however, the effluent concentration still maintained a steady-state. For this experiment, seismic waves at a frequency of 50 *Hz* were applied for durations of 7 minutes at strain levels between 1.3×10^{-3} % and 1.3×10^{-2} %. The authors observed free-phase TCE in the effluent for strain levels above 1.2×10^{-2} %, and conversely, no significant increase in effluent TCE concentration for strain levels below 4×10^{-3} %.

For the third experiment, the effluent TCE concentration had again decreased, however still maintained steady-state levels. The authors applied a seismic wave at a frequency of 50 *Hz* continuously for 35 minutes at a strain level of 1.2×10^{-2} %. The effluent TCE concentration rose well above the saturation limit initially, but then leveled off to a value near saturation until the wave source was shut off. The fourth experiment was similar to the third, with the wave stimulation lasting a total of 50 minutes. The results of the fourth experiment initially showed a large spike in the effluent TCE concentration to a level just above saturation, but unlike the third experiment, the concentration returned to its original value before the stimulation had ceased. The authors speculated that only about 10 % of the original TCE mass remained in the column at that point, and that the remaining mass had formed residual pockets and ganglia with little free-phase mass.

Overall, an estimated 92 % of the original TCE mass was removed from the column by the end of this study. The authors estimated that during seismic stimulation, TCE recovery

rates averaged about 5 % per hour, compared to an average recovery rate of 1.8 % with fluid flow alone. The authors do not offer an explanation of the mechanisms at work behind the increased DNAPL flow, but rather refer to previous studies to infer possible mechanisms.

2.5 Field Applications of Seismic Stimulation on Fluid Flow

In situ application of low-frequency seismic waves are employed at many oil production sites around the world for rehabilitation of production wells. This practice was first instituted in the mid-twentieth century in the United States and Russia. The waves act to remove the buildup of mud or other deposits which lower the permeability of the geological formations which surround the well. There are several companies in North America which offer tools and expertise to aid in field applications of pressure pulsing technology, including Applied Seismic Research (Texas), PerfClean (Texas), Sonic Production Systems (Idaho), Prism Production Technologies (Edmonton) and Wavefront Environmental Technologies (Edmonton).

Prism Production Technologies claim pressure pulsing technology (PPT) is a viable approach to enhance the flow rate, overcome capillary and mineral blockages, and reduce the magnitude of advective instabilities (Dusseault, 2002). The mechanism responsible for producing these effects is the creation of slow-moving porosity dilation waves by pulsing a fluid (water) through an injection well into an oil reservoir at very low frequencies (0.1 – 1 *Hz*). Three methods of field applications of PPT are employed:

- application of reservoir-wide continuous field stimulation (CFS) through a single well,
- application of borehole dynamic pulse workover technology (DPWT) through a single well to re-habilitate poorly-flowing production wells, and
- application of DPWT for treatment chemical injection.

Reservoir-wide CFS involves installation of a pressure-pulsing device in a selected well, where a volume of fluid is pushed out into the surrounding soil matrix over a time period of about a second, followed by a recharge stroke over a longer time period. The fluid pulses reorganize soil particle structure in the immediate vicinity of the well and also create porosity dilation waves which propagate outwards radially from the source into the medium. Permanent deformation occurs near the pulsing source, while elastic deformation occurs at

further distances as the soil particles return to their original position after the dilation wave has passed. As a result of the deformation energy introduced by the pulsing device, fluid flow increases due to an increased hydraulic gradient in the reservoir, reduced capillary barriers and less pore-throat blockage.

Borehole DPWT also uses a pressure-pulsing device installed in a single borehole, and follows the same methodology of pulsing a fluid through the surrounding soil matrix. However, unlike CFS, DPWT pulsing lasts for up to 2 hours after which it is suspended and the pressure in the borehole is measured to determine what effect (if any) the pulsing has on the reservoir. If the measured pressure does not indicate any improvement in well flow rates, the cycle may be repeated up to 24 hours after the initial pulsing. DPWT has the effect of deforming the localized soil matrix to increase the permeability; essentially, the pressure-pulsing un-clogs the pore throats.

Current practice includes the use of chemical additives to lower the viscosity or surface tension in heavy oil deposits to increase fluid mobility. By combining the use of borehole DPWT and chemical addition, greater well rehabilitation is realized. The pulsing opens up closed pore throat space, allowing enhanced penetration of the chemical into the soil matrix. Greater mixing of reservoir fluid and chemical additive are achieved not only by the pulsing of liquid into the soil matrix, but also during the recharge cycle, when the pore fluid is drawn back into the pressure-pulsing device. Finally, DWPT limits channeling of the chemical additive within the reservoir, allowing a greater interface area for mixing between pore fluid and chemical.

DPWT has been used in field applications in Canada since 1998. As understanding of the mechanism behind flow enhancement has increased, the success rate of the technology has also increased (currently greater than 90 %) (Dusseault, 2002). The first CFS field trial was held in 1999, using a pressure-pulsing device (without an injection fluid) in a single injection well for a heavy oil reservoir 580 *m* below the surface. The porosity of the reservoir matrix was estimated at 0.3 while the degree of oil saturation was estimated to be 0.88. After about 11 weeks of continuous stimulation, falling production rates in 13 surrounding production wells had changed to rising production rates with an overall increase in oil production of 37 %. The injection well itself became the highest-producing well in the vicinity of the CFS test. CFS

technology was used twice more, each time having the same result of increased oil production in wells with falling production rates.

CFS technology has also been used in a shallow aquifer to enhance the removal of a viscous resin LNAPL, with the removal rate increasing by a factor of 20 in some instances (Dusseault, 2002). The author speculates that the mechanism behind the enhanced removal is lowering the capillary barriers holding the resin in the aquifer matrix.

Limited studies of in-situ seismic stimulation of underground oil reservoirs with the use of surface vibrators have also been conducted during last 30 years. Vibrators weighing 20-30 tons operating at a frequency within the seismic bandwidth are currently used at many oilfields in Russia. Near the country of Georgia, 20-ton vibrators were placed 250 *m* from a production well tapped into a depleted reservoir (Beresnev and Johnson, 1994). The reservoir thickness was reported as 10 *m*, and located 1200 *m* below the surface. The percentage of oil in the production well increased from 10 % before the stimulation, to 20 % during stimulation. The vibrations lasted 20 minutes each day during the test interval and were reported to cause elevated oil percentages in production wells for up to 60 days after stimulation. The tests were conducted the following year with the same results. Beresnev and Johnson (1994) speculate that vibration of reservoir fluids from surface waves increases the rate of migration of sparse immiscible fluid droplets.

2.6 Summary

The idea of using dynamic excitation to alter fluid flow in soils originally came from anecdotal evidence of oil and groundwater production rate fluctuations following seismic events. The literature shows that earthquakes are more likely to cause permanent deformations of the formation (i.e. fracturing, compaction, etc.) which alter fluid flow rates; however, subsequent research has shown that non-destructive dynamic excitation could potentially be used to change flow rates in certain conditions.

According to previous works in the literature, increased single-phase flow relies on the viscous coupling of the pore fluid and the solid skeleton of a porous matrix. The out-of-phase motion between the solid and fluid components gives an added inertial component to the fluid flow and causes a standing wave to form in the pore fluid. The passing wave in the soil

skeleton also temporarily increases the porosity on a local scale, thus increasing the hydraulic conductivity of the matrix. The experimental component of this study attempts to reproduce these effects using dynamic excitation in varying modes of vibration and frequency range.

Increased multi-phase flow also relies on the viscous coupling of the fluid and solid; however, the capillary forces present due to the separate phases present in the matrix complicate the process. Residual droplets of pore water (in the vadose zone) or NAPL mass (in a contaminated aquifer) are formed with the help of capillarity. Capillary effects, coupled with material anisotropy, cause by-passing and snap-off of the NAPL mass as it moves through the soil. These effects leave behind residual droplets that, in the case of NAPL migration, produce plumes of dissolved phase contaminant that remain in the aquifer long after the free-phase mass has migrated through the soil. In an aquifer, water is generally the wetting phase; thus, the residual NAPL droplets in the pore spaces are surrounded by a layer of pore water. By assuming the pore water provides a frictionless surface for the droplet to slide on, Beresnev (2006) develops a yield-stress model for NAPL droplet mobilization. In words, a droplet is mobilized when inertial force and external pressure gradients overcome the capillary force holding the droplet in place.

The inertial force is supplied by applying dynamic excitation that causes both the soil skeleton and the residual droplets to oscillate. Of course, the soil skeleton has a resonant frequency at which the ratio of output vibration to input energy is maximized. In a resonant column sand specimen, the resonant frequency is generally below 200 *Hz* for axial vibration; in situ, the resonant frequency of a sandy aquifer is much lower. However, Hilpert et al. (2000) theorize the residual droplets themselves act as single degree-of-freedom oscillators that also have a resonant frequency, related to soil grain size, contact angle at the immiscible fluid interface and surface tension. In an aquifer composed of fine to medium sand, the resonant frequency of a typical DNAPL droplet (i.e. TCE) is on the order of 1-10 *kHz*, significantly higher than the resonant frequency of the soil skeleton. Recalling that the goal of the applied dynamic excitation is to overcome the capillary force holding the droplet in place, a question arises: what is the optimum input excitation frequency? This question is not easy to answer because high frequencies are attenuated more than low frequencies in soil, thus range of application is limited. On the other hand, low frequency excitation may not be as efficient at delivering enough inertial energy to liberate the entrapped residual droplets.

Unfortunately for this study, experimentation on multi-phase systems using NAPLs is not possible due to equipment design and laboratory restrictions. NAPLs are heavily sorbed to organic materials such as rubber membranes and flexible plastic tubing, both of which are used in the resonant column. Also, most NAPLs, particularly chlorinated solvents, are hazardous and often carcinogenic, so proper laboratory ventilation is required. However, Roberts et al. (2001) published the results of their study of the use of dynamic excitation to hasten the removal of TCE from a sand specimen which demonstrates the need for future study. In their experiments, a sand specimen under a confinement pressure of approximately 415 *kPa* is axially vibrated at frequencies between 25 *Hz* and 100 *Hz* at strain levels on the order of 10^{-2} *%* to 10^{-3} *%*. Higher removal rates of NAPL are observed during excitation compared with baseline removal rates measured during applied pressure gradient alone; thus, the study serves as a proof of concept. However, more in-depth study is needed before the technique can be applied in situ. First, the confinement pressure is much too high; for future study, the soil specimen must be subjected to conditions more accurately representing a shallow aquifer, which is the intended field application. Second, and most importantly, no justification is given for the frequencies used during experimentation. No effort is made to characterize the resonant properties of either the specimen or the residual droplets - the choice of frequencies used appears to be based on an educated guess, rather than optimized design. Before this technique is used in the field, more study must be conducted in order to minimize input energy and time of operation required such that the remaining residual droplets no longer pose a threat of aquifer contamination.

Finally, for those individuals in the field of environmental engineering, contaminant remediation is more of an art than a science. Success is based on good site characterization, knowledge of hydrogeology and contaminant chemistry, and often luck is a significant factor as well. Laboratory experimentation represents the most ideal conditions; moving from the lab to the field is complicated by the randomness that anisotropy adds to the equation. However, it is important to always remember the physical mechanisms at the heart of the process and hopefully this study helps to solidify the foundation upon which further research can be built.

There are some important issues that facilitate the need for further investigation. First, many studies published in the literature are vague and don't include concise, detailed specifications of experimental parameters and equipment (i.e. it is impossible to replicate

results because important information about the experimental setup is missing). Second, no study attempts to link a mathematical model of capillary trapping to experimental data. Model development appears to be nearly complete, and there are a few good sets of experimental results, yet no elegant link between the model and experimental results exists. Third, the vast majority of the research into this mobilization mechanism has been focused on enhanced oil recovery with groundwater remediation included as an afterthought in the published work.

3.0 THEORETICAL BACKGROUND

The purpose of this section is to outline the physical mechanisms which affect wave propagation and fluid flow in a uniform porous medium at the pore scale. The problem of heterogeneity and scales describing these phenomena macroscopically is addressed including a discussion of how these effects are observed and quantified in a laboratory setting.

3.1 Pore-Scale Phenomena

3.1.1 Unsaturated Soil

In a uniform, homogeneous unsaturated coarse soil matrix, the individual grains form an interconnected pore structure filled with pore gas. Depending on the grain packing, the void ratio e of the soil may be high ($e \approx 0.90$) or low ($e \approx 0.30$). The simple cubic (SC) packing model represents a low-density configuration; a simplified conceptual diagram of SC packing is shown as Figure 3.1.

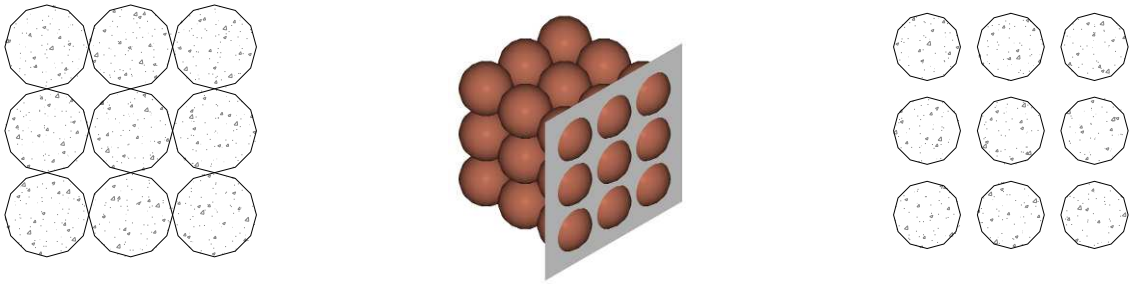

(a) (b) (c)

Figure 3.1 - Conceptual diagram of SC packing
(a) 2-dimensional cross-sectional view through centre of grains,
(b) 3-dimensional representation with cross-section plane for
(c) offset 2-dimensional cross-section

Figure 3.1 (a) shows the 2-dimensional cross-section view through the centroid of the grains; however, to develop most concepts in this study, a slightly offset cross-section view as shown in (c) is used to show the pore space in 2-dimensional form.

The void ratio *e* is related to the porosity *n*; both essentially quantify the amount of void space in the soil (Craig, 2002). These two parameters are defined as

$$e = \frac{V_v}{V_s} \quad \text{.....[3.1]}$$

$$n = \frac{V_v}{V} \quad \text{.....[3.2]}$$

where V_v is the volume of void space, V_s is the volume occupied by the soil grains and V is the total volume of the porous matrix. For SC packing with uniform spherical grains, $e = 0.91$.

The bulk density ρ of a soil is the ratio of total mass M to total volume V. If the grain density ρ_s is known, the bulk density can also be calculated using the porosity using

$$\rho = \frac{M}{V} = (1-n)\rho_s \quad \text{.....[3.3]}$$

For quartz sands, $\rho_s = G_s \rho_w$, where $G_s = 2.65$.

The unit weight of the soil is the ratio of total soil weight (force) to total volume, or the bulk density multiplied by gravitational acceleration $g = 9.81$ *N/kg*

$$\gamma = \rho g \quad \text{.....[3.4]}$$

The contact points between the grains allow the soil to carry and distribute external loads (which may be due to overburden material or structural loads). The external load exerts a normal stress σ, which is essentially the pressure applied to the bulk soil mass.

Under normal loading conditions in an aquifer setting, individual soil grains are virtually indestructible; rather it is the soil matrix on a bulk scale which is prone to compression (settlement) or shear failure. The compression and shear stiffness of a soil matrix are described by Young's modulus *E* and the shear modulus *G*, respectively. These moduli are simply stress-strain ratios and are related through Poisson's ratio ν, as

$$G = \frac{E}{2(1+\nu)} \quad \text{.....[3.5]}$$

The moduli of a soil can be determined by examining the propagation characteristics of a wave traveling through the soil matrix. The most basic definition of a wave is a state at one location of a system which is transmitted to another location in the system (Carlin, 1960). Virtually all materials which possess some degree of elasticity are capable of propagating mechanical waves. Successive elements of the medium are displaced, while a restoring force acts to return the element to the initial position. The inertia of the element causes displacement in the opposite direction, which is subjected to the same restoring force, and the cycle repeats.

There are two types of vibratory motion that could be applied to a medium (Kramer, 1996):

- Periodic waves which are repeated at regular time intervals, such as simple harmonic motion (i.e.: sinusoidal variation with time), and
- Non-periodic waves which do not repeat, induced by impulse loadings such as earthquakes or passing trains.

A simple harmonic wave motion of a soil grain, with amplitude *A*, angular frequency ω and phase φ, is shown in Figure 3.2.

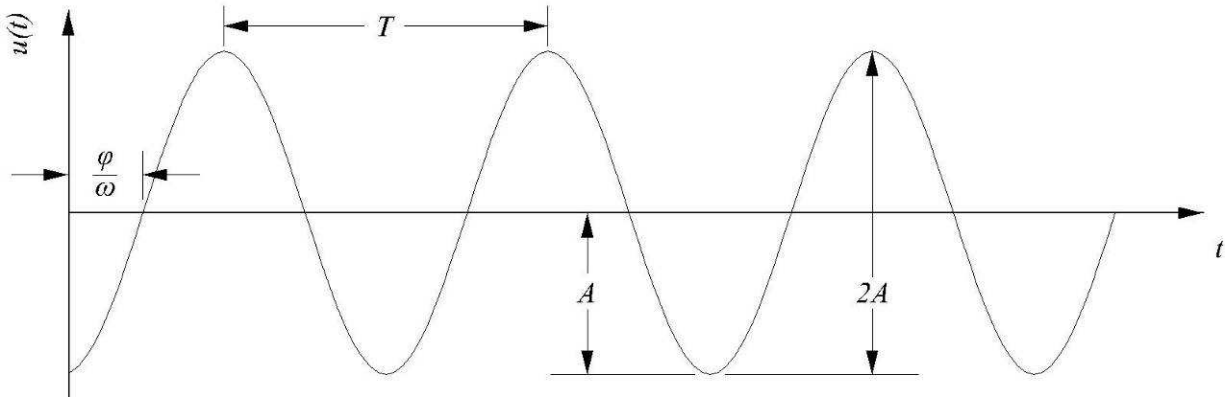

Figure 3.2 - Simple harmonic motion

The amplitude *A* is a measure of the maximum displacement, angular frequency ω is a measure of the time from wave crest to crest (one period, *T*), and phase angle φ is a measure of the displacement of the sinusoidal wave.

The angular frequency ω, period *T*, frequency *f*, and wavelength λ are related by

$$\omega = \frac{2\pi}{T} = 2\pi f = \frac{2\pi V_i}{\lambda} \quad \text{.....[3.6]}$$

where V_i is the velocity of i^{th} wave propagation through the medium which is an elastic property of the material. Compression-wave and shear-wave deformations are shown in Figure 3.3.

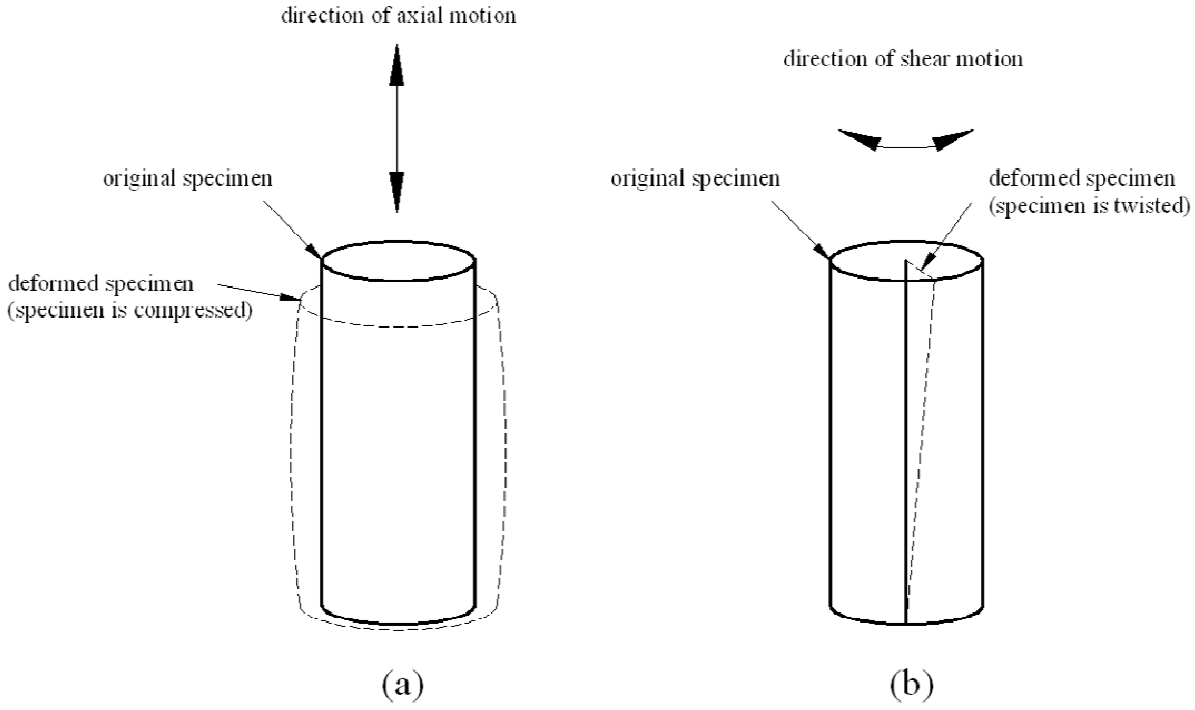

Figure 3.3 - Deformation caused by (a) compression and (b) shear waves

In a simplified one-dimensional compression wave, the specimen is compressed and displaced longitudinally (Figure 3.3 (a)), while in a shear wave, the specimen is twisted in the direction of wave propagation (Figure 3.3 (b)). Longitudinal wave velocity V_L and shear wave velocity V_s are related to the soil moduli by

$$V_L = \sqrt{\frac{E}{\rho_s}} \quad \text{.....[3.7]}$$

$$V_s = \sqrt{\frac{G}{\rho_s}} \quad \text{.....[3.8]}$$

Combining Equations [2.2], [2.5], [3.7] and [3.8] gives

$$\nu = \frac{3V_L^2 - 4V_s^2}{2\left(V_L^2 - V_s^2\right)} - 1 \quad \text{.....[3.9]}$$

Thus, Poisson's ratio can be computed if both the p- and s-wave velocities of the medium are known. Published values of various materials pertinent to this thesis are listed in Table 3-1.

Table 3-1 - Published Poisson ratio values for various materials (after Gercek, 2007)

Material	Poisson ratio
Quartz (SiO_2)	0.079
Loose sand	0.20 - 0.40
Medium dense sand	0.25 - 0.40
Dense sand	0.30 - 0.45

Although the velocity that is measured in this study is V_L, it makes sense to compute the Poisson ratio as if the measured velocities actually correspond to the compression wave velocity V_p because of the confining conditions of the specimen. The lateral deformation is essentially nil, so the constraint conditions apply and V_L is equal to V_p and therefore the computation of Poisson's ratio is the ratio of V_s to V_p.

These equations are valid at low strains (i.e. low amplitude). However, as the strain increases the behaviour becomes non-linear. The limit at which non-linear behaviour begins is known as the linear cyclic shear threshold value γ_{th}. The linear threshold value is approximately 30 times smaller than the volumetric threshold shear strain γ_{tv}. The volumetric

threshold value is a function of confinement pressure σ and can be computed for quartz sands as (Vucetic, 1994)

$$\gamma_{tv} = 0.000175 \cdot \sigma^{2/3} \quad \text{.....[3.10]}$$

where γ_{tv} is given as a percentage. The relationship between strain and material stiffness is expressed as a hyperbolic model; many of these models are given in the literature for various soil types (e.g. Ishibashi and Zhang, 1993).

In a soil matrix, wave energy is dissipated; this phenomenon is known as material damping ξ. In addition, a wave in a semi-infinite medium propagates in three dimensions outward from the source. As a result, the input energy is spread over an increasing area; this effect is known as geometric damping.

There are three phenomena at the pore scale which are responsible for material damping: particle inertial forces, frictional forces and viscous coupling (Gajo, 1996). A particle undergoing dynamic excitation experiences a force due to acceleration (momentum). When input wave energy is given to a soil particle moving in an arbitrary direction, a fraction of the energy input is used to change the momentum of the particle such that it begins to move in the opposing direction. When two adjacent soil grains are in motion and slippage at the contact occurs, then part of the wave energy will be lost as heat energy due to friction. Finally, when a pore fluid is present, a force is exerted on a moving soil grain due to drag created by the viscous forces acting on the grain. In an unsaturated soil matrix, viscous damping is essentially null.

3.1.2 Vadose Behaviour

In a typical groundwater aquifer setting, there is a zone above the water table which remains partially saturated with pore water; this zone is known as the vadose zone (Schwartz and Zhang, 2003). In the vadose zone, water is present due to infiltration (from the surface) and capillary rise (from the water table). In a three-phase soil/water/air system, water is a wetting fluid – as it moves through the vadose zone it forms a thin layer of water around each soil grain. Flow only occurs in localized areas where continuous streams are present;

otherwise, the films become stagnant. Pore water may also be entrapped due to the formation of small droplets which coalesce due to heterogeneities in the soil matrix (Section 3.2).

In order to understand fully the concepts of vadose zone behaviour, it is beneficial to review the phenomenon of capillary forces. In a three-phase groundwater system, capillary forces develop among the different phases, with the magnitude varying due to interaction geometries (i.e. fluid-solid interaction vs. fluid-fluid interaction), surface tension, and the grain size distribution of the solid soil skeleton (Alvarellos, 2003).

At the surface of a fluid, the capillary force is caused by unbalanced Van der Waals attractive forces. In order to achieve the lowest possible energy configuration, a fluid droplet maximizes its volume while minimizing surface area. A droplet in a zero-gravity environment is a perfect sphere; in a capillary tube (small radius), the surfaces of the droplet perpendicular to the tube walls curve and form a meniscus.

In a fluid droplet at equilibrium, surface tension σ develops at the surface to counteract the internal droplet pressure ΔP; this relationship is formally known as the Young-Laplace equation, given as

$$\Delta P = \sigma\left(\frac{1}{R_x}+\frac{1}{R_y}\right) \quad \text{.....[3.11]}$$

where R_x and R_y represent the radii of the droplet in the *x*- and *y*-axis, respectively. Surface tension causes meniscus formation in a capillary tube, as well as capillary rise in a porous medium. Using Equation [3.11], as droplet radius (or capillary tube radius) decreases, internal droplet pressure increases, thus larger tensile forces are generated to keep the droplet at equilibrium. As pore fluid drains from a soil specimen, the average size of the remaining droplets decreases due to the extremely large tensile forces small droplets exert on surrounding pore walls; essentially, larger droplets preferentially drain first due to lower tensile forces (lower resistance to flow). Hence, as water content decreases, extremely large negative pore pressure values are observed.

On a molecular scale, each fluid molecule experiences unbalanced forces when located at a boundary between two phases, and the work required to move the molecule away from the boundary is known as surface free energy. The surface tension in a fluid is considered equal to

the surface free energy at equilibrium (constant temperature, volume, mass and chemical equilibrium) (Alvarellos, 2003).

At a fluid-solid boundary, the fluid droplet meets the solid surface at a theoretical angle, defined as the contact angle θ_0, and is computed using Young's equation, given as

$$\cos(\theta_0) = \frac{\sigma_{sg} - \sigma_{sl}}{\sigma_{gl}} \quad \text{.....[3.12]}$$

where σ_{sg}, σ_{sl} and σ_{gl} are the surface tensions between the solid-gas, solid-liquid and liquid-gas phases, respectively. In practice, the observed contact angle θ often differs from the predicted angle θ_0 due to the presence of external forces (gravity and pressure), solid surface contamination, non-homogeneous surfaces, and surface roughness (Alvarellos, 2003).

In a capillary tube system where the liquid droplet is surrounded by a different phase (Figure 3.4), a phenomenon known as Jamin's effect occurs. If the droplet is subjected to a pressure gradient or if the angle of the tube α with respect to the horizontal (i.e. gravity component of force induced in the droplet), the droplet often remains stable (no movement in the tube), however, the meniscus radii (R_1 and R_2) change to maintain equilibrium of forces (Alvarellos, 2003).

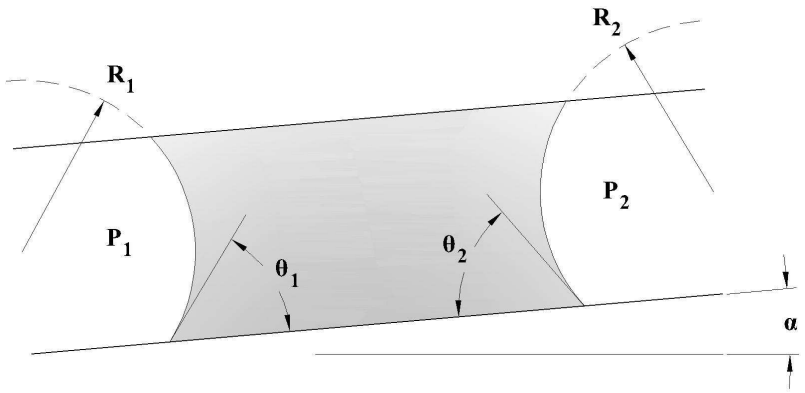

Figure 3.4 - Liquid droplet at equilibrium in an inclined capillary tube

The contact angle describes the wettability of a fluid. A fluid can be classified as perfectly wetting, partially wetting, partially non-wetting and perfectly non-wetting, where the conditions on θ for each classification are given as Table 3-2. A perfectly wetting fluid will spontaneously spread over the tube surface, whereas a perfectly non-wetting fluid will retain a near-spherical shape within the tube. The wettability of a fluid may change depending on the second fluid phase and the capillary tube material. In a soil/water/air system, water is the wetting fluid.

Table 3-2 - Fluid wettability classification

θ **(degrees)**	**Classification**
0	perfectly wetting
0 - 90	partially wetting
90 - 180	partially non-wetting
180	perfectly non-wetting

Surface tension in water droplets generates a capillary force F_c, which causes droplets to become immobile as soon as the fluid phase becomes discontinuous (i.e. in the vadose zone). As a result, the hydraulic conductivity K of the fluid for a completely saturated specimen is reduced to a lesser value, known as the relative hydraulic conductivity K_r. Relative hydraulic conductivity is used to represent the lower flow rate due to discontinuities in the pore fluid, and is generally expressed as a fraction of the saturated hydraulic conductivity. Capillary force, relative hydraulic conductivity and water saturation S_w are all inter-related through Brooks-Corey or van Genuchten relationships (Thomson, 2006), as shown in Figure 3.5.

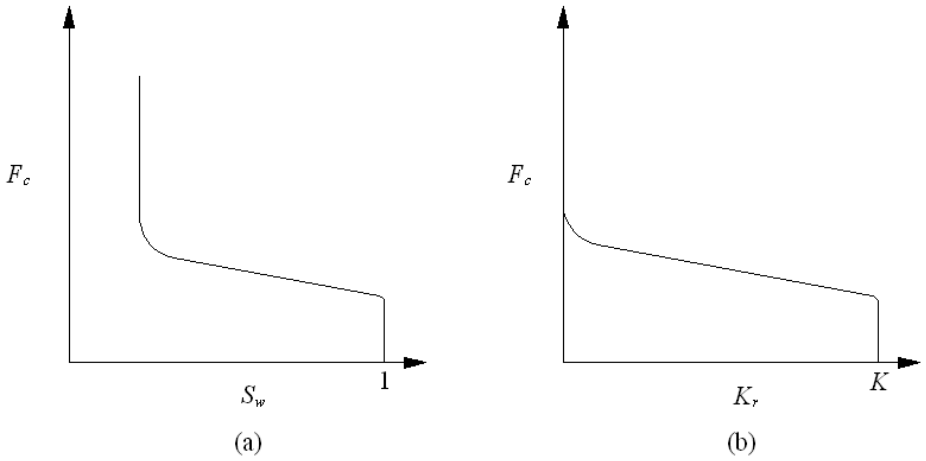

Figure 3.5 - Capillary force versus (a) water content, and (b) hydraulic conductivity in unsaturated soils

Figure 3.5 (a) shows conceptually the variation of capillary force with water saturation – as the saturation decreases, the capillary forces increase. At the minimum saturation level, capillary force jumps dramatically, indicating the remaining water is held under extreme tension. On the other hand, as saturation reaches 100%, capillary force is null. A similar trend is observed for relative hydraulic conductivity. At some capillary force limit (related to saturation), no flow occurs. As the capillary force decreases, the relative hydraulic conductivity increases until $K_r = K$, the saturated hydraulic conductivity.

Theoretically, it should be possible to liberate entrapped water droplets within the vadose zone using dynamic excitation to induce droplet resonance (Hilpert et al., 2000) and a revised droplet force balance model (Beresnev, 2006), as shown in Figure 3.6 (a). If the droplet is stationary (held in place by capillary force F_c that is greater than gravitational force F_g), there is no flow. Also, since water is the wetting fluid, a thin film exists around each soil grain such that there are no frictional forces resisting droplet motion. When an external dynamic force $Q = A\mathbf{sin}(\omega t)$ is applied to the soil matrix, the entrapped droplet responds as a single degree of freedom (SDOF) system equivalent to a point mass attached to a frictionless spring undergoing forced oscillation.

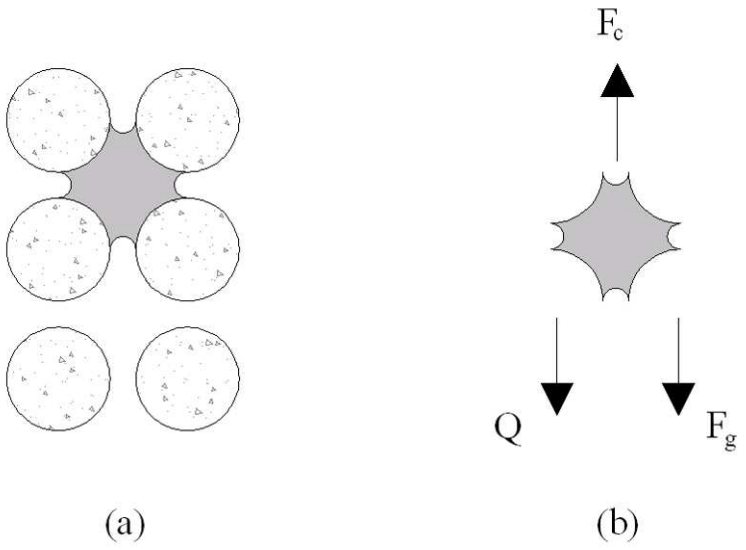

Figure 3.6 - Entrapped water droplet (a) conceptual diagram and (b) force balance

The droplet has a natural resonant frequency (given by Equation [2.19]). Ideally, to minimize energy input, the forced vibration frequency should be $\omega = \omega_0$; however, if $\omega \neq \omega_0$ it is still possible to induce droplet motion by increasing the input vibration amplitude.

It is possible to specify mobilization conditions for an entrapped water droplet by looking at the force balance (Figure 3.6 (b)), as

$$F_g + Q \geq F_c \quad \text{.....[3.13]}$$

Thus, the sum of gravity and vibration force must be greater than the capillary force holding the droplet in place in order for mobilization to occur. This equation assumes that input excitation forces are parallel to gravity forces. The Brooks-Corey and van Genuchten relationships predict a large increase of capillary force at minimum saturation; therefore, the mobilization criteria (Equation [3.13]) fails after the dynamic force makes the saturation level approach lower values. This mechanism may once again be activated if additional water is re-introduced to the system, if existing water (contained in the film coating the soil grains) coalesces to re-form trapped water droplets or if the input energy is further increased.

3.1.3 Fully-Saturated Soil

Once the saturation of water S_w = 1.0, the entire void space between soil grains is a continuous phase of fluid. The fluid will flow if, on a macroscopic scale, there exists a hydraulic gradient *i* between the inlet and outlet faces of the porous matrix.

Darcy's equation describes the one-dimensional flow of groundwater through a soil as

$$v = Ki \quad \text{.....[3.14]}$$

where *v* is the specific discharge (or Darcy velocity). Darcy's equation is valid for laminar groundwater flow (Schwartz and Zhang, 2003).

A hydraulic head differential ∂h between two points creates a hydraulic gradient. Hydraulic head *h* is a measure of the total energy available for groundwater flow, and is given by the Bernoulli equation

$$h = z + \frac{P}{\gamma_w} + \frac{V_f^2}{2g} \quad \text{.....[3.15]}$$

where *z* is the elevation head (relative to a given datum), *P* is the pressure exerted by the water column, γ_w is the unit weight of water (9.81 kN/m^3), V_f is the velocity of groundwater flow, and *g* is the gravitational constant (9.81 m/s^2). In most groundwater settings, the velocity of groundwater flow is so small that it is considered negligible, and the total hydraulic head becomes a function of elevation head and pressure head.

The hydraulic conductivity *K* of a soil is a function of the soil properties (intrinsic permeability *k*) and the pore fluid properties (viscosity μ and density ρ), as given by

$$K = \frac{k \cdot \rho \cdot g}{\mu} \quad \text{.....[3.16]}$$

The intrinsic permeability is a function of the grain size of the solid particles and the effective porosity of the soil. There are several empirical equations available in the literature for calculating the permeability of a soil (Schwartz & Zhang, 2003).

At the pore scale, water flows through pore throats due to pressure gradients between the inlet and outlet; essentially, the pore network is equivalent to a network of interconnected pipes. The local velocity of the water flowing through pore orifices is larger than the Darcy velocity *v*, which is an average flow value for a given volume of water. Darcy velocity takes into account the tortuosity τ of the medium. In a pore network as shown in Figure 3.7, path (a) is much shorter than path (b); thus an elemental volume of pore water following path (a) would arrive at the exit point much faster than an elemental volume traveling path (b) in a homogeneous porous matrix. The Darcy velocity is an average value of all the elemental volumes traveling through the matrix and representative of the bulk soil matrix. Tortuosity increases with soil heterogeneity, and increases viscous damping in a soil specimen.

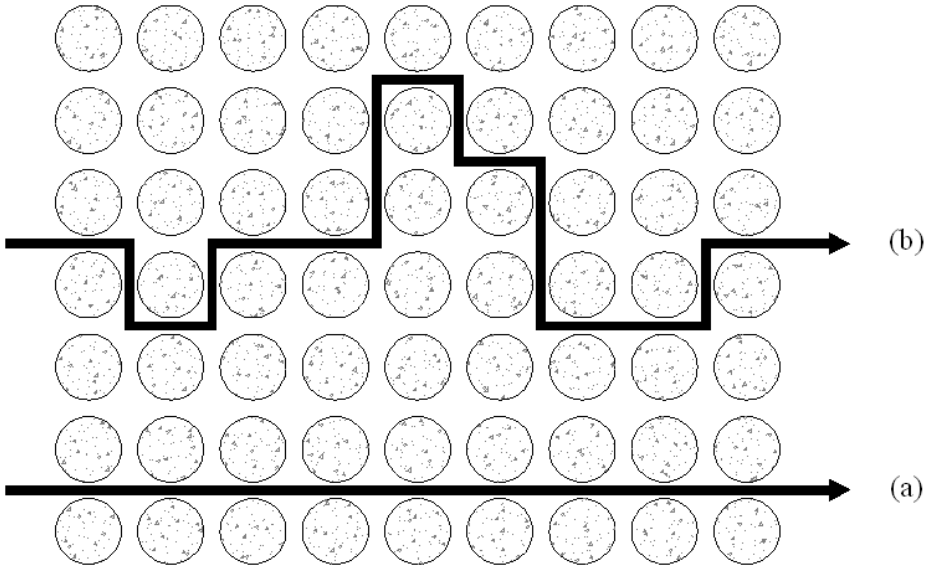

Figure 3.7 - Tortuosity in a pore matrix

When dynamic wave excitation is applied to a saturated soil matrix, the material damping ξ increases due to the viscous coupling between the fluid and solid grains; this added component of damping is referred to as viscous damping ξ_v. Input wave energy is dissipated by viscous drag forces created as the soil grains move through the pore fluid.

Assuming the soil grains are perfect spheres, the pore fluid motion relative to the soil grain motion is represented by three flow lines (Figure 3.8). There are components of flow which pass above and below the grain, exerting a viscous drag force F_d on the grain, and there are stagnation points at the centre of the grain both upstream and downstream. The formula for

computing the drag force F_d on a sphere in a laminar flow regime is given as (Vennard and Street, 1976)

$$F_d = 6\pi \cdot \mu \cdot V_f \cdot r \quad \text{.....[3.17]}$$

where μ and V_f are the viscosity and velocity of the displacing fluid, respectively, and r is the sphere radius. Thus, as the viscosity of the displacing fluid is increased, drag force is also increased. The same applies for the velocity of the displacing fluid; however, Equation [3.17] is only applicable in the laminar flow regime (i.e. low flow velocity).

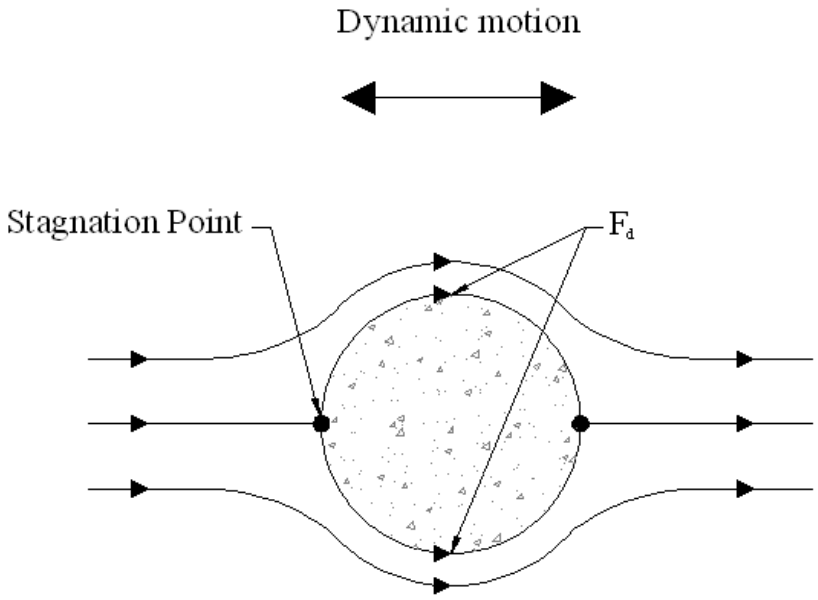

Figure 3.8 - Drag forces on a soil grain undergoing dynamic excitation

As viscosity of the pore fluid in a soil specimen decreases, wave energy dissipation should also decrease. However, as the viscosity decreases, the drag force decreases; thus inertia forces become stronger and so does the associated damping component. These two competing phenomena complicate the damping response of the soil (Gajo et al, 1996).

The viscous coupling between pore fluid and soil skeleton is also responsible for the success of the pressure pulsing technique (PPT) for increasing flow in oil extraction wells (Dusseault et al., 2002). PPT works by creating a standing wave in the pore fluid; the pore

fluid translates through the pore matrix. As discussed earlier, fluid flow in a soil occurs when a hydraulic gradient is imposed. During PPT, flow rates increase due to the inertial force of the moving fluid mass. Frequencies in the low seismic range (i.e. less than 10 *Hz*) are optimum for inducing a standing wave in the pore fluid (Dusseault, 2007).

Since PPT only works when there is viscous coupling present in the soil matrix, there are several limitations for its application. First, there must be a continuous phase of liquid in the medium; a significant amount of pore gas (which is highly compressible) dissipates the momentum energy of the standing wave and limits the effectiveness of the technique. Second, the coupling between the soil skeleton and pore fluid begins to break down at high frequencies (i.e. greater than 100 *Hz*), so there is a limited range of input excitation bandwidth. Finally, although Dusseault et al. (2002) outline PPT using a system which creates pressure waves in the pore fluid, stimulating the soil matrix itself should have the same effect.

3.1.4 Immiscible Phase Behaviour

When the soil matrix is fully saturated and an immiscible phase enters the system (i.e. in a contaminant release or in an oil reservoir) flow in the system becomes more complex. Before proceeding with a discussion of flow, a general review of contaminants is presented.

Schwartz & Zhang (2003) define a contaminant to be a non-natural constituent in the environment which is toxic to humans or other life, or which adversely affects the natural state of the environment. Groundwater contaminants can be broadly grouped into two categories: miscible and immiscible. Miscible contaminants completely dissolve in groundwater to form a homogeneous mixture. Immiscible contaminants remain in a phase which is separate from groundwater. In contaminant hydrogeology, immiscible fluids are more commonly referred to as non-aqueous phase liquids (NAPLs).

Organic contaminants may be either miscible or NAPLs depending on the molecular structure of the compound. The primary source of organic contaminants is the petroleum industry, including the extraction and refining process, distribution and storage. Examples of common miscible organic contaminants include benzene (C_6H_6), toluene ($C_6H_5CH_3$), ethylbenzene (C_8H_{11}) and xylene ($C_6H_4(CH_3)_2$). These contaminants are present in gasoline,

and are more commonly referred to as BTEX compounds. Fuel additives, such as methyl-tertiary butyl ether (MTBE), are often highly miscible and toxic to humans (Barker, 2005).

NAPLs can be further divided into two categories: light (LNAPLs) and dense (DNAPLs). LNAPLs are less dense than groundwater, and when present in a groundwater system pool in the vadose zone. LNAPLs are mostly gasoline-related products; common examples are crude oil and gasoline. DNAPLs are denser than groundwater, and pool on low hydraulic conductivity layers at the bottom of an aquifer. Examples of common DNAPLs include halogenated aliphatic compounds such as tetrachloroethene (PCE) and trichloroethene (TCE), halogenated aromatic compounds such as chlorobenzene and polychlorinated biphenyls (PCBs). Figure 3.9 shows a conceptual diagram of NAPL pooling in a groundwater system.

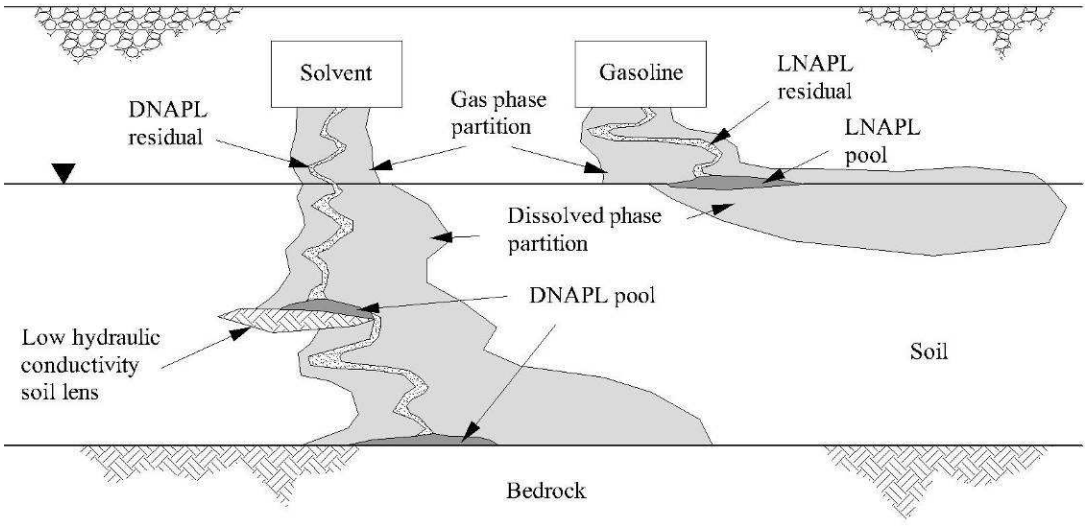

Figure 3.9 - NAPL contamination conceptual diagram

NAPLs form pools of free-product in the groundwater system on top of the water table (in the case of LNAPLs) and on top of low-conductivity layers (in the case of DNAPLs). The NAPL free-product remains mobile until it encounters one of these layers, or until there is not enough free-product in the plume to maintain a positive pressure head. As the NAPL free-product advances, a fraction is left behind, which is known as the NAPL residual. The residual is held by capillary forces to the soil skeleton, and is immobile.

NAPL may partition into different phases through dissolution, volatilization and sorption mechanisms (Thomson, 2006). The degree of dissolution depends on the octanol-

water partition coefficient K_{ow} of the contaminant; high K_{ow} values indicate a hydrophobic substance (low solubility in water). The degree of volatilization depends on the Henry's law constant K_H of the contaminant; low K_H values indicate the substance is very volatile. The degree of sorption depends on the sorption distribution coefficient K_p of the contaminant; high K_p values indicate the substance is highly sorbed to the solid skeleton.

The rate of free-phase flow depends on several factors. First, there must be a continuous phase of mass in order for the NAPL to flow at all; disconnected ganglia are immobile. Second, the NAPL can only enter the soil matrix by overcoming the capillary entry pressure of the matrix. In multi-phase groundwater flow where a non-wetting immiscible fluid is migrating downwards due to gravity forces, there is an apparent capillary pressure which must be overcome in order for the non-wetting fluid to advance. This apparent pressure is referred to as capillary entry pressure; it is one type of barrier which restricts the rate of gravity drainage flow.

In a porous matrix saturated with a wetting fluid (i.e. water), the pore throats at the upper layer are filled with fluid droplets which are held in place by the capillary force which attracts the droplet to the pore throat walls. When an immiscible, denser fluid is incorporated into the flow system, it migrates down due to gravity force until it reaches the wetting-fluid saturated boundary (Figure 3.10 (a)).

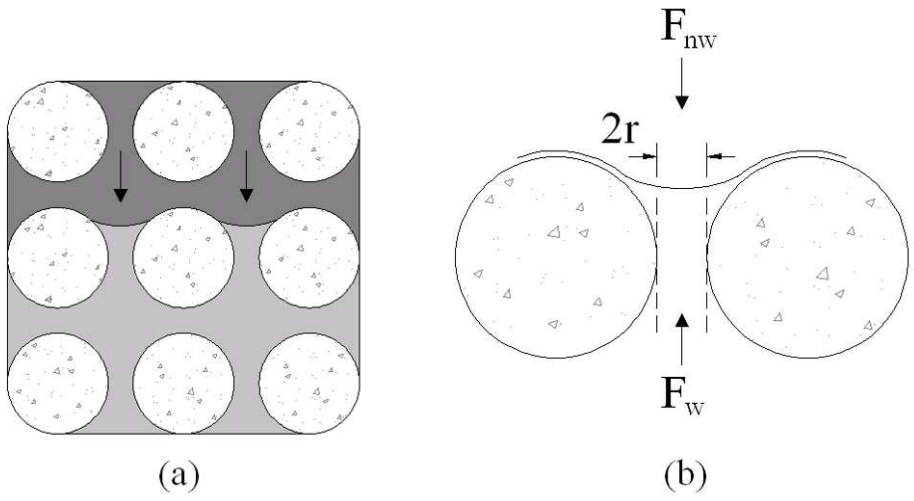

Figure 3.10 - Conceptual diagram of capillary entry pressure

A force balance on the wetting fluid which is being held in place by capillary pressure is shown in Figure 3.10 (b). There is a displacement force acting downward on the droplet, F_{nw}, due to the gravity force exerted on the denser non-wetting fluid, and a restoring force acting upward on the droplet, F_w, due to the pressure head of the standing column of pore wetting fluid beneath the droplet. Both forces act over the same surface area; thus, they can be expressed as pressures P_{nw} and P_w, given by

$$P_{nw} = \rho_{nw} \cdot g \cdot z_{nw} \quad \text{.....[3.18]}$$

$$P_w = \rho_w \cdot g \cdot z_w \quad \text{.....[3.19]}$$

where ρ_i is the density of phase i, z_i is the standing height of phase i and g is the gravitational constant 9.81 m/s^2.

Assuming the pore throat between soil grains acts like a capillary tube (producing a meniscus effect), the difference between these two pressures is the apparent capillary pressure P_c due to the capillary forces holding the wetting droplet in place, which is given by

$$P_c = \rho_{nw} \cdot g \cdot z_{nw} - \rho_w \cdot g \cdot z_w = \frac{2\sigma \cdot \mathbf{cos}\,\theta}{r} \quad \text{.....[3.20]}$$

where σ is the surface tension between the non-wetting and wetting phases (varies for different fluid combinations), θ is the contact angle between the wetting phase and the soil grain and r is the pore throat radius. In a clean sand specimen, water is perfectly wetting; therefore, $\theta = 0$.

Equation [3.20] can be rearranged to calculate the pressure head required in the non-wetting phase before the fluid can continue to migrate downward under gravity drainage (Thomson, 2006) as

$$z_{nw} = \frac{2\sigma \cdot \mathbf{cos}\,\theta}{\rho_{nw} \cdot g \cdot r} + \frac{z_w \cdot \rho_w}{\rho_{nw}} \quad \text{.....[3.21]}$$

In a real aquifer system, the phenomenon is more complex owing to the relationship between capillary pressure P_c, relative saturation $S_{w,i}$ and relative hydraulic conductivity K_i of each phase i (Das et al., 2006). Intuitively, as the degree of saturation of the wetting phase decreases the non-wetting phase begins to migrate downward, and the capillary entry pressure decreases; therefore, at the immiscible fluid interface, discontinuities begin to form in the wetting phase and the net capillary pressure required to displace the wetting phase droplet goes down due to the absence of a restoring force (no longer a continuous standing height of wetting fluid). Similarly, as discontinuities are formed in the wetting phase, hydraulic conductivity is lowered because detached droplets of wetting fluid are immobilized; flow only occurs in a continuous stream of wetting fluid. The relationship between these parameters in a two-phase system has been well studied and is described by the Brooks-Corey relationship (Thomson, 2006).

The drawback of this relationship is that it differs for varying soils (due to heterogeneities and different grain size distributions) because of the use of a pore size distribution index λ (a fitting factor used to make the model consistent with laboratory data generated from different soils). There are both empirical methods (Timlin et al., 1999) and computer modeling methods (Das et al., 2006) based on physical mechanisms available to estimate λ. Nonetheless, scaling up from the pore scale level to the macroscopic level currently presents a significant challenge in terms of predicting effects of this mechanism on multi-phase flow.

In a homogenous pore matrix, the interface between non-wetting and wetting fluids migrates downwards uniformly. However, in reality, heterogeneities exist at the pore scale which causes apparent random effects when viewed at a larger scale. Equation [3.20] predicts that a pore throat with a smaller radius has a larger capillary pressure; thus a larger pressure head of non-wetting fluid is required to overcome the capillary entry pressure. In terms of heterogeneity at the pore scale, the non-wetting phase flows through large pores first. On a larger scale, this translates to fingering at the interface of a downward migrating non-wetting fluid.

It is possible to estimate the values of σ and θ for various combinations of immiscible fluids in the laboratory. Usually it is more convenient to express the capillary entry pressure of a soil matrix in terms of height of standing fluid, which is essentially a measure of the bulk

properties of the soil matrix (heterogeneities are incorporated by averaging over the entire volume of soil).

During multiphase flow through a porous medium, there may be two types of flow mechanisms present (Dullien, 1979): steady-state or non-steady-state. During steady-state flow, the distribution of each fluid phase remains constant on a macroscopic scale (i.e. there is no displacement of fluid mass). In this case, the two immiscible fluids can either simultaneously flow through the same channel (with the wetting-fluid along the pore throat walls, and the non-wetting fluid in the centre of the pore throat) or the two fluids may flow through separate pore throat networks (with the wetting fluid preferentially flowing through the narrow pore throats in a heterogeneous pore matrix). When a wetting (or non-wetting) fluid is pumped through the steady-state pore matrix at a higher pressure gradient, non-steady-state multiphase flow begins and displacement of the lower-pressure fluid occurs. This phenomenon is responsible for high water cuts in aggressively pumped oil extraction wells, as well as high water cuts from extraction wells used for pump-and-treat remediation of NAPL contaminants.

Non-steady-state flow causes instabilities along the interface between fluids when the viscosity of the displacing fluid is significantly lower than that of the displaced fluid. Instability occurs when viscous drag forces caused by the displacing fluid flowing around the displaced fluid are not large enough to overcome the capillary forces holding the displaced fluid in place. When this happens, a phenomenon known as viscous fingering occurs (Barker, 2005), and the displacing fluid bypasses the displaced fluid, leaving entrapped ganglia behind. At this point, the system essentially becomes single-phase flow, with the entrapped ganglia acting as barriers to flow (Dullien, 1979).

At the pore scale of a homogeneous soil matrix, an entrapped spherical immiscible droplet is depicted in Figure 3.11 (a).

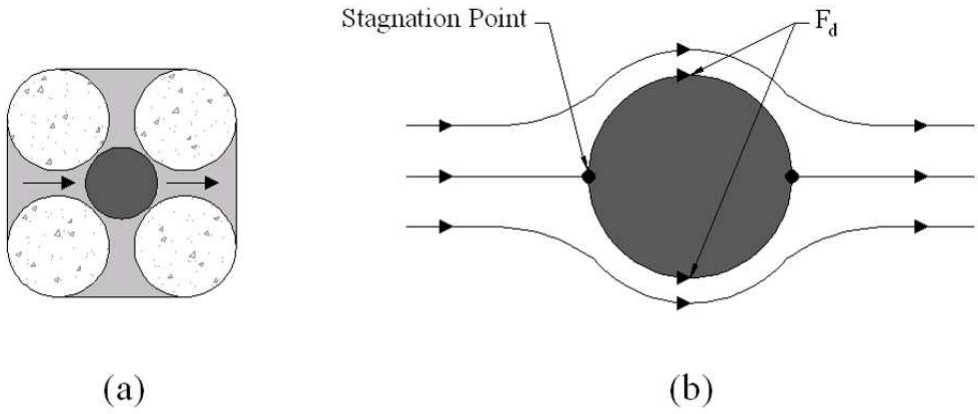

Figure 3.11 - Conceptual diagram of drag forces on an immiscible fluid droplet

The displacing fluid (wetting phase) flows horizontally past the entrapped droplet. A force diagram of the droplet is shown in Figure 3.11 (b). The displacement force F_d from the wetting fluid acts along the surface of the sphere in the direction of flow. In this scenario, both lift forces (due to a pressure gradient between upstream and downstream faces of the sphere) and drag forces (due to viscous drag along the immiscible fluid interface at the surface of the sphere) are present; however, in a laminar flow regime (i.e. Reynold's number $R_e < 0.1$), lift forces are minimal and the majority of the displacement force is due to drag. As R_e increases, the ratio between drag and lift forces becomes smaller until essentially the entire displacement force is due to lift only (Vennard and Street, 1976).

The displacement force F_d acting on a sphere in a laminar flow regime is given by Equation [3.17]. As indicated earlier, the restoring force holding the immiscible droplet in place is the capillary pressure P_c in the droplet due to the surface tension σ between the two phases. Essentially, the capillary pressure holds the droplet in a spherical shape (lowest stable configuration of a liquid droplet) which is too large to flow through the pore throat. An expression for P_c is given by Equation [3.20]. To compute the restoring force F_c provided by the capillary pressure of the droplet, the droplet is considered to be completely non-wetting ($\theta = 180$), and P_c is assumed to act uniformly over the entire surface area of the spherical droplet ($A = 4\pi r^2$). Thus, F_c is given by

$$F_c = 8\pi \cdot \sigma \cdot r \quad \text{.....[3.22]}$$

A convenient way to express the ratio between capillary and viscous drag forces is the capillary number N_c, given by

$$N_c = \frac{\mu \cdot V_f}{n \cdot \sigma} \quad \text{.....[3.23]}$$

This relationship can be derived by dividing Equation [3.17] by [3.22]; the only difference is the addition of a term to account for the porosity of the matrix. Equation [3.23] is reported in Melrose and Brandner (1974); although derivation for N_c is given, it is likely that the porosity is included to account for the relationship porosity and pore throat radius (maximum droplet size).

On a macroscopic scale in a heterogeneous matrix, this phenomenon causes ganglia of immobile droplets to be bypassed, creating viscous fingering of the displacing fluid. The criterion for mobilizing an entrapped droplet is given as the inequality

$$F_p + F_d \geq F_c \quad \text{.....[3.24]}$$

In other words, the sum of the force caused by the pressure gradient in the displacing fluid F_p and the drag force F_d on the droplet must exceed the capillary force F_c in order for mobilization to occur. The capillary number gives the mobility criterion for an entrapped immiscible droplet: when viscous forces outweigh capillary forces, mobilization occurs. Eventually, preferential flow pathways are formed by the unblocked pore throats, and the displacing fluid fingers out into the matrix, as shown in Figure 3.12.

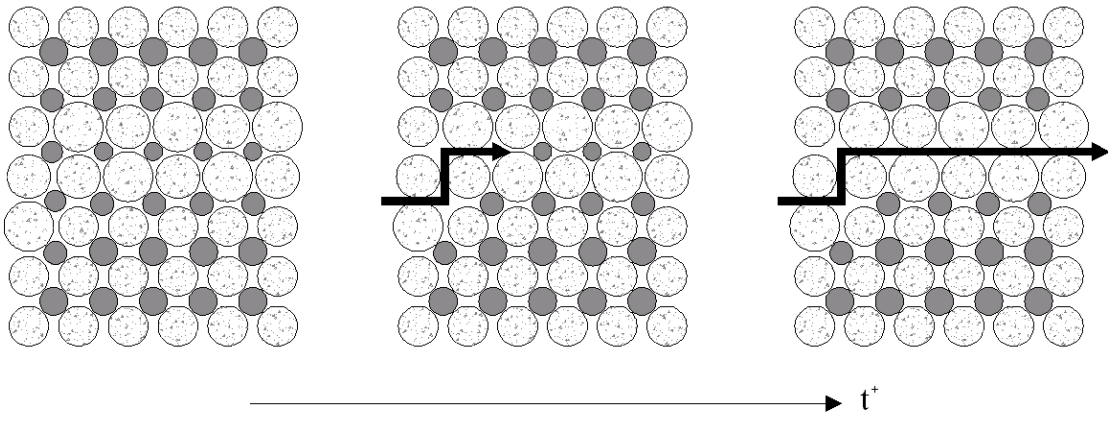

Figure 3.12 - Conceptual diagram of viscous fingering in a porous matrix

Ganglia formation is a phenomenon that occurs in multi-phase flow in a porous medium, and has the effect of trapping immiscible fluid mass in the matrix. This entrapped mass is referred to as the immobile phase (White et al, 2004). The immobile phase consists of entrapped mass (which is present in the saturated zone of the pore matrix) and residual mass (which is present in the vadose zone of the pore matrix). In either case, a minimum of two immiscible phases are present in the matrix.

During imbibition of the immiscible phase under gravity flow, a wetting front is formed at the interface between the two phases. Instability in the wetting front is the primary cause of ganglia formation - essentially there is a build-up of the imbibing fluid in the pore space. Instabilities have been proven to be caused by several factors at the wetting front, including decrease in soil wettability, increase in saturated hydraulic conductivity (while imbibition velocity remains constant), or inadequate imbibing fluid pressure (Bernadiner, 2004). Thus, instability is caused by a barrier to flow in the matrix. The two mechanisms which are known to cause ganglia formation are pinch-off and bypass (Bernadiner, 2004).

Bernadiner (2004) conducted a series of experiments on different Hele-Shaw cells to observe the pinch-off phenomenon in detail. The pinch-off mechanism occurs in four steps, as illustrated in Figure 3.13. During the first step, the imbibed fluid (undergoing a gravity drainage process) flows from an upper pore throat to a lower pore throat by means of a thin film along the pore walls. This step of the process is referred to as film-flow and is illustrated in Figure 3.13 (a).

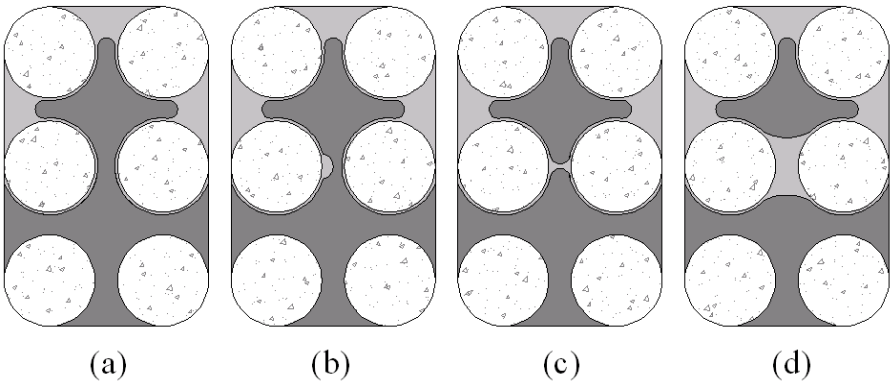

Figure 3.13 - Conceptual diagram of pinch-off mechanism
(after Bernadier, 2004)

When instability at the wetting front is present, a build-up of imbibing fluid is observed in the pore throat. This is referred to as neck formation (Figure 3.13 (b)). Imbibing fluid will build up in this neck until some critical mass is reached. At this point, the neck diameter is large enough to block the entire pore throat. This step is influenced by capillary forces drawing the neck to the opposite channel wall. An important factor is the ratio of surface tension forces of the two immiscible fluids (Kaluarachchi, 1992). As soon as a discontinuity is formed by the imbibing fluid, the draining fluid droplet becomes immobile and forms a small ganglion. This step in the process is referred to as snap-off (Figure 3.13 (c)). As time progresses, the interface between imbibing and draining fluid moves outward from the original neck location and encompasses the entire pore throat. This final step is known as interface movement (Figure 3.13 (d)).

Heterogeneity of the pore matrix at the pore scale (i.e. pore throat diameter and grain shape/orientation) leads to a non-uniform distribution of ganglia in the matrix. The imbibing fluid preferentially forms pinch-offs in small diameter pore throats, which is attributed to higher capillary forces acting on the neck. In smaller diameter pore throats, it is easier for the capillary forces to form a snap-off due to the stronger attraction of the imbibing fluid to the pore walls. This condition is the bypass phenomenon.

As previously mentioned, the bypass mechanism is largely due to heterogeneity in the porous matrix. Pinch-off preferentially occurs in smaller diameter pore throats, so as a result, larger pore throats are bypassed by the imbibing fluid, as illustrated in Figure 3.14.

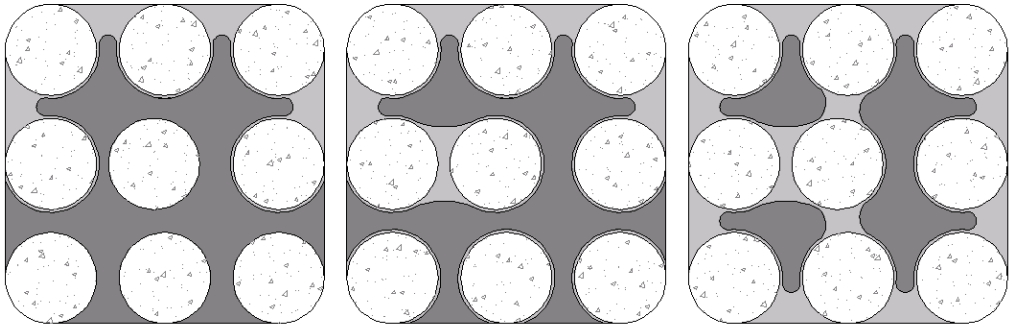

Figure 3.14 - Conceptual diagram of bypass mechanism

The imbibing fluid is shown infiltrating the top of the pore structure in Figure 3.14 (a) through film-flow. The first pore throat to experience pinch-off has the smallest diameter, as shown in Figure 3.14 (b). The heterogeneity in pore throat diameter in this conceptual diagram is due to non-uniformity in the grain distribution; however, the same throat size heterogeneity could be caused by non-uniform grain size distribution or angularity/orientation of grains. Finally, the intermediate-size pore throats suffer pinch-offs, as shown in Figure 3.14 (c). The largest pore throat may or may not suffer a pinch-off and this is governed by a number of factors. If the instability and capillary force is large enough, then pinch-off may occur, albeit in a larger time frame.

It is quite common for ganglia formed through bypassing to be much larger than ganglia formed through pinch-off. In this case, the ganglion spans two connected pore throats. However, it is possible for even longer chains of immobile fluid to form; it just depends on the extent of the enlarged pore throat, which is related to heterogeneity in the soil matrix. Dullien (1979) reports that it is possible for interconnected ganglia to form in up to ten contiguous pore throats.

Using the concepts of droplet resonance and a modified yield-stress mobilization model, it should be theoretically possible to liberate entrapped droplets by applying dynamic excitation. When an immiscible phase is added to a saturated system, two forces must be added to the inequality given as Equation [3.13]: viscous drag forces F_v on the entrapped droplet and the hydraulic gradient i acting across the continuous phase liquid. Therefore, Equation [3.13] becomes

$$F_g + Q + i + F_v \geq F_c \quad \text{.....[3.25]}$$

Equation [3.25] states that the sum of gravity, vibration, hydraulic gradient and viscous forces must be greater than the capillary force holding the droplet in place in order for mobilization to occur. Similar to Equation [3.13], this equation assumes that input excitation forces are parallel to gravity forces. As residual NAPL mass is removed, it is expected that the effectiveness of applied dynamic excitation should become lower as the average size of the remaining droplets grows smaller (higher capillary forces holding the smaller droplets in place). This equation is quite similar to the model proposed by Beresnev (2006); however that model does not include the effect of viscous forces.

3.2 Heterogeneity and Scale

In order to fully understand flow and wave propagation in a porous medium at a macroscopic scale, it is necessary to investigate physical mechanisms that occur at the pore scale. The problem with modeling these physical mechanisms is that investigations are generally done on homogeneous specimens (e.g. Hele-Shaw cell) and at scales (i.e. permeability) much greater than encountered in a real aquifer or reservoir. In order to develop macroscopic models of flow and wave propagation, the scale effect must be accounted for (by ensuring the relative magnitude of forces at the pore scale are accounted for when scaling down the permeability of the matrix) and heterogeneity in the matrix must also somehow be incorporated.

Heterogeneity essentially describes the non-uniformity of soil grains in a porous medium due to grain size, shape, composition, angularity, orientation and rugosity. These parameters of the soil grains affect the compressibility, porosity, tortuosity and permeability of the matrix from the single-grain scale to aquifer scale.

The main factors that contribute to heterogeneity at the single-grain scale are composition and rugosity. The composition of a soil grain is uniform over its entire mass, but different compositions govern the behaviour at the surface of the grain. For example, sand grains (which are predominantly composed of different variations of silicon molecules, i.e.

quartz) are neutrally-charged at the surface, while clay grains always contain a charge imbalance at the surface, thus clay and sand grains behave differently at the grain-scale. A conceptual diagram of sand and clay grains is shown as Figure 3.15.

Figure 3.15 - Conceptual diagram of sand and clay grains

The sand grain depicted in Figure 3.15 (a) is mostly round; however the surface is rough. The rugosity of the grain describes the surface roughness. Figure 3.15 (b) depicts a typical clay grain. Compared to the sand grain, the clay grain is more elliptical or plate-like, and because of the imbalanced charge on the surface, clay grains always are surrounded by a layer of adsorbed water and any cations that may be present in the surrounding pore liquid (Craig, 2002). The relative size between the clay and sand grain is greatly exaggerated. Clearly the flow behaviour over each of these surfaces is different at the single-grain scale.

The pore scale is considered to be a small group of soil grains. At this scale, the effects of grain size, shape, angularity and orientation play a large role in the heterogeneity of the porous matrix. Figure 3.16 depicts the relative size of grains ranging from cobble to clay (Craig, 2002).

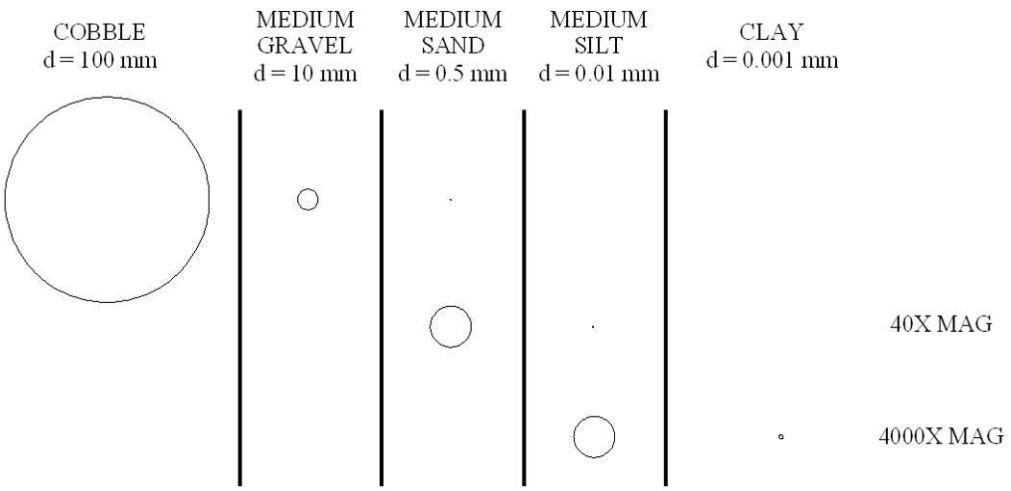

Figure 3.16 - Relative grain size comparison
(after Craig, 2002)

Figure 3.16 shows an immense range in particle size – several orders of magnitude. Soils which are poorly sorted (i.e. wide range in grain size distribution) behave differently from soils which are well sorted. Smaller grains fill in the gaps between larger grains of soil, so that the end result is a soil that has a much lower permeability (smaller pathways for water to flow).

Shape, angularity, and orientation are all related to soil density. For example, a soil sample with angular grains is expected to be much less permeable than a soil with rounded grains, simply because of the geometry of the sample at the pore scale. Figure 3.17 shows conceptually the effects of size, shape, angularity and orientation of particles on the permeability of the soil. In Figure 3.17 (a), the grains are uniformly distribute; this is referred to as simple cubic packing (Craig, 2002). Many experiments and models of physical mechanisms have been conducted using this type of distribution for simplification. In Figure 3.17 (b), the grains are uniform in shape and angularity, but varied in size; finally, in Figure 3.17 (c) all grain parameters are varied.

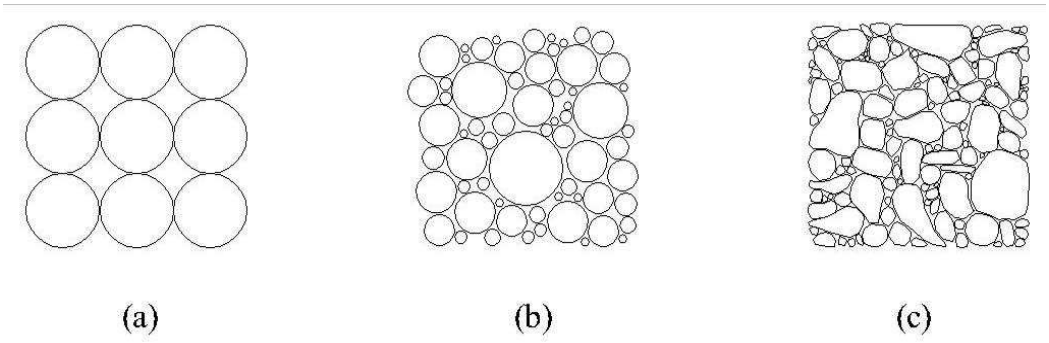

Figure 3.17 - Conceptual drawing of soil matrices with differing grain size, shape, angularity and orientation

In a single-phase groundwater system, flow varies among the three matrices shown in Figure 3.17 due to porosity differences. In terms of contaminant transport (dissolved phase), the concentration versus time profile for each matrix varies due to tortuosity (i.e. contaminant pathway) differences.

Dullien (1979) defines the macroscopic scale as the level at which the various parameters (i.e. porosity, permeability) remain constant as the size of an arbitrary sample increases. Below the macroscopic scale, there are large fluctuations in the running average of the soil parameters. Thus, at the macroscopic scale, the soil is essentially uniform, even though it is heterogeneous at the pore scale.

Figure 3.18 illustrates the concept of macroscopic scale. The soil matrix in Figure 3.18 (a) is non-uniform, containing lenses of smaller particles, while the soil matrix shown in Figure 3.18 (b) is uniform at this scale, even though at the pore scale, it is heterogeneous. This example shows how the macroscopic scale differs for various types of soil. The soil matrix shown in Figure 3.18 (a) has low permeability lenses uniformly distributed throughout the soil, and thus it is uniform at a larger macroscopic scale.

Anisotropy describes the soils dissimilarity in opposing directions. For example, a soil matrix in a shallow aquifer may be much more permeable in the horizontal direction than the vertical direction. The anisotropy of a soil depends on its geological history and the complexity of the formation. One reason for anisotropic behaviour is the orientation of soil grains (on average for the bulk of the formation); in other cases, the existence of a horizontal low-permeability layer within the aquifer is sufficient to induce anisotropic behaviour.

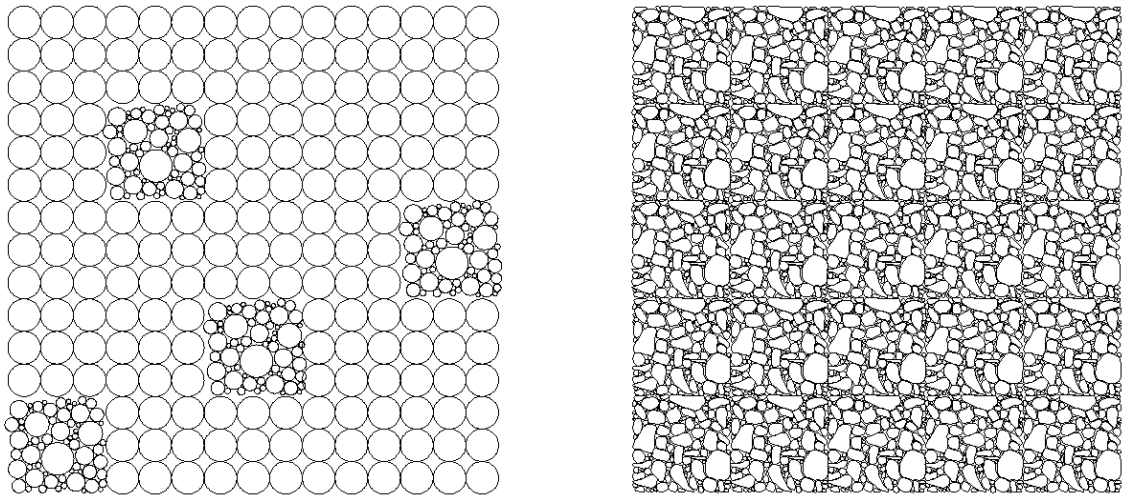

Figure 3.18 - Schematic of macroscopic uniformity

The percentage of fine particles is also an important factor that determines the nature of the soil mass. Fine particles are considered to be silt or clay particles; when the percentage of fine particles in a soil mass reaches 12 %, the soil tends to behave cohesively (Craig, 2002). The fines barrier has important implications on the soil strength and permeability.

At the aquifer scale, there are heterogeneities in the vertical plane (i.e. beds of varying soil and rock composition) and the horizontal plane. In the vertical plane, different layers of material are deposited in a geological timeframe and later buried by subsequent deposition. In the horizontal plane, material is deposited in specific locations based on the climate, parent rock characteristics, presence of biological organisms, topography and timeframe (Monroe, 2005). The placement of uniform soil deposits depends on weathering of the parent rock and erosion; weathering creates soil grains from rock while erosion transports the soil grains to their final resting place in the aquifer.

In a cross-section of a typical aquifer, it is common to see different soil types confined to clearly delineated units (layers in the case of the vertical plane, and areas in the case of the horizontal plane). Generally speaking, the soil within each of these delineated units is considered to be uniform on a macroscopic scale, with the exception of lenses of dissimilar material. Within these units, properties such as porosity, permeability and fracturing (in the

case of rock) are all considered to be uniform on average across the entire soil unit. Examples encountered in the field are silt/clay deposits in ancient streambeds, sandy deposits along buried shorelines of ancient oceans or shales formed by compression of clay beds.

These various soil units in an aquifer shape the macroscopic flow conditions. For example, a sandy soil layer confined below by an unfractured shale and above by a silty clay is considered to be an aquifer. In the aquifer, the groundwater moves fast horizontally (relative to the silty clay overburden) and confined vertically by the surrounding aquitard layers; this is known as a confined aquifer. The heterogeneity of the soil on the scale of the aquifer is responsible for this flow pattern. Similarly, in the horizontal plane, the majority of (fast-moving) flow may occur in a sand deposit lying in the valley between two ancient mountain ranges. Non-uniformities in the different soil units themselves (such as clay lenses) form perched aquifers and NAPL pools, another artifact of heterogeneity at the aquifer scale.

In order to understand the non-uniform nature of flow in a porous matrix, it is also necessary to have some understanding of the scaling effect when physical mechanisms are studied at the laboratory scale. In a laboratory, the porosity and permeability of soil matrices are higher than encountered in reality (due to the time requirements of the lab). However, when applying the same principles to in-situ soil matrices, it is necessary to consider the scale. The most critical factor is the difference in grain size distribution between the lab and the field – generally speaking, soil grains are much smaller in-situ, therefore the effect on physical flow mechanisms also changes. Field results are also complicated by local fracturing which dramatically increases hydraulic conductivity – this effect is very difficult to model in the lab.

When pore throat diameter decreases, a couple of important changes occur: the relative importance of dispersion increases, as does the magnitude of capillary forces. These changes have an effect both in single- and multi-phase flow. In single-phase flow, a decrease in the ratio between advective and dispersive flow (i.e. the Peclet number) means that dissolved contaminant mass tends to form relatively confined plumes as opposed to long fingers. Similarly, in multi-phase flow, a decrease in pore throat size increases the magnitude of capillary force, which affects ganglia formation (by-passing and viscous fingering). It is crucial to have some understanding of how the differences between the laboratory and in-situ matrices affect model predictions.

Heterogeneity and scaling are the root cause of the vast majority of uncertainty in the field of environmental engineering. In most cases, the physical flow mechanisms in a soil matrix are well understood; however, in order to apply them to in-situ conditions, empirical formulations are required, based on averages of bulk soil masses.

3.3 Macroscopic Behaviour

At the macroscopic scale, pore-scale phenomena are represented using mathematical models which describe the output of a uniform, isotropic medium. For this study, models which describe one-dimensional wave propagation (i.e. the non-resonant (NR) method) and one-dimensional flow through a porous media are used. The derivations of these models are given in the subsequent sections.

3.3.1 Wave Propagation

There are two types of vibrating systems: rigid and compliant. In a rigid system, no strain is generated with the imposed stress, and all elements of the system move in phase. In a compliant system, the elements move out of phase. Particulate media, including soil, falls under the latter category.

The number of independent variables required to describe the position of the centre of mass of each element in a system is referred to as the dynamic degrees of freedom (DOF). Systems which undergo translational or rotational displacement (uni-directional) are single DOF (SDOF) systems. For the scope of this study, the theory presented is restricted to SDOF systems.

An analogy of a SDOF system is a mass m attached to a fixed surface with a spring of stiffness k and a damper of viscous damping coefficient c, as shown in Figure 3.19 (a). The mass is subjected to a dynamic external load $Q(t)$. Figure 3.19 (b) illustrates the force balance on the mass used to develop the differential equation of motion. In Figure 3.19 (b), F_s is the force of the spring (material stiffness), F_d is the force of the damper (material damping), and F_i is the inertial force (system mass). The equation of motion for a SDOF system is given by

$$m\ddot{u}(t) + c\dot{u}(t) + ku(t) = Q(t) \quad \text{.....[3.26]}$$

This equation is linear and can therefore be solved analytically. Non-linear equations of motion are generally solved numerically.

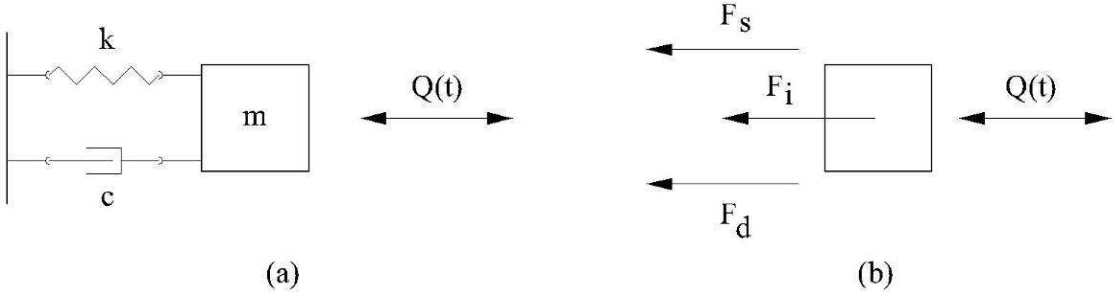

Figure 3.19 - SDOF system (a) analogy and (b) force diagram

To solve Equation [3.26], four different cases are possible: undamped free vibration, undamped forced vibration, damped free vibration and damped forced vibration. In reality, undamped vibration ($c = 0$) does not occur, since virtually all materials possess some degree of damping. However, the concept is useful for understanding the undamped natural frequency of vibration of a system. The undamped natural frequency ω_0 is the frequency at which a system with no damping responds with the maximum amplitude of vibration to a sinusoidal excitation and is given by

$$\omega_0 = \sqrt{\frac{k}{m}} \quad \text{.....[3.27]}$$

Thus, the natural frequency is proportional to the mass and material stiffness of the system.

In systems undergoing damped vibration ($c \neq 0$) material damping is quantified using the damping ratio ξ, defined as the ratio of the viscous damping c and the critical damping coefficient c_{cr} as

$$\xi = \frac{c}{c_{cr}} = \frac{c}{2\sqrt{k \cdot m}} \quad \text{.....[3.28]}$$

The critical damping coefficient is the point at which no oscillations of the mass occur for a given initial displacement. The damping ratio is proportional to viscous damping and inversely proportional to the mass and material stiffness of the system. In a damped system, the damped natural frequency of vibration ω_d is given by

$$\omega_d = \omega_0\sqrt{1-\xi^2} \quad \text{.....[3.29]}$$

As the damping ratio of the system increases, the damped natural frequency of vibration decreases.

During damped free vibrations ($c \neq 0$, $Q(t)=0$), damping is often quantified by measuring the logarithmic decrement δ, given as

$$\delta = \ln\left(\frac{u_n}{u_{n+1}}\right) = \frac{2\pi\xi}{\sqrt{1-\xi^2}} \quad \text{.....[3.30]}$$

where u_n and u_{n+1} are successive peak amplitudes of displacement.

In forced vibration (χ), the tuning ratio χ is the ratio of the frequency of vibration ω to the natural frequency of the system ω_0. As $\chi \rightarrow 1$, resonance is achieved.

The resonant column is used to measure the dynamic properties of soils under various confining stresses and shear strain levels (ASTM, 2000). In a Stokoe-type resonant column (RC), the base of the specimen is fixed against rotation and a known moment M_0 is applied to the top of the specimen using a magnet-coil drive plate. To model the response of the specimen to the load, Holzer's method is used, as outlined by Hardin (1965). A series of thin disks of material are shown in Figure 3.20.

For the n^{th} disk (thickness dx, mass m, moment of inertia I_n, stiffness k_n, damping coefficient c_n), Newton's equation of motion is given as

$$I_n\ddot{\theta}_n + c_n\left(\dot{\theta}_n - \dot{\theta}_{n-1}\right) + c_{n-1}\left(\dot{\theta}_n - \dot{\theta}_{n-1}\right) + k_n\left(\theta_n - \theta_{n-1}\right) + k_{n-1}\left(\theta_n - \theta_{n-1}\right) = 0 \quad \text{.....[3.31]}$$

where $\ddot{\theta}_n$, $\dot{\theta}_n$, and θ_n are the angular acceleration, velocity and magnitude of the applied angle of twist.

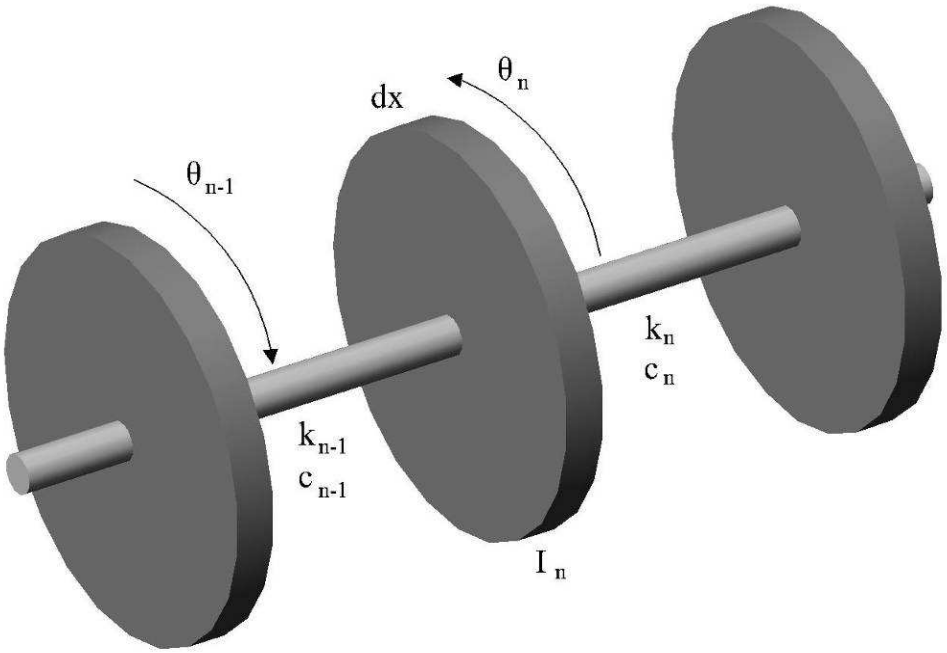

Figure 3.20 - Thin disk undergoing applied acceleration

Using Taylor's theorem and Equation [3.31] (Bisshopp, 1959), for a cylinder of length ℓ that is comprised of an infinite number of these thin disks, then the equation of motion is given as

$$I_x \frac{\partial^2 \theta}{\partial t^2} - c \frac{\partial^3 \theta}{\partial t \partial x^2} - k \frac{\partial^2 \theta}{\partial x^2} = 0 \quad \text{.....[3.32]}$$

If the moment of inertia $I_x = J_x \cdot \rho \cdot \ell$, where J_x is the area polar moment of inertia, the dynamic viscosity μ and shear modulus G are expressed as

$$\mu = \frac{c}{J_x \cdot \ell} \quad \text{.....[3.33]}$$

$$G = \frac{k}{J_x \cdot \ell} \quad \text{.....[3.34]}$$

Substituting these relationships into Equation [3.32], the following is obtained:

$$\frac{\partial^2 \theta}{\partial t^2} - \frac{\mu}{\rho}\frac{\partial^3 \theta}{\partial t \partial x^2} - \frac{G}{\rho}\frac{\partial^2 \theta}{\partial x^2} = 0 \quad \text{.....[3.35]}$$

where ρ is the density of the material. To solve Equation [3.35], the boundary condition at the top of the cylinder is used, given as

$$\frac{M_0}{\varphi} = J_x \frac{\rho \cdot \omega^2 \cdot \ell}{\beta \cdot \mathbf{tan}(\beta)} - I_0 \cdot \omega^2 \quad \text{.....[3.36]}$$

where M_0 is the applied moment at the top of the cylinder, φ is the rotation angle, and β is given by

$$\beta = \frac{\omega \cdot \ell}{V_s} \cdot \sqrt{\frac{q+1}{2q^2}} \quad \text{.....[3.37]}$$

where

$$q = \sqrt{1 + (\mu \cdot \omega / G)^2} \quad \text{.....[3.38]}$$

In a standard RC test (at resonance), the rotation angle $\varphi \rightarrow \infty$ (if damping is assumed null) and Equation [3.36] becomes

$$\frac{I}{I_0} = \beta \, \mathbf{tan}(\beta) \quad \text{.....[3.39]}$$

where I is the moment of inertia of the cylinder and I_0 is the moment of inertia of the drive plate (determined experimentally). If zero damping is assumed, $q = 1$. In this study, a dynamic

signal analyzer is used to find ω_0, Equation [3.39] is used to find V_s and the damping ratio ξ is determined using the half-power bandwidth method (Kramer, 1996).

For axial excitation, the methodology is the same; however Equation [3.39] changes, shown as (Kramer, 1996)

$$\frac{m}{m_0} = \beta \cdot \mathbf{tan}(\beta) \quad \text{.....[3.40]}$$

where m is the specimen mass and m_0 is the drive system mass. In axial mode, shear wave velocity V_s is replaced by longitudinal wave velocity V_L in Equation [3.37].

In a standard resonant column test, the soil properties are computed for the resonant frequency of the sample by measuring the response over a range of frequencies by using a frequency sweep (sinusoidal chirp signal) as the excitation source. However, both soil properties measured in a standard resonant column test are frequency dependent. In order to measure the properties of the soil as a function of frequency, the standard test cannot be used. Since a constant excitation voltage is used over the entire frequency range, the strain level imposed on the sample is not constant, and this leads to erroneous measurements of soil properties as a function of frequency (Khan et al., 2007).

In the non-resonance (NR) method test, the soil properties are computed at various frequencies over a range of interest at a constant strain level by adjusting the excitation voltage of a sine wave at a constant frequency (Lai et al., 2001; Rix and Meng, 2005; Khan et al., 2007). To determine the soil properties as a function of frequency, the transfer function and phase difference are measured experimentally at each frequency interval to solve the complex shear modulus $G_s^*(\omega)$ given as

$$G_s^*(\omega) = G_1(\omega) + i \cdot G_2(\omega) \quad \text{.....[3.41]}$$

where $G_1(\omega)$ and $G_2(\omega)$ are the real and imaginary components of the complex shear modulus. The damping ratio is computed from the phase lag between the real and imaginary components (Lai et al., 2001). The complex modulus is obtained using the Newton-Raphson root-finding

algorithm of the complex equation derived from Equation [3.36], using the experimentally measured torque $M_0(\omega)$, rotation $\theta(\omega)$ and phase difference $\varphi(\omega)$, given as

$$\frac{M_o(\omega)\, e^{-i\theta(\omega)}}{\varphi(\omega)} = \frac{I\,\omega^2}{\left[\sqrt{\frac{\rho\,\omega^2 l^2}{G_S^*(\omega)}}\,\tan\left(\sqrt{\frac{\rho\,\omega^2 l^2}{G_S^*(\omega)}}\right)\right]} - I_o\,\omega^2 \quad \text{.....[3.42]}$$

Specimen torque and rotation angle are computed using

$$T_o(\omega) = B_L \frac{V_{res}(\omega)}{R_0}\, r_m \quad \text{.....[3.43]}$$

$$\varphi(\omega) = \frac{\ddot{x}(\omega)}{\omega^2\, r_a} \quad \text{.....[3.44]}$$

where B_L is the coil factor (B_L = 14.6 *N/Amp*), $V_{res}(\omega)$ is the measured voltage across a high-precision resistor, R_0 is the resistance of the calibrated resistor (R_0 = 1 *Ohm*) and r_m is the radial distance from the centre of the specimen to the driving magnets (r_m = 11.71 *cm*), $\ddot{x}(\omega)$ is the measured acceleration of the specimen as a function of angular frequency, and r_a is the radial distance from the centre of the specimen to the accelerometer (r_a = 6.87 *cm*).

As the frequency of excitation increases during an NR test, the required input voltage also increases because of the inductance of the coils.

3.3.2 Fluid Flow

Darcy's law describes one-dimensional fluid flow in a fully saturated porous medium, given previously as Equation [3.14]. For vadose zone or multi-phase flow, the model is more complex.

Flow in the vadose zone is related to the volumetric water content θ of the soil, the relative hydraulic conductivity K_r of the soil to the water phase, and the capillary pressure head ψ (Brooks-Corey or van Genuchten relationships). One-dimensional unsaturated fluid flow is described by (Schwartz & Zhang, 2003)

$$\frac{\partial \theta}{\partial t} = \frac{\partial}{\partial x}\left(K_r(\psi) \cdot K_x \cdot \left(\frac{\partial \psi}{\partial x} + 1 \right) \right) \quad \text{.....[3.45]}$$

This equation states that the rate of outflow minus the rate of inflow equals the rate of change of water storage in the medium. According to the relationships for relative hydraulic conductivity, saturation, and capillary pressure, if the water saturation decreases, the capillary forces increase and relative hydraulic conductivity drops. Therefore, if the degree of saturation of a specimen decreases, the flow rate is expected to decrease as well.

Similarly, for a multi-phase system with a NAPL, the rate of flow depends on the saturation of each phase and relative hydraulic conductivities, which are related through a Brooks-Corey relationship. The equation for one-dimensional flow for wetting and non-wetting phases are given as (Thomson, 2006)

$$v_i = \frac{K_x \cdot K_{r,i}}{\mu_i} \left(\frac{\partial P_i}{\partial x} + \rho_i \cdot g \cdot \frac{\partial h}{\partial x} \right) \quad \text{.....[3.46]}$$

where v_i is the flow, $K_{r,i}$ is the relative hydraulic conductivity, μ_i is the viscosity, P_i is the internal fluid pressure, ρ_i is the fluid density for each phase *i*, and K_x and h are the hydraulic conductivity and head in the soil matrix. A careful inspection of the above equations indicates that these models account for viscous drag forces, buoyant forces, relative hydraulic conductivity and hydraulic gradient.

The hydraulic conductivity of a saturated soil specimen can be computed using empirical formulae, or it can be experimentally determined using a falling head test. The main empirical formula utilized is the Hazen equation, given as

$$K = 0.01 \cdot d_{10}^2 \quad \text{.....[3.47]}$$

where d_{10} is the effective grain size (in *mm*), and K is given in *m/s*. Equation [3.47] is valid for loose sand samples with d_{10} between 0.1 and 0.2 *mm*. Alternatively, the hydraulic conductivity can be estimated using the Carmen-Kozeny equation, given as

$$K = \left(\frac{\rho_w \cdot g}{\mu}\right)\left(\frac{n^3}{(1-n)^2}\right)\left(\frac{d_m^2}{180}\right) \quad \text{.....[3.48]}$$

where μ is the dynamic viscosity of the pore fluid, and d_m is a representative grain size diameter. Equation [3.48] takes the porosity of the specimen into account, and therefore differs for each specimen. The porosity n of a prepared specimen is computed using

$$n = \frac{e}{1+e} \quad \text{.....[3.49]}$$

where void ratio e is determined as

$$e = \frac{G_s \cdot \rho_w}{\rho_d} - 1 \quad \text{.....[3.50]}$$

where G_s is the relative density of the soil grains, ρ_w is the density of water, and ρ_d is the dry density of the prepared sample (ratio of soil mass m_T to total specimen volume V_T).

For a falling head test, hydraulic conductivity K is given by

$$K = \frac{aL}{At} \cdot \mathbf{ln}\left(\frac{h_1}{h_2}\right) \quad \text{.....[3.51]}$$

where a is the cross-sectional area of the column of water, A is the cross-sectional area of the specimen, L is the length (height) of the sample, t is the elapsed flow time, and h_1 and h_2 are the height of the surface of the water column initially and at the end of the elapsed time interval, respectively.

4.0 EXPERIMENTAL SETUP AND METHODOLOGY

4.1 Equipment Setup

For this study, a modified Stokoe-type resonant column (RC) is used. This section outlines the physical equipment setup including modifications for axial excitation and more uniform flow and a schematic diagram of the signal processing equipment.

4.1.1 Physical Setup

The physical equipment setup is illustrated in Figure 4.1. There are three main groups of physical equipment used: sample and chamber pressurization, change in sample height measurement, and RC drive coils and monitoring apparatus.

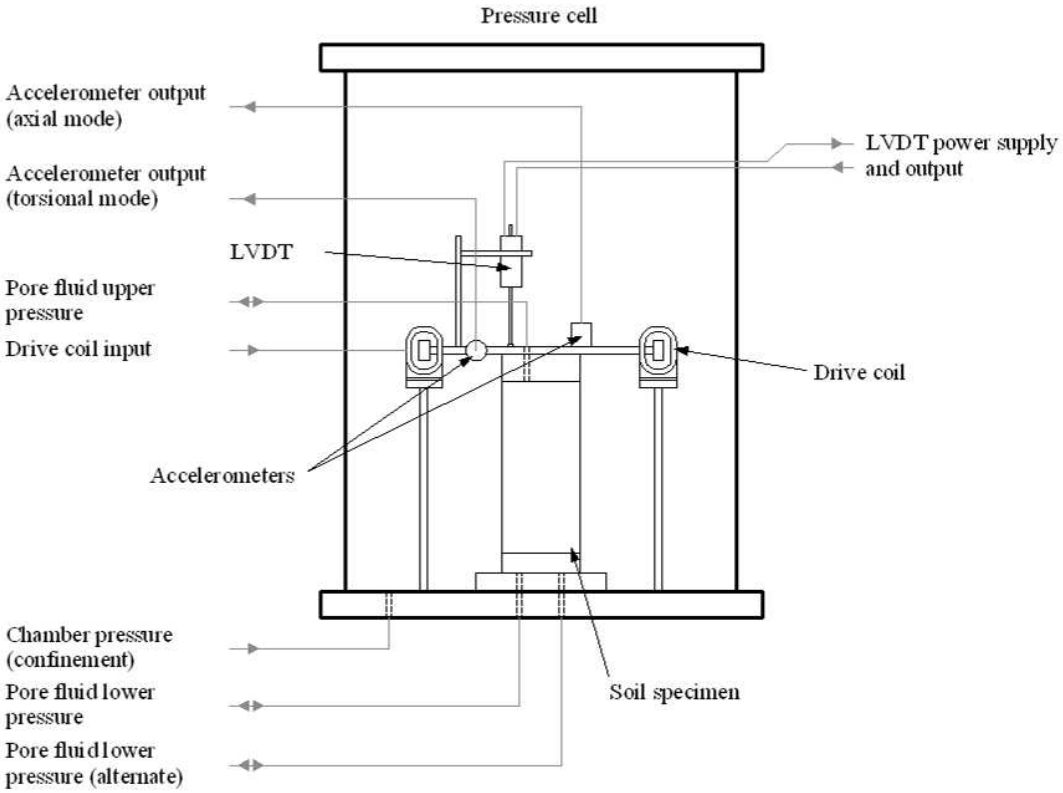

Figure 4.1 - Physical equipment setup

A triaxial chamber is used to provide confinement pressure for the sample. Both upper and lower pore fluid pressure can be regulated (including vacuum). Pressures are regulated independently by a pneumatic control board (Brainard-Kilman E-400, maximum confinement σ_0 = 700 *kPa*) and vacuum pressure is supplied by a vacuum pump. Distilled water is used as the pore fluid, supplied by a pressurized reservoir.

Changes in sample height are measured using a linear variable differential transformer (LVDT) (Trans-Tek 0242-0000 D-6) coupled to the RC driving plate. The LVDT core maintains constant contact with the driving plate indicating changes in sample height.

The drive coils fixed to the base of the RC supply energy for dynamic excitation. The coils may be configured for torsional mode (Figure 4.2) or axial mode (Figure 4.3) by pivoting the plexiglass angle brackets and the magnets on the driving plate. The plexiglass angle brackets are designed to limit the effect of eddy-current damping (Cascante et al, 2005). In the torsional mode, the response of the sample is monitored using an accelerometer fixed horizontally to the driving plate (Dytran 3056A3, sensitivity = 495.70 *mV/g*). In axial mode, the response of the sample is monitored by fixing the accelerometer vertically to the drive plate. To calibrate the RC equipment, the mass m_0 and moment of inertia I_0 of the driving plate are determined experimentally using an aluminum probe (Appendix B).

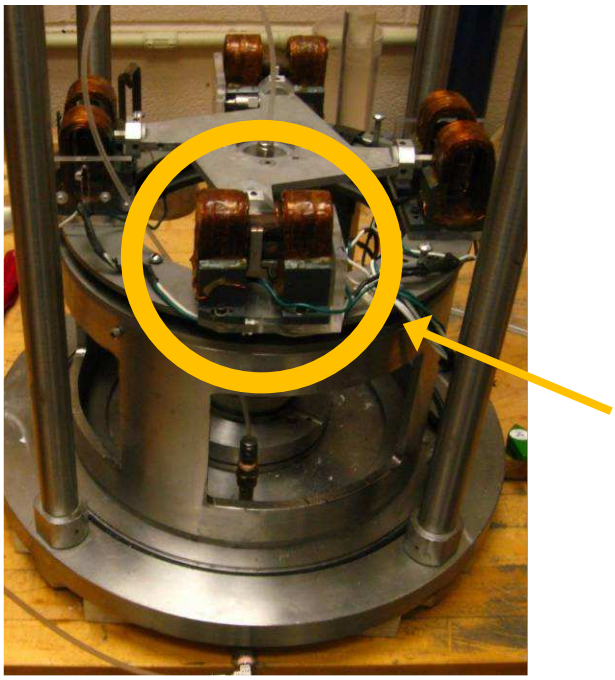

Figure 4.2 - Resonant column in torsional mode

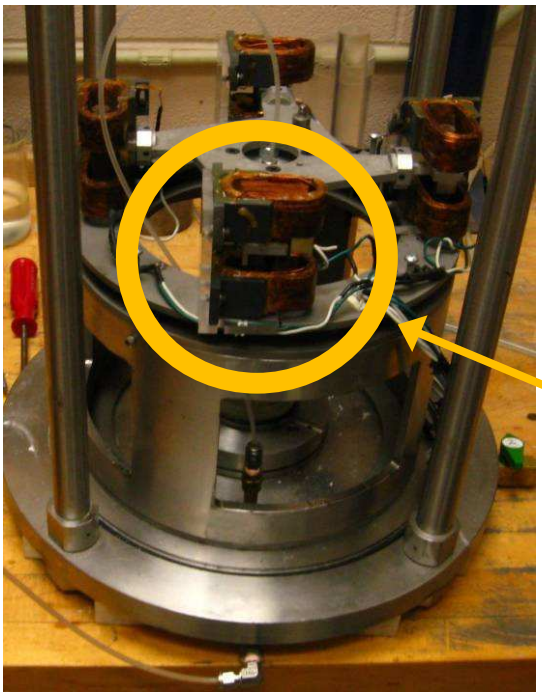

Figure 4.3 - Resonant column in axial mode

In a traditional Stokoe-type RC, the end plates have small holes which disperse fluid through the soil sample. In order to enhance flow uniformity across the face of the specimen, porous stone discs were machined to fit in redesigned end plates.

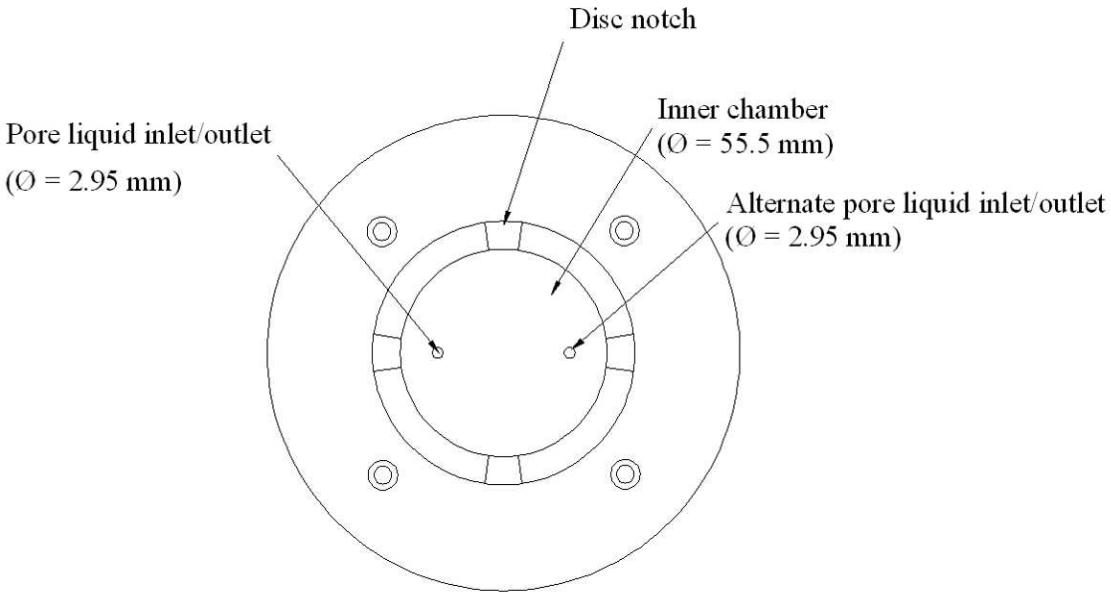

Figure 4.4 - Base plate plan view (from top plate)

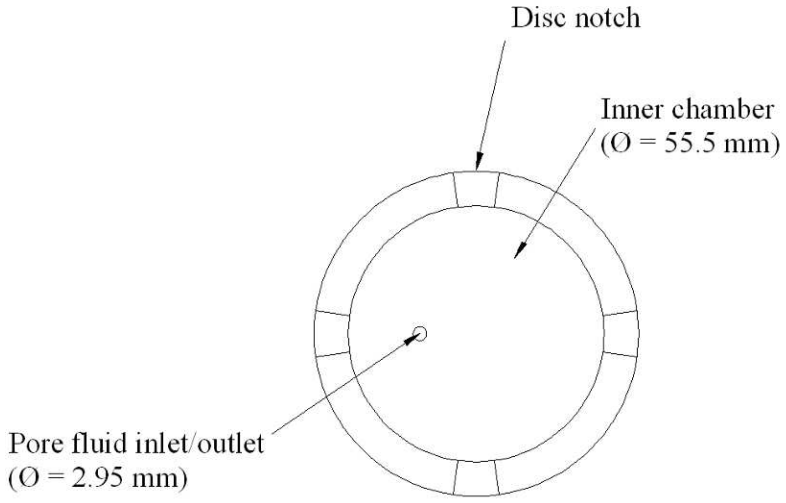

Figure 4.5 - Top plate plan view (from bottom plate)

Figure 4.4 shows the details of the modified base plate, while Figure 4.5 shows the modified top plate. The plates contain hollowed inner chambers (directly below the porous discs) for pore fluid accumulation and dispersal uniformly across the entire surface area. The base plate inner chamber contains two perforations which allow pore fluid to flow into or out of the chamber using two separate flow control valves. The top plate inner chamber has only one pore fluid flow perforation. The porous discs are placed on the face of each plate and held in place by four notches designed to prevent rotational motion. The porous discs have a manufacturer-specified hydraulic conductivity of 2×10^{-8} *m/s*; however, separate falling-head hydraulic conductivity tests performed on the discs consistently give a much higher conductivity, approximately 3.7×10^{-4} *m/s*. There is no justification for the discrepancy between reported and measured hydraulic conductivities given by the manufacturer.

The completed assembly is shown as Figure 4.6.

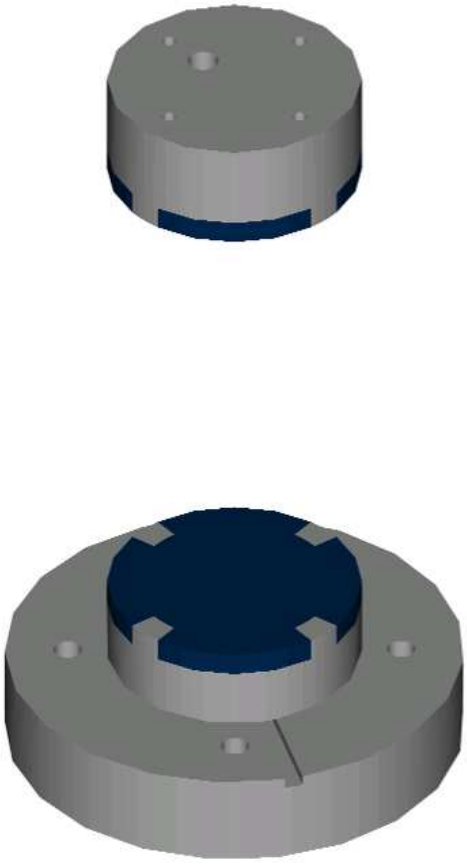

Figure 4.6 - Modified RC end plates

4.1.2 Signal Processing Schematic

The signal processing schematic diagram is shown in Figure 4.7. The LVDT signal is monitored using a digital multimeter (Hewlett-Packard 34401A). Power is supplied to the LVDT using a constant voltage power supply (Hewlett-Packard E3620A).

The RC drive coils are excited with a signal generated by a dynamic signal analyzer (Hewlett-Packard 35665A) which is amplified by a power amplifier (Bogen 250) and fed into the drive coil switchbox. The switchbox can be operated in torsional, axial or flexural mode. The drive coil signal is monitored on both the signal analyzer and a digital oscilloscope (Hewlett-Packard 54645A). The specimen response signals are amplified by a power amplifier (Dytron 4121), filtered (Krohn-Hite 3384) and monitored by both the signal analyzer and oscilloscope. In a traditional RC test, the resonant frequency and damping are computed automatically using the half-power bandwidth method (Kramer, 1996). For the NR method

test, data from the signal analyzer is recorded and manually entered into a MathCAD worksheet for analysis (Appendix C). Results from both the signal analyzer and oscilloscope are stored on a personal computer for further analysis.

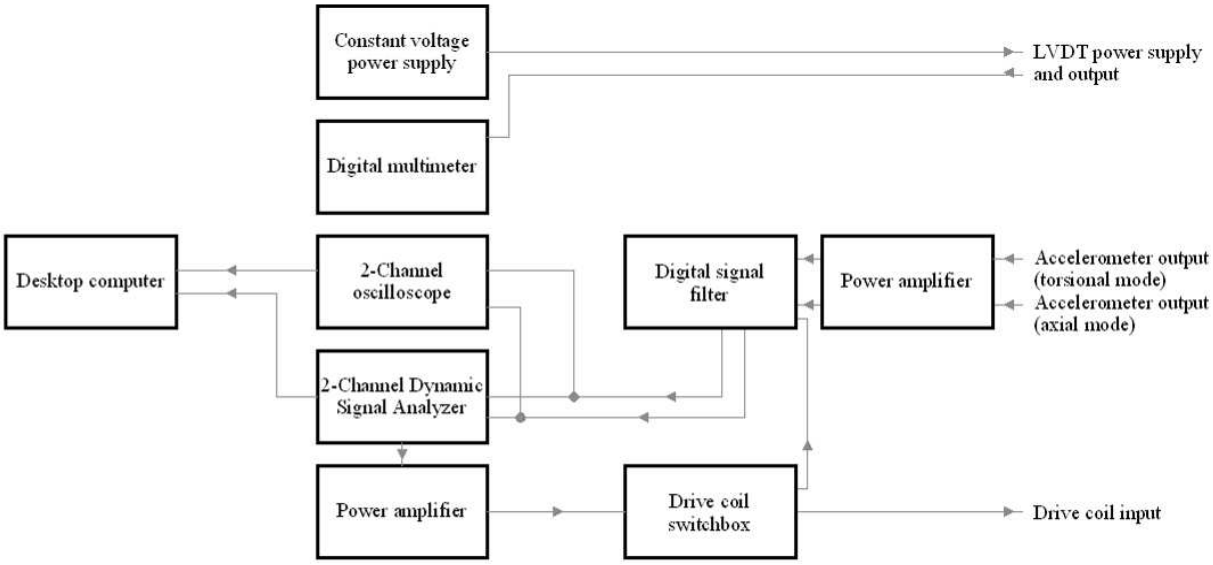

Figure 4.7 - Signal processing schematic diagram

4.2 Experimental Methodology

A total of seven specimens are tested for this study. The first specimen serves as a calibration for the equipment to ensure the modifications are functioning as intended. The second specimen is prepared to attempt to reproduce enhanced flow by creating a standing wave in the pore fluid as described by Dusseault et al. (2002), using very low frequencies (≤ 20 *Hz*) in both torsional and axial modes. Specimens three, four and five are prepared to determine if excitation at resonant modes of the specimen produce enhanced flow using frequencies across a larger bandwidth (≤ 1600 *Hz*) in all three modes of vibration in sands of varying grain size. Specimens 6 and 7 are an attempt to repeat specimen 3 and 4 saturated testing with a higher degree of saturation. The top and bottom plates used for these tests differ from the previous 5 specimens; the change in inertial and mass properties is accounted for in the NR method analysis. A wideband sweep is used to identify the resonant peaks in each mode of vibration. Large strains are produced when the specimen is vibrated at resonant frequencies, so enhanced fluid flow is more likely to occur. Next, resonance method tests are performed using a burst-chirp signal with a 50 *Hz* bandwidth to determine the resonant frequency and damping ratio at resonance. For all resonant method tests, the signal analyzer amplitude and power amplifier gain settings are constant (250 *mV* peak-to-peak and 25), unless otherwise specified. A total of 20 averages are taken to compute the transfer function. Non-resonance method tests are performed for the 100 Hz bandwidth around the resonant peak at a constant strain level to determine how wave velocity and damping ratio vary with frequency. Five averages are taken at each frequency interval. For all tests using the dynamic signal analyzer, the input auto-range function is used for both channels to ensure maximum sensitivity and prevent saturation of the recorded signal.

For these tests, dry sand specimens are prepared inside the resonant column using a split mould. After fixing the base plate to the resonant column base, a rubber membrane is secured to the platen with an O-ring. The split mould is placed over the base platen and the membrane is stretched over it. Vacuum is applied to the split mould to keep the membrane flush with the inside of the mould. A porous stone disc is inserted on the base plate. Dry sand is poured in layers of 20 to 30 mm. The split mould is tamped gently to densify the layers to desired void ratio (height). Next, a second porous stone disc is inserted on to the top plate and

the entire assembly is fitted to the top of the specimen, the rubber membrane is secured with another O-ring and the mould is removed after applying the vacuum to the pore fluid lower pressure valve. During this procedure, the total mass m_T of sand used to create the sample is recorded. After the sample is completed, the height of the sand column is measured to compute the total sample volume V_T.

Three different sands are used (grain size distributions are shown in Appendix A). Basic characteristics of the sands are given in Table 4-1.

Table 4-1 - Sand parameters

Sand	d_{10}	d_{30}	d_{60}	C_u	C_z	G_s	***USCS***
	mm	*mm*	*mm*	--	--	--	--
Silex Regular	0.0018	0.006	0.018	10.0	1.11	2.65	SM
Barco 71	0.12	0.17	0.2	1.78	1.20	2.65	SW
Indusmin 2010	0.28	0.4	0.58	2.07	0.99	2.65	SW

The maximum and minimum void ratios for the Barco sand are 0.53 and 0.75, respectively. These values are not known for the Indusmin sand.

After the connections are made and the pressure chamber sealed, the confinement pressure is gradually increased to 80 *kPa* while the vacuum pressure in the soil specimen is gradually decreased.

To saturate the specimen, slight vacuum is applied to the top port, while distilled water is flushed through the bottom port. This process continues until roughly two pore volumes have passed through the specimen. During the saturation of specimen 1, many air bubbles were observed in the pipette on the pneumatic control board. To attempt to eliminate the leak, the control board was first checked to ensure no leaks in the pore fluid supply lines. Next, the resonant column was disassembled, and the pore fluid openings in the top and bottom plate were plugged. The pore fluid tubes were put under a back-pressure of 600 kPa; no leaks were observed. However, when the tubes were sealed in the chamber under a confinement pressure of 600 kPa, the connector between the top plate and pore fluid tube appeared to be the cause of the leak and was replaced with a more rigid tube. The metal furl in the Swagelok connector was also replaced with a plastic furl to attempt to provide a better seal between the tube and connector. Even with all of these checks completed, there was still a significant air leak into

the subsequent specimens. The source of the leak is likely due to either a small tear in the membrane occurring during specimen preparation or the membrane-plate seal provided by the O-rings is not sufficient.

Hydraulic conductivity is measured using a falling-head test. The main lower fluid pressure valve is closed, and the elapsed time t is measured for a known head level drop through the alternate lower fluid pressure valve with an initial head $h_1 = 0.592\ m$. Hydraulic conductivity K is computed using Equation [3.51].

5.0 EXPERIMENTAL RESULTS AND DISCUSSION

5.1 Results

The results of wide-bandwidth, RC and NR method tests are presented next.

5.1.1 Wave Velocity Degradation Curves

Shear and compression wave velocity degradation curves for Barco sand and Indusmin sand under dry and partially saturated conditions are given as Figure 5.1, Figure 5.2, Figure 5.3 and Figure 5.4.

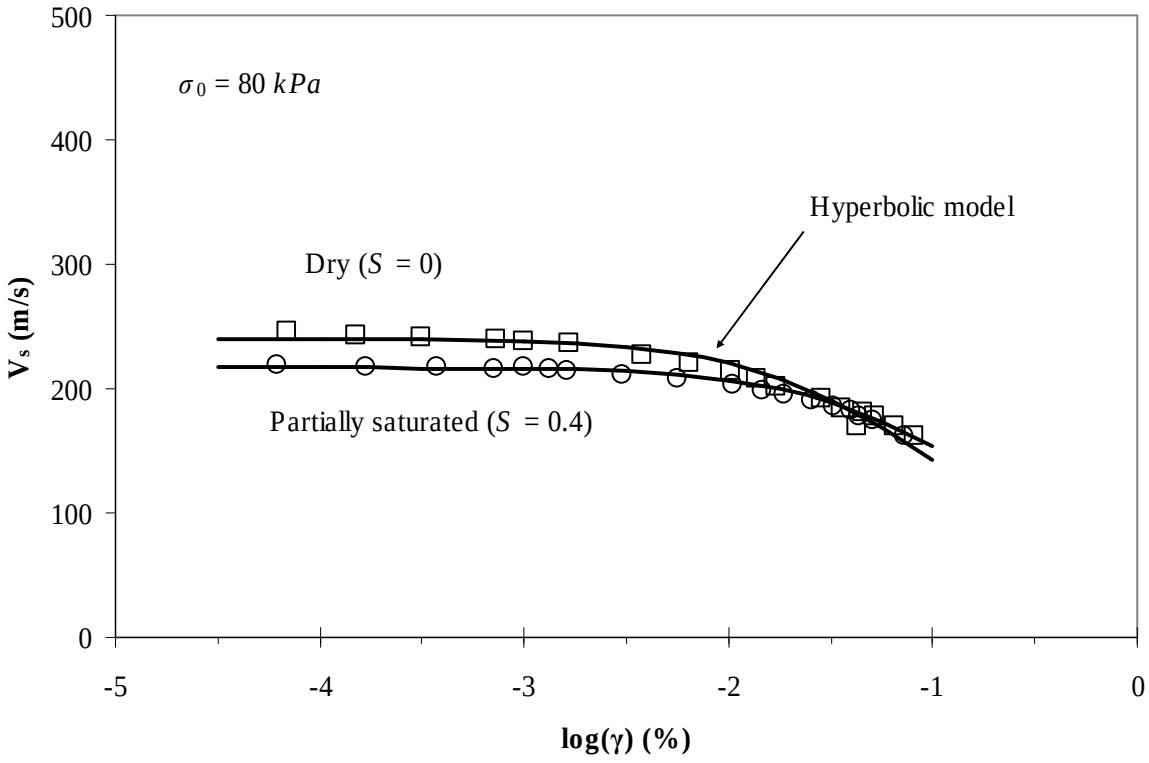

Figure 5.1 - Barco sand torsional wave velocity degradation curve

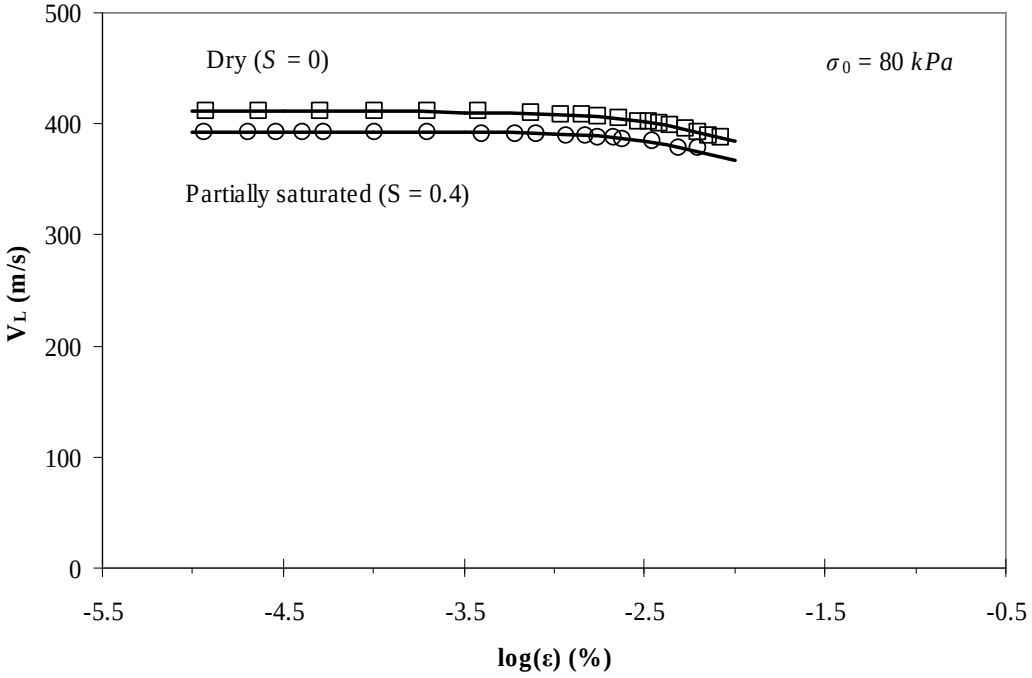

Figure 5.2 - Barco sand compression wave velocity degradation curve

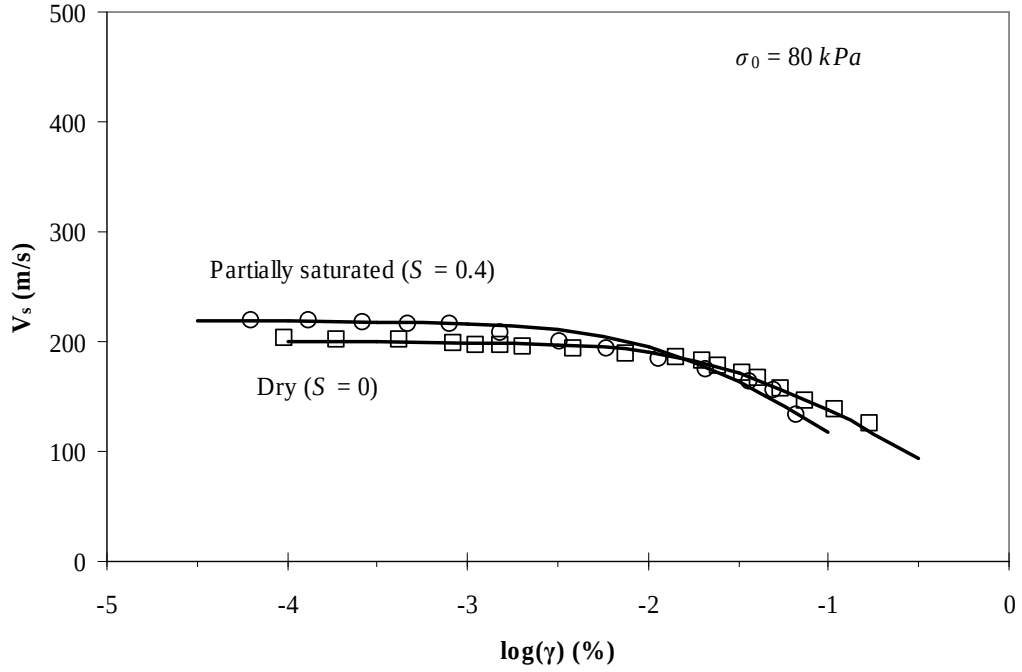

Figure 5.3 - Indusmin sand torsion wave velocity degradation curve

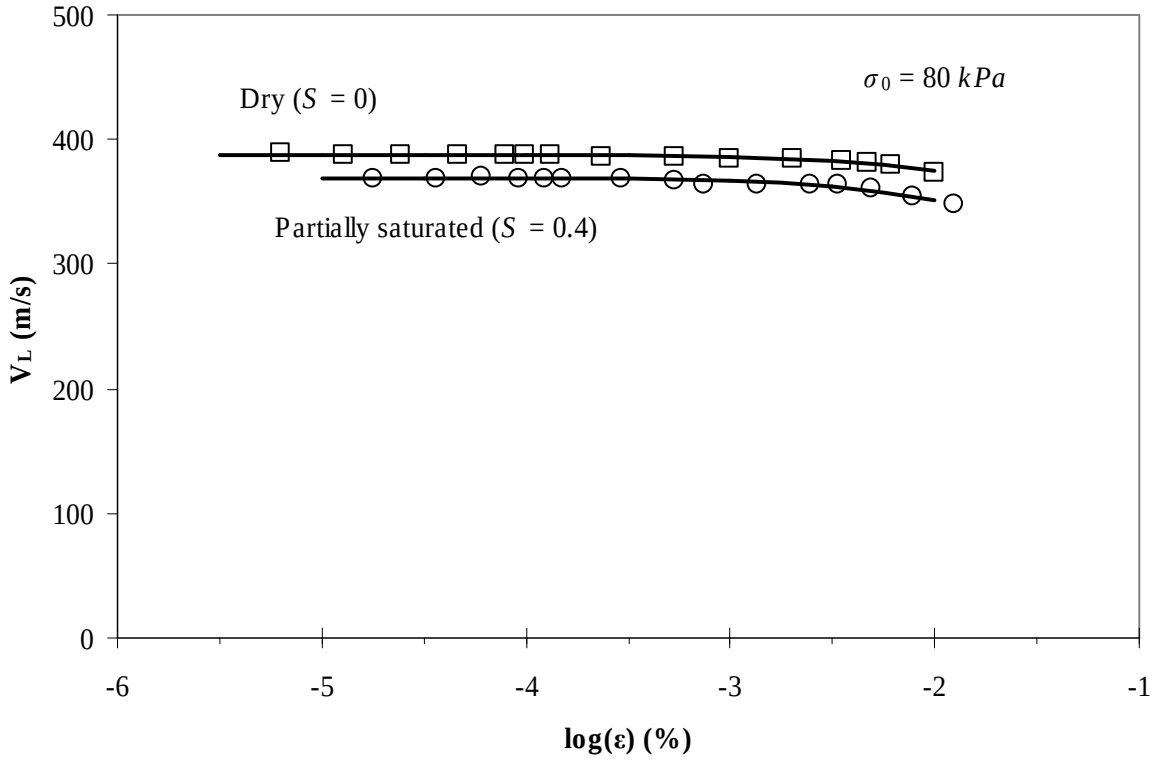

Figure 5.4 - Indusmin sand compression wave velocity degradation curve

The degradation curve is computed first in the dry torsional mode, then the magnets and coils are pivoted for dry axial mode. Next, the specimen is partially saturated and tested in the axial mode. Finally, the magnets and coils are pivoted back for partially saturated torsional mode testing. Hyperbolic models are fitted to each set of data to determine the threshold strain limit γ_{th}. The hyperbolic model parameters are summarized in Table 5-1.

Table 5-1 - Summary of hyperbolic model parameters

Excitation Mode	Barco Sand		Indusmin Sand	
	γ_{th} (%)	V_{max} (m/s)	γ_{th} (%)	V_{max} (m/s)
Torsional (S = 0)	5.5×10^{-2}	240	9.0×10^{-2}	200
Torsional (S = 0.4)	1.0×10^{-1}	217	4.0×10^{-2}	219
Axial (S = 0)	7.0×10^{-2}	411	1.5×10^{-1}	388
Axial (S = 0.4)	7.0×10^{-2}	393	1.0×10^{-1}	369

The threshold strain does not vary significantly between dry and partially saturated conditions in axial mode, however there is a much wider variation for the torsional mode. The

threshold strain is approximately doubled for the partially saturated condition. The added pore water in the partially saturated condition acts as a lubricant which reduces the stiffness of the contacts thus reducing the elastic behavior of the specimen.

For both specimens in axial mode the partially saturated specimen exhibits a lower wave velocity compared with the dry specimen. This pattern is also observed in the Barco sand for the torsional mode; however, for the Indusmin sand, the opposite occurs. This is likely due to the order of operations for the test sequence - the torsional saturated mode for the sands were completed last, so the fabric of the specimen was probably altered. If the specimen was compacted during the dynamic tests, the corresponding wave velocity would also decrease which is what is observed here.

Table 5-2 summarizes maximum strain levels achieved for each test, and the corresponding degradation as a percentage of maximum wave velocity. The maximum degradation in axial mode is smaller than the corresponding degradation in torsional mode because of the greater specimen stiffness in the axial direction.

Table 5-2 - Summary of maximum degradation

Excitation Mode	**Barco Sand**		**Indusmin Sand**	
	γ_{max} **(%)**	V/V_{max} **(%)**	γ_{max} **(%)**	V/V_{max} **(%)**
Torsional (S = 0)	8.1×10^{-2}	67.5	1.7×10^{-1}	62.5
Torsional (S = 0.4)	7.3×10^{-2}	74.7	1.3×10^{-1}	61.2
Axial (S = 0)	8.4×10^{-3}	94.2	9.9×10^{-3}	96.1
Axial (S = 0.4)	6.3×10^{-3}	96.2	1.2×10^{-2}	94.3

5.1.2 Specimen 1

Specimen 1 is made of Barco 71 sand; its physical properties are given in Table 5-3. The purpose of specimen 1 flow testing is to verify the equipment is functioning properly and that repeatable flow rate measurements are observed. There are also some initial measurements of flow during dynamic excitation. One RC test of the partially saturated sample is performed in torsional mode; the transfer function is shown as Figure 5.5 and the dynamic properties of the specimen are summarized in Table 5-4. The normalization factor H_0 is the ratio of filtered output voltage to filtered input voltage in the computed transfer function.

Table 5-3 - Specimen 1, physical properties

Mass	m_T	1.007	*kg*
Height	L	0.146	*m*
Volume	V_T	562	*mL*
Dry density	ρ_d	1792	kg/m^3
Void ratio	e	0.520	--
Relative density	d_r	1.0	--
Porosity	n	0.342	--
Volume of voids	V_v	181	*mL*
Conductivity (Hazen)	K	1.4×10^{-4}	*m/s*
Conductivity (C-K)	K	4.8×10^{-5}	*m/s*
Permeability	k	13.0	*darcy*

Table 5-4 - Specimen 1, dynamic properties

		Torsional	
Resonant frequency	f_0	65	*Hz*
Damping ratio	ξ_0	0.74	*%*
Strain level	γ	1.7×10^{-3}	*%*
	γ/γ_{th}	3.1	*%*

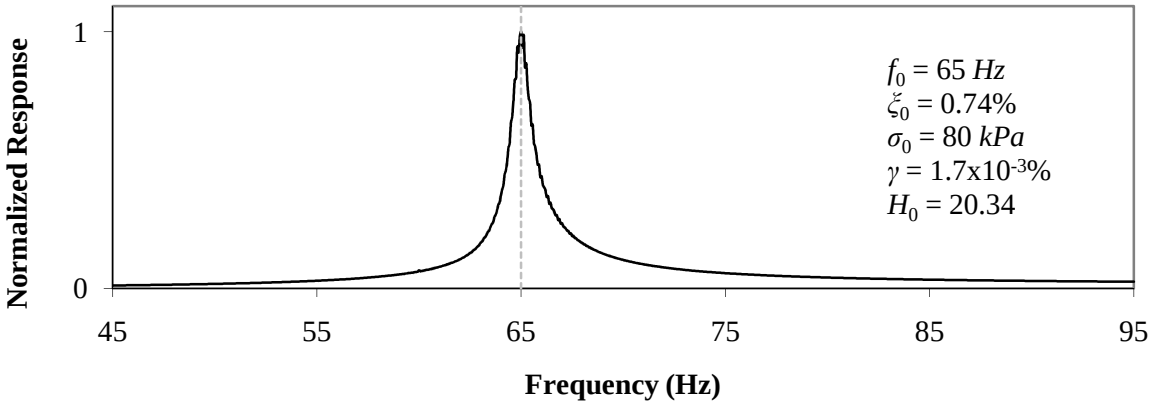

Figure 5.5 - Specimen 1 partially saturated, RC test, torsional mode

A total of 11 flow test trials are performed on the specimen, with 20 time measurements for each trial. Table 5-5 summarizes the dynamic properties of each flow test.

Table 5-5 - Specimen 1, flow test dynamic properties

Trial	Mode	Frequency	Strain	γ/γ_{th}
		Hz	%	%
5	torsional	65	$1.7x10^{-3}$	3.1
7	torsional	10	$1.7x10^{-3}$	3.1
10	torsional	5	$1.7x10^{-3}$	3.1

The shear strains used during this test are only 3 % of the threshold strain; thus the fabric changes in the specimen are minimal. During the flow test trials, large amounts of air are observed in the outflow. As the tests progress, the air bubbles become larger and more frequent and the measured time intervals generally increased, while at the same time becoming more erratic. Measured time intervals for each trial are shown as Figure 5.6. The average measured time interval for each trial is shown as a solid diamond and the 95 % confidence intervals are shown as thick dashes above and below the mean values.

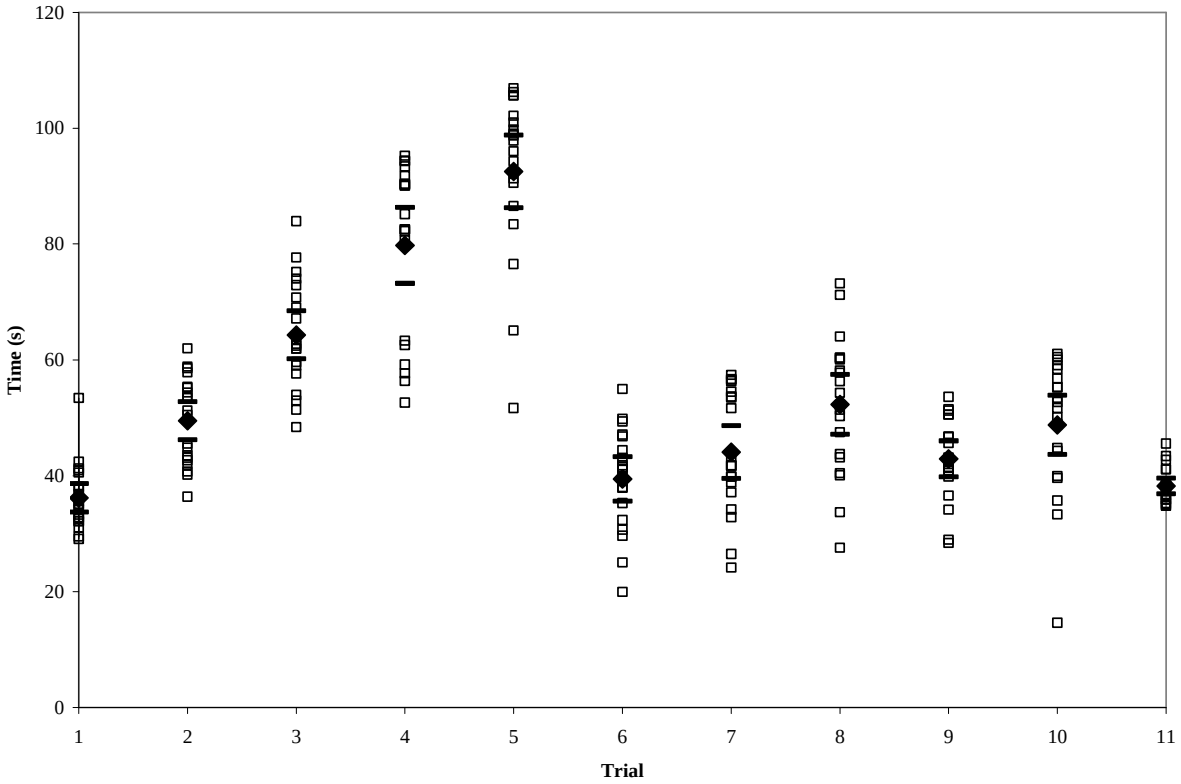

Figure 5.6 - Specimen 1, flow test measured time intervals

After trial 5, the head differential is decreased from 0.164 *m* to 0.055 *m* to decrease the test duration. Thus, the measured time intervals for trials 6 through 11 are noticeably smaller.

Figure 5.7 shows a time series plot of computed hydraulic conductivities to illustrate the effect of air bubbling on measured permeability. The solid line on the plot represents the hydraulic conductivity of the porous discs at the top and bottom of the specimen, $K = 3.7\text{x}10^{-4}$ *m/s*; therefore, this represents the upper limit of specimen hydraulic conductivity that can be detected using this equipment setup. The long-dashed line represents the estimate of hydraulic conductivity of the specimen given by Equation [3.47] and the short-dashed line represents the estimate of conductivity given by Equation [3.48]. The measurements for each of the 11 trials are plotted consecutively, giving a time-series representation of the conductivity measurements.

The air leak into the specimen occurs in the flow tubing connections inside the pressurized chamber. Swagelok connectors are not normally designed to withstand external pressurized environments; thus pressurized air is forced into the tubing lines and accumulates within the specimen. From the theory outlined in Section 3.3.2, it is expected that as the air content of the porous matrix increases, the hydraulic conductivity of the specimen decreases, which is clearly shown in Figure 5.7. There is an exponential decay with good correlation of the data ($R^2 = 0.806$) until the rate of conductivity decrease plateaus at 30 minutes and there is poor correlation of the data ($R^2 = 0.0034$) after that time.

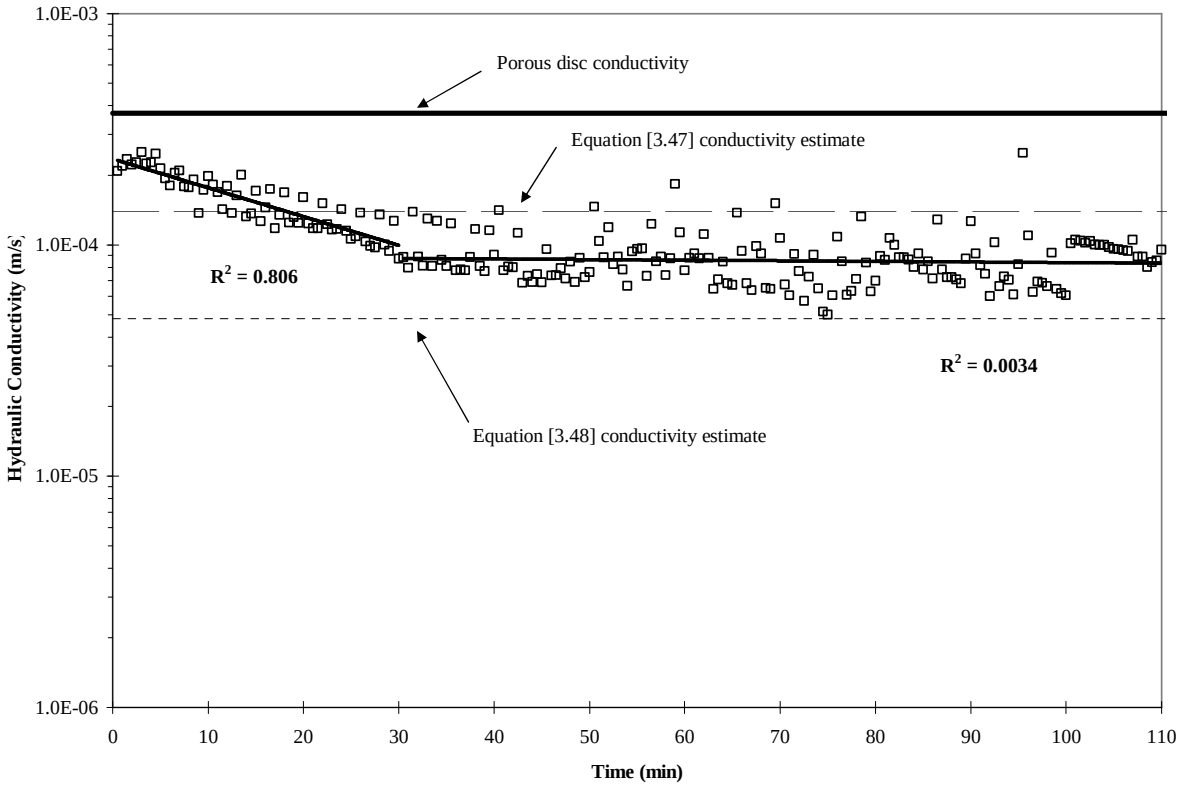

Figure 5.7 - Specimen 1, flow test computed hydraulic conductivities

After specimen 1 evaluation is complete, the metal furls on the Swagelok connectors are replaced with plastic furls that form a better seal around the flow tubing, thereby allowing less air to enter the specimen. These modifications have mixed results - a slow air leak is observed in subsequent specimens, in spite of the flow tubing modifications, which affects conductivity measurements in much the same way as observed during specimen 1 testing, only on a slightly slower timescale. For subsequent flow tests, the specimen is flushed with water before each time trial commences. This procedural change is designed to mitigate the effects of air accumulation in the specimen and to allow more repeatable measurements over the duration of the trial. Unfortunately, this procedure is not always effective.

The degree of specimen saturation *S* is also evaluated by determining the pore pressure coefficient *B*, both initially after saturation and later after allowing air bubbles to accumulate in the specimen. The chamber pressure is increased from 80 *kPa* to 180 *kPa*, with a 100 *kPa* pore water backpressure applied to both the top and bottom pore pressure valves; thus, the effective

confinement pressure remains 80 *kPa*. Next, the pore pressure valves are closed and the specimen pore pressure is monitored using a pore pressure transducer at the top valve. The chamber pressure is increased by 100 *kPa* and the corresponding pore pressure change is monitored with time. The ratio of the change in chamber pressure to the change in pore pressure is the pore pressure coefficient *B*. Figure 5.8 shows the pore pressure changes as a function of time just after initial saturation, as well as an hour later.

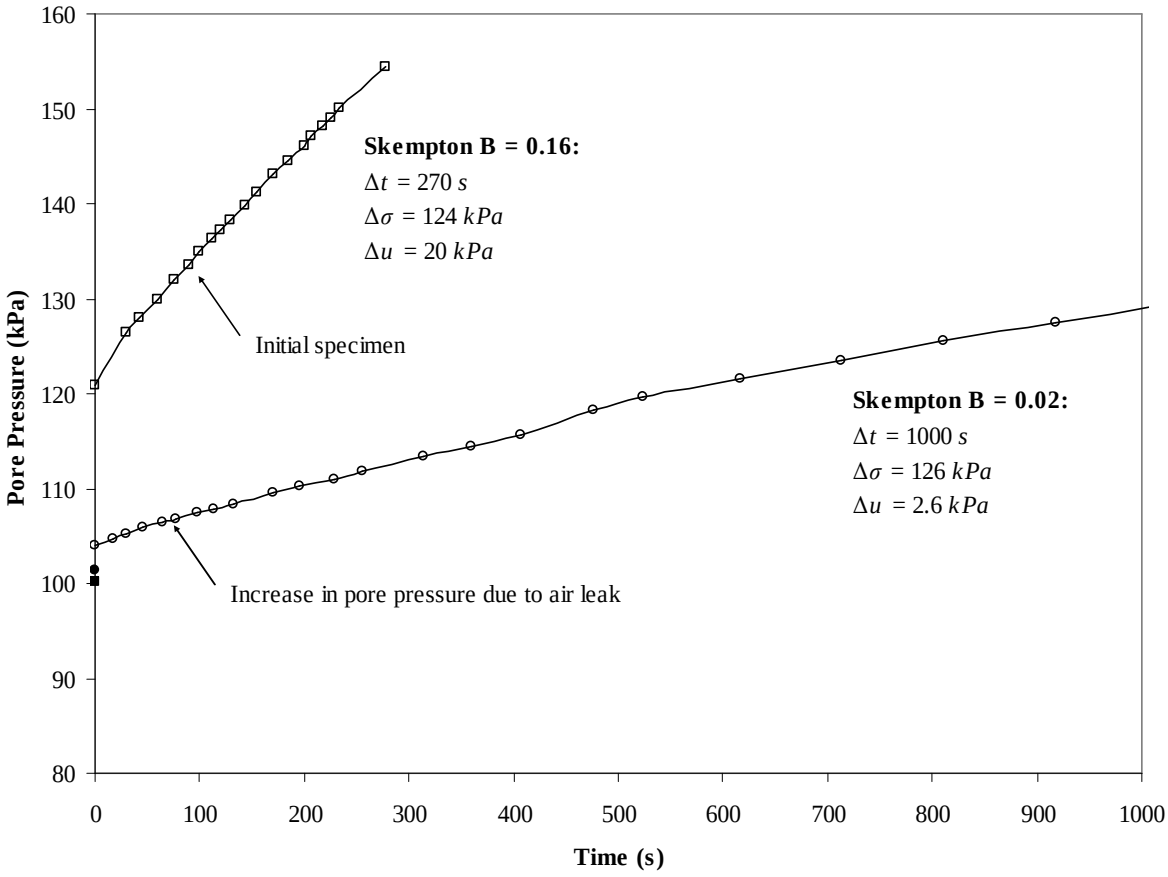

Figure 5.8 - Barco sand pore pressure coefficient *B* measurement results

Just after saturation, $B = 0.16$, which corresponds to $S = 0.75$ (Craig, 2002). After an hour, $B = 0.02$, meaning $S = 0.6$. These results indicate that 100 % saturation of the specimens is not achieved during testing and the problem is compounded by the air leak.

5.1.3 Specimen 2

Specimen 2 is made of Barco 71 sand; its physical properties are given in Table 5-6.

Table 5-6 - Specimen 2, physical properties

Mass	m_T	1.027	*kg*
Height	L	0.146	*m*
Volume	V_T	562	*mL*
Dry density	ρ_d	1827	kg/m^3
Void ratio	e	0.515	--
Relative density	d_r	1.0	--
Porosity	n	0.340	--
Volume of voids	V_v	174	*mL*
Conductivity (Hazen)	K	1.4×10^{-4}	*m/s*
Conductivity (C-K)	K	4.9×10^{-5}	*m/s*
Permeability	k	13.0	*darcy*

The purpose of specimen 2 flow testing is to characterize the dynamic properties of the soil in both torsional and axial mode of vibration and to attempt to reproduce the effect of the pressure-pulsing technique (PPT) described by Dusseault et al. (2002), and outlined in Section 3.1.3 of this thesis. Two RC tests of the partially saturated sample are performed, in torsional and axial modes. The results for the axial mode are unavailable due to computer disk failure. The torsional dynamic properties of the specimen are given in Table 5-7 and the transfer function is shown as Figure 5.9.

Table 5-7 - Specimen 2, dynamic properties

		Torsional	
Resonant frequency	f_0	68	*Hz*
Damping ratio	ξ_0	1.22	*%*
Strain level	γ	4.5×10^{-4}	*%*
	γ/γ_{th}	0.8	*%*

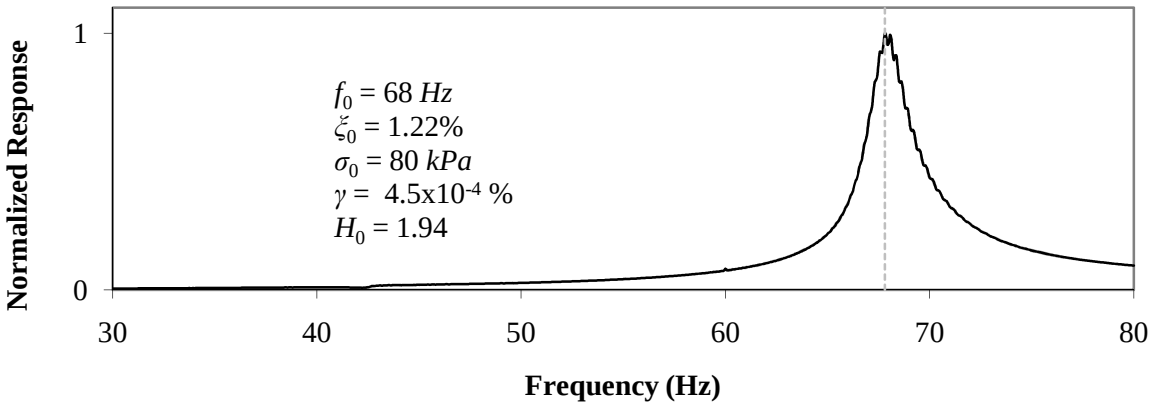

Figure 5.9 - Specimen 2 partially saturated, RC test, torsional mode

The normalization factor for specimen 2 is much smaller than for specimen 1 because the air leak reduces the effective stress. The air leak is much more prevalent in specimen 2, therefore the normalization factor is much smaller.

An NR method test (Section 3.3.1) is performed in torsional mode to determine the shear wave velocity and damping ratio at varying frequencies. Plots of shear wave velocity (squares) and damping ratio (circles) versus frequency of excitation are given as Figure 5.10. The RC (solid symbols) and NR method (hollow symbols) results for the torsional mode dynamic properties are consistent.

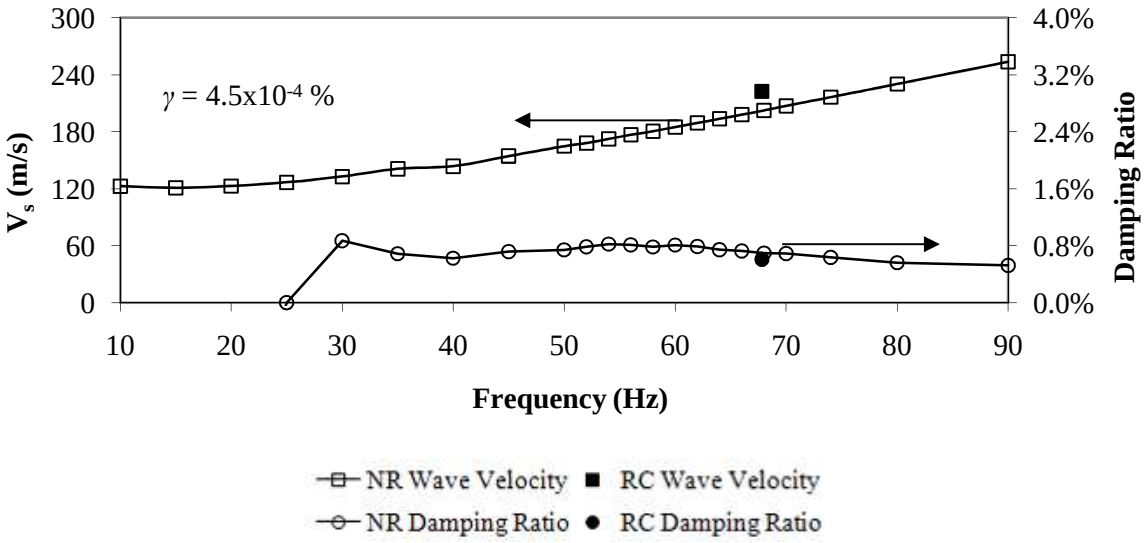

Figure 5.10 - Specimen 2 partially saturated, NR test, torsional mode

A total of 12 flow test trials are performed on the specimen, with 20 time measurements for each trial. Table 5-8 summarizes the dynamic properties of each flow test. Measured time intervals for each trial are shown as Figure 5.11. After trial 6, the head differential is reduced from 0.164 *m* to 0.055 *m* to shorten the duration of each trial; thus, the measured time intervals for trials 7 through 12 are noticeably smaller. Figure 5.12 summarizes the hydraulic conductivity results for specimen 2 saturated single-phase flow.

Table 5-8 - Specimen 2, flow test dynamic properties

Trial	Mode	Frequency Hz	Strain %	γ/γ_{th} %
4	torsional	20	$4.5x10^{-4}$	0.8
5	torsional	10	$4.5x10^{-4}$	0.8
6	torsional	5	$4.5x10^{-4}$	0.8
10	axial	20	$5.0x10^{-5}$	0.07
11	axial	15	$5.0x10^{-5}$	0.07
12	axial	10	$5.0x10^{-5}$	0.07

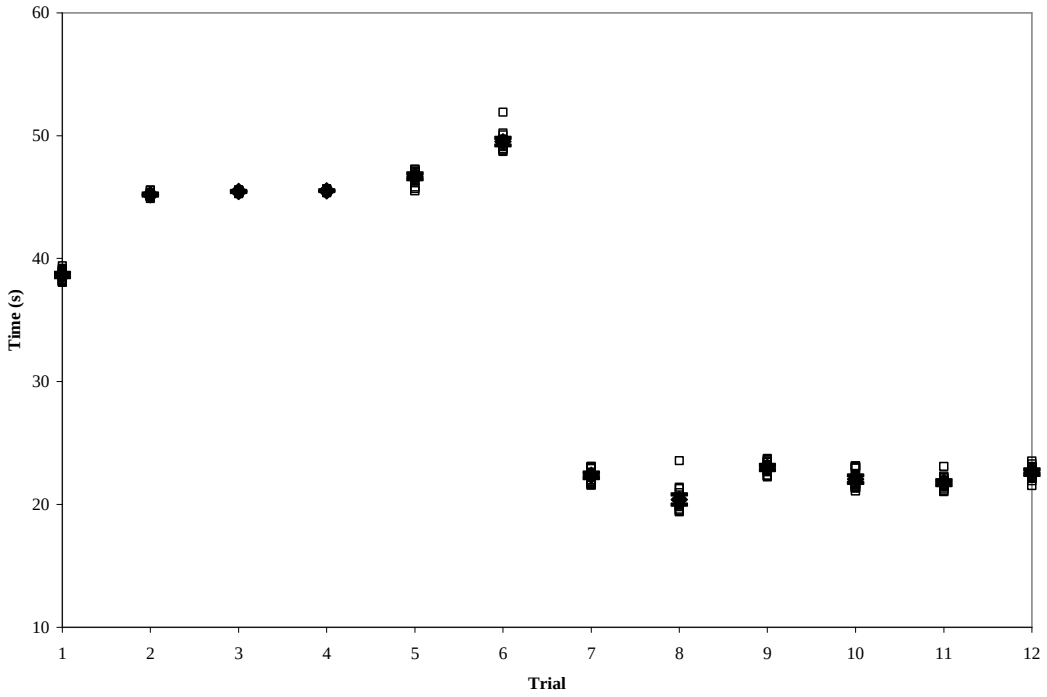

Figure 5.11 - Specimen 2, flow test measured time intervals

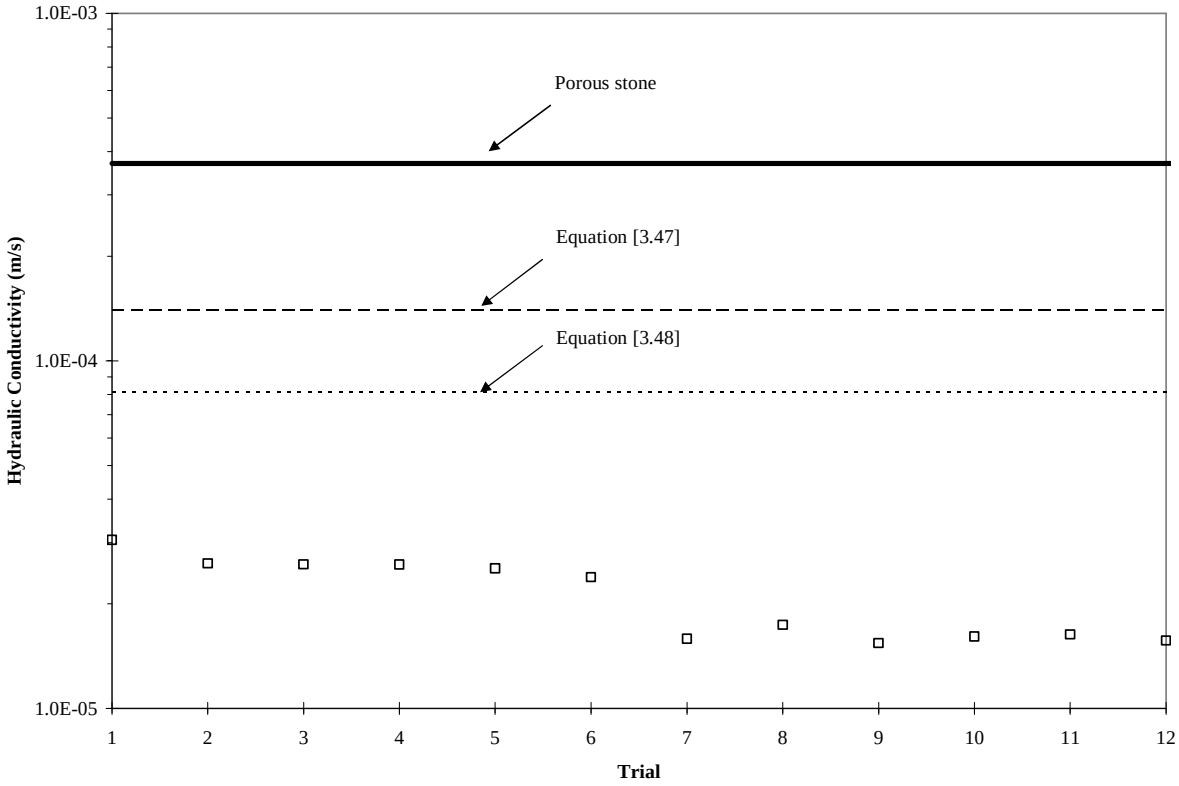

Figure 5.12 - Specimen 2, flow test computed hydraulic conductivities

The virgin hydraulic conductivity of the specimen is almost one order of magnitude lower than the value predicted for a loose sand sample. It is more accurately predicted by Equation [4.5], but there is still a slight discrepancy between the two values. There are two distinct drops in hydraulic conductivity, one between trial 1 and trial 2, and another between trial 6 and trial 7. Following trial 1, the first dynamic tests are performed on the sample. The air leak into the specimen likely played a role in the reduced conductivity. After trial 6, the sample is drained and put under vacuum as the pressure chamber is removed and the drive coil reconfigured for axial excitation. The low conductivity values are probably due to poor saturation of the specimen. The time measurement confidence intervals for each trial are very small, indicating good repeatability of measurements within each trial, and in most cases (other than the previously noted decreases) between trials.

The dynamic conductivity tests performed indicate that there is virtually no change in partially saturated single-phase flow in the presence of low frequency dynamic excitation,

either in torsional or axial mode. The purpose of these partially saturated single-phase flow tests is to attempt to reproduce the effect of the pressure-pulsing technique (PPT) described by Dusseault et al. (2002). If the PPT were reproduced by these dynamic tests, there should be a noticeable increase in hydraulic conductivity due to the added influence of inertial energy to the flowing pore fluid as well as the porosity dilation waves which move through the matrix. However, increased conductivity is not observed when low frequency dynamic excitation is applied. Thus, the PPT may require a high level of saturation to work.

5.1.4 Specimen 3

Specimen 3 is made of Barco 71 sand; its physical properties are given in Table 5-9.

Table 5-9 - Specimen 3, physical properties

Mass	m_T	1.009	*kg*
Height	L	0.153	*m*
Volume	V_T	589	*mL*
Dry density	ρ_d	1713	kg/m^3
Void ratio	e	0.544	--
Relative density	d_r	0.94	--
Porosity	n	0.352	--
Volume of voids	V_v	207	*mL*
Conductivity (Hazen)	K	1.4×10^{-4}	*m/s*
Conductivity (C-K)	K	8.2×10^{-5}	*m/s*
Permeability	k	13.0	*darcy*

The purpose of specimen 3 flow testing is to characterize the dynamic properties of the soil in both torsional and axial mode of vibration over a wide frequency bandwidth (1600 *Hz*). Once the wide-bandwidth excitation is applied, the resonant frequencies for the first modes in flexural, torsional and axial directions are identified. Then, narrow-band excitation (50 *Hz* bandwidth) is used around the resonant frequencies. Dynamic excitation in all three modes is applied at frequencies corresponding to the resonant peaks of the specimen in each mode, both in narrow bandwidths around the peaks as well as fixed sine waves at resonance. Unfortunately specimen height changes are not monitored using the LVDT for these tests due to equipment malfunction.

Wide-bandwidth sweeps are performed on the unsaturated specimen in all three modes of vibration, shown as Figure 5.13. First resonant peaks are noted at approximately 45 *Hz* in flexural mode, 70 *Hz* in torsional mode and 385 *Hz* in axial mode. This figure shows that there is no mode coupling for the first vibration modes.

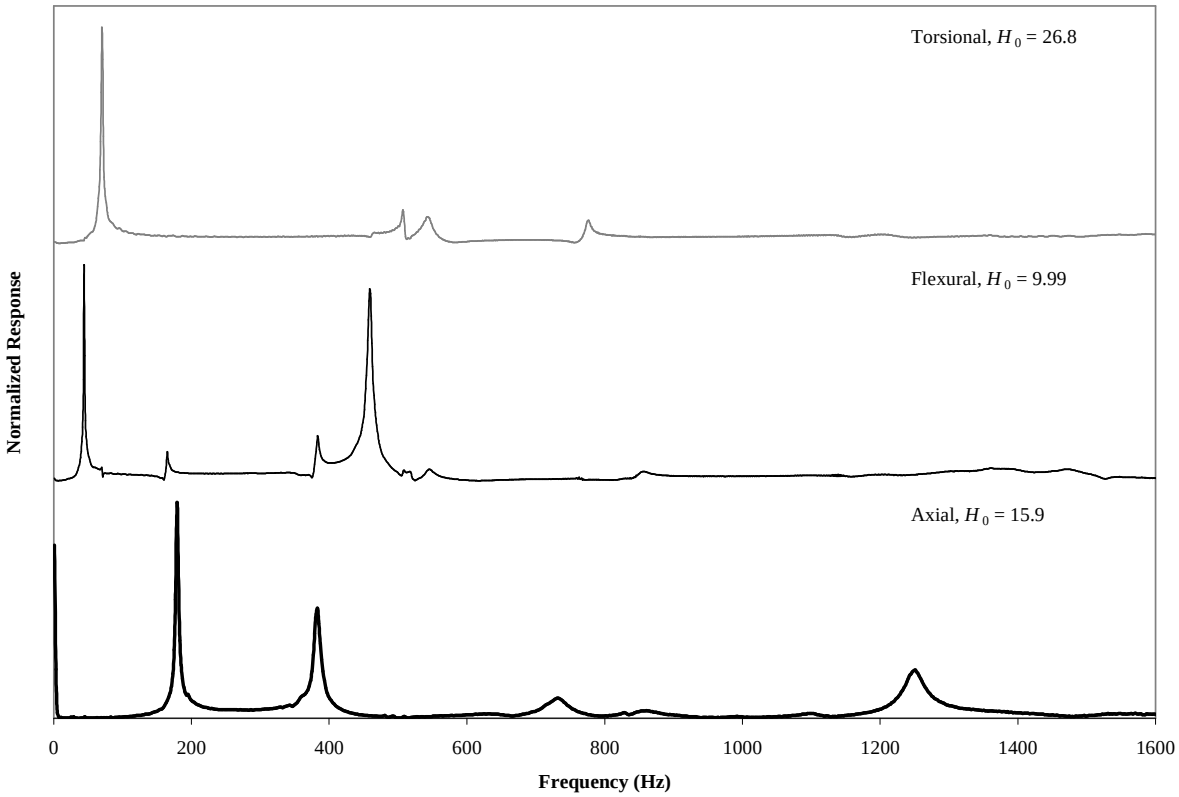

Figure 5.13 - Wideband frequency sweep of specimen 3 dry

Although there is a strong peak at 180 *Hz* in axial mode, this is likely a vibration of the driving plate. To prove that the axial resonant frequency is indeed 385 Hz, wide-band sweeps are performed at confinement pressures of 50 *kPa*, 80 *kPa* and 160 *kPa*, shown in Figure 5.14.

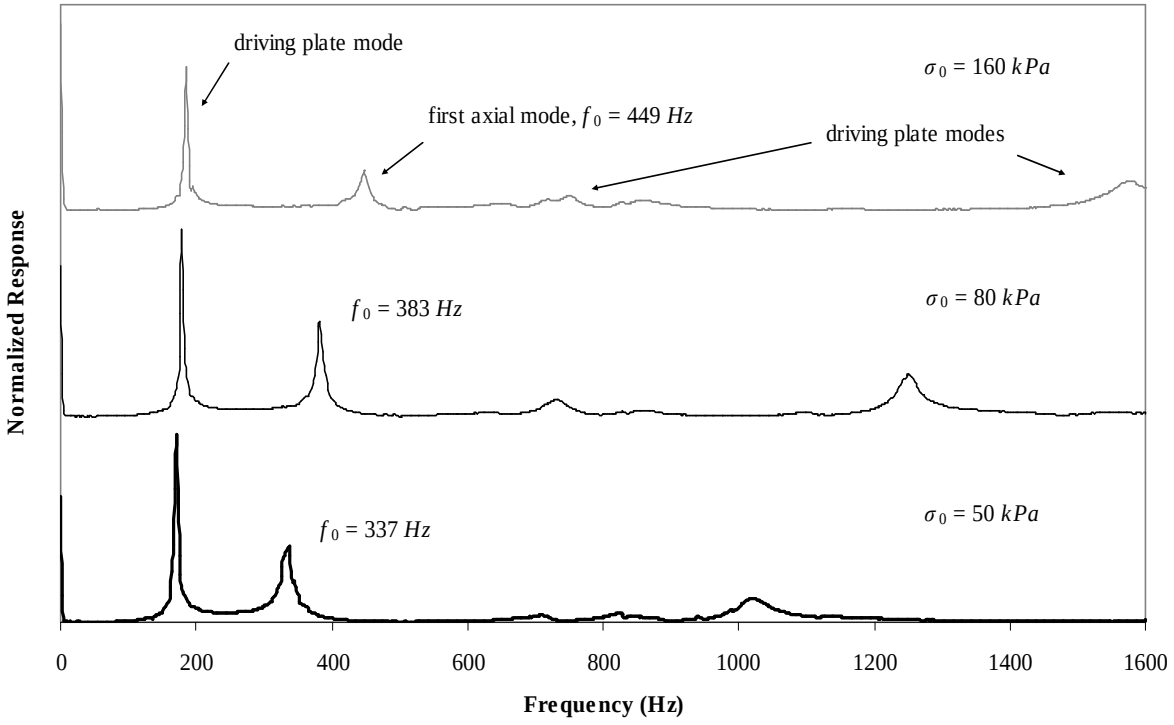

Figure 5.14 - Axial wideband frequency sweep of specimen 3 dry at varying confinement

As confinement pressure increases, the stiffness of the soil also increases; thus the resonant frequency increases as well. The peaks at 180 *Hz*, 740 *Hz* and 860 *Hz* are likely caused by driving plate vibrations because they are not affected by confining pressure differences (Appendix E). It is clear that the peak at 337 *Hz* under 50 *kPa* confinement corresponds with the 383 *Hz* peak under 80 *kPa* confinement, and that it increases with increased confinement. This frequency is confirmed as the axial resonant frequency using Rayleigh's method (Appendix F).

Next, two narrow-band RC tests and two NR method tests are performed on the unsaturated specimen in torsional and axial modes. The resonant properties of the dry specimen are given in Table 5-10 and the transfer functions are shown in Figure 5.15 and Figure 5.16. The Poisson ratio for the dry specimen is computed using Equation [3.9]. This ratio has not been computed previously in the lab using compression and shear wave measurements at seismic frequencies.

Table 5-10 - Specimen 3, dry dynamic properties

		Torsional	Axial	
Resonant frequency	f_0	68.3	376.2	*Hz*
Damping ratio	ξ_0	1.03	0.96	*%*
Strain level	γ-ε	$8.8x10^{-3}$	$7.1x10^{-4}$	*%*
Wave velocity	V_s-V_L	226.4	406	*m/s*
	V/V_{max}	94.1	98.8	*%*
Poisson ratio	v	0.558		

According to theoretical equations of constant fabric arrangements of spherical particles, the Poisson ratio for dry soils should be between v = 0.04 and v = 0.08 (Petrakis and Dobry, 1987). The computed value of v = 0.558 is quite interesting because it implies that the elastic models of spherical particles are not realistic for the calculation of Poisson ratio.

From the NR tests, plots of dry shear wave velocity, longitudinal wave velocity and damping ratio versus frequency of excitation are given as Figure 5.17 and Figure 5.18.

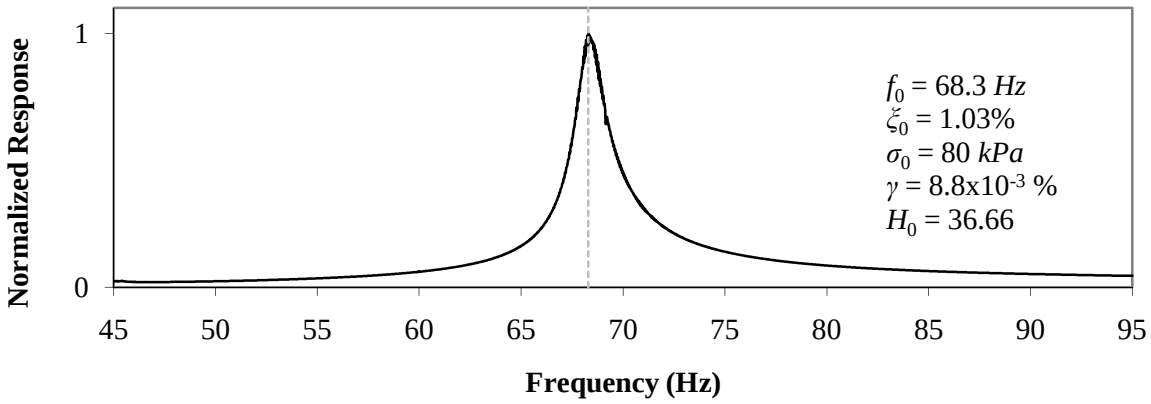

Figure 5.15 - Specimen 3 dry, RC test, torsional mode

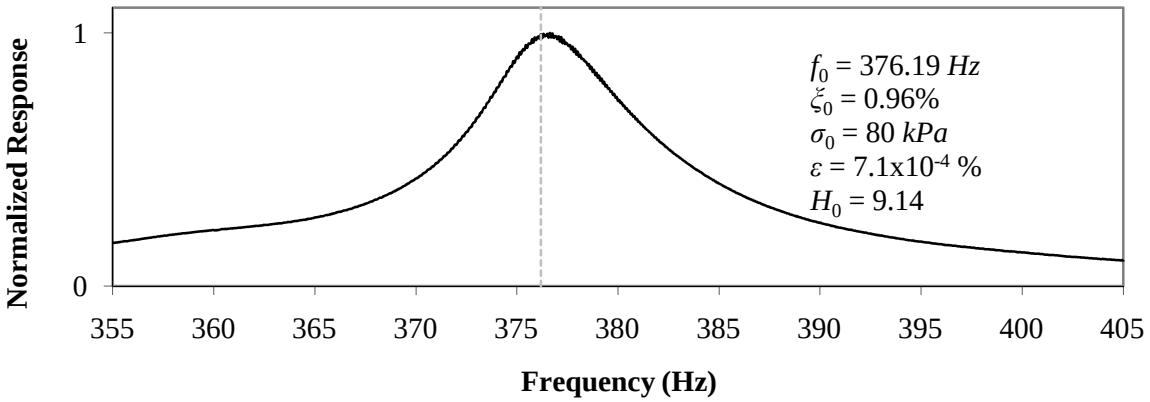

Figure 5.16 - Specimen 3 dry, RC test, axial mode

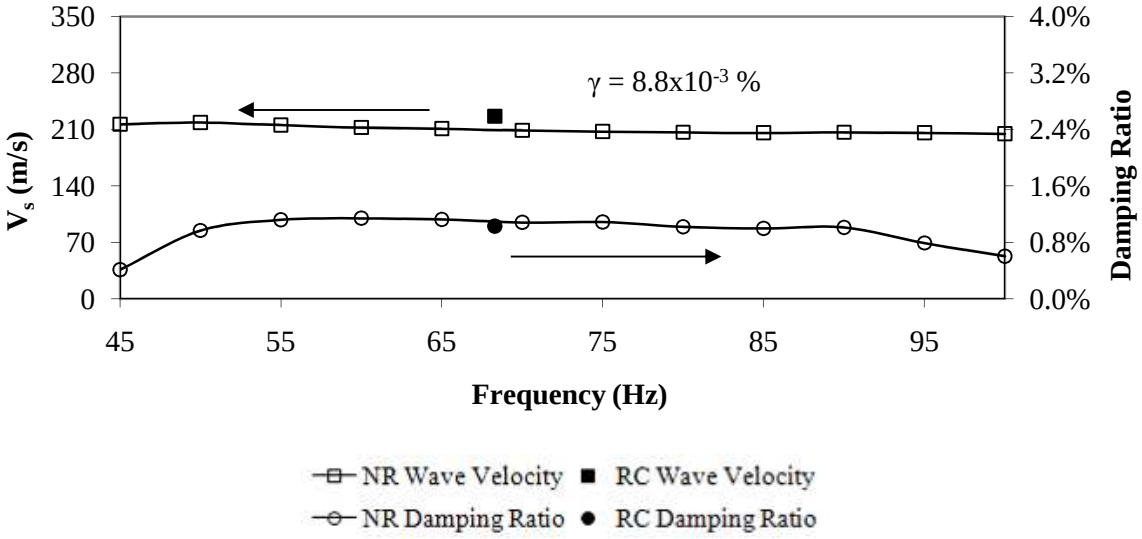

Figure 5.17 - Specimen 3 dry, NR test, torsional mode

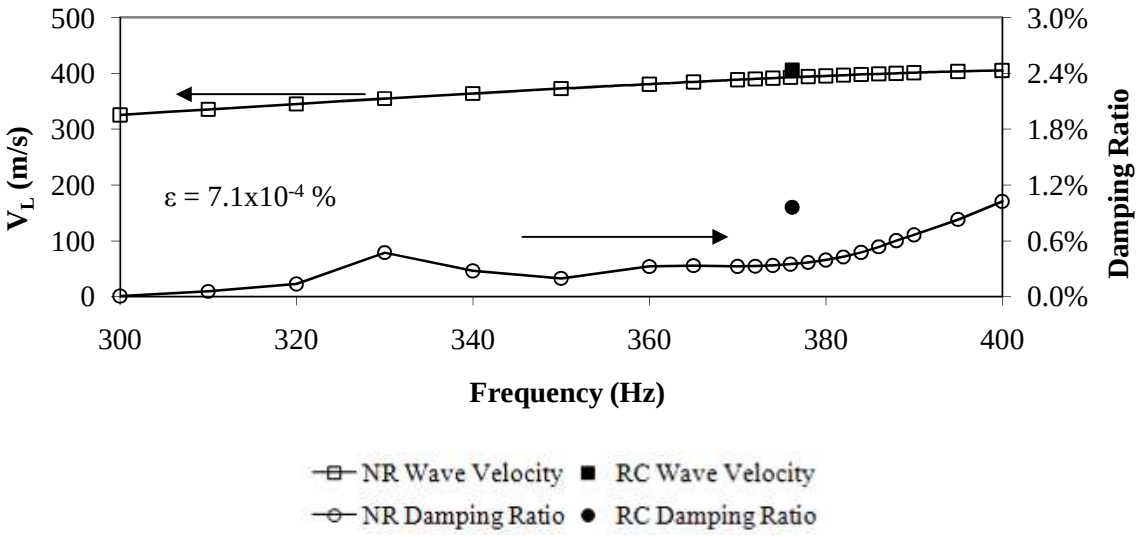

Figure 5.18 - Specimen 3 dry, NR test, axial mode

The specimen is partially saturated and this sequence of tests is performed again. From the wide-bandwidth frequency sweeps shown in Figure 5.19, first resonant peaks are noted at approximately 37 *Hz* in flexural mode, 63 *Hz* in torsional mode and 385 *Hz* in axial mode. Figure 5.20 shows the difference between the partially saturated and dry normalized transfer functions for the axial and torsional modes.

Next, two RC tests and two NR method tests are performed on the partially saturated specimen in torsional and axial modes. The resonant properties of the partially saturated specimen are given in Table 5-11 and the transfer functions are shown as Figure 5.21 and Figure 5.22.

Table 5-11 - Specimen 3, partially saturated dynamic properties

		Torsional	**Axial**	
Resonant frequency	f_0	56.4	368	*Hz*
Damping ratio	ξ_0	3.75	2.44	*%*
Strain level	γ-ε	2.7×10^{-2}	3.8×10^{-3}	*%*
Wave velocity	V_s-V_L	186.9	397	*m/s*
	V/V_{max}	86.2	100	*%*
Poisson ratio	ν	0.471		

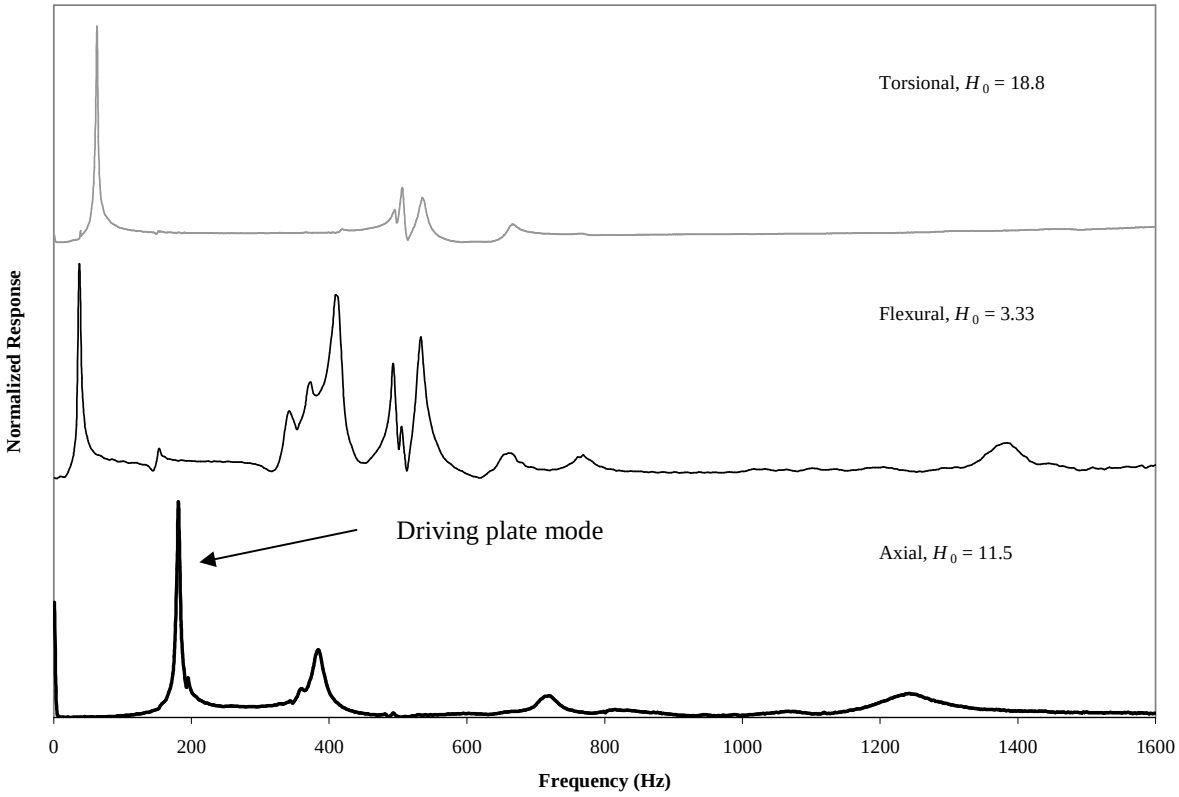

Figure 5.19 - Wideband frequency sweep of specimen 3 partially saturated

The torsional resonant frequency shifts from 68 *Hz* in dry condition to 56 *Hz* in partially saturated condition, an 18 % decrease. The axial resonant frequency shifts from 376 *Hz* to 368 *Hz*, a 2 % decrease. The damping ratio in torsional mode increases from 1.03 % to 3.75 %, a 264 % increase. The damping ratio in axial mode increases from 0.96 % to 2.44 %, a 154 % increase. Thus, the water increases the slippage among particles. The presence of pore water may increase or decrease the slippage depending on the chemical composition of the contacts (Skinner, 1969).

All of the normalization factors decrease for the partially saturated condition because the added inertia of the water reduces the response of the specimen for the same excitation force. Thus, the water is not significantly changing the stiffness of the specimen in axial or transverse directions.

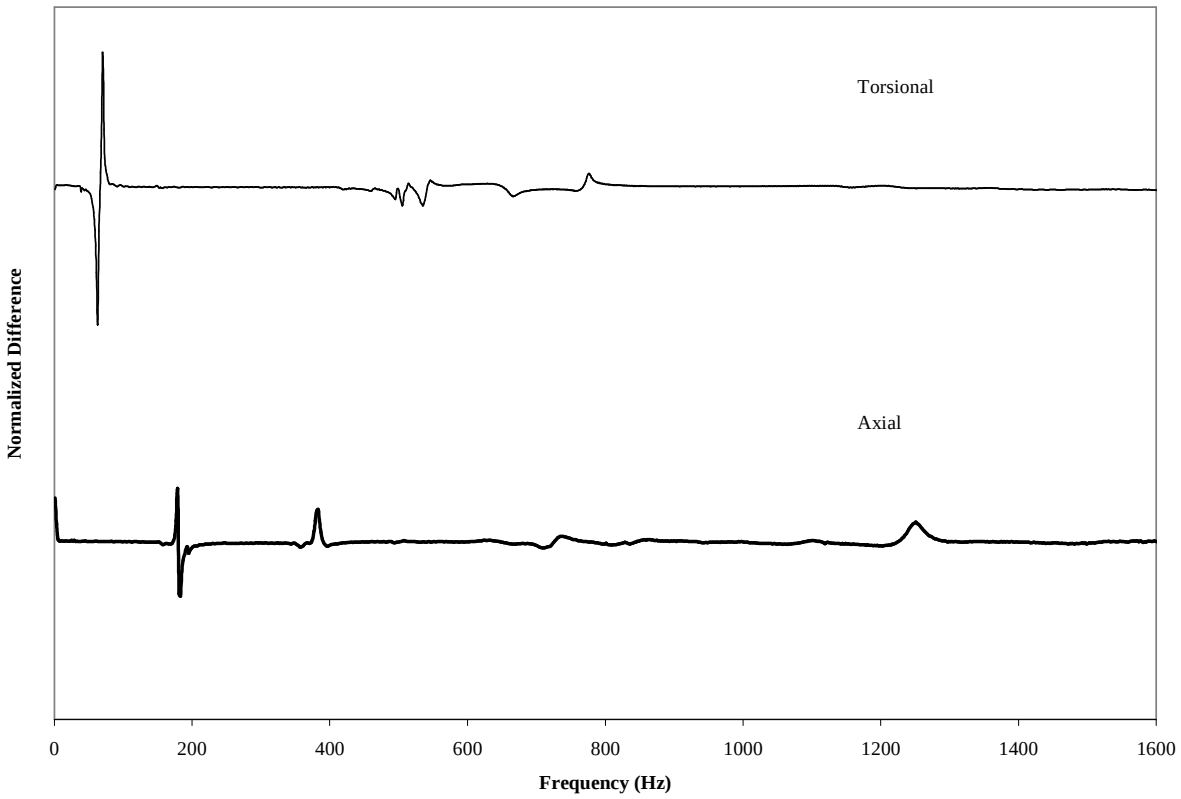

Figure 5.20 - Difference between partially saturated and dry specimen 3 normalized transfer functions

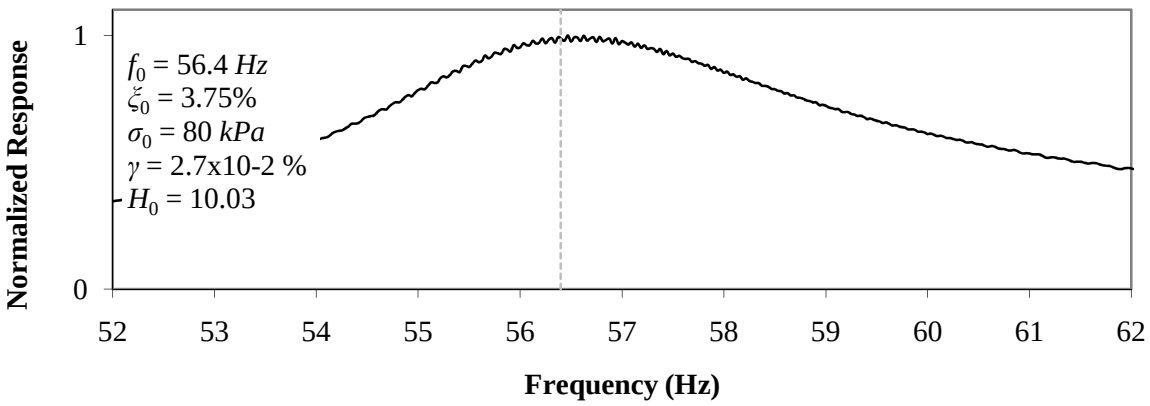

Figure 5.21 - Specimen 3 partially saturated, RC test, torsional mode

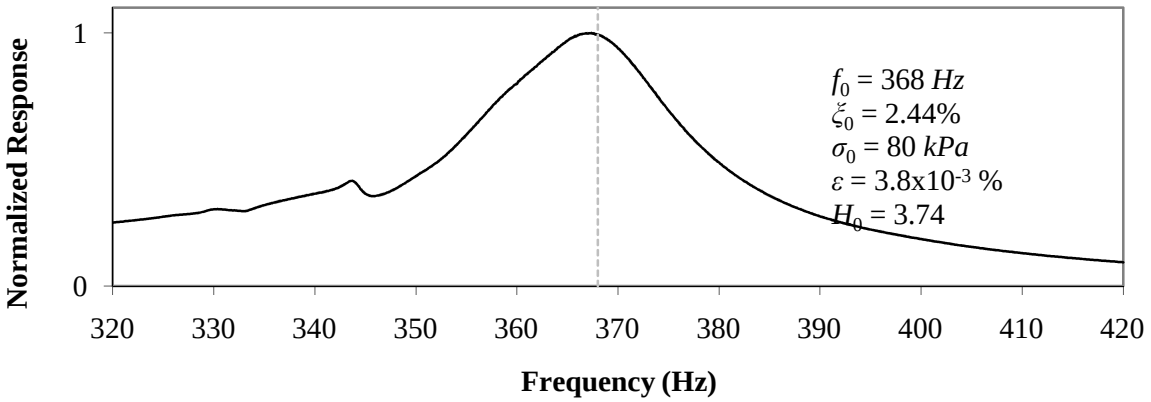

Figure 5.22 - Specimen 3 partially saturated, RC test, axial mode

From the NR tests, plots of partially saturated shear wave velocity, longitudinal wave velocity and damping ratio versus frequency of excitation are given as Figure 5.23 and Figure 5.24.

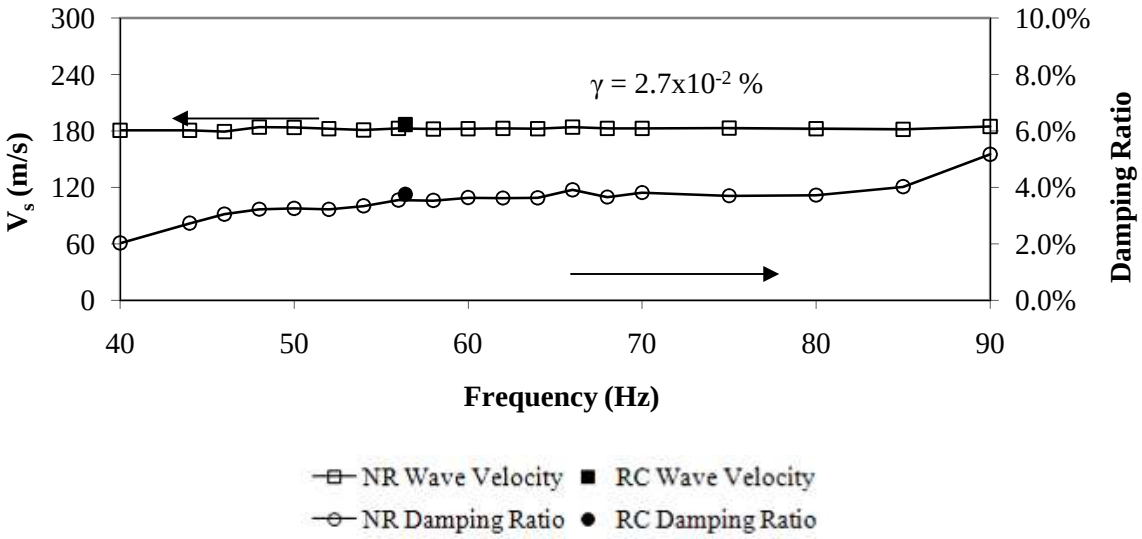

Figure 5.23 - Specimen 3 partially saturated, NR test, torsional mode

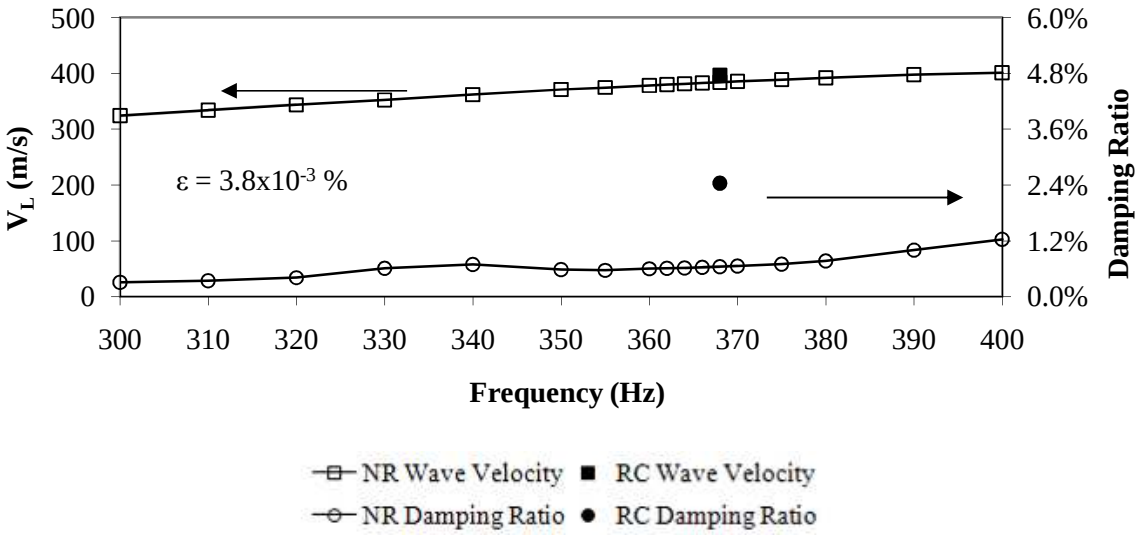

Figure 5.24 - Specimen 3 partially saturated, NR test, axial mode

A total of 19 flow test trials are performed on the specimen, with 20 time measurements for each trial. Table 5-12 summarizes the dynamic properties of each flow test. Measured time intervals for each trial are shown as Figure 5.25. Figure 5.26 summarizes the hydraulic conductivity results for specimen 3 partially saturated single-phase flow.

Table 5-12 - Specimen 3, flow test dynamic properties

Trial	Excitation Mode	Central Frequency	Bandwidth	Max Strain	γ/γ_{th}
		Hz	*Hz*	%	%
2	axial burst chirp	172.5	12.5	$4.9\text{x}10^{-3}$	7.0
5	axial burst chirp	350	100	$9.0\text{x}10^{-4}$	1.3
7	axial fixed sine	170.5	1	$5.0\text{x}10^{-3}$	7.1
9	axial fixed sine	350	1	$3.0\text{x}10^{-4}$	0.4
12	torsional burst chirp	60	12.5	$5.0\text{x}10^{-2}$	50
14	torsional fixed sine	56.4	1	$5.6\text{x}10^{-2}$	56
16	flexural burst chirp	37	50	n/a	n/a
18	flexural fixed sine	37	1	n/a	n/a

Flow rates are tested both before and after each dynamic trial in order to compare baseline flow to stimulated flow and to ensure measurement repeatability (i.e. continuity in

specimen hydraulic conductivity). The frequencies chosen for the dynamic flow tests correspond to the resonant frequency in axial, torsional and flexural mode. At these frequencies, the ratio of input force to output force is maximized; thus, maximum inertial energy is added to the flow system. It is surmised that if any flow increase is to occur in the specimen under dynamic excitation, it should occur at large strain levels.

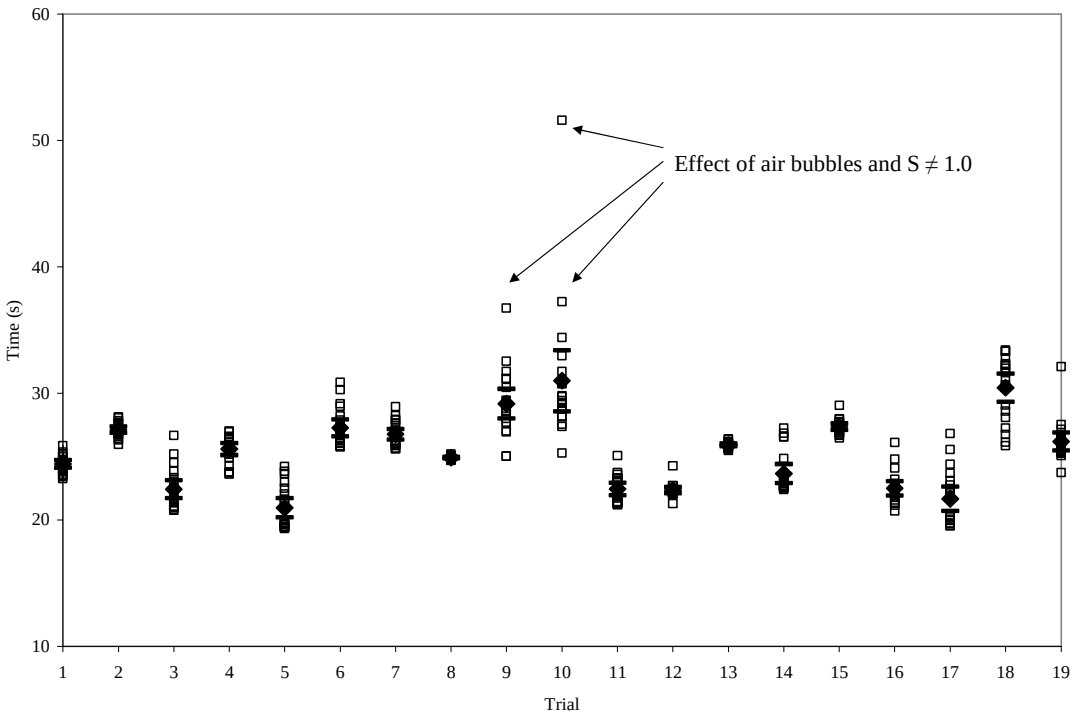

Figure 5.25 - Specimen 3, flow test measured time intervals

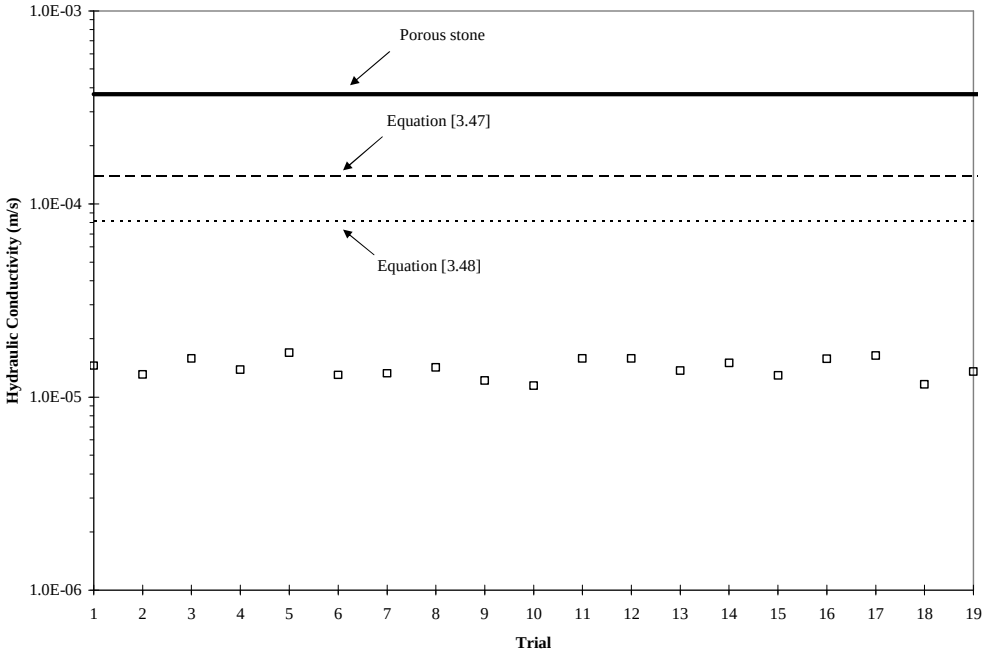

Figure 5.26 - Specimen 3, flow test computed hydraulic conductivities

The 95 % confidence intervals for the measured time intervals are shown for each trial (thick dashes) as well as the mean value (solid diamonds). From Figure 5.25 and Figure 5.26 there appears to be no correlation between dynamic excitation and flow rate. Some trials are well-behaved (i.e. time measurement variability is low) while others are very poorly behaved; this is due to the air leak and poor initial specimen saturation discussed in section 5.1.1. Before each trial, the specimen is flushed to remove accumulated gas bubbles; however, to demonstrate the effect of gas in the sample, this procedure is not followed for trials 9 and 10. During trial 8 (after flushing) the results are well-behaved. During trials 9 and 10 (no flushing prior to time measurement) the results get progressively more erratic as accumulated gas builds in the specimen, reducing the observed hydraulic conductivity. Flushing the gas prior to testing appears to help in some trials; however this is not always the case (e.g. trials 17 and 18). In the end, it is impossible to separate the effects of the air leak on conductivity from the possible effects of dynamic excitation because the specimen is not 100 % saturated.

5.1.5 Specimen 4

Specimen 4 is made of Indusmin 2010 sand; its physical properties are given in Table 5-13. The purpose of specimen 4 flow testing is to characterize the dynamic properties of the soil in both torsional and axial mode of vibration over a wide frequency bandwidth (1600 *Hz*). Dynamic excitation in all three modes is applied at frequencies corresponding to the resonant peaks of the specimen in each mode, both in narrow bandwidths around the peaks as well as fixed sine waves at resonance. Specimen height changes are monitored using the LVDT during any applied dynamic excitation.

Table 5-13 - Specimen 4, physical properties

Mass	m_T	0.837	*kg*
Height	L	0.144	*m*
Volume	V_T	554	*mL*
Dry density	ρ_d	1511	kg/m^3
Void ratio	e	0.750	--
Porosity	n	0.429	--
Volume of voids	V_v	238	*mL*
Conductivity (Hazen)	K	7.8×10^{-4}	*m/s*
Conductivity (C-K)	K	1.0×10^{-3}	*m/s*
Permeability	k	79.5	*darcy*

Wide-bandwidth sweeps are performed on the dry specimen in all three modes of vibration, shown as Figure 5.27. First resonant peaks are noted at approximately 40 *Hz* in flexural mode, 61 *Hz* in torsional mode and 355 *Hz* in axial mode.

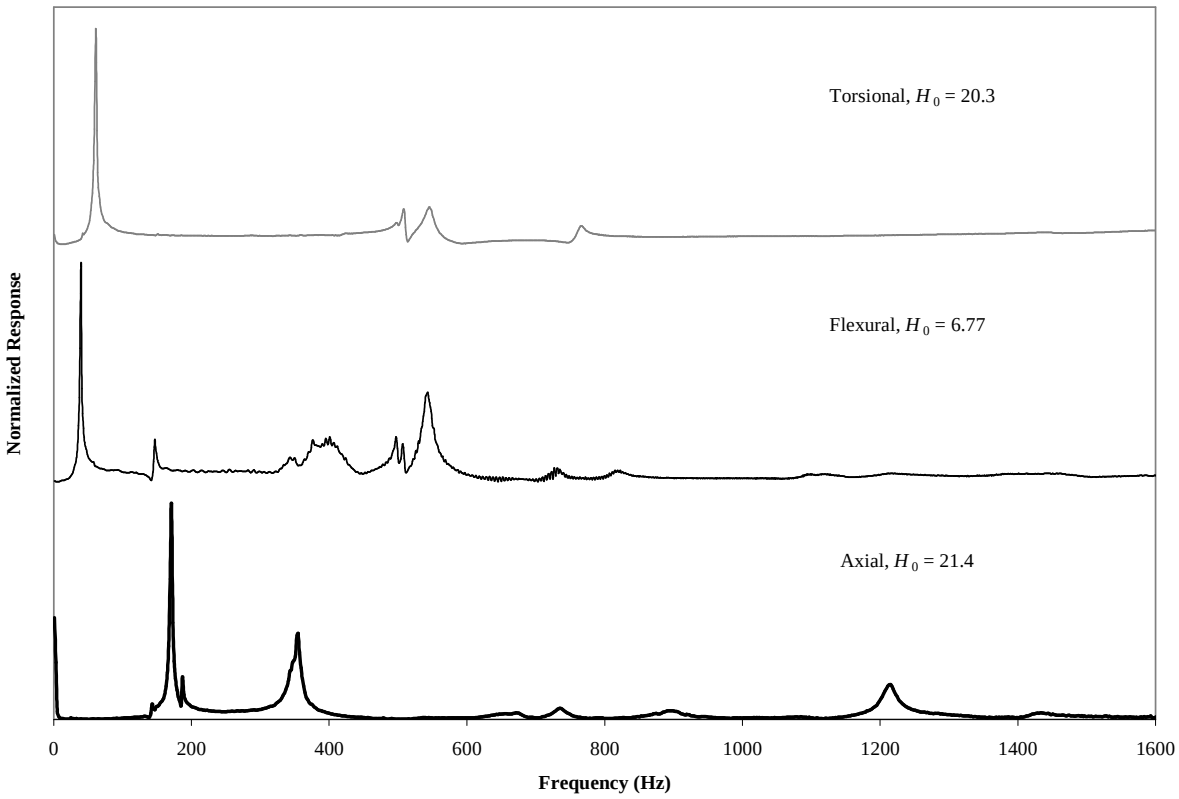

Figure 5.27 - Wideband frequency sweep of specimen 4 dry

Again, to prove that the axial resonant frequency is indeed 355 *Hz*, wide-band sweeps are performed at confinement pressures of 50 *kPa*, 80 *kPa* and 160 *kPa*, shown in Figure 5.28.

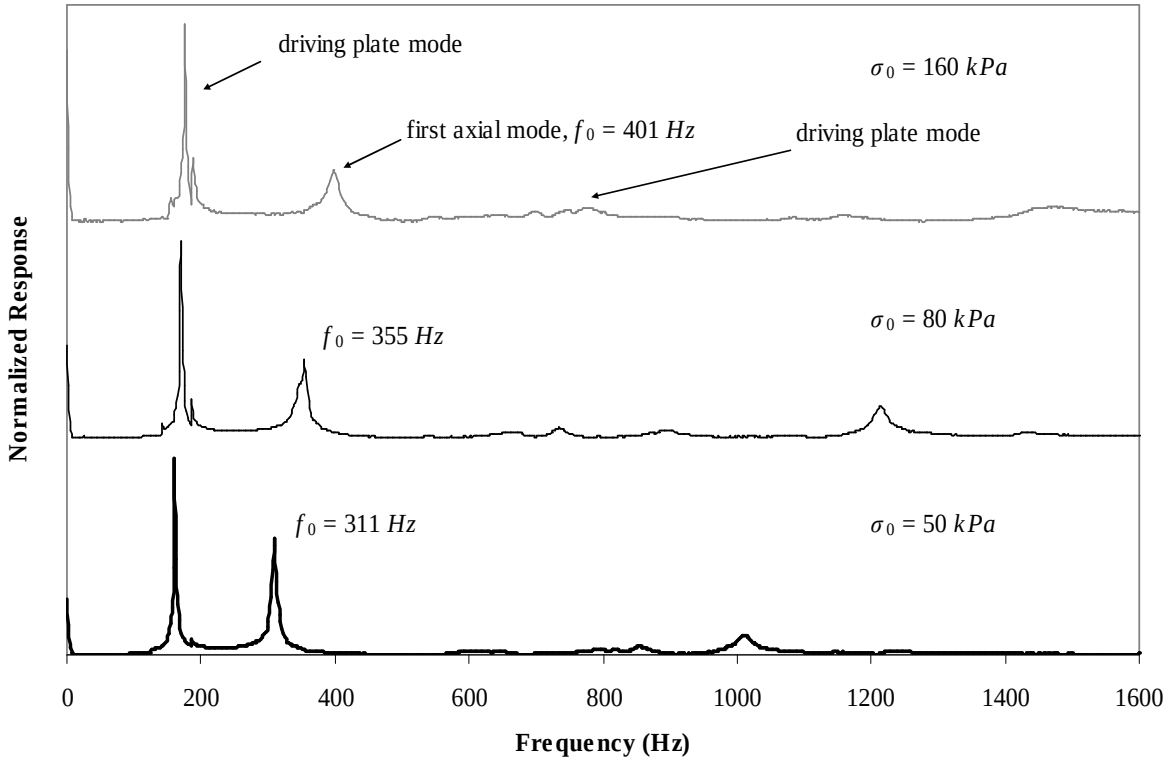

Figure 5.28 - Axial wideband frequency sweep of specimen 4 dry at varying confinement

The peak at 309 *Hz* under 50 *kPa* confinement corresponds with the 355 *Hz* peak under 80 *kPa* confinement, and that it increases with increased confinement. The driving plate vibration peaks appear at 180 *Hz*, 740 *Hz* and 860 *Hz*.

Next, two RC tests and two NR method tests are performed on the dry specimen in torsional and axial modes. The resonant properties of the dry specimen are given in Table 5-14 and the transfer functions are shown as Figure 5.29 and Figure 5.30. The transfer function for the dry specimen in torsional mode is not symmetrical because it is at a larger strain level in comparison to similar tests performed on specimen 7.

Even though the input excitation voltage is the same used for the identical tests on specimen 3, the strains experienced for specimen 4 are much smaller. This effect is again due to the reduction in effective stress caused by the air leak.

Table 5-14 - Specimen 4, dry dynamic properties

		Torsional	Axial	
Resonant frequency	f_0	53.5	349	*Hz*
Damping ratio	ξ_0	3.81	1.67	*%*
Strain level	γ-ε	$3.1x10^{-2}$	$1.0x10^{-3}$	*%*
Wave velocity	V_s-V_L	182.8	386.6	*m/s*
	V/V_{max}	91.5	100	*%*
Poisson ratio	ν	0.473		
Height change	ΔL	-8.9	-6.8	μm

From the NR tests of the dry specimen plots of shear wave velocity, longitudinal wave velocity and damping ratio versus frequency of excitation are given as Figure 5.31 and Figure 5.32. During the torsional and axial NR method tests, the LVDT indicated specimen height decreases of 6.6 μm and 0.3 μm, respectively.

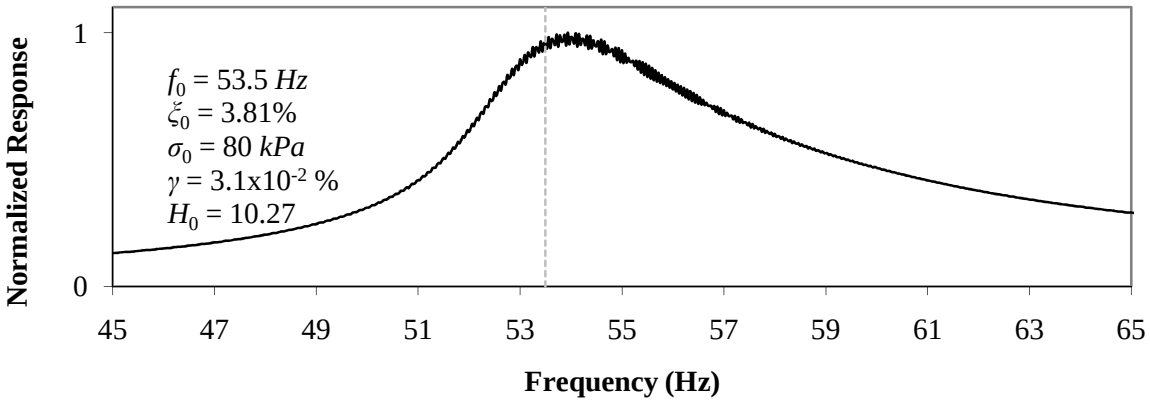

Figure 5.29 - Specimen 4 dry, RC test, torsional mode

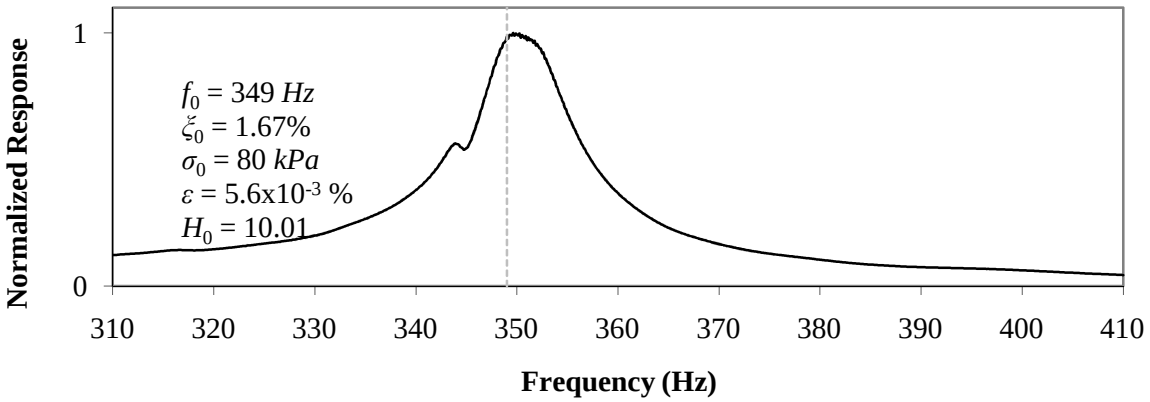

Figure 5.30 - Specimen 4 dry, RC test, axial mode

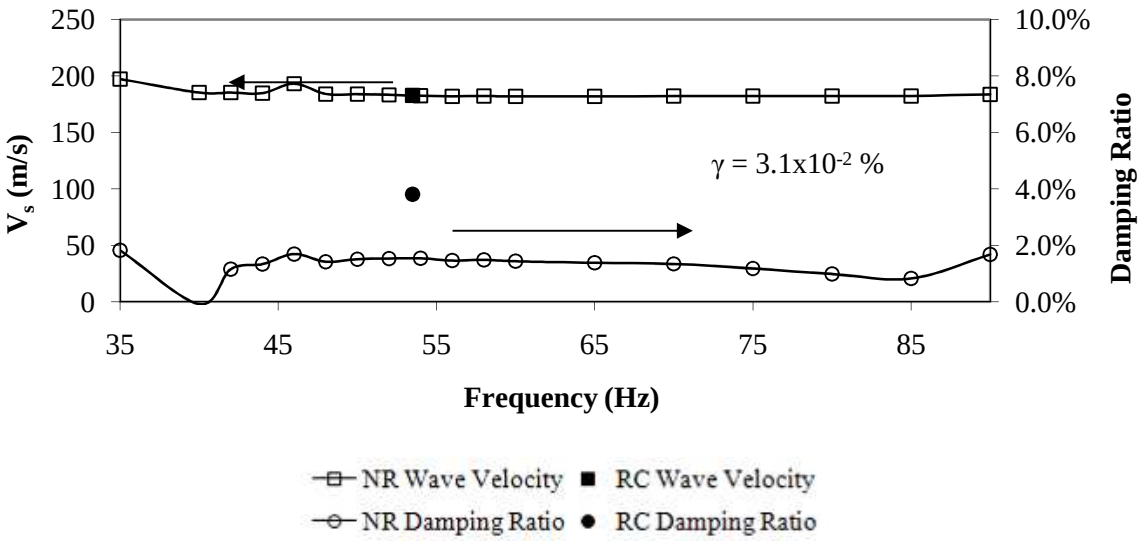

Figure 5.31 - Specimen 4 dry, NR test, torsional mode

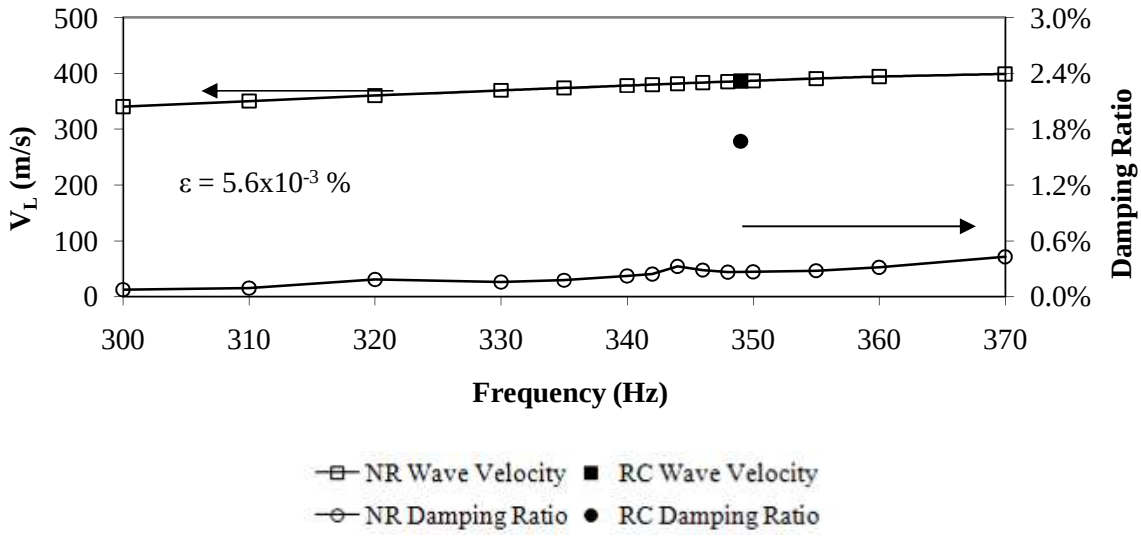

Figure 5.32 - Specimen 4 dry, NR test, axial mode

The specimen is partially saturated and this sequence of tests is performed again. From the wide-bandwidth frequency sweeps shown in Figure 5.33, first resonant peaks are noted at approximately 37 *Hz* in flexural mode, 55 *Hz* in torsional mode and 172 *Hz* in axial mode. Figure 5.34 shows the difference between the partially saturated and dry normalized transfer functions for the axial and torsional modes. An additional pore pressure coefficient test is performed on the coarse sand to determine the initial degree of saturation, shown in Figure 5.35. For the coarse sand, $B = 0.17$, which corresponds to $S = 0.75$ (Craig, 2002). These results show again that the initial saturation of the specimen is not effective.

Next, two RC tests and two NR method tests are performed on the partially saturated specimen in torsional and axial modes. The resonant properties of the partially saturated specimen are given in Table 5-15 and the transfer functions are shown as Figure 5.36 and Figure 5.37.

Similar to the Barco sand, all of the normalization factors decrease for the partially saturated condition due to the added inertia plus the reduction in effective stress caused by the air leak. Thus, the water is not significantly changing the stiffness of the specimen in axial or transverse directions.

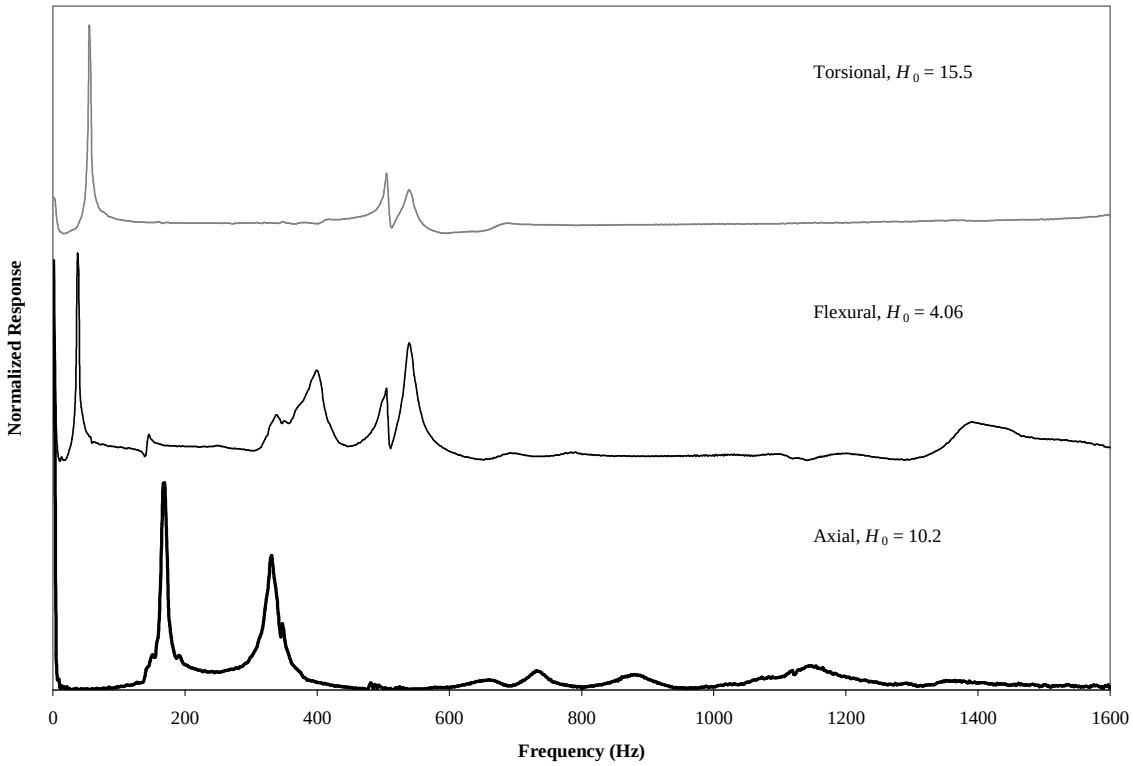

Figure 5.33 - Wideband frequency sweep of specimen 4 partially saturated

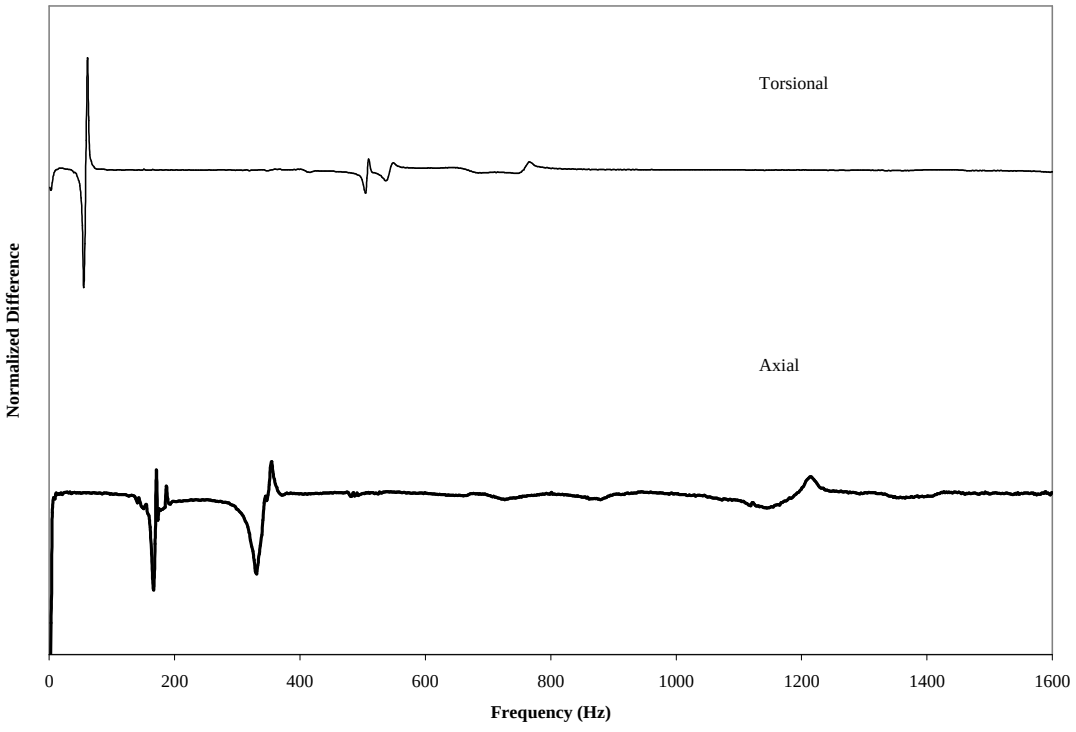

Figure 5.34 - Difference between partially saturated and dry specimen 4 normalized transfer functions

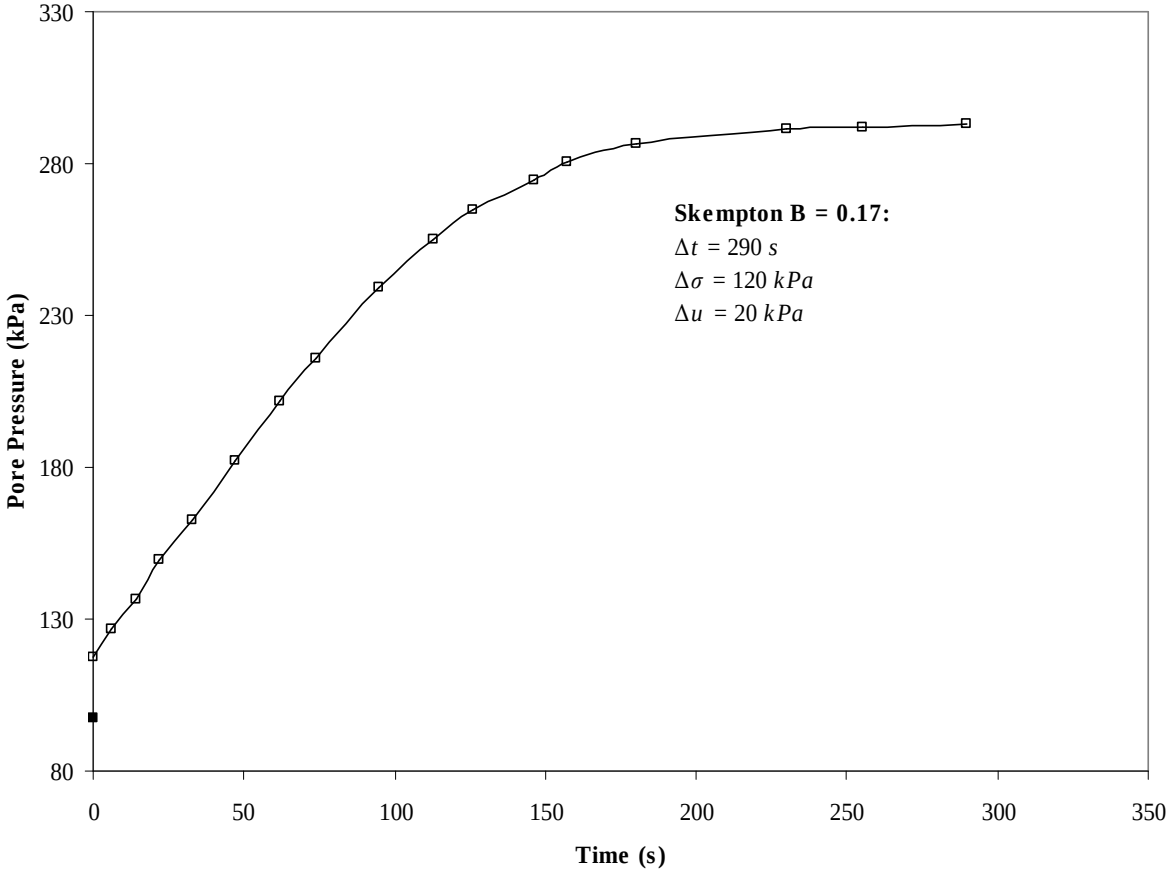

Figure 5.35 - Indusmin sand pore pressure coefficient *B* measurement results

Table 5-15 - Specimen 4, partially saturated dynamic properties

		Torsional	**Axial**	
Resonant frequency	f_0	50.375	330.6	*Hz*
Damping ratio	ξ_0	4.41	1.88	*%*
Strain level	γ-ε	3.6×10^{-2}	1.3×10^{-4}	*%*
Wave velocity	V_s-V_L	172.1	366.2	*m/s*
	V/V_{max}	78.5	99.3	*%*
Poisson ratio	ν	0.470		
Height change	ΔL	-6.8	-3.3	μm

The torsional resonant frequency shifts from 53.5 *Hz* in dry conditions to 50.4 *Hz* in partially saturated conditions, a decrease of 6 %. The axial resonant frequency shifts from 349 *Hz* to

331 *Hz*, a decrease of 5 %. Using Equation [3.7] and [3.8], if no change of stiffness in the specimen occurs, then the change in resonant frequency for the axial and torsional modes should be equal, which is the phenomenon observed during this experiment. Thus, the specimen stiffness likely did not change during the dynamic testing. The damping ratio in torsional mode increases from 3.81 % to 4.41 %, a 16 % increase. The damping ratio in axial mode increases from 1.67 % to 1.88 %, a 13 % increase. There is a measured decrease in specimen height during both the torsional and axial dynamic tests, indicating some change in the fabric of the specimen is occurring. The measured height decrease corresponds to an axial strain of 2.9×10^{-3} %. This is a magnitude higher than the value computed using input excitation voltage and measured accelerometer response.

From the NR tests, plots of partially saturated shear wave velocity, longitudinal wave velocity and damping ratio versus frequency of excitation are given as Figure 5.38 and Figure 5.39. During the torsional and axial NR method tests, the LVDT indicated specimen height decreases of 34.5 μm and 1.8 μm, respectively. The application of the NR method analytical technique to the axial mode results shows that the method is much more sensitive in axial mode compared to torsional. It is much more difficult to match the damping results between the NR and RC methods.

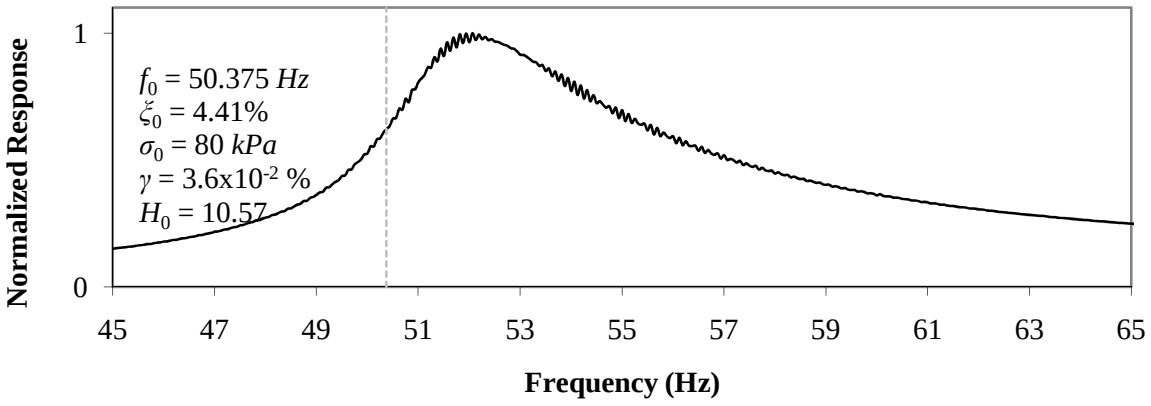

Figure 5.36 - Specimen 4 partially saturated, RC test, torsional mode

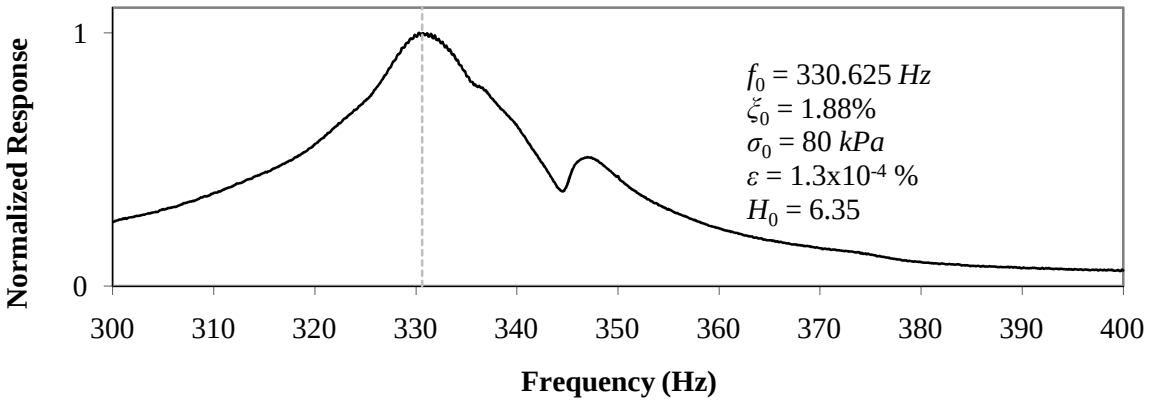

Figure 5.37 - Specimen 4 partially saturated, RC test, axial mode

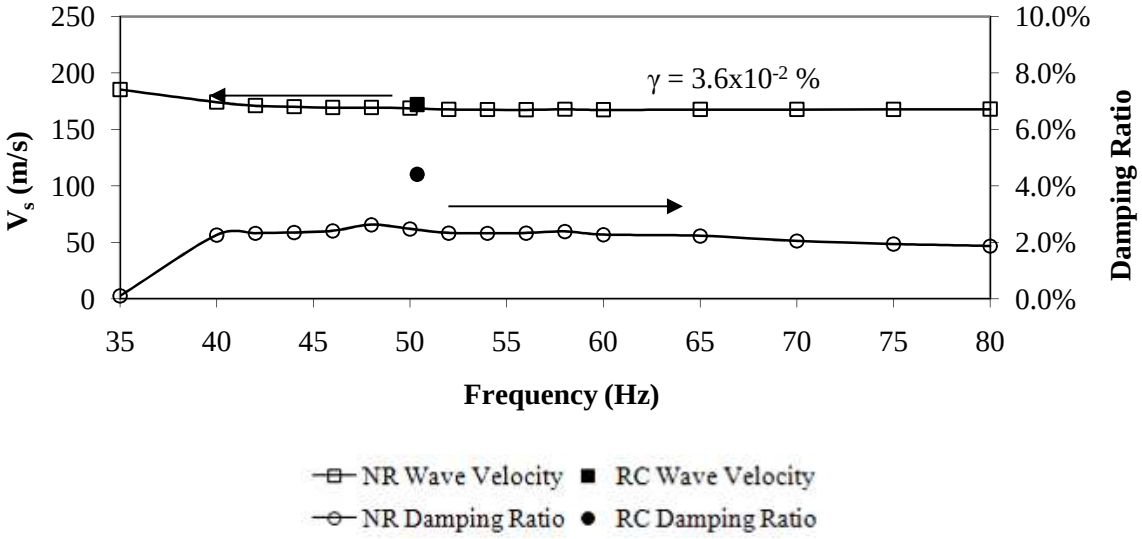

Figure 5.38 - Specimen 4 partially saturated, NR test, torsional mode

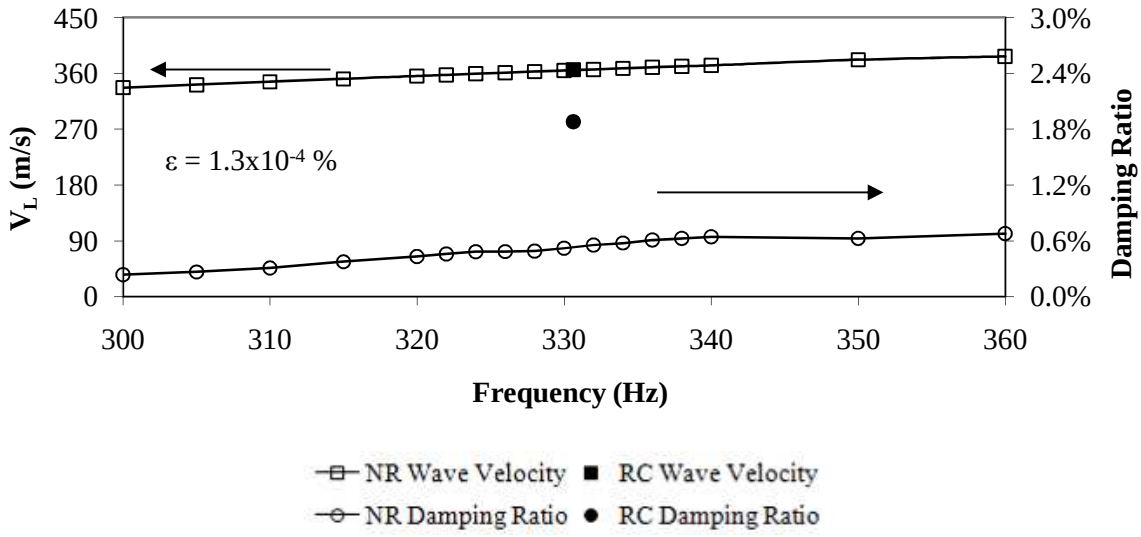

Figure 5.39 - Specimen 4 partially saturated, NR test, axial mode

A total of 18 flow test trials are performed on the specimen, with 20 time measurements for each trial. Table 5-16 summarizes the dynamic properties of each flow test. Measured time intervals for each trial are shown as Figure 5.40. Figure 5.41 summarizes the hydraulic conductivity results for specimen 4 partially saturated single-phase flow. As before, baseline flow is measured before and after stimulation for comparison with dynamic excitation results and to verify continuity between tests.

Table 5-16 - Specimen 4, flow test dynamic properties

Trial	Excitation Mode	Central Frequency	Bandwidth	Max Strain	γ/γ_{th}	ΔL	Δe
		Hz	*Hz*	%	%	*μm*	%
2	axial burst chirp	170	50	$4.4x10^{-3}$	4.4	+11.3	0.2
4	axial burst chirp	330	50	$4.5x10^{-4}$	0.5	+10.0	0.2
6	axial fixed sine	170	1	$5.6x10^{-3}$	5.6	+79.4	0.3
8	axial fixed sine	330	1	$1.8x10^{-4}$	0.2	+4.6	0.1
11	torsional burst chirp	50	50	$6.4x10^{-2}$	160	+77.9	0.3
13	torsional fixed sine	50	1	$7.2x10^{-2}$	180	+135	0.4
15	flexural burst chirp	37	50	n/a	n/a	-15.3	-0.1
17	flexural fixed sine	37	1	n/a	n/a	-43.2	-0.2

Like specimen 3, the frequencies chosen for the dynamic flow tests correspond to the resonant frequency in axial, torsional and flexural mode. At these frequencies, the ratio of input force to output force is maximized; thus, maximum inertial energy is added to the flow system. It is surmised that if any flow increase is to occur in the specimen under dynamic excitation, it should occur at large strain levels.

The LVDT measurements show that for the baseline measurement trials, specimen height increases anywhere between a minimum of 0.1 μm to a maximum of 8.4 μm. The pore water flowing through the specimen likely produces excess pore pressure that counteracts the confinement pressure, essentially causing the specimen to swell. When dynamic excitation is applied, much larger changes in specimen height are measured for all three modes of vibration. Torsional excitation produces the largest increases in specimen height. Axial excitation also produces height increases, although not as dramatic (on average) when compared to the torsional results. Finally, flexural excitation actually causes significant decreases in specimen height.

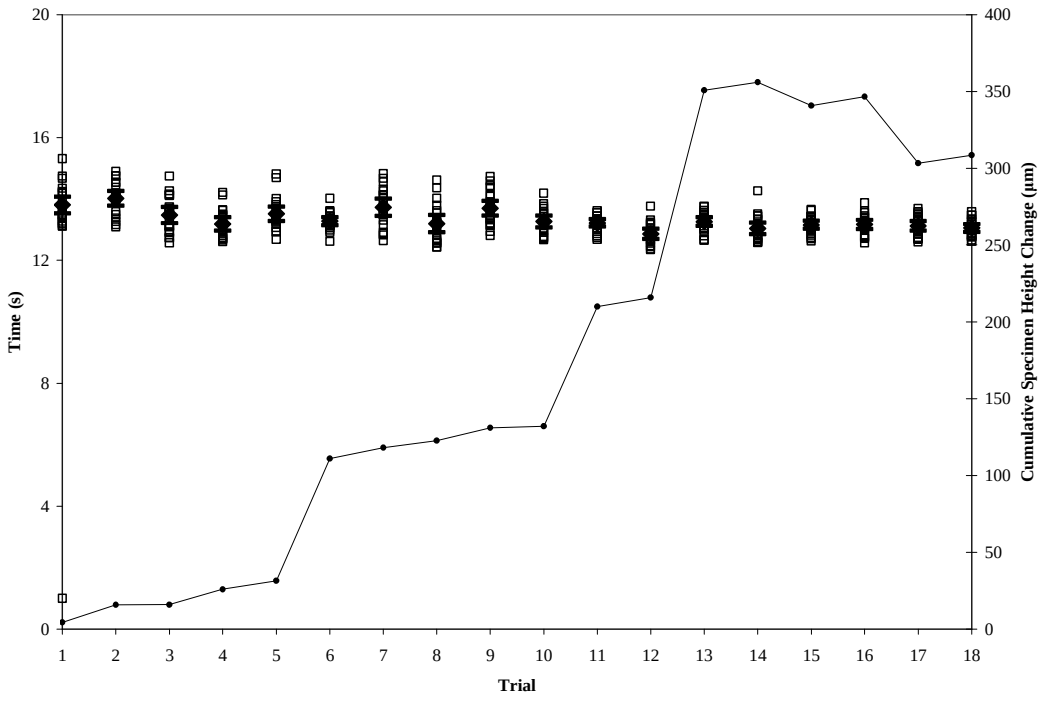

Figure 5.40 - Specimen 4, flow test measured time intervals

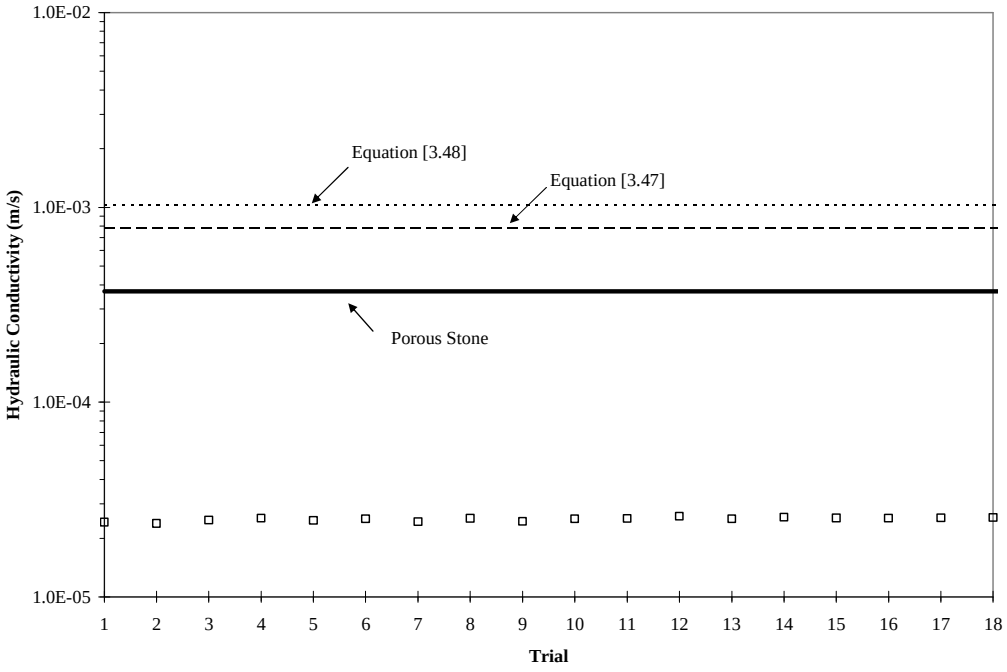

Figure 5.41 - Specimen 4, flow test computed hydraulic conductivities

In general, the results are very well-behaved compared to specimen 3; however, there still appears to be no correlation between dynamic excitation and fluid flow rate. Figure 5.41 indicates that the theoretical hydraulic conductivity of specimen 4 actually exceeds that of the porous stone (i.e. the porous stone should be limiting the flow) and the observed conductivity should equal that of the stone. However, the measured conductivity is much lower than the conductivity of the stone. This may also be due to accumulation of air bubbles in the specimen. On the other hand, the low conductivity values could simply be due to specimen compaction under the applied confinement pressure (i.e. the theoretical equations for computing conductivity may no longer be applicable because the specimen can no longer be considered a loose sand). However, the change in height monitored by the LVDT is quite small, so it is unlikely that major reorganization of the grains occurred during testing.

5.1.6 Specimen 5

Specimen 5 is made of Silex regular silica flour. Equation [3.47] and Equation [3.48] are not applicable in this case since the silica flour d_{10} is well below that of sands. In fact, when flow tests are attempted using the saturated silica flour specimen, no flow is observed even with very high pressure gradients applied. Compared to previous tests, the d_{10} of this material is nearly two orders of magnitude smaller.

The physical properties of the specimen are given in Table 5-17.

Table 5-17 - Specimen 5, physical properties

Mass	m_T	0.653	*kg*
Height	L	0.139	*m*
Volume	V_T	535	*mL*
Dry density	ρ_d	1221	kg/m^3
Void ratio	e	1.166	--
Porosity	n	0.538	--
Volume of voids	V_v	288	*mL*

The purpose of specimen 5 testing is to characterize the dynamic properties of the soil in the torsional mode of vibration over a wide frequency bandwidth (1600 *Hz*) and to examine the effects of capillary force on these properties. Specimen height changes are monitored using the LVDT during any applied dynamic excitation as well as during specimen saturation.

Wide-bandwidth sweeps are performed on the dry specimen in torsional and flexural modes of vibration, shown as Figure 5.42. First resonant peaks are noted at 31 *Hz* in flexural mode and 39 *Hz* in torsional mode.

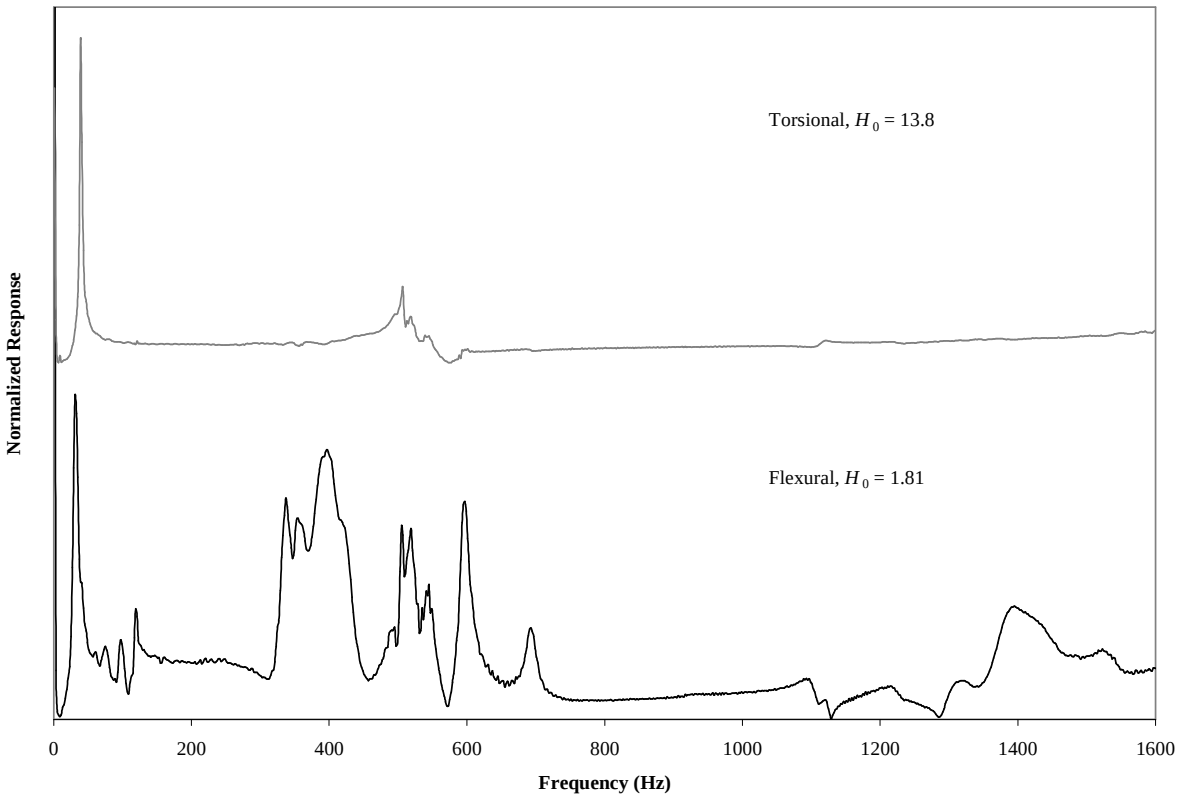

Figure 5.42 - Wideband frequency sweep of specimen 5 dry

The flexural response contains many significant peaks observed at 400 *Hz*, 500 *Hz*, 600 *Hz* and 1400 *Hz*. Compared to the sands used for specimens 3 and 4, the flexural resonant frequency is lower. The torsional response has a peak at 500 *Hz*. The torsional resonant frequency is significantly lower than those of the sands. For the sand specimens, the ratio of flexural resonant frequency to torsional resonant frequency is approximately 2:3; whereas for specimen 5, this ratio is nearly 3:4, a 12 % increase.

The resonant properties of the dry specimen are given in Table 5-18 and the transfer functions are shown as Figure 5.43.

Table 5-18 - Specimen 5, dry dynamic properties

		Torsional	
Resonant frequency	f_0	33.31	*Hz*
Damping ratio	ξ_0	3.95	*%*
Strain level	γ	6.9×10^{-2}	*%*
Wave velocity	V_s	124.1	*m/s*
Height change	ΔL	-7.7	μm

From the NR test, a plot of dry shear wave velocity and damping ratio versus frequency of excitation are given as Figure 5.44. During the NR method test, the LVDT indicated a specimen height decrease of 8.6 μm.

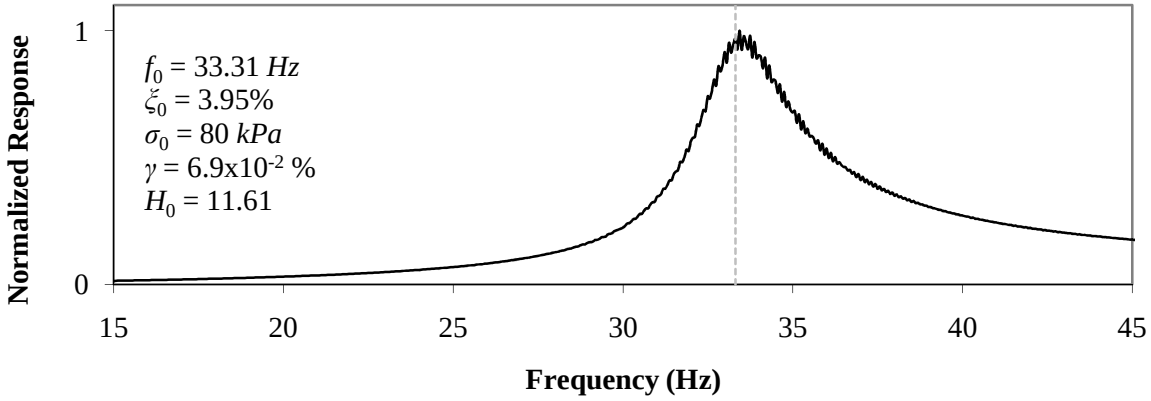

Figure 5.43 - Specimen 5 dry, RC test, torsional mode

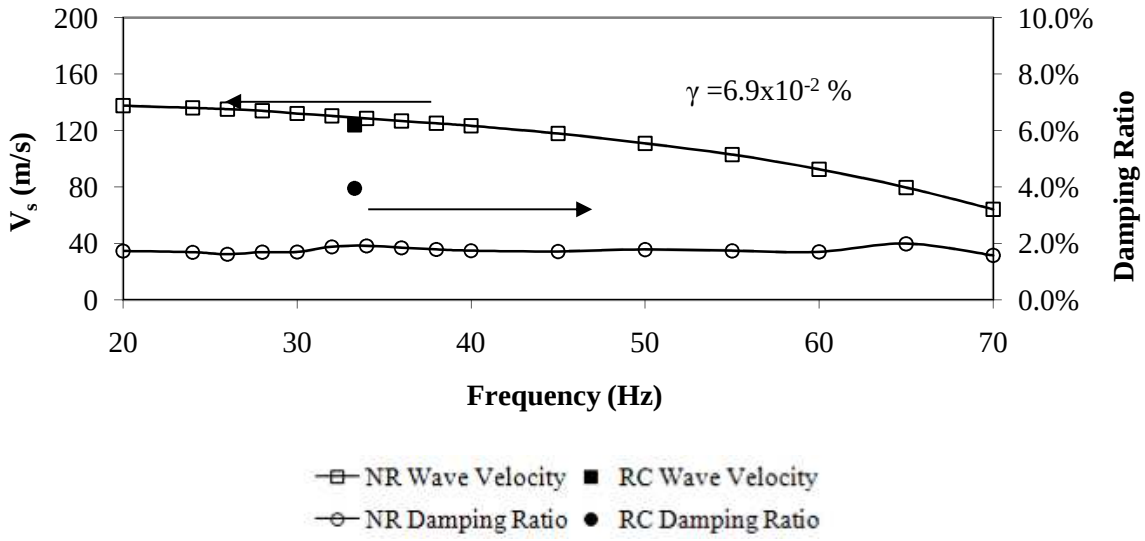

Figure 5.44 - Specimen 5 dry, NR test, torsional mode

The specimen is partially saturated and this sequence of tests is performed again. The physical properties of the saturated specimen are given in Table 5-19.

Table 5-19 - Specimen 5, partially saturated physical properties

Mass	m_T	0.653	*kg*
Radius	r	0.030	*m*
Height	L	0.136	*m*
Volume	V_T	385	*mL*
Dry density	ρ_d	1696	kg/m^3
Void ratio	e	0.559	--
Porosity	n	0.359	--
Volume of voids	V_v	138	*mL*

After the resonant column was disassembled, the radius of the specimen had decreased, in addition to the height decrease. This significant decrease in specimen volume (approximately a 28% decrease) during saturation is likely due to compaction of the specimen with the help of the added capillary forces. Also significant is the effect of the added water on the dynamic properties of the specimen. From the wide-bandwidth frequency sweeps shown in Figure 5.45, first resonant peaks are noted at approximately 171 *Hz* in flexural mode and 195 *Hz* in torsional mode, a dramatic change from the dry specimen.

Figure 5.46 shows a plot of the normalized difference between dry and partially saturated torsional mode spectrum. The flexural response contains many peaks; in fact, the choice of 171 *Hz* is not certain. There are several small peaks in the lower frequency range and the highest peak actually occurs at 400 *Hz*, with other significant peaks at 300 *Hz* and 600 *Hz*. From the torsional mode transfer function plot, the resonant peak appears to be non-symmetric. All of these results suggest that the driving plate of the resonant column may have been in contact with the coils during the saturated tests after the specimen shrinkage occurred.

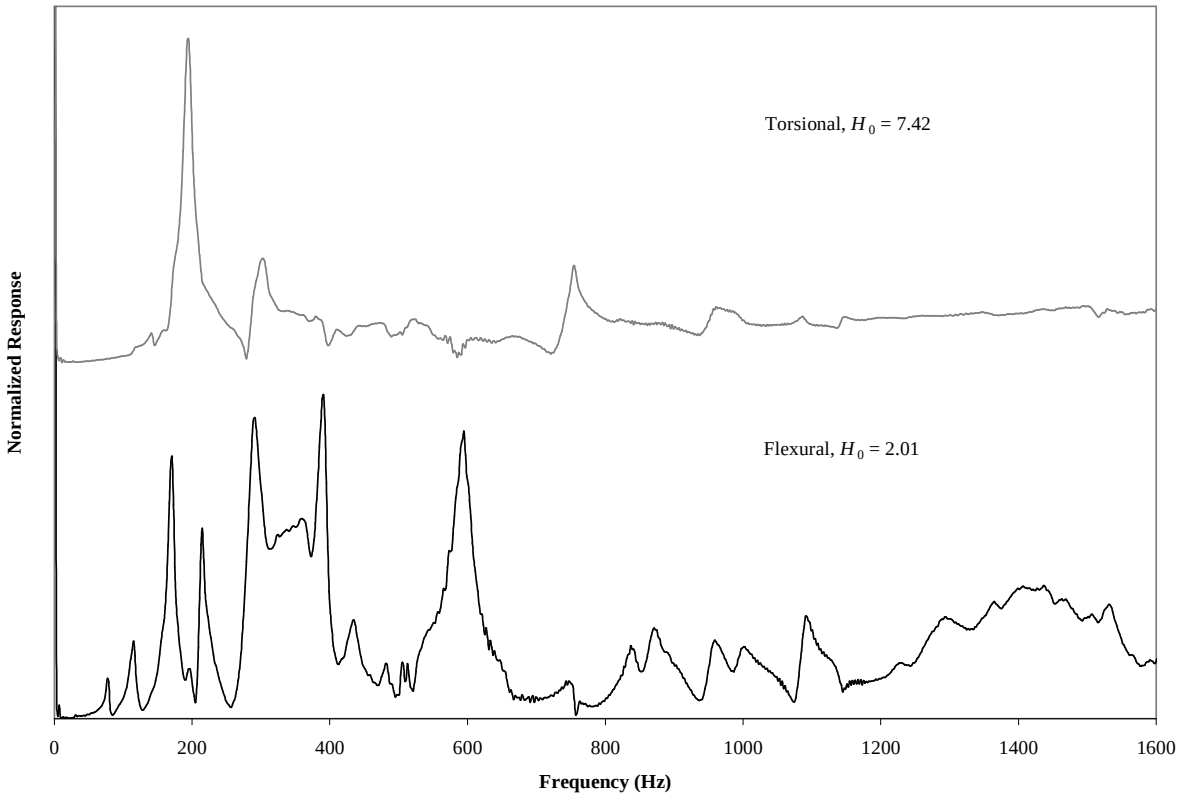

Figure 5.45 - Wideband frequency sweep of specimen 5 partially saturated

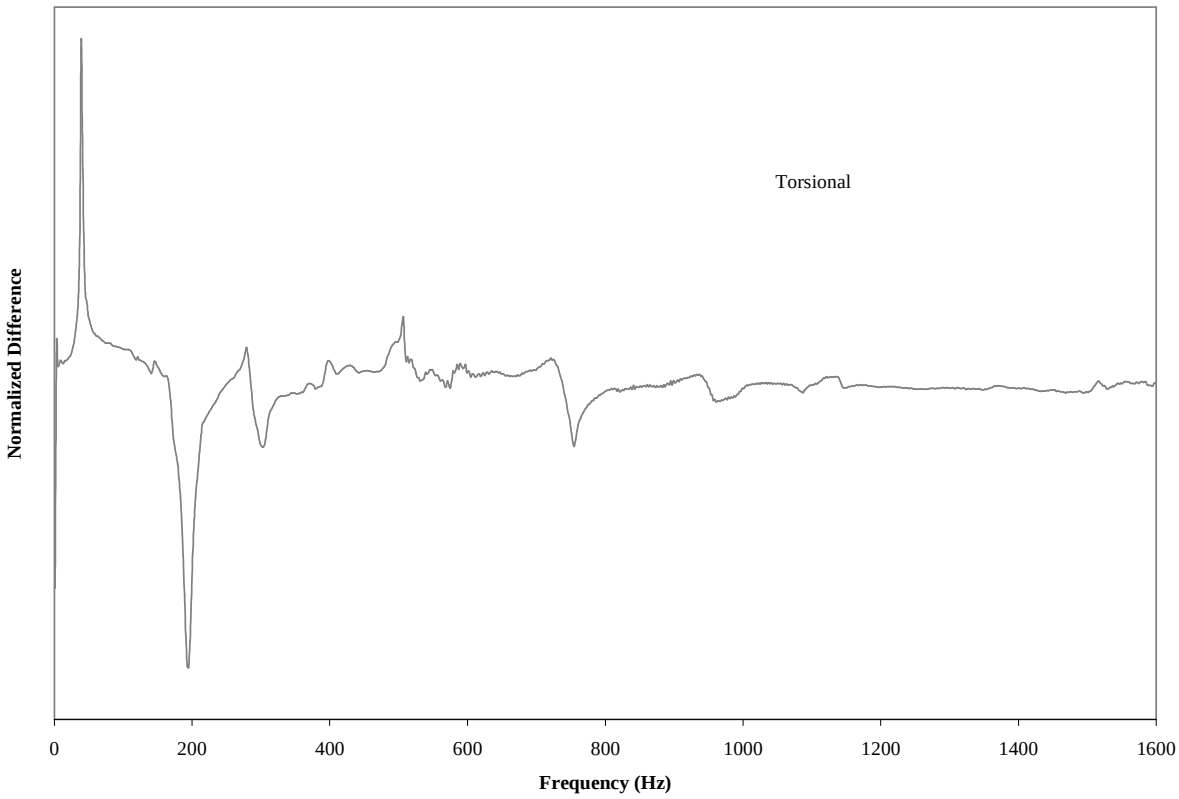

Figure 5.46 - Difference between partially saturated and dry specimen 5 normalized transfer function

The resonant properties of the partially saturated specimen are given in Table 5-20 and the transfer functions are shown as Figure 5.47.

Table 5-20 - Specimen 5, partially saturated dynamic properties

		Torsional	
Resonant frequency	f_0	189.375	*Hz*
Damping ratio	ξ_0	2.39	*%*
Strain level	γ	2.4×10^{-3}	*%*
Wave velocity	V_s	803	*m/s*
Height change	ΔL	0	μm

The torsional mode resonant frequency shifts from 33 *Hz* to 189 *Hz*, an increase of 473 %. The damping ratio in torsional mode decreases from 3.95 % to 2.39 %, a decrease of 39 %. These results also suggest that the driving plate was in contact with the coils during testing.

From the NR test, a plot of partially saturated shear wave velocity and damping ratio versus frequency of excitation is given as Figure 5.48. During the NR method test, the LVDT indicated a specimen height decrease of 26.5 μm. The spike in damping ratio observed at 150 *Hz* is the typical response observed when other modes of vibration interfere with the measured response.

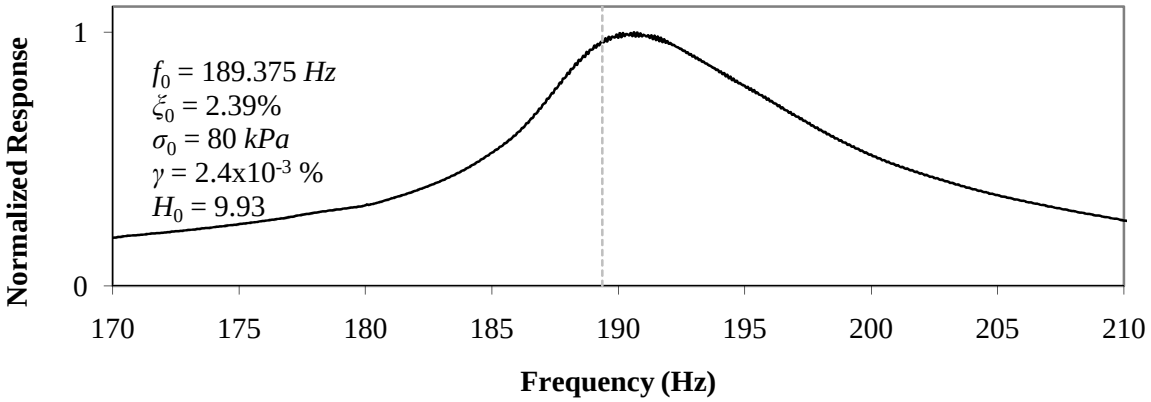

Figure 5.47 - Specimen 5 partially saturated, RC test, torsional mode

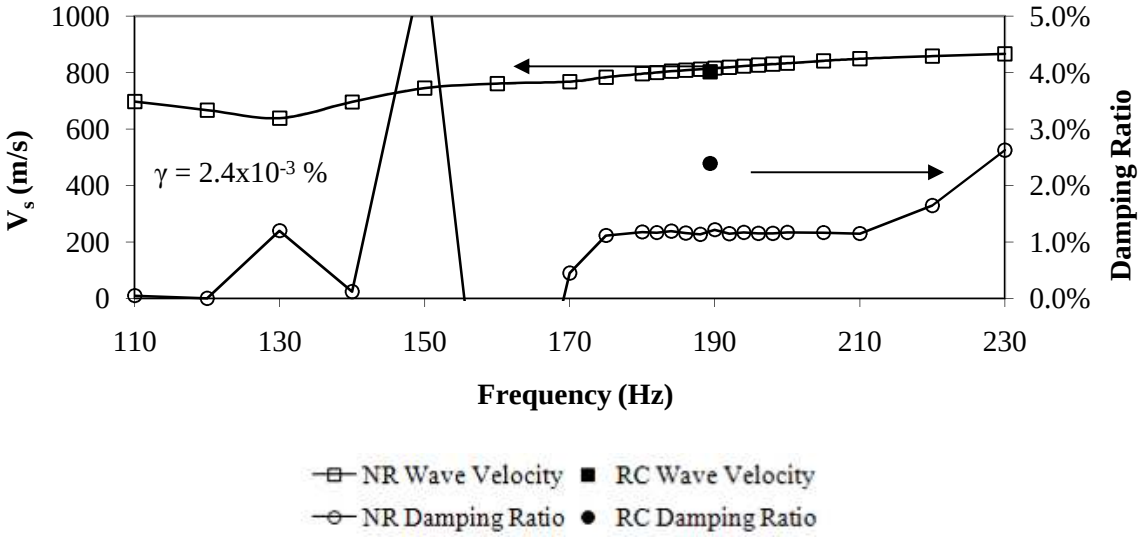

Figure 5.48 - Specimen 5 partially saturated, NR test, torsional mode

Several flow rate measurements of specimen 5 are attempted; however, even under maximum possible hydraulic gradients, no flow is observed.

5.1.7 Specimen 6

Specimen 6 is made of Indusmin 2010 sand; its physical properties are given in Table 5-21. The purpose of specimen 6 flow testing is to characterize the dynamic properties of the soil in both torsional and axial mode of vibration over a wide frequency bandwidth (1600 *Hz*). This is a repeat of specimen 4 testing to attempt to better saturate the specimen. Dynamic excitation in shear and torsional modes is applied at frequencies corresponding to the resonant peaks of the specimen in each mode, both in narrow bandwidths around the peaks as well as fixed sine waves at resonance. A backpressure of 100 kPa is used during saturated condition testing. First, the torsional mode saturated test is completed, followed by the saturated axial mode test. Next, the specimen is partially desaturated and the order of modal testing is reversed (in order to minimize the number of times the drive coils must be reoriented).

Table 5-21 - Specimen 6, physical properties

Mass	m_T	0.886	*kg*
Height	L	0.146	*m*
Volume	V_T	562	*mL*
Dry density	ρ_d	1577	kg/m^3
Void ratio	e	0.685	--
Porosity	n	0.407	--
Volume of voids	V_v	229	*mL*
Conductivity (Hazen)	K	7.8×10^{-4}	*m/s*
Conductivity (C-K)	K	1.0×10^{-3}	*m/s*
Permeability	k	79.5	*darcy*

Wide-bandwidth sweeps are performed on the saturated specimen in both modes of vibration, shown as Figure 5.49. First resonant peaks are noted at approximately 67 *Hz* in torsional mode and 370 *Hz* in axial mode.

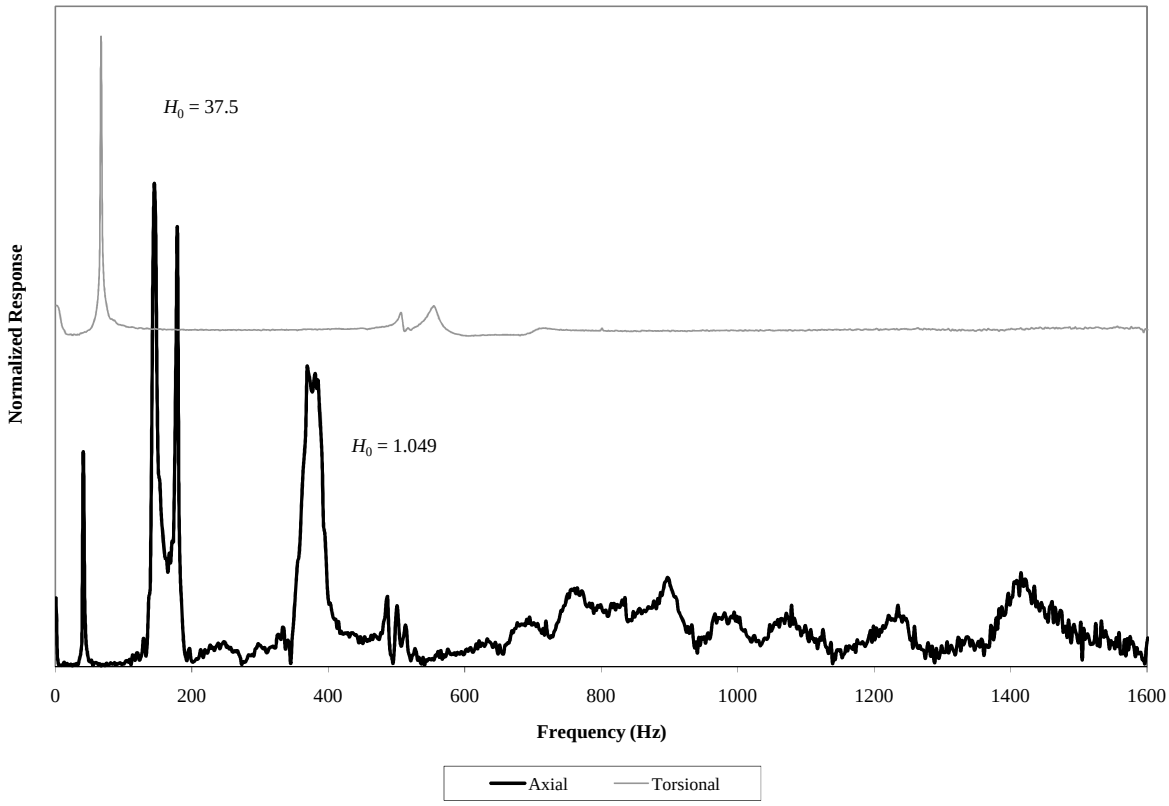

Figure 5.49 - Wideband frequency sweep of specimen 6 saturated

A pore pressure coefficient test is performed on the Indusmin sand to determine the initial degree of saturation, shown in Figure 5.50. For the coarse sand, B = 0.32, which corresponds to S = 0.84 (Craig, 2002)

Next, two RC tests are performed on the saturated specimen in both axial and torsional modes, using low and high strains. The low-strain test is performed with the power amplifier gain setting lowered to 15 from 25. The resonant properties of the saturated specimen are given in Table 5-22 and the transfer functions are shown as Figure 5.51 and Figure 5.52.

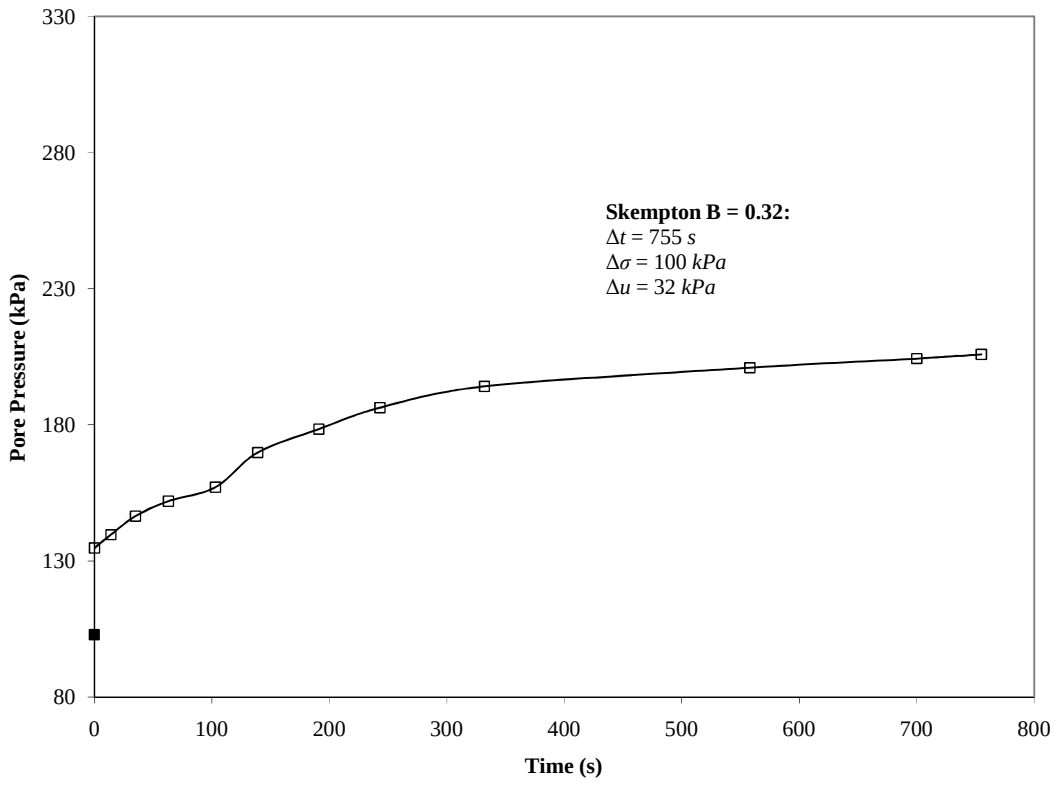

Figure 5.50 - Indusmin sand pore pressure coefficient *B* measurement results

Table 5-22 - Specimen 6, saturated dynamic properties

		Low Strain		High Strain		
		Torsional	**Axial**	**Torsional**	**Axial**	
Resonant frequency	f_0	66.875	382.625	61.125	362.5	*Hz*
Damping ratio	ξ_0	0.3	1.05	1.23	1.46	*%*
Strain level	γ-ε	1.8×10^{-4}	2.5×10^{-5}	1.2×10^{-2}	2.5×10^{-3}	*%*
Wave velocity	V_s-V_L	225.3	421.2	205.9	399.1	*m/s*
	V/V_{max}	103	114	94	108	*%*
Poisson ratio	v	0.535		0.516		

From the NR tests, plots of saturated longitudinal wave velocity, shear wave velocity and damping ratio versus frequency of excitation are given as Figure 5.53 and Figure 5.54.

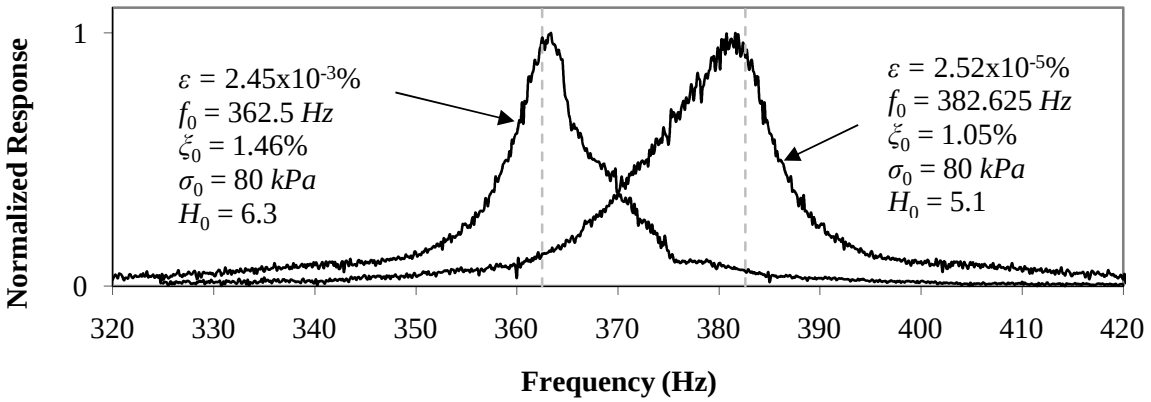

Figure 5.51 - Specimen 6 saturated, RC test, axial mode

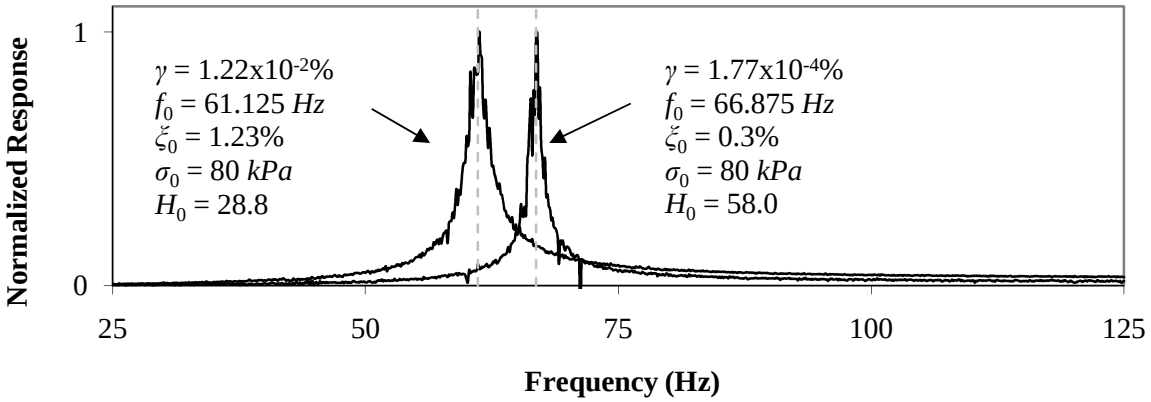

Figure 5.52 - Specimen 6 saturated, RC test, torsional mode

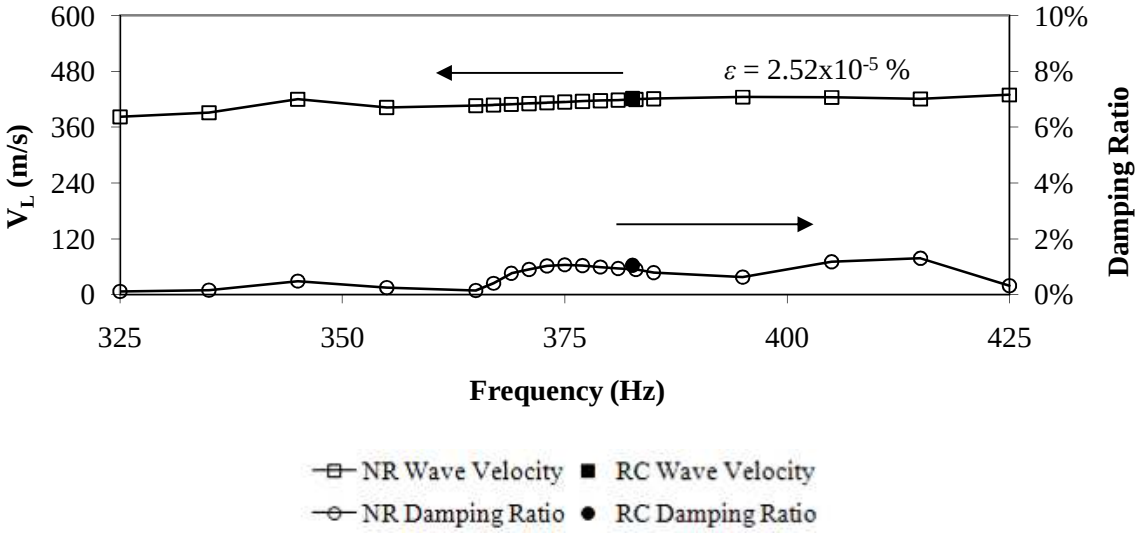

Figure 5.53 - Specimen 6 saturated, NR test, axial mode

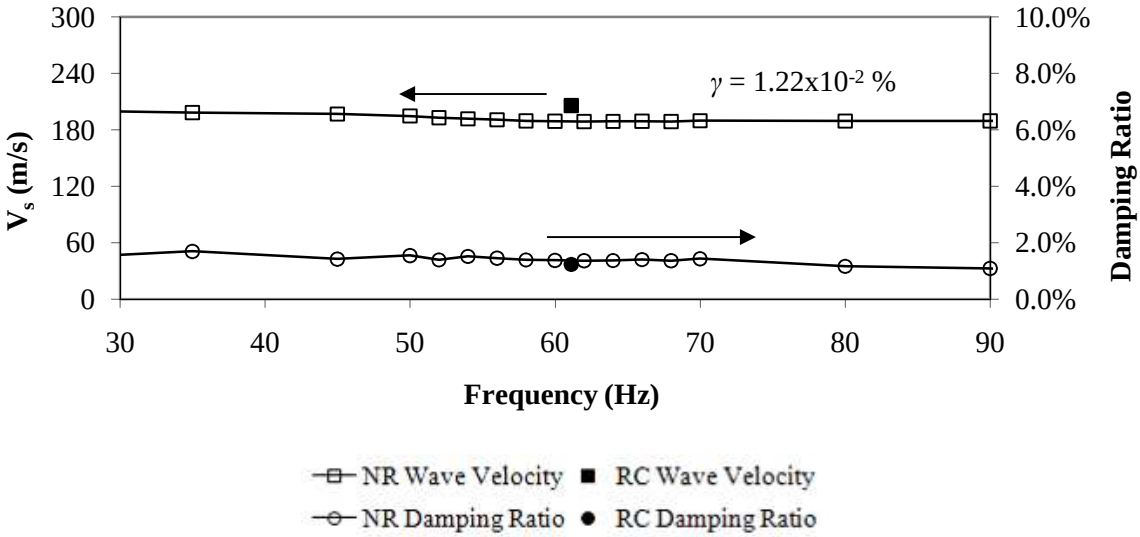

Figure 5.54 - Specimen 6 saturated, NR test, torsional mode

A total of 8 flow test trials are performed on the fully-saturated specimen, with 10 time measurements for each trial. Table 5-23 summarizes the dynamic properties of each flow test. Measured time intervals for each trial are shown as Figure 5.55. Figure 5.56 summarizes the hydraulic conductivity results for specimen 6 saturated single-phase flow. Baseline flow is measured before stimulation for comparison with dynamic excitation results.

Table 5-23 - Specimen 6, flow test dynamic properties

Trial	Excitation Mode	Central Frequency Hz	Bandwidth Hz	Strain %	γ/γ_{th} %
2	axial burst chirp	801	1600	$1.7x10^{-3}$	1.7
3	axial burst chirp	362.5	100	$1.7x10^{-3}$	1.7
4	axial fixed sine	362.5	1	$1.9x10^{-3}$	1.9
6	torsional burst chirp	801	1600	$2.2x10^{-2}$	55
7	torsional burst chirp	61.125	100	$4.1x10^{-2}$	103
8	torsional fixed sine	61.125	1	$4.8x10^{-2}$	120

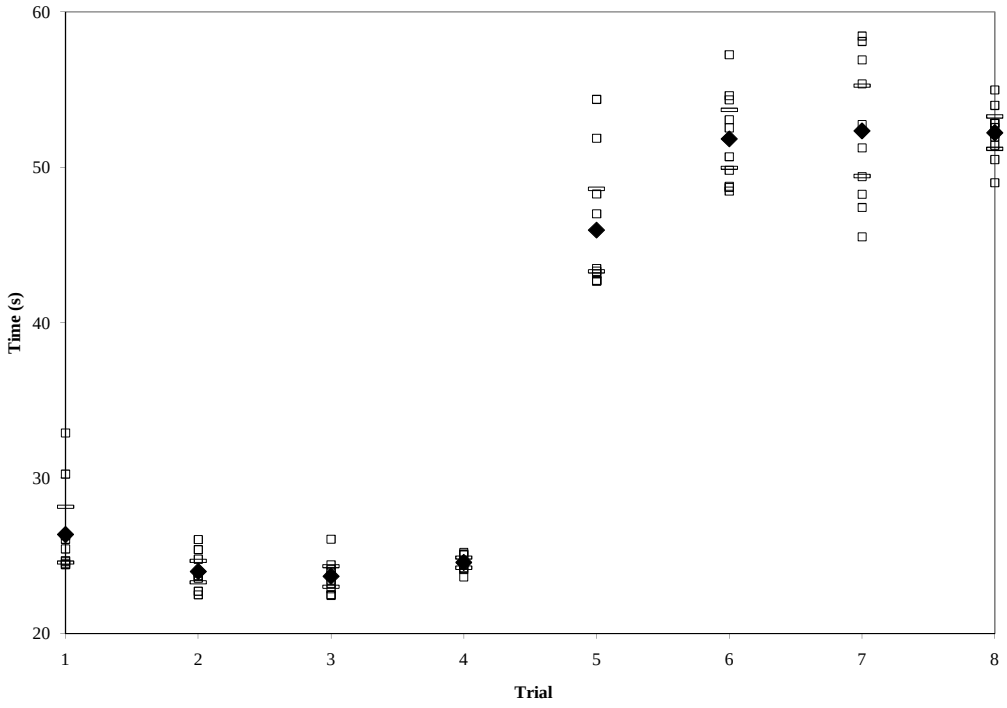

Figure 5.55 - Specimen 6, flow test measured time intervals

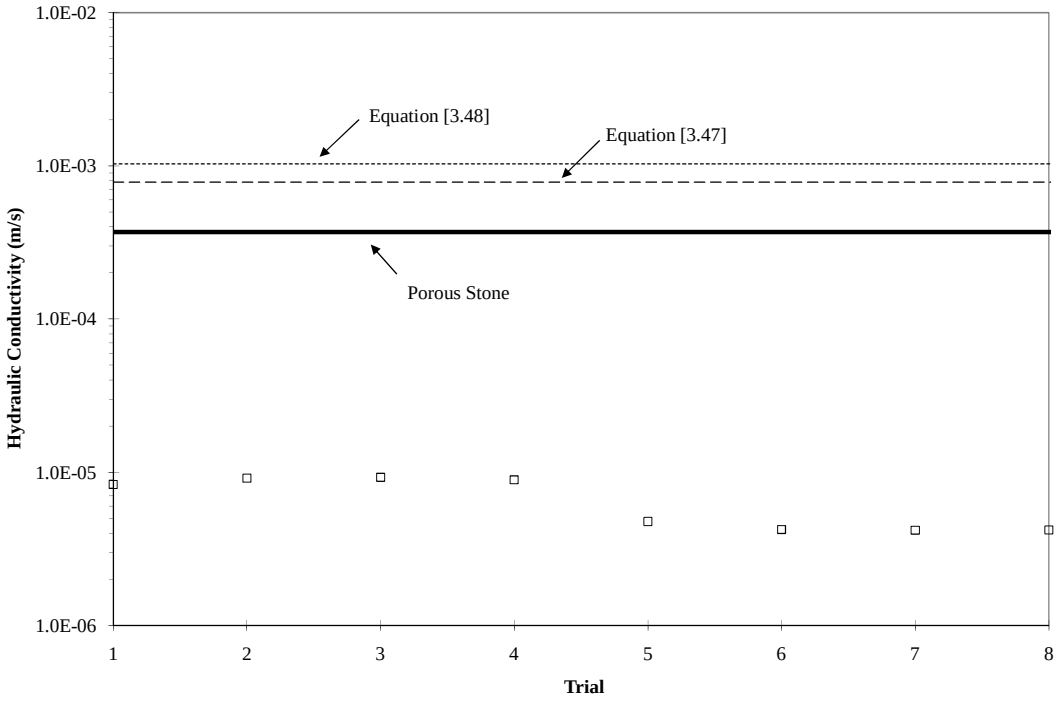

Figure 5.56 - Specimen 6, flow test computed hydraulic conductivities

From Figure 5.55, there appears to be no correlation between dynamic excitation and fluid flow rate.

Approximately half of the computed specimen pore volume is extracted and this sequence of tests is performed again. From the wide-bandwidth frequency sweeps shown in Figure 5.57, first resonant peaks are noted at approximately 55 *Hz* in torsional mode and 172 *Hz* in axial mode. After the entire series of tests are completed, the partially saturated specimen is weighed and determined to have a saturation of $S = 0.424$.

Next, two RC tests and two NR method tests are performed on the partially saturated specimen in torsional and axial modes. The resonant properties of the partially saturated specimen are given in Table 5-24 and the transfer functions are shown as Figure 5.58 and Figure 5.59.

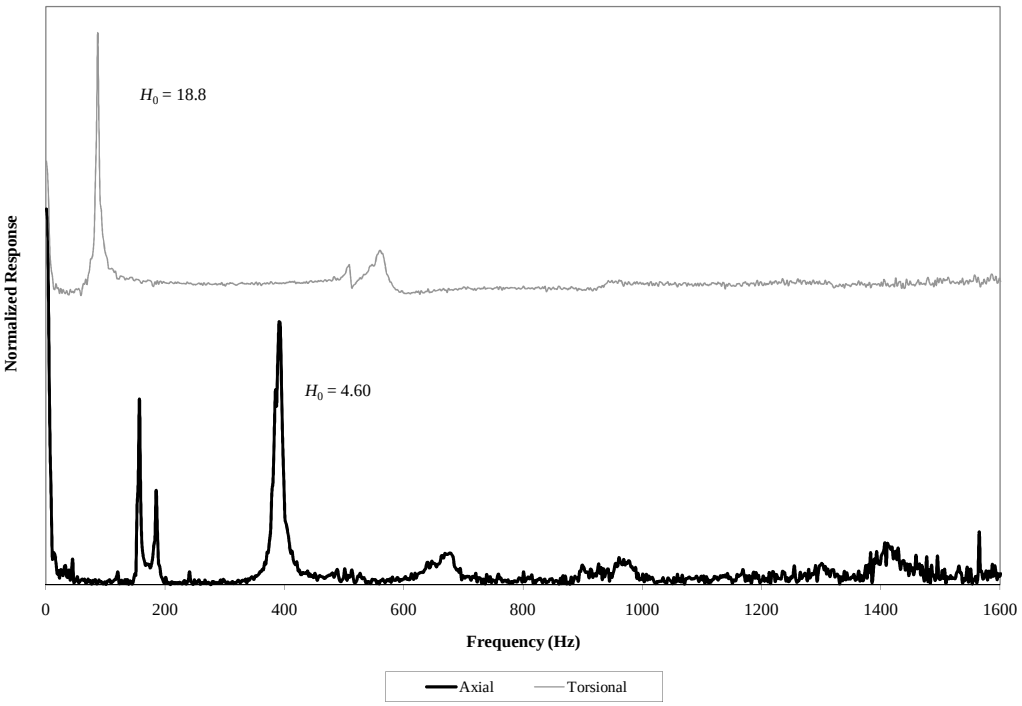

Figure 5.57 - Wideband frequency sweep of specimen 6 partially saturated

Table 5-24 - Specimen 6, partially saturated dynamic properties

		Torsional	**Axial**	
Resonant frequency	f_0	86.875	395.125	*Hz*
Damping ratio	ξ_0	0.4	0.91	*%*
Strain level	γ-ε	1.1×10^{-4}	2.5×10^{-5}	*%*
Wave velocity	V_s-V_L	292.7	435.0	*m/s*
	V/V_{max}	134	118	*%*
Poisson ratio	ν	0.673		

The low-strain torsional resonant frequency shifts from 66.9 *Hz* in saturated conditions to 86.9 *Hz* in partially saturated conditions, an increase of 30 %. The low-strain axial resonant frequency shifts from 382.6 *Hz* to 395.1 *Hz*, an increase of 3 %. The low-strain damping ratio in torsional mode increases from 0.3 % to 0.4 %, a 33 % increase. The low-strain damping ratio in axial mode decreases from 1.05 % to 0.91 %, a 13 % decrease.

Again, there is a large difference in normalization factors between dry and partially saturated tests; this effect is caused by the reduction in effective stress due to the air leak.

From the NR tests, plots of partially saturated shear wave velocity, compression wave velocity and damping ratio versus frequency of excitation are given as Figure 5.60 and Figure 5.61.

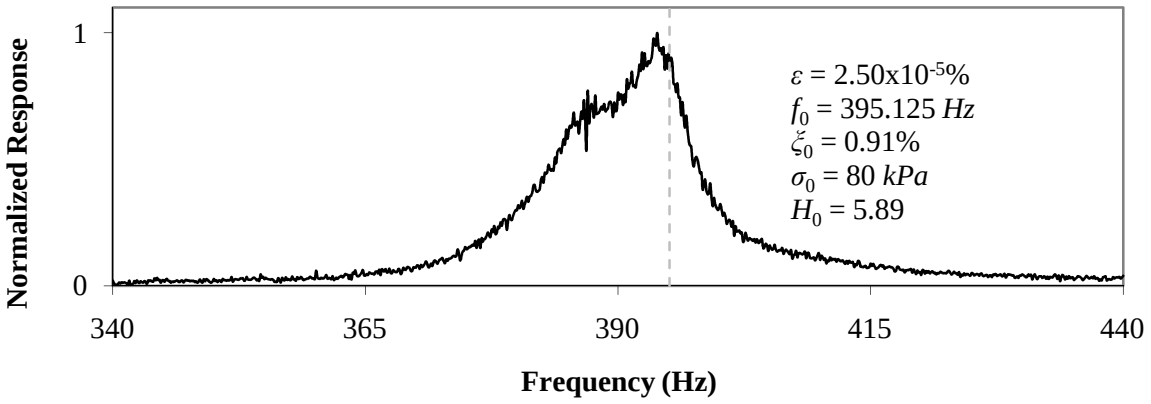

Figure 5.58 - Specimen 6 partially saturated, RC test, axial mode

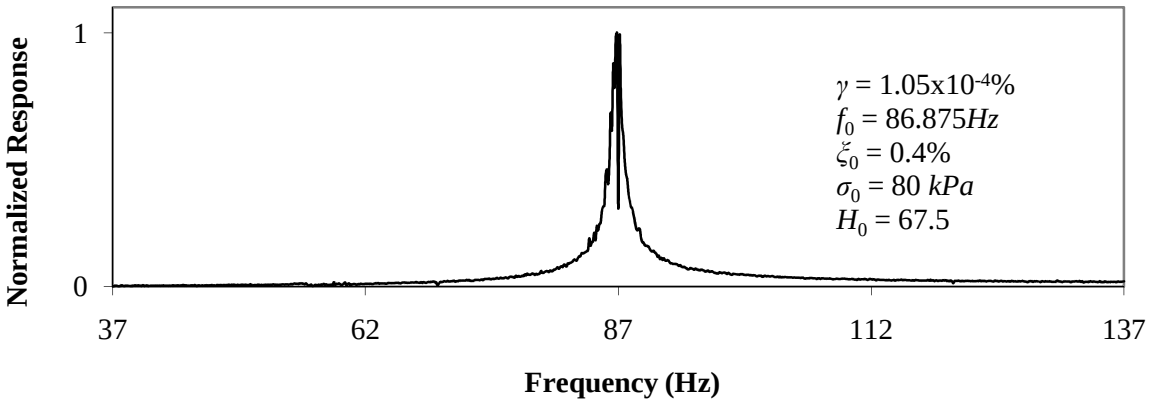

Figure 5.59 - Specimen 6 partially saturated, RC test, torsional mode

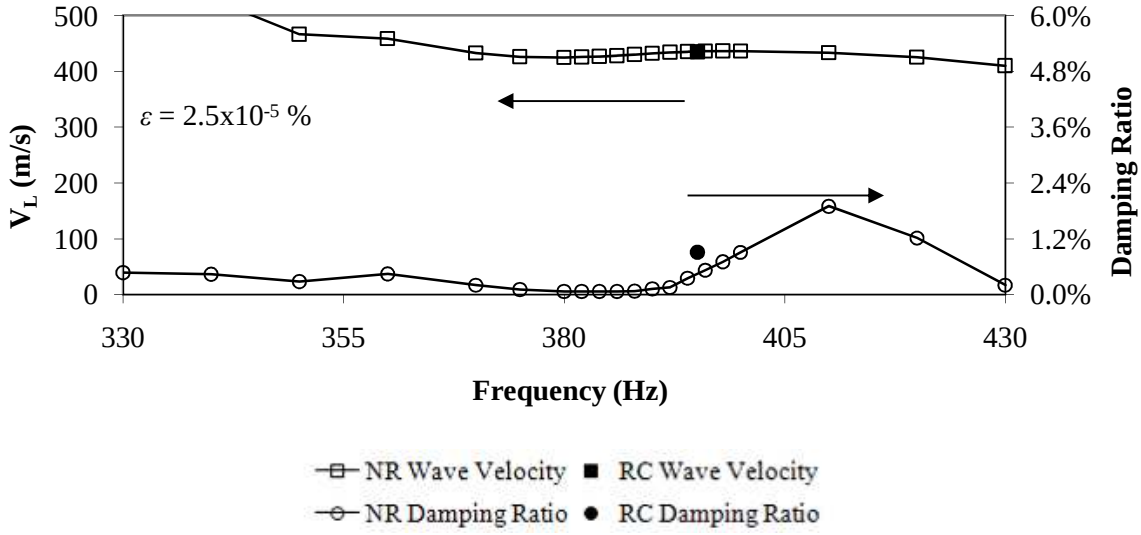

Figure 5.60 - Specimen 6 partially saturated, NR test, axial mode

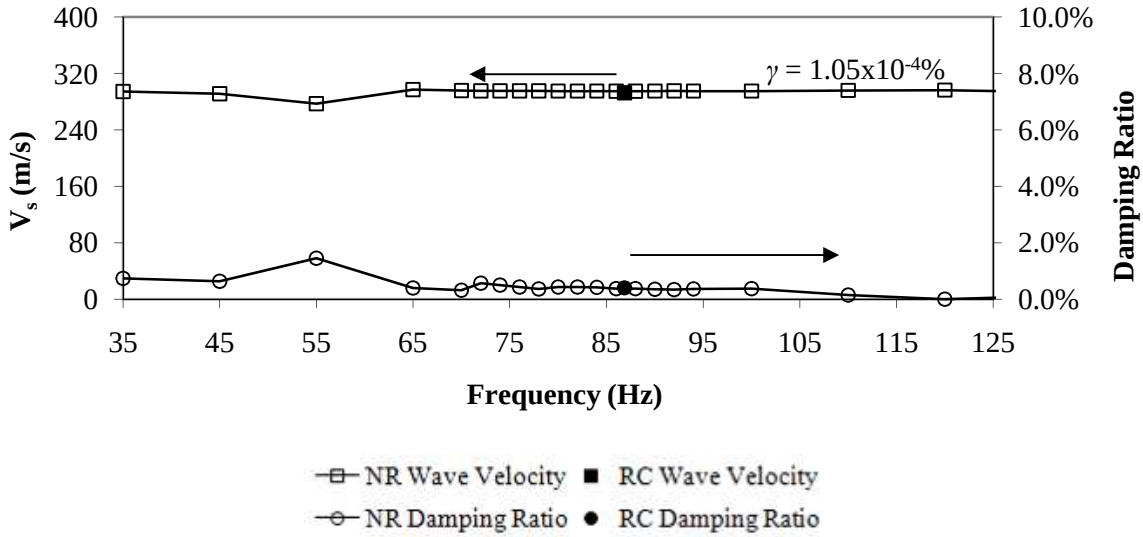

Figure 5.61 - Specimen 6 partially saturated, NR test, torsional mode

5.1.8 Specimen 7

Specimen 7 is made of Barco 71 sand; its physical properties are given in Table 5-25. The purpose of specimen 7 flow testing is to characterize the dynamic properties of the soil in both torsional and axial mode of vibration over a wide frequency bandwidth (1600 *Hz*). This specimen is a repeat of specimen 3 to attempt to achieve a higher degree of saturation.

Dynamic excitation in shear and torsional modes is applied at frequencies corresponding to the resonant peaks of the specimen in each mode, both in narrow bandwidths around the peaks as well as fixed sine waves at resonance. A backpressure of 100 kPa is used during saturated condition testing. First, the torsional mode saturated test is completed, followed by the saturated axial mode test. Next, the specimen is partially desaturated and the order of modal testing is reversed (in order to minimize the number of times the drive coils must be reoriented).

Table 5-25 - Specimen 7, physical properties

Mass	m_T	1.012	*kg*
Height	L	0.150	*m*
Volume	V_T	577	*mL*
Dry density	ρ_d	1754	kg/m^3
Void ratio	e	0.511	--
Relative density	d_r	1.0	--
Porosity	n	0.338	--
Volume of voids	V_v	195	*mL*
Conductivity (Hazen)	K	1.4×10^{-4}	*m/s*
Conductivity (C-K)	K	8.2×10^{-5}	*m/s*
Permeability	k	14	*darcy*

Wide-bandwidth sweeps are performed on the saturated specimen in both modes of vibration, shown as Figure 5.62. First resonant peaks are noted at approximately 71 *Hz* in torsional mode and 431 *Hz* in axial mode.

A pore pressure coefficient test is performed on the Barco sand to determine the initial degree of saturation, shown in Figure 5.63. For the coarse sand, $B = 0.26$, which corresponds to $S = 0.82$ (Craig, 2002)

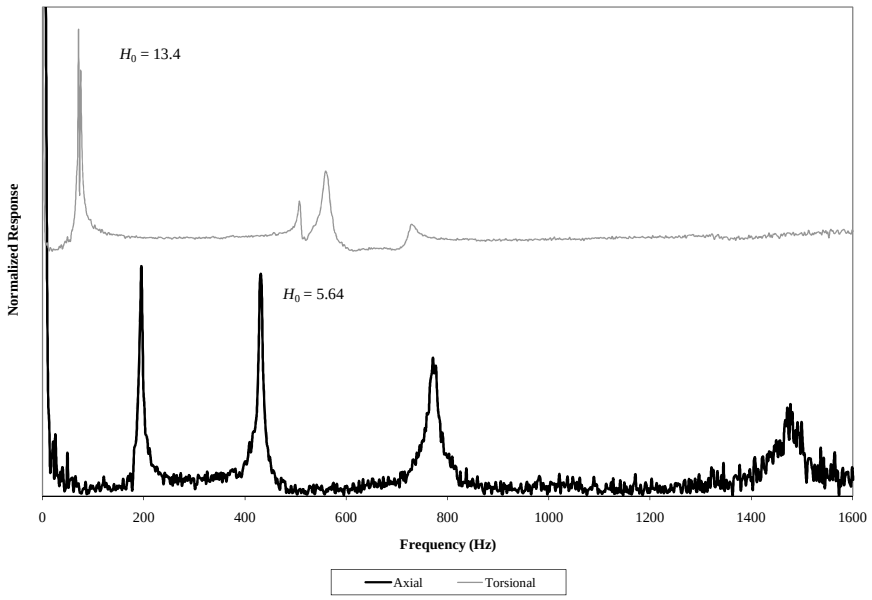

Figure 5.62 - Wideband frequency sweep of specimen 7 saturated

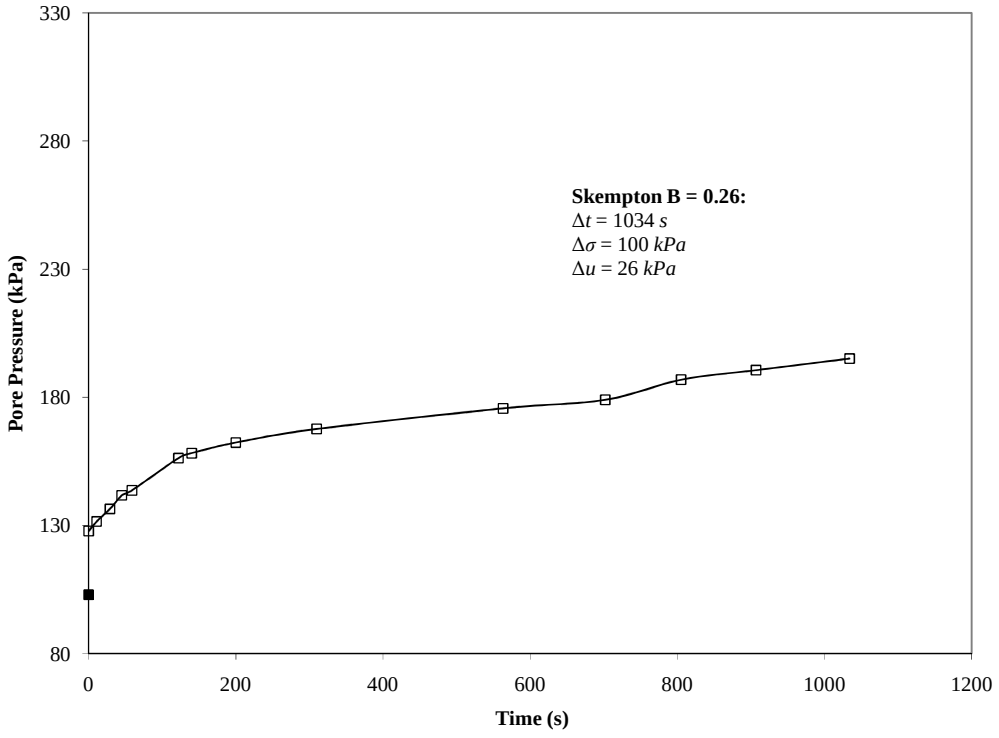

Figure 5.63 - Barco sand pore pressure coefficient *B* measurement results

Next, two RC tests are performed on the saturated specimen in both axial and torsional modes, using low and high strains. The low-strain test is performed by lowering the power amplifier gain to 15 from 25. The resonant properties of the saturated specimen are given in Table 5-26 and the transfer functions are shown as Figure 5.64 and Figure 5.65.

Table 5-26 - Specimen 7, saturated dynamic properties

		Low Strain		High Strain		
		Torsional	**Axial**	**Torsional**	**Axial**	
Resonant frequency	f_0	73	431.375	68.625	428.875	*Hz*
Damping ratio	ξ_0	0.3	0.7	0.7	0.8	*%*
Strain level	γ-ε	$1.5\text{x}10^{-4}$	$2.7\text{x}10^{-5}$	$9.4\text{x}10^{-3}$	$6.9\text{x}10^{-4}$	*%*
Wave velocity	V_s-V_L	236.8	464.7	222.7	462.0	*m/s*
	V/V_{max}	109	118	103	118	*%*
Poisson ratio	ν	0.510		0.482		

From the NR tests, plots of saturated longitudinal wave velocity, shear wave velocity and damping ratio versus frequency of excitation are given as Figure 5.66 and Figure 5.67.

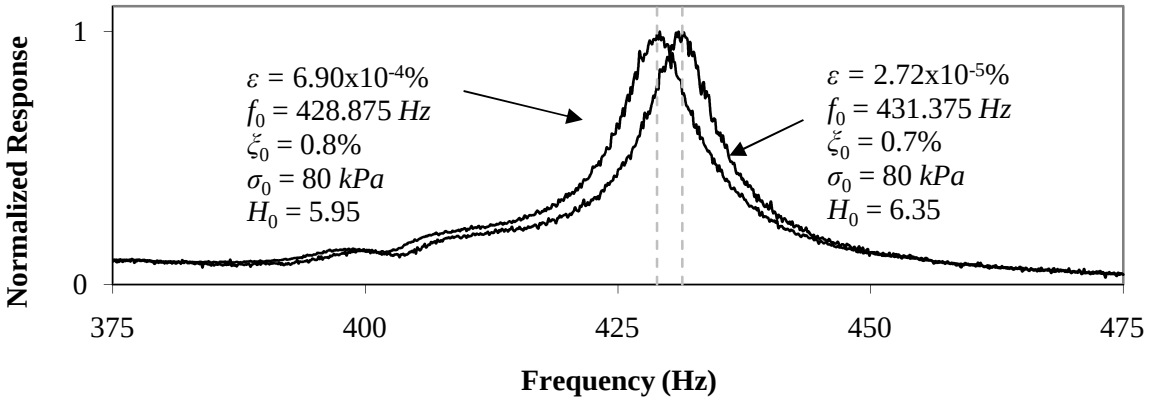

Figure 5.64 - Specimen 7 saturated, RC test, axial mode

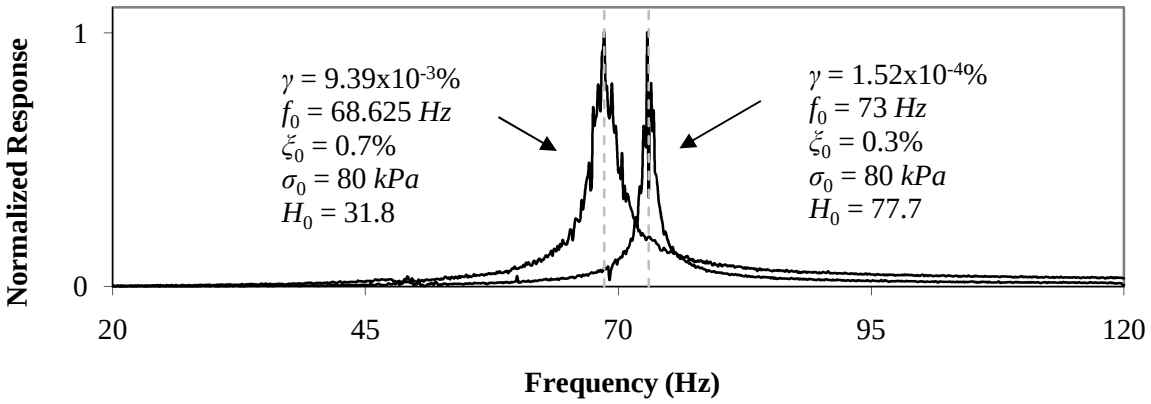

Figure 5.65 - Specimen 7 saturated, RC test, torsional mode

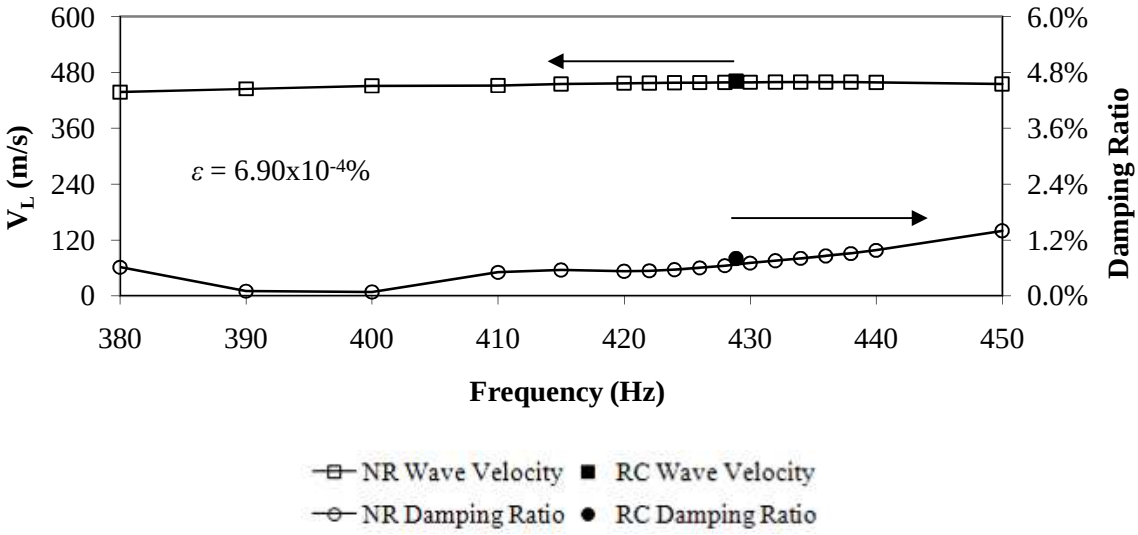

Figure 5.66 - Specimen 7 saturated, NR test, axial mode

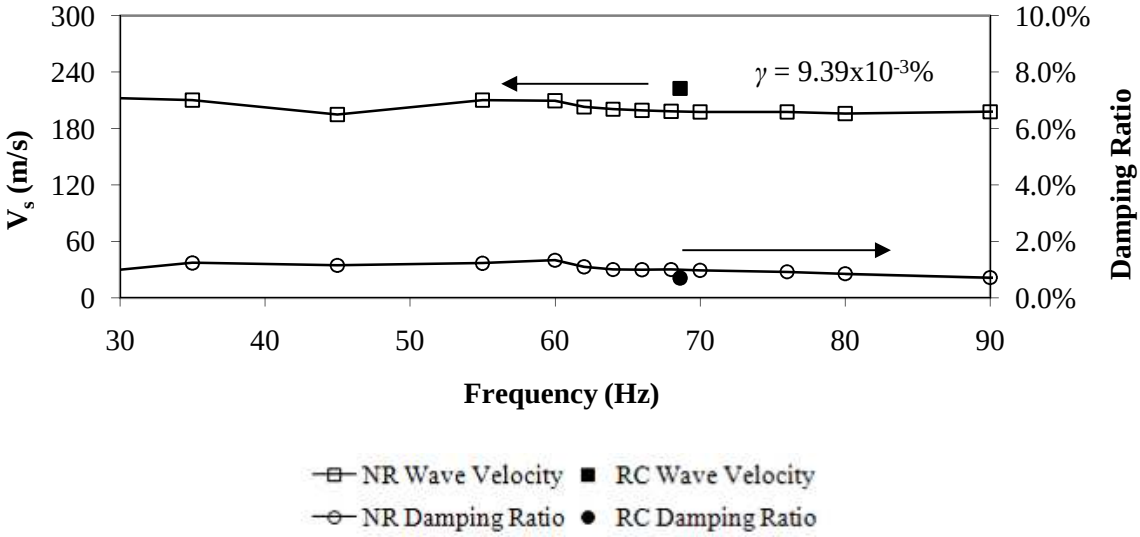

Figure 5.67 - Specimen 7 saturated, NR test, torsional mode

A total of 8 flow test trials are performed on the fully-saturated specimen, with 10 time measurements for each trial. Table 5-27 summarizes the dynamic properties of each flow test. Measured time intervals for each trial are shown as Figure 5.68. Figure 5.69 summarizes the hydraulic conductivity results for specimen 7 saturated single-phase flow. Baseline flow is measured before stimulation for comparison with dynamic excitation results.

Table 5-27 - Specimen 7, flow test dynamic properties

Trial	Excitation Mode	Central Frequency Hz	Bandwidth Hz	Strain %	γ/γ_{th} %
2	torsional burst chirp	801	1600	$3.5\text{x}10^{-2}$	35
3	torsional burst chirp	68.625	100	$3.9\text{x}10^{-2}$	39
4	torsional fixed sine	68.625	1	$3.7\text{x}10^{-2}$	37
6	axial burst chirp	801	1600	$3.9\text{x}10^{-4}$	0.6
7	axial burst chirp	428.875	100	$5.5\text{x}10^{-4}$	0.8
8	axial fixed sine	428.875	1	$1.0\text{x}10^{-4}$	0.1

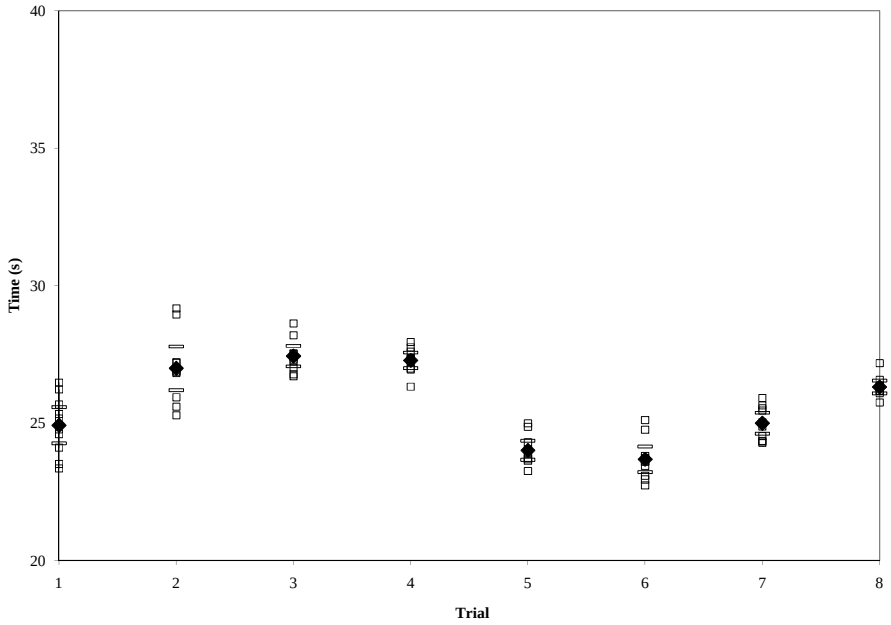

Figure 5.68 - Specimen 7, flow test measured time intervals

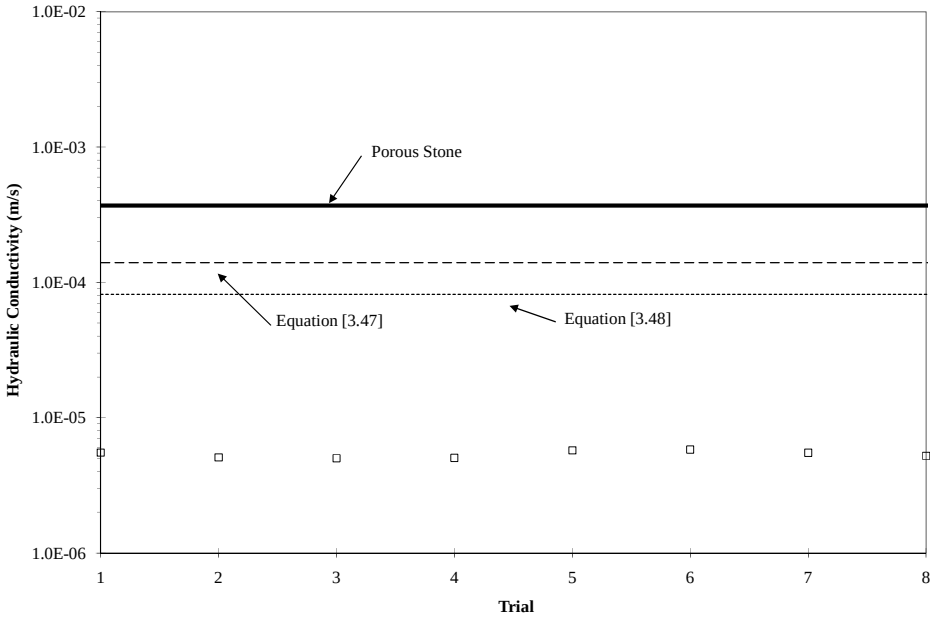

Figure 5.69 - Specimen 7, flow test computed hydraulic conductivities

From Figure 5.68, there appears to be no correlation between dynamic excitation and fluid flow rate.

Approximately half of the computed specimen pore volume is extracted and this sequence of tests is performed again. From the wide-bandwidth frequency sweeps shown in Figure 5.70, first resonant peaks are noted at approximately 101 *Hz* in torsional mode and 447 *Hz* in axial mode. After the entire series of tests are completed, the partially saturated specimen is weighed and determined to have a saturation of $S = 0.056$.

Next, two RC tests and two NR method tests are performed on the partially saturated specimen in torsional and axial modes. The resonant properties of the partially saturated specimen are given in Table 5-28 and the transfer functions are shown as Figure 5.71 and Figure 5.72.

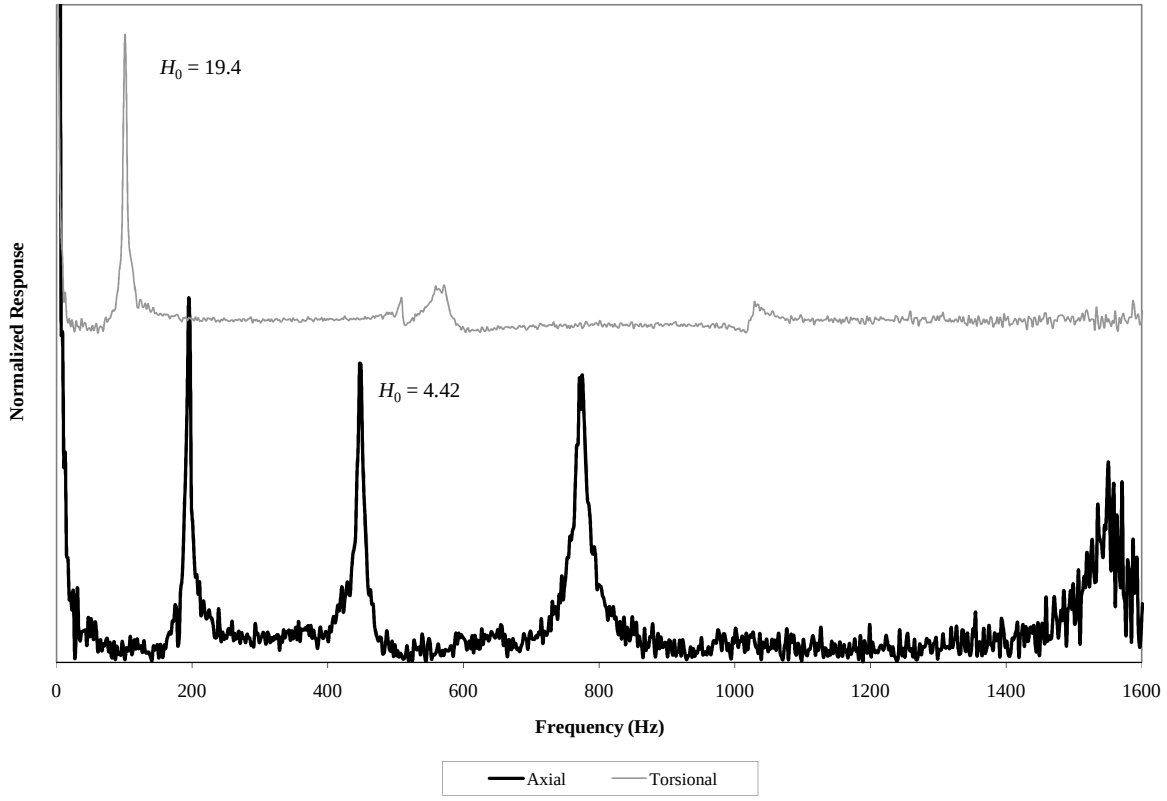

Figure 5.70 - Wideband frequency sweep of specimen 7 partially saturated

Table 5-28 - Specimen 7, partially saturated dynamic properties

		Torsional	Axial	
Resonant frequency	f_0	101.25	449.125	*Hz*
Damping ratio	ξ_0	0.2	0.7	*%*
Strain level	γ-ε	7.5×10^{-5}	2.1×10^{-5}	*%*
Wave velocity	V_s-V_L	328.5	483.8	*m/s*
	V/V_{max}	151	123	*%*
Poisson ratio	ν	0.679		

The low-strain torsional resonant frequency shifts from 73 *Hz* in saturated conditions to 101.3 *Hz* in partially saturated conditions, an increase of 39 %. The low-strain axial resonant frequency shifts from 431.4 *Hz* to 449.1 *Hz*, an increase of 4 %. The low-strain damping ratio in torsional mode decreases from 0.3 % to 0.2 %, a 33 % decrease. The low-strain damping ratio in axial mode remains constant at 0.7 %.

From the NR tests, plots of partially saturated shear wave velocity, compression wave velocity and damping ratio versus frequency of excitation are given as Figure 5.73 and Figure 5.74.

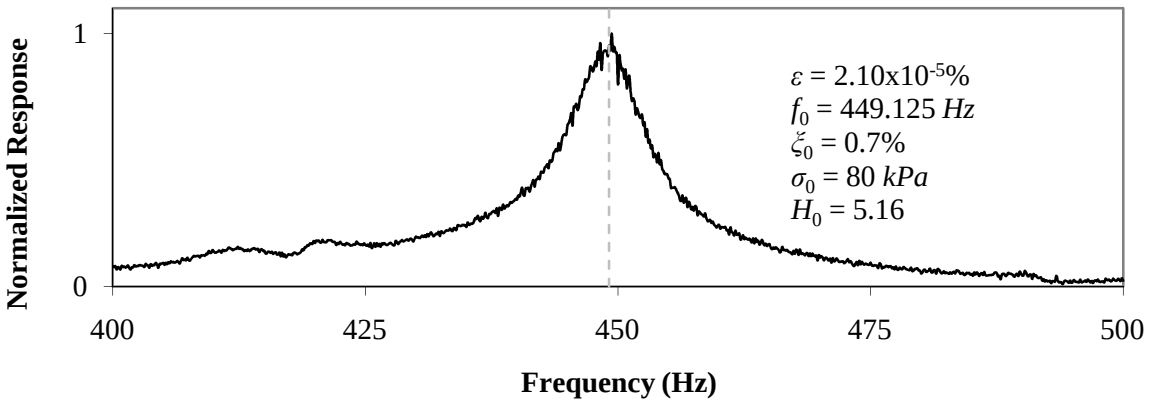

Figure 5.71 - Specimen 7 partially saturated, RC test, axial mode

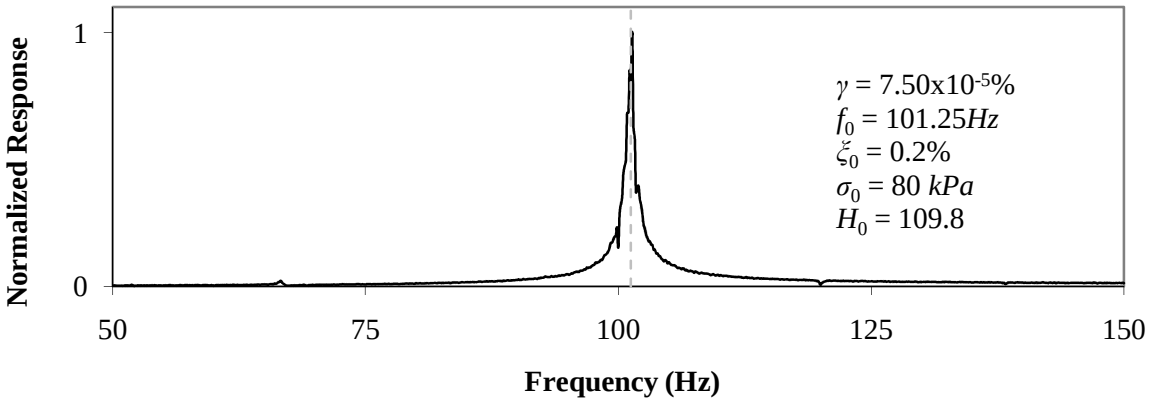

Figure 5.72 - Specimen 7 partially saturated, RC test, torsional mode

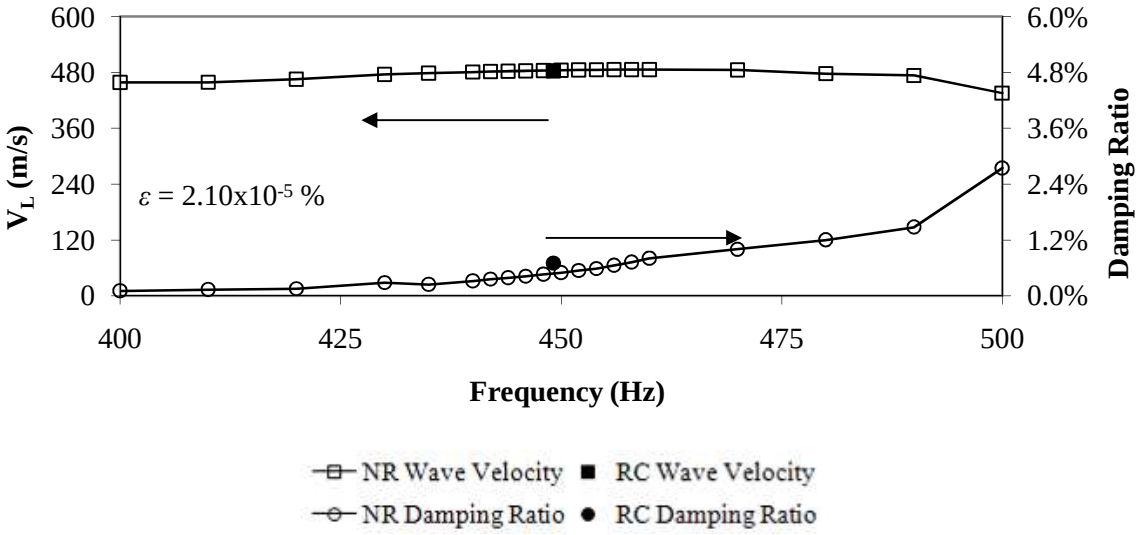

Figure 5.73 - Specimen 7 partially saturated, NR test, axial mode

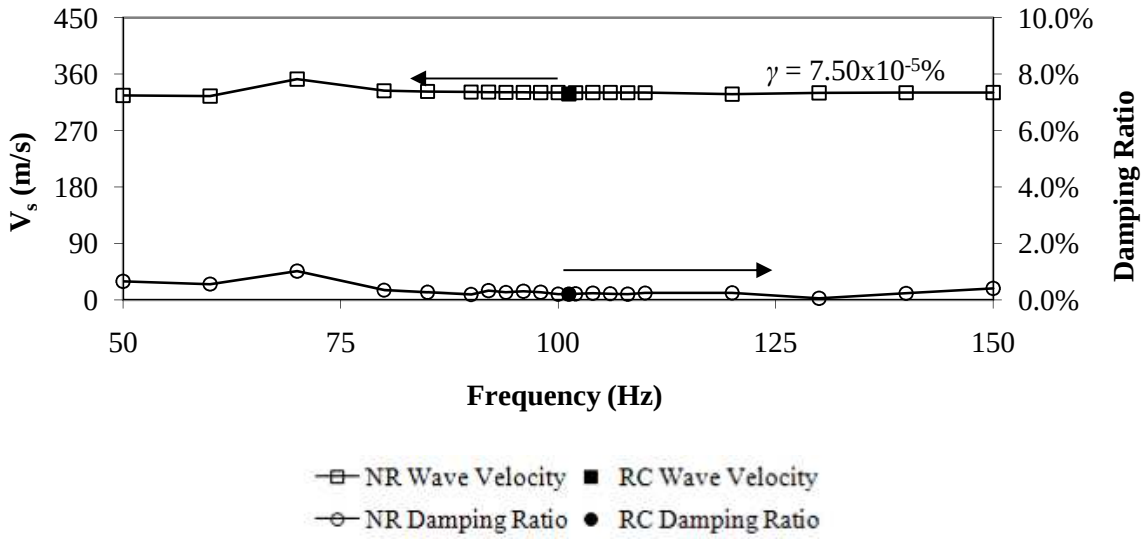

Figure 5.74 - Specimen 7 partially saturated, NR test, torsional mode

5.2 Summary

The purpose of these single-phase saturated flow tests is to determine whether dynamic excitation increases the fluid flow rate through the specimen either through porosity dilation, added inertial energy or the creation of standing waves within the pore fluid. Three soil types are used to determine if initial hydraulic conductivity/dynamic properties of the soil play a role in enhanced fluid flow. Additionally, a wide range of frequencies are used in all three modes of vibration, including very low frequencies ($\leq$ 20 Hz) as per the PPT methodology, as well as higher frequencies related to the dynamic properties of the soil (i.e. vibration at specimen resonance).

In specimens 1 through 5, an air leak into the specimen due to flow connections has a significant impact on the results; thus, it is inconclusive whether dynamic excitation does in fact increase saturated fluid flow. The 'B' parameter for all 7 specimens was low. For specimens 6 and 7, the air leak is reduced (the 'B' parameter is greater); however, the results still do not show any correlation between dynamic excitation and increased fluid flow.

It is possible that the excitation energy applied is not high enough to cause any noticeable increase in flow. Table 5-29 lists the maximum strain applied for each specimen and the corresponding ratio of maximum strain applied to threshold strain from the degradation curves presented in Section 5.1.1.

Table 5-29 - Summary of strain ratios

Specimen	Excitation Mode	Maximum Strain %	γ/γ_{th} %
2	torsional	$5x10^{-3}$	5.0
	axial	$5x10^{-4}$	0.7
3	torsional	$5x10^{-2}$	50
	axial	$5x10^{-3}$	7.1
4	torsional	$6x10^{-2}$	150
	axial	$2x10^{-3}$	2.0
6	torsional	$5x10^{-2}$	120
	axial	$2x10^{-3}$	1.9
7	torsional	$4x10^{-2}$	37
	axial	$6x10^{-4}$	0.8

To enhance the flow rate, it is more effective to add inertial energy in the direction of flow; therefore, intuitively, axial excitation is the best method for increasing fluid flow rates. In this study, the resonant column is capable of applying up to 150 % of the shear strain threshold value, compared to approximately 7 % of the axial strain threshold value. Much higher energy inputs in the axial mode are likely required before any increase in flow is measured.

Shear and compression wave velocities are given in the degradation curves shown in Section 5.1.1. These values are used to compute the Poisson ratio for the Barco and Indusmin sands as shown in Table 5-30. Also shown are the damping ratios measured during the RC method tests. As mentioned in Section 3.1.1, although the measured velocity during the axial tests is V_L, because of the constraint conditions, it is assumed equal to V_p.

Table 5-30 - Summary of soil properties

Soil	Condition	γ %	ε %	V_s m/s	V_L m/s	$\xi_{torsional}$ %	ξ_{axial} %	ν [-]
Barco sand	dry	$8.8\text{x}10^{-3}$	$7.1\text{x}10^{-4}$	226.6	406	1.03	0.96	0.558
	partially saturated	$7.5\text{x}10^{-5}$	$2.1\text{x}10^{-5}$	328.5	483.8	0.2	0.7	0.679
	saturated (low strain)	$1.5\text{x}10^{-4}$	$9.4\text{x}10^{-3}$	236.8	464.7	0.3	0.7	0.510
	saturated (high strain)	$9.4\text{x}10^{-3}$	$6.9\text{x}10^{-4}$	222.7	462.0	0.7	0.8	0.482
Indusmin sand	dry	$3.1\text{x}10^{-2}$	$1.0\text{x}10^{-3}$	171.5	386.6	3.81	1.67	0.444
	partially saturated	$1.1\text{x}10^{-4}$	$2.5\text{x}10^{-5}$	292.7	435.0	0.4	0.91	0.673
	saturated (low strain)	$1.8\text{x}10^{-4}$	$1.2\text{x}10^{-2}$	225.3	421.2	0.3	1.05	0.535
	saturated (high strain)	$1.2\text{x}10^{-2}$	$2.5\text{x}10^{-3}$	205.9	399.1	1.23	1.46	0.516

Finally, the wave velocities are used to back-calculate specimen saturation, using shear wave velocity (Table 5-31) and longitudinal wave velocity (Table 5-32).

Table 5-31 - Calculation of shear modulus

Soil	Condition	V_s m/s	G MPa	ρ kg/m^3	$\Delta\rho$ kg/m^3	V_w mL	V_v mL	S [-]
Barco sand	dry	226.6	86.4	1683	0	0	205	0
	partially saturated	328.5	210.0	1946	192	11		0.056
	saturated (low strain)	236.8	117.3	2092	338	195	195	1.0
	saturated (high strain)	222.7	103.8	2092	338	195		1.0
Indusmin sand	dry	171.5	44.1	1499	0	0	238	0
	partially saturated	292.7	149.8	1749	172	97		0.424
	saturated (low strain)	225.3	100.7	1984	407	229	229	1.0
	saturated (high strain)	205.9	84.1	1984	407	229		1.0

Table 5-32 - Calculation of Young's modulus

Soil	Condition	V_L m/s	E MPa	ρ kg/m^3	$\Delta\rho$ kg/m^3	V_w mL	V_v mL	S [-]
Barco sand	dry	406	277.4	1683	0	0	205	0
	partially saturated	483.8	455.5	1946	192	11		0.056
	saturated (low strain)	464.7	451.8	2092	338	195	195	1.0
	saturated (high strain)	462.0	446.5	2092	338	195		1.0
Indusmin sand	dry	386.6	224.0	1499	0	0	238	0
	partially saturated	435.0	331.0	1749	172	97		0.424
	saturated (low strain)	421.2	352.0	1984	407	229	229	1.0
	saturated (high strain)	399.1	316.0	1984	407	229		1.0

From Table 5-31 and Table 5-32, it appears that partially saturated specimens have the greatest elastic moduli. These moduli decrease for the saturated specimen (at both low and high strains) and are at their minimal values in the dry condition.

The ratio of axial resonant frequency to torsional resonant frequency is present in Table 5-33.

Table 5-33 - Summary of resonant frequency ratio

Soil	**Condition**	$f_{0,s}$ **Hz**	$f_{0,L}$ **Hz**	$f_{0,L} / f_{0,s}$ **%**
Barco sand	dry	68.3	376.2	551
	partially saturated	101.25	449.125	444
	saturated (low strain)	73	431.375	591
	saturated (high strain)	68.625	428.875	625
Indusmin sand	dry	53.5	349	652
	partially saturated	86.875	395.125	455
	saturated (low strain)	66.875	382.625	572
	saturated (high strain)	61.125	362.5	593

6.0 CONCLUSIONS

6.1 Enhanced Fluid Flow

The purpose of this study is to examine the use of applied dynamic excitation as a method for enhancing fluid flow in a porous matrix. The ultimate goal is to increase the efficiency of existing groundwater remediation techniques. This research is challenging due to the fact that in order to understand how dynamic forces affect fluid flow in a soil, the distinct subjects of soil dynamics, hydrogeology and contaminant transport must all be brought together to form a unified elegant model that can be used in future field applications of the technique. It is very difficult to simultaneously investigate all three areas of study in a laboratory setting, as the equipment to do so currently does not exist. The results of this study are not conclusive, however several important issues are addressed that will help to guide future research on this technique.

According to previous works in the literature, increased single-phase flow relies on the viscous coupling of the pore fluid and the solid skeleton of a porous matrix. The out-of-phase motion between the solid and fluid components gives an added inertial component to the fluid flow and causes a standing wave to form in the pore fluid. The passing wave in the soil skeleton also temporarily increases the porosity on a local scale, thus increasing the hydraulic conductivity of the matrix. For single-phase flow, the specified frequency range is seismic ($\leq$ 20 *Hz*); however, for this study, resonant frequencies in both torsional and axial mode were also used to provide the largest strain energy. The experimental component of this study attempts to reproduce these effects using dynamic excitation in varying modes of vibration and frequency range. In all tests performed, there is no observed correlation between dynamic excitation and fluid flow rate.

There are several reasons why the results are inconclusive; however the main reason is air bubble accumulation in the specimen during testing. The gas comes from a leak in the flow tube connections of the resonant column device. The flow tubing must be redesigned for future tests with a strong emphasis on eliminating sources of gas accumulation in the specimen. Another factor to consider may be input dynamic signal amplitude. For the experiments performed during this study, the highest amplitude possible is selected at each frequency of

excitation (limited by maximum signal analyzer input voltage). The resonant column is only capable of producing 7 % of the threshold strain in the axial mode; therefore, it is likely that the amplitudes utilized are simply not large enough to cause a measurable increase in fluid flow rates. Finally, increased flow rates observed in previous studies may be the result of local increases in fluid pressure that increase the fluid flow rate, rather than an added inertial component or porosity dilation. In their study, Dusseault et al. (2002) specify that input energy is applied to the pore fluid in the form of induced pressure waves in the fluid. In this study, the input energy is applied to the soil skeleton and pore fluid. In theory, inertial force may be added to the pore fluid using either approach; thus, an increase in flow would be observed in both cases. However, increased flow is not observed in this study because of the reasons outlined above.

6.2 Axial and Torsional RC Tests

The RC device used in this study is unique because it has been modified to allow both axial and torsional measurements on the same specimen. From the RC data obtained during this study, there are some general conclusions that can be drawn regarding the dynamic properties of sands with varying degrees of saturation. The damping ratio of the unsaturated sand increases 270 % in torsional mode and 74 % in axial mode with a 133 % increase in d_{10}. This makes sense, since larger grains provide a larger contact area, thus more friction is created which adds to the energy dissipated due to material damping. In general, damping is minimal at the partially saturated and saturated conditions and much higher in the dry condition. This also makes sense since less friction at the contacts is occurring in the partially saturated conditions (i.e. water allows grains to slide easier). The damping ratio at dry condition is 243 % more than in the partially saturated condition in torsional mode and 37 % in axial mode for the Barco sand, and 1170 % more in torsional mode and 59 % in axial mode for the Indusmin sand.

The Poisson ratio is computed from the RC results for the first time in this study using the shear and longitudinal wave velocities. Although the compression velocity is not directly measured during these tests, it is assumed to equal the measured longitudinal velocity due to the constraint conditions of the specimen. For the dry and saturated conditions, the computed

values are within the range of a loose to medium-dense sand specimen; however, the values computed for the partially saturated condition in both sands are an order of magnitude lower and are quite close to the reported value for the mineral quartz. In general, the Poisson ratio increases for high strains; 7.4 % for the Barco sand and 6.3 % for the Indusmin sand.

Also for the first time in this study, the dynamic properties of the sands were measured as a function of frequency in both the axial and torsional modes using the NR method. In general, the NR results match well with the RC results, although there are some test results in this study where this is not the case, specifically in the axial mode. For most tests, the dynamic properties remain constant over the frequency range selected. These results for cohesion-less soils differ from some previous studies conducted on cohesive soils which exhibited large increases in damping at the resonant frequency. The solution method for determining the complex moduli is highly sensitive to the phase information measured during experimentation. The presence of other modes of vibration during testing (i.e. flexural mode) also affects the accuracy of the results. Thus, great care must be taken to select an appropriate frequency range which avoids interference from other modes of vibration.

A number of resonant method results show very large normalization factors (specifically specimen 6 and 7). A possible explanation for these results is that all saturated specimens (3, 4, 6 and 7) are only kept under partially-saturated conditions because of the air leak. Thus, the effective stress is reduced to a degree which cannot be determined. This decrease in effective stress explains why for most saturated specimens the transfer functions show a reduction in the normalization factor (H_0) in excess to what is expected due to the increased inertia of the specimen. As noted in Section 4.2, the setting for the signal analyzer and power amplifier gain were the same for all tests (250 *mV* peak-to-peak and 25) except the low-strain RC tests on specimens 6 and 7. Given that the excitation is constant the changes in resonant frequencies as shown in Figs. 5.15 and 5.21 justify the hypothesis of the reduction in effective stresses because of the air-leak in partially saturated specimens.

7.0 RECOMMENDATIONS

More study is required before this technique can be applied in situ. However, quantity is not so important as quality. Future study must be able to characterize the dynamic properties of the soil specimen and NAPL droplets, in addition to quantifying the observed increase in flow. Therefore, the main recommendation of this study is the design of equipment which is capable of not only measuring the response of a soil specimen to dynamic stimuli, but is also capable of accurately measuring flow through the specimen. The optimal design will probably be based on the design of the resonant column. However, effort must be made to ensure the device does not impede flow through the matrix, and it is recommended that all flow connections be located on the exterior of the confinement chamber to minimize the potential for gas leaks into the specimen. Thought should be put into the type of NAPL to be utilized and the degree of sorption to organics. Membranes and plastic tubing should be selected to minimize NAPL loss due to sorption.

REFERENCES

Aarts, A, and Ooms, G, et al, 1999, "Enhancement of Liquid Flow Through a Porous Medium by Ultrasonic Radiation," Society of Petroleum Engineers Journal, vol. 4, pp. 321-327.

Alvarellos, J., 2003, "Fundamental Studies of Capillary Forces in Porous Media," Unpublished Doctoral thesis, Department of Civil Engineering, Georgia Institute of Technology, Atlanta, GA.

ASTM Standard D4015-92, 2000, "Standard Test Methods for Modulus and Damping of Soils by the Resonant-Column Method," *Annual Book of Standards*, ASTM International, West Conshohocken, PA.

Barker, J., 2005, "Organic Contaminants: Sources, Migration and Fate – Processes and Remediation," *Lecture notes in Earth Sciences*, Department of Earth Sciences, University of Waterloo, Waterloo, ON.

Beresnev, I., 2006, "Theory of Vibratory Mobilization on Nonwetting Fluids Entrapped in Pore Constrictions," Geophysics, vol. 71, pp. N47-N56.

Beresnev, I., and Iassonov, I., 2003, "A Model for Enhanced Fluid Percolation in Porous Media by Application of Low-Frequency Elastic Waves," Journal of Geophysical Research, vol. 108, pp. 2138-2146.

Beresnev, I., and Johnson, P., 1994, "Elastic-wave Stimulation of Oil Production: A Review of Methods and Results," Geophysics, vol. 59, pp. 1000-1017.

Bernadiner, M., 2004, "A Capillary Microstructure of the Wetting Front," Transport in Porous Media, vol. 30, pp. 251-265.

Biot, M. A., 1956, "Theory of Propagation of Elastic Waves in a Fluid-Saturated Porous Solid, Low-Frequency Range," Journal of the Acoustical Society of America, vol. 28, pp. 168-178.

Bisshopp, K., 1959, "Forced Torsional Vibration of Systems with Distributed Mass and Internal and External Damping," Journal of Applied Mechanics, ASME, part 3, pp. 8-12.

Bolton, M., and Wilson, J., 1990, "Soil Stiffness and Damping," 1st European Conference on Structural Dynamics, Rotterdam, DE, Proceedings, Krätzig et al eds., Balkema, pp. 209-216.

Carlin, B., 1960, 2nd Ed., "Ultrasonics," McGraw-Hill Book Company, Inc., Toronto, ON, pp: 309.

Cascante, G., Vanderkooy, J., and Chung, W., 2005, "A new mathematical model for resonant-column measurements including eddy-current effects," Canadian Geotechnical Journal, vol. 42, pp. 121-135.

Chrysikopoulos, C., and Vogler, E., 2002, "Application of Acoustic Pressure Waves in Aquifer Remediation and Mobilization of Entrapped Organic Liquids," Technical Completion Report, Project Number UCAL-WRC-W-938, Department of Civil and Environmental Engineering, University of California, Irvine, CA, pp: 26.

Craig, R., 2002, 6th Ed., "Soil Mechanics," Spon Press, New York, NY, pp: 485.

Cooper, H., Bredehoeft, J., Papadopoulos, I., and Bennett, R., 1965, "The Response of Well-Aquifer Systems to Seismic Waves," Journal of Geophysical Research, vol. 70, pp. 3915-3926.

Das, D., Mirzaei, M., Widdows, N., 2006, "Non-Uniqueness in Capillary Pressure-Saturation-Relative Permeability Relationships for Two-Phase Flow in Porous Media: Interplay between Intensity and Distribution of Random Micro-Heterogeneities," Chemical Engineering Science, vol. 61, pp. 6786-6803.

Duhon, R., 1964, "An Investigation of the Effect of Ultrasonic Energy on the Flow of Fluids in Porous Media," Unpublished Doctoral thesis, Faculty of Engineering, University of Oklahoma, Norman, OK.

Dullien, F., 1979, "Porous Media: Fluid Transport and Pore Structure," Academic Press, Toronto, ON, pp: 396.

Dusseault, M., 2007, "Pressure Pulse Flow Enhancement, A New Concept: Mechanics and Micromechanisms," *Lecture notes in Earth Sciences*, Department of Earth Sciences, University of Waterloo, Waterloo, ON

Dusseault, M., et al, 2002, "Field Applications of Pressure Pulsing in Porous Media," 2nd Biot Conference on Poromechanics, Grenoble, FR, Proceedings, pp. 639-646.

Ellis, E. A., et al, 2000, "Resonant Column Testing of Sands with Different Viscosity Pore Fluids," Journal of Geotechnical and Geoenvironmental Engineering, vol. 126, pp. 10-17.

Fleeger, G., et al, 1999, "Hydrologic Effects of the Pymatuning Earthquake of September 25, 1998, in Northwestern Pennsylvania," US Geological Survey Water-Resources Investigations Report 99-4170, pp: 8.

Gajo, A., Fedel, A., and Mongiovì, L., 1996, "Experimental analysis of the effects of fluid-solid coupling on the velocity of elastic waves in a saturated porous media," Géotechnique, vol. 47, pp. 993-1008.

Gercek, H., 2007, “Poisson’s ratio values for rocks,” International Journal of Rock Mechanics and Mining Sciences, vol. 44, pp. 1-13.

Hardin, B., 1965, “The Nature of Damping in Sands,” Journal of the Soil Mechanics and Foundations Division, ASCE, vol. 91, pp. 63-97.

Hilpert, M., Jirka, G., and Plate, E., 2000, “Capillarity-Induced Resonance of Oil Blobs in Capillary Tubes and Porous Media,” Geophysics, vol. 65, pp. 874-883.

Ishibashi, I., and Zhang, X., 1993, “Unified Dynamic Shear Moduli and Damping Ratios of Sand and Clay,” Soils and Foundations, vol. 33, pp. 182-191.

Kaluarachchi, J., and Parker, J., 1992, “Multi-Phase Flow with a Simplified Model for Oil Entrapment,” Transport in Porous Media, vol. 7, pp. 1-14.

Khan, Z., Cascante, G., and El-Naggar, M. H., 2007a, “Micromechanical Evaluation of Damping in Sand with High Viscosity Pore Mixture.” (In press).

Khan, Z., Cascante, G., El-Naggar, M. H., and Lai, C., 2007, “Measurement of Frequency Dependent Dynamic Properties of Soils Using the Resonant Column Device.” (In press).

Kramer, S., 1996, “Geotechnical Earthquake Engineering,” Prentice-Hall Inc., Upper Saddle River, NJ, pp: 653.

Lai, C., et al, 2001, “Low-strain stiffness and material damping ratio coupling in soils,” Advanced Laboratory Stress-strain Testing of Geomaterials, Tatsuoka, T., Shibuya, S., and Kuwano, R., eds, Balkema, Lisse, pp. 265-274.

Manga, M., 2001, “Origin of Postseismic Streamflow Changes Inferred from Baseflow Recession and Magnitude-Distance Relations,” Geophysical Research Letters, vol. 28, pp. 2133-2136.

Melrose, J., and Brandner, C., 1974, “Role of Capillary Forces in Determining Microscopic Displacement Efficiency for Oil Recovery by Waterflooding,” Journal of Canadian Petroleum Technology, vol. 13, pp. 54-62.

Monroe, J., and Wicander, R., 2005, “Physical Geology: Exploring the Earth,” 5th ed., Brooks/Cole – Thomson Learning, Toronto, ON, pp.: 644.

Odeh, A., 1987, “Mathematical Modeling of the Behaviour of Hydrocarbon Reservoirs – The Present and the Future,” Advances in Transport Phenomena in Porous Media, Bear, J., and Corapcioglu, M., eds, NATO Advanced Study Institute on Fundamentals of Transport Phenomena in Porous Media, Series E, no. 128, pp. 821-848.

Petrakis, E., and Dobry, R., 1987, "Micromechanical Modeling of Granular Soil at Small Strain by Arrays of Elastic Spheres," Department of Civil Engineering, Rensselaer Polytechnic Institute, Troy, NY, pp.: 300.

Rix, G., and Meng, J., 2005, "A Non-Resonance Method for Measuring Dynamic Soil Properties," Geotechnical Testing Journal, vol. 28, pp. 1-8.

Roberts, P., et al, 2001, "Enhanced DNAPL Transport in a Sand Core During Dynamic Stress Stimulation," Environmental Engineering Science, vol. 18, pp. 67-79.

Schwartz, F., and Zhang, H., 2003, "Fundamentals of Groundwater," John Wiley & Sons, Inc., New York, NY, pp: 583.

Skinner, A., 1969, "A Note on the Influence of Interparticle Friction on a Shearing Strength of a Random Assembly of Spherical Particles". Géotechnique, vol. 19, pp. 150-157.

Sneed, M., et al, 2003, "Earthquakes – Rattling the Earth's Plumbing System," US Geological Survey Fact Sheet 096-03, pp: 4.

Structural Behaviour Engineering Laboratories (SBEL), Inc., 1982, "Stokoe Torsional Shear Resonant Column Device," Phoenix, AZ.

Thomson, N., 2006, "Contaminant Transport," *Lecture notes in Environmental Engineering*, Department of Civil and Environmental Engineering, University of Waterloo, Waterloo, ON.

Timlin, D., Ahuja, L., Pachepsky, Y., Williams, R., Gimenez, D., and Rawls, W., 1999, "Use of Brooks-Corey Parameters to Improve Estimates of Saturated Conductivity from Effective Porosity," Soil Science Society of America Journal, vol. 63, pp. 1086-1092.

Vennard, J., and Street, R., 1976, "Elementary Fluid Mechanics," 5th Ed., John Wiley and Sons, Inc., Toronto, ON, pp: 740.

Vorhis, R., 1967, "Hydrologic Effects of the Earthquake of March 27, 1964, Outside Alaska," US Geological Survey Professional Paper 544-C, pp: 136.

Vucetic, M., 1994, "Cyclic Threshold Shear Strains in Soils," Journal of Geotechnical Engineering, ASCE, vol. 120, pp. 29-46.

White, M., Oostrom, M., and Lenhard, R., 2004, "A Practical Model for Mobile, Residual and Entrapped NAPL in Water-Wet Porous Media," Ground Water, vol. 42, pp. 734-746.

Wilson, J., 1988, "A Theoretical and Experimental Investigation into the Dynamic Behaviour of Soils," Unpublished Doctoral Thesis, Department of Engineering, University of Cambridge, Cambridge, UK.

Wolfe, W., Haugh, C., Webbers, A., and Diehl, T., 1997, “Preliminary Conceptual Models of the Occurrence, Fate and Transport of Chlorinated Solvents in Karst Regions of Tennessee,” US Geological Survey, Water Resources Report 97-4097, pp: 88, available on-line at: http://pubs.usgs.gov/wri/wri974097/new4097.pdf.

APPENDIX A

Sand Grain Size Distributions

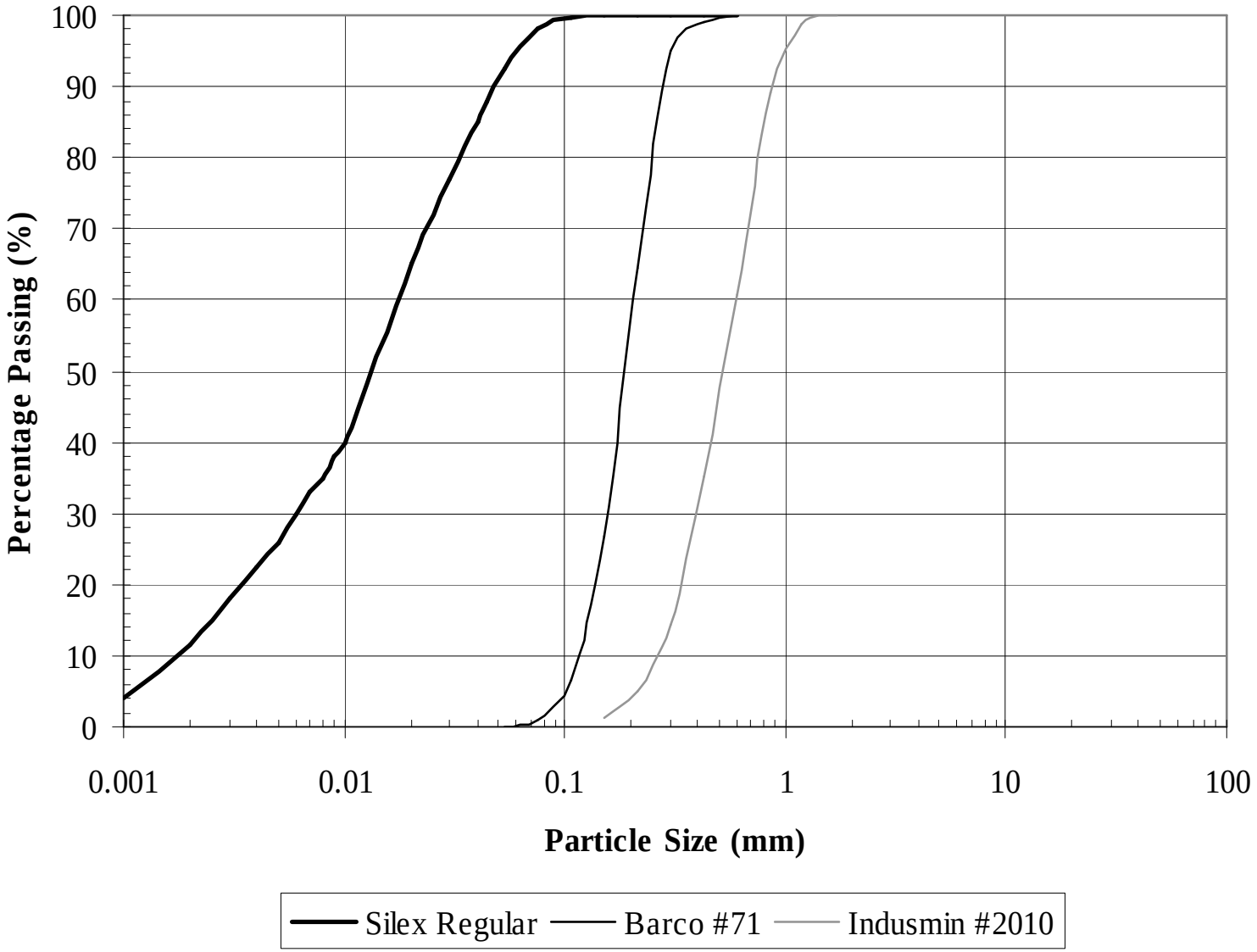

Figure A.1 – Grain size distributions

APPENDIX B

Computation of Driveplate I_0 and m_0

B.1 Resonant Column Calibration

In order to analyze RC experimental data for the NR method test, the moment of inertia I_0 of the drive plate and top cap must be known (in the case of torsional excitation) as well as the mass m_0 (in the case of axial excitation). This appendix documents the calibration procedure.

B.1.1 Estimation of I_0

To estimate the value of I_0 for the driving plate, the RC coils are set for torsional excitation. An aluminum probe (which theoretically has negligible damping) is fixed to the base and the drive plate. A standard RC test is performed to measure the resonant frequency ω_0 of two different diameter probes. For the small diameter probe, the resonant frequency is 55.9 *Hz* (Figure B.1).

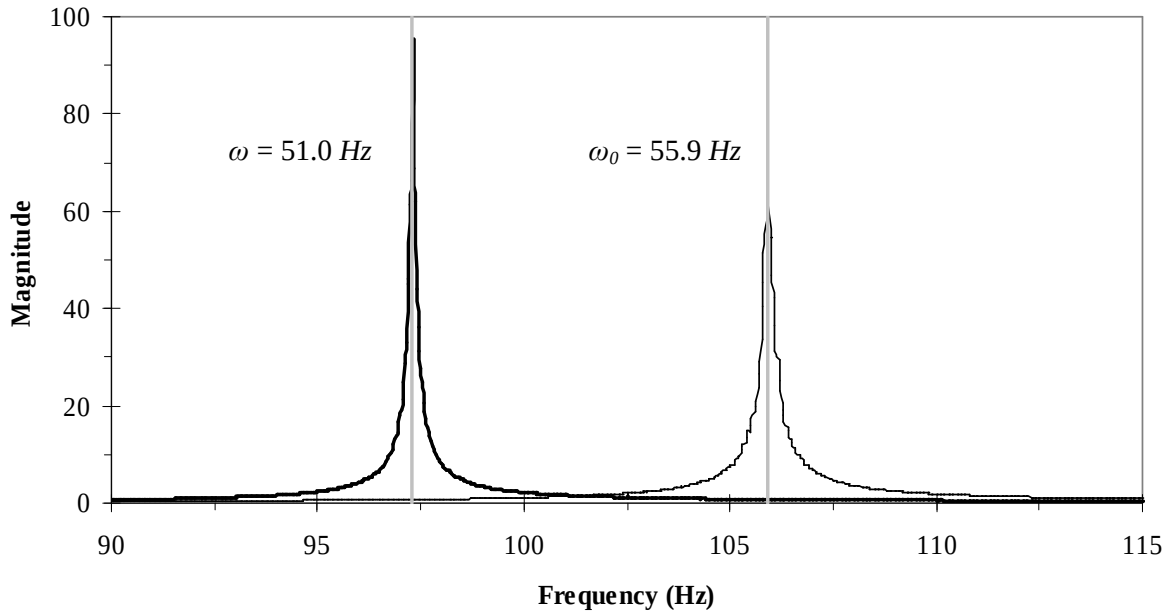

Figure B.1 - Response spectra of small diameter aluminum probe

Next, a steel plate of known moment of inertia $I_{plate} = 1.426 \times 10^{-3}\, kg \cdot m^2$ is fixed to the top of the drive plate. The RC test is repeated on the small diameter probe and a new resonant frequency ω = 51.0 *Hz* is measured (Figure B.1).

This procedure is repeated for a large diameter aluminum probe, with measured resonant frequencies of ω_0 = 105.9 *Hz* and ω = 97.3 *Hz* (Figure B.2).

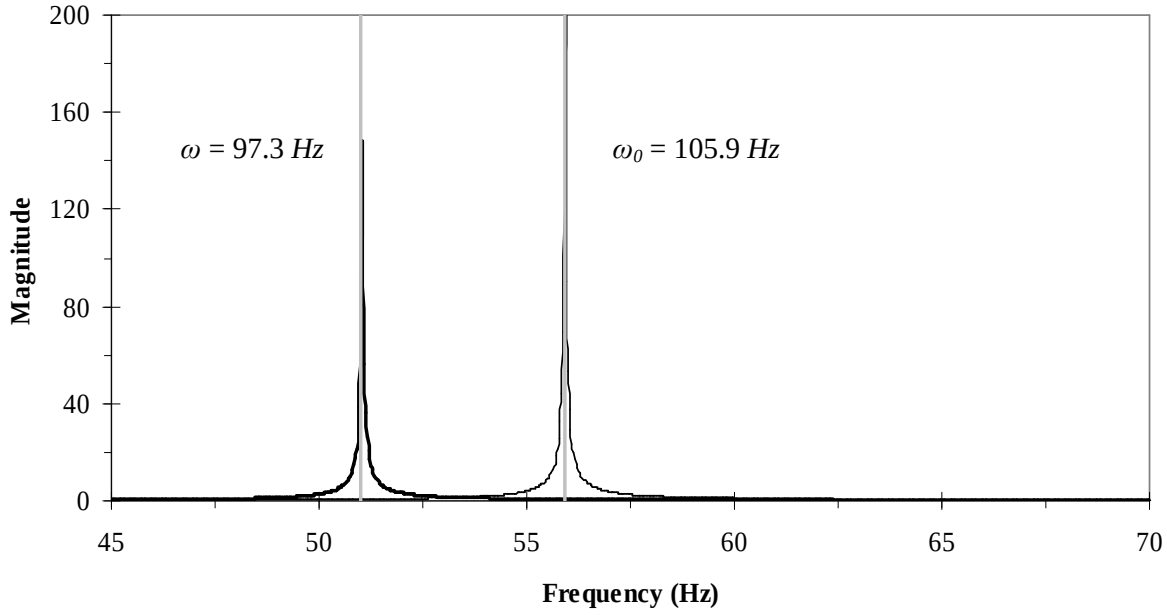

Figure B.2 - Response spectra of large diameter aluminum probe

The moment of inertia of each probe is less than 10% of the moment of inertia of the drive plate and top cap; therefore, the system is considered a simple SDOF system (i.e. a mass attached to a frictionless spring), for which ω_0 is determined using

$$\omega_0 = \sqrt{\frac{k}{I_{driveplate}}} \quad \text{.....[B.1]}$$

where k is the spring constant and $I_{driveplate}$ is the moment of inertia of the drive plate. When I_{plate} is added to the system, Equation [B.1] becomes

$$\omega = \sqrt{\frac{k}{I_{driveplate} + I_{plate}}} \quad \text{.....[B.2]}$$

If [B.1] and [B.2] are solved for *k* and equated, some manipulation gives

$$I_{driveplate} = \frac{I_{plate} \cdot \omega^2}{\omega_0^2 - \omega^2} \quad \text{.....[B.3]}$$

which is used to solve for $I_{driveplate}$. From the small diameter probe, $I_{driveplate} = 7.081 \times 10^{-3}$ *kg-m*^{2}, and from the large diameter probe, $I_{driveplate} = 7.725 \times 10^{-3}$ *kg-m*^{2}; these results are within 8% of each other. The value used in this study is taken as the average, or $I_{driveplate} = 7.403 \times 10^{-3}$ *kg-m*^{2}.

To complete the estimate of I_0, the moment of inertia of the top cap $I_{top\text{-}cap}$ must also be considered. Using AutoCAD, $I_{top\text{-}cap} = 4.383 \times 10^{-4}$ *kg-m*^{2}; therefore, $I_0 = 7.841 \times 10^{-3}$ *kg-m*^{2}. The moment of inertia of the top-cap does not include the case where the chamber between the porous disc and the top-cap is full of water (i.e. saturated conditions). When this chamber is full, there is an additional 0.05% moment of inertia added to I_0; thus, saturation conditions have negligible impact on the experimental results.

B.1.2 Estimation of m_0

To compute m_0, the driving plate and top cap are weighed using a scale. The mass of the driving plate $m_{driveplate} = 0.719$ *kg*, and the mass of the top cap $m_{top\text{-}cap} = 0.277$ *kg*; therefore $m_0 = 0.996$ *kg*.

APPENDIX C

Sample NR Method MathCAD Worksheet

C.1 NR Method, Torsional Mode (Specimen 2 Dry)

This MathCAD worksheet takes measured specimen characteristics as well as frequency, transfer function and phase measurements from an input text file to compute the complex modulus. The shear wave velocity and damping ratio versus frequency are output to a text file and imported to an Excel spreadsheet. The input text files are included in Appendix D.

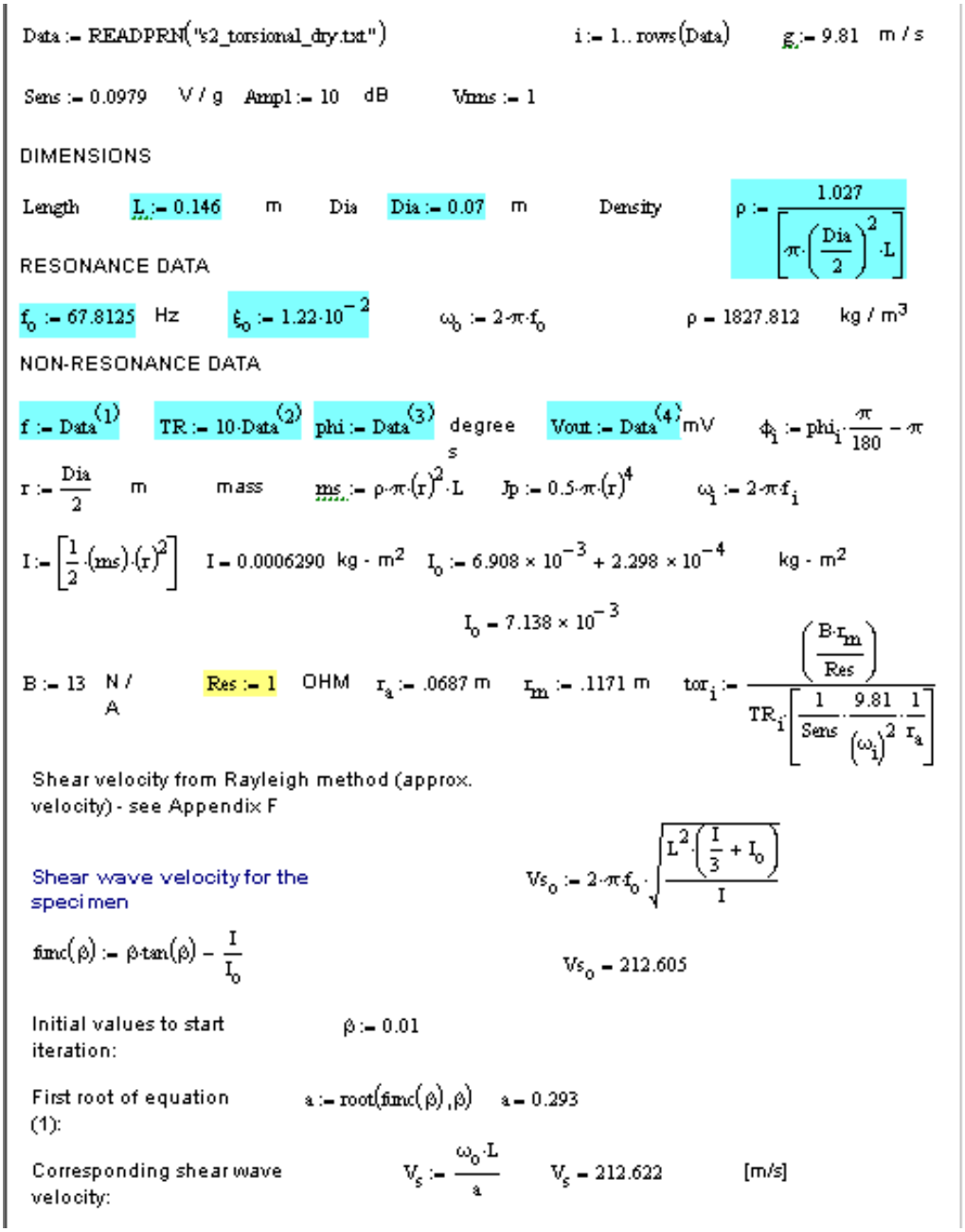

Initial guess value $GG := \rho \cdot V_s^2 \cdot (1 + 2 \cdot \xi_0 \cdot i)$

GG:

Given

$$0 = tor \cdot e^{-i \cdot \phi} - \left[\frac{\pi \cdot r^4}{2} \cdot \rho \cdot (\omega)^2 \cdot L \cdot \frac{1}{\sqrt{\frac{\rho \cdot (\omega)^2 \cdot L^2}{GG}} \cdot \tan\left[\sqrt{\frac{\rho \cdot (\omega)^2 \cdot L^2}{GG}} \right]} - (I_0) \cdot (\omega)^2 \right]$$

$SSE(tor, \omega, \phi) := Find(GG)$

Results =

$Gcmplx_i := SSE(tor_i, \omega_i, \phi_i)$ $\quad Vsr_i := \sqrt{\frac{Re(Gcmplx_i)}{\rho}}$ $\quad \xi_i := \frac{Im(Gcmplx_i)}{Re(Gcmplx_i) \cdot 2}$

Results from Resonant method:

$V_s = 212.622$ m / s $\quad G_0 := V_s^2 \cdot \rho$ $\quad G_0 \cdot 10^{-6} = 82.632$

Shear strains $\gamma_i := \frac{100 \cdot Vrms \cdot Dia \cdot g \cdot 0.707 \cdot \left(\frac{Vout_i}{1000} \right)}{\pi^2 \cdot 16 \cdot r_a \cdot Sens \cdot L \cdot (f_i)^2 \cdot 10^{\left(\frac{Ampl}{20} \right)}}$ $\quad \gamma =$

	1
1	$4.95045 \cdot 10^{-3}$
2	$4.95045 \cdot 10^{-3}$
3	$4.95045 \cdot 10^{-3}$
4	$4.94253 \cdot 10^{-3}$
5	$4.95045 \cdot 10^{-3}$
6	$4.94641 \cdot 10^{-3}$
7	$4.95045 \cdot 10^{-3}$
8	$4.948 \cdot 10^{-3}$
9	$4.95045 \cdot 10^{-3}$
10	$4.95045 \cdot 10^{-3}$
11	$4.95045 \cdot 10^{-3}$
12	$4.95045 \cdot 10^{-3}$
13	$4.95045 \cdot 10^{-3}$
14	$4.9477 \cdot 10^{-3}$
15	$4.94787 \cdot 10^{-3}$
16	...

%

$0^{(1)} := f$ $\quad 0^{(2)} := Vsr$ $\quad 0^{(3)} := \xi$ $\quad 0 := WRITEPRN("out\_s2\_torsional\_dry.txt", 0)$

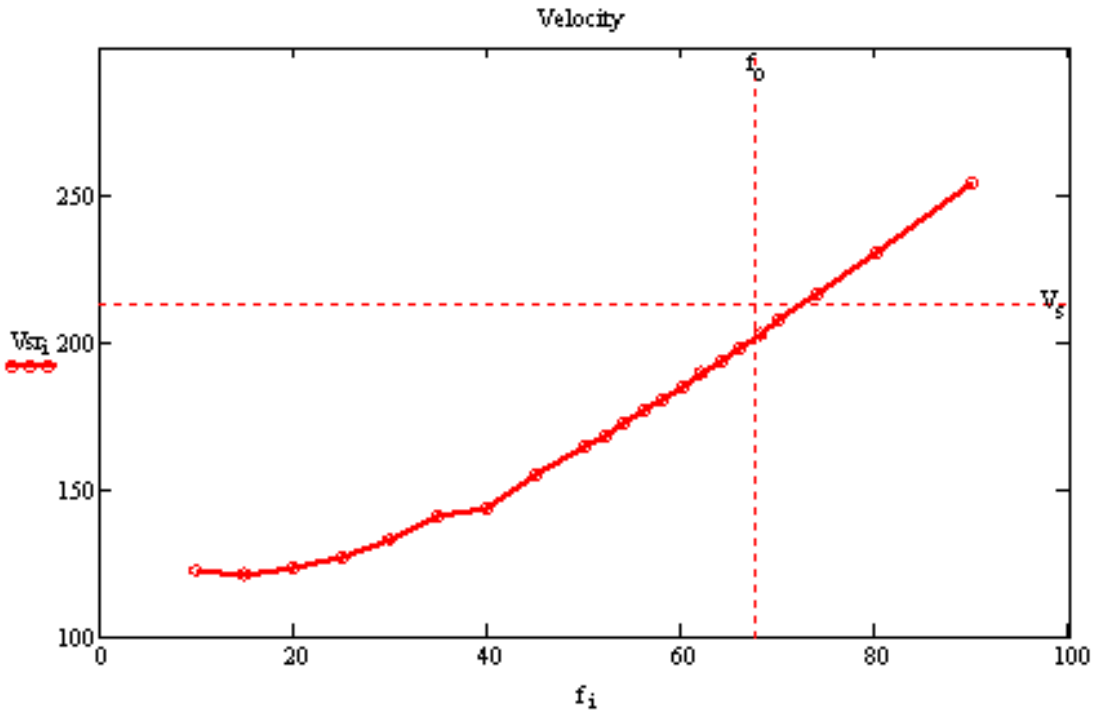
Velocity
f_o
250
200
150
100
V_s
Vsr_i
0
20
40
60
80
100
f_i

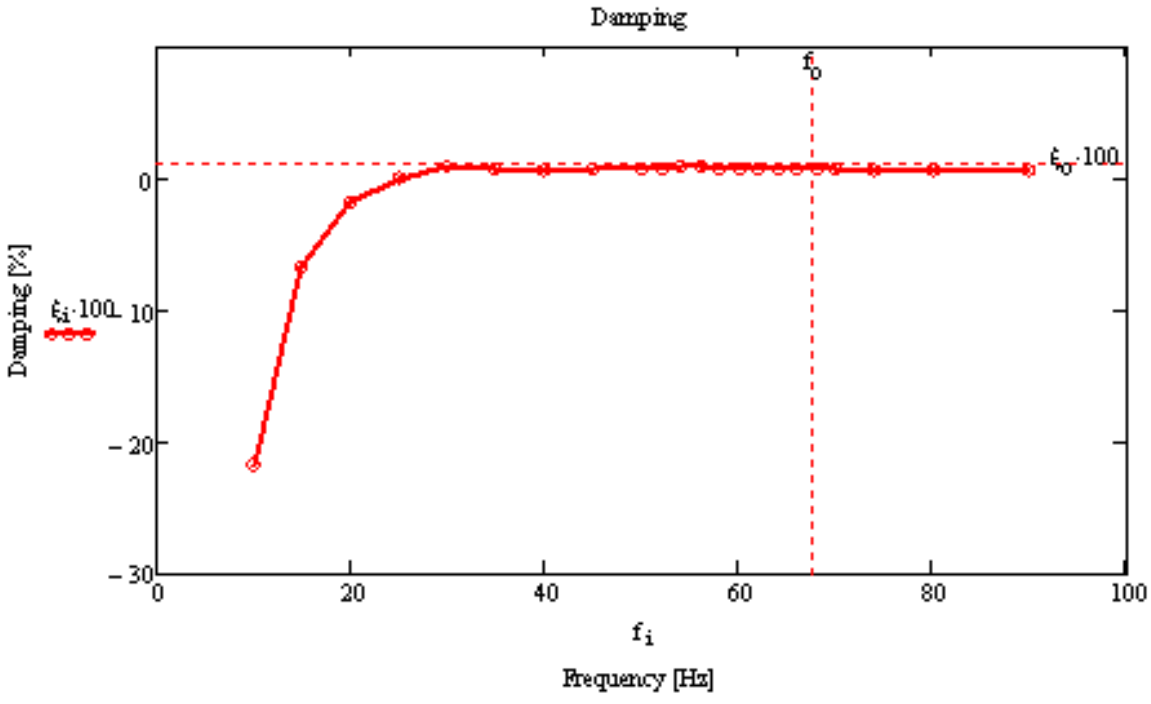
Damping
f_o
$\xi_o \cdot 100$
0
10
– 20
– 30
Damping [%]
$\xi_i \cdot 100$
0
20
40
60
80
100
f_i
Frequency [Hz]

C.2 NR Method, Axial Mode (Specimen 4 Unsaturated)

This MathCAD worksheet takes measured specimen characteristics as well as frequency, transfer function and phase measurements from an input text file to compute the complex modulus. The compression wave velocity and damping ratio versus frequency are output to a text file and imported to an Excel spreadsheet. The input text files are included in Appendix D.

Data := READPRN("s3_axial_dry.txt") i := 1.. rows(Data) g := 9.81 m / s

Sens := 0.4957 V / g Ampl := 10 dB Vrms := 1 ORIGIN := 1

DIMENSIONS

Length L := 0.147 m Dia Dia := 0.07 m Density $\rho := \frac{1.027}{\left[\pi \cdot \left(\frac{Dia}{2}\right)^2 \cdot L\right]}$

RESONANCE DATA

$f_0 := 376.18$ Hz $\xi_0 := 1.13 \cdot 10^{-2}$ $\omega_0 := 2 \cdot \pi \cdot f_0$ $\rho = 1815.378$ kg / m^3

NON-RESONANCE DATA

$f := Data^{(1)}$ $TR := 10 \cdot Data^{(2)}$ $phi := Data^{(3)}$ degree $Vout := Data^{(4)}$ mV $\phi_i := phi_i \cdot \frac{\pi}{180} - \pi$

s

$r := \frac{Dia}{2}$ m mass $ms := \rho \cdot \pi \cdot (r)^2 \cdot L$ $\omega_i := 2 \cdot \pi \cdot f_i$

$I := ((ms))$ $I = 1.0270000$ kg $I_0 := 0.966$ kg

B := 13. N / A Res := 1 OHM $tor_i := \frac{\left(\frac{B}{Res}\right)}{TR_i \cdot \left[\frac{1}{Sens} \cdot \frac{9.81}{(\omega_i)^2}\right]}$

Shear velocity from Rayleigh method (approx. velocity) - see Appendix F

Shear wave velocity for the specimen $VL_0 := 2\pi \cdot f_0 \cdot \sqrt{\frac{L^2 \cdot \left(\frac{I}{3} + I_0\right)}{I}}$

$fimc(\beta) := \beta \cdot \tan(\beta) - \frac{I}{I_0}$ $VL_0 = 392.163$ [m/s]

Initial values to start iteration: $\beta := 0.2$

First root of equation (1): $a := root(fimc(\beta), \beta)$ $a = 3.441$

Corresponding shear wave velocity: $V_L := \frac{\omega_0 \cdot L}{a}$ $V_L = 100.967$ [m/s]

Initial guess value GG: $GG := \rho \cdot V_L^{\,2} \cdot (1 + 2 \cdot \xi_0 \cdot i)$

Given

$$0 = tor \cdot e^{-i \cdot \phi} - \left[I \cdot (\omega)^2 \cdot \frac{1}{\sqrt{\frac{\rho \cdot (\omega)^2 \cdot L^2}{GG}} \cdot \tan\left[\sqrt{\frac{\rho \cdot (\omega)^2 \cdot L^2}{GG}}\right]} - (I_0) \cdot (\omega)^2 \right]$$

$SSE(tor, \omega, \phi) := Find(GG)$

Results =

$Gcmplx_i := SSE(tor_i, \omega_i, \phi_i)$ $\quad VLr_i := \sqrt{\frac{Re(Gcmplx_i)}{\rho}}$ $\quad \xi_i := \frac{Im(Gcmplx_i)}{Re(Gcmplx_i) \cdot 2}$

Results from Resonant method:

$V_L = 100.967$ m / s $\quad E_0 := V_L^{\,2} \cdot \rho$ $\quad E_0 \cdot 10^{-6} = 18$ $\quad 13$ %

Shear strains $\gamma_i := \frac{Vrms \cdot g \cdot 0.707 \cdot \left(\frac{Vout_i}{1000}\right)}{\pi^2 \cdot 8 \cdot Sens \cdot L \cdot (f_i)^2 \cdot 10^{\left(\frac{Ampl}{20}\right)}}$ $\quad \gamma =$

	1
1	$4.94724 \cdot 10^{-6}$
2	$4.95055 \cdot 10^{-6}$
3	$4.94752 \cdot 10^{-6}$
4	$4.94976 \cdot 10^{-6}$
5	$4.94977 \cdot 10^{-6}$
6	$4.94793 \cdot 10^{-6}$
7	$4.95041 \cdot 10^{-6}$
8	$4.9502 \cdot 10^{-6}$
9	$4.94819 \cdot 10^{-6}$
10	$4.95022 \cdot 10^{-6}$
11	$4.9492 \cdot 10^{-6}$
12	$4.94792 \cdot 10^{-6}$
13	$4.94906 \cdot 10^{-6}$
14	$4.9499 \cdot 10^{-6}$
15	$4.94784 \cdot 10^{-6}$
16	...

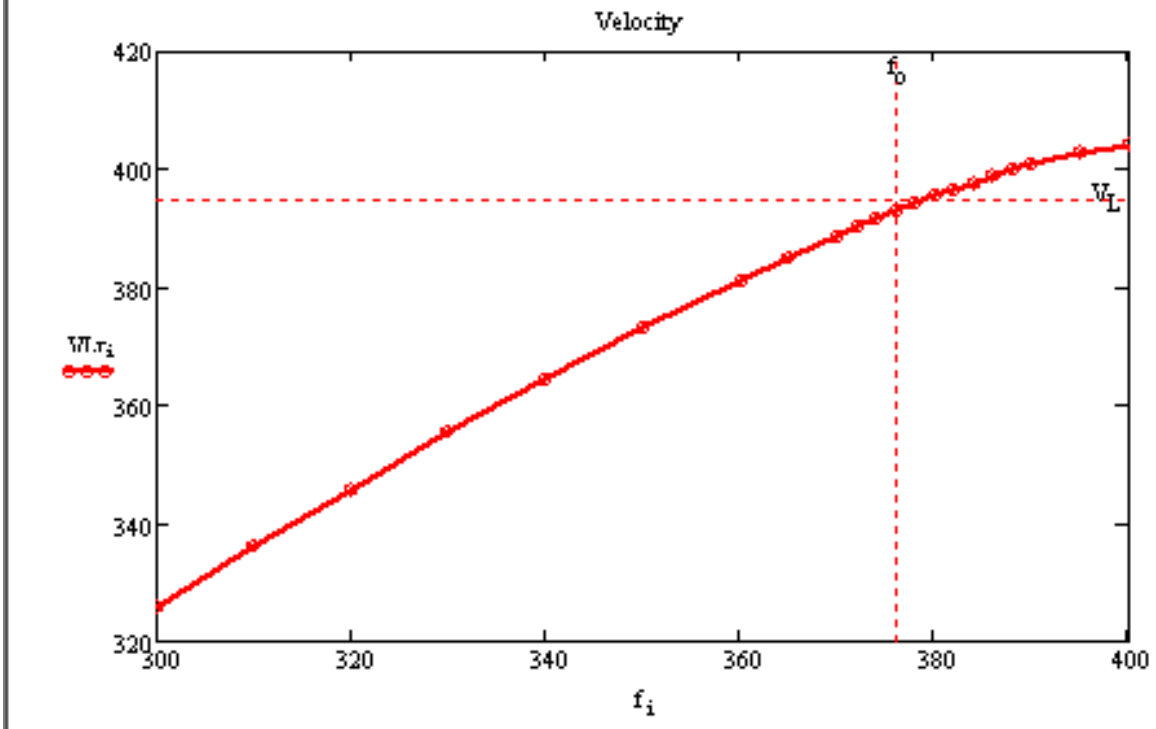
Velocity
420
400
380
360
340
320
300
320
340
360
380
400
f_o
V_L
$Vf.r_i$
f_i

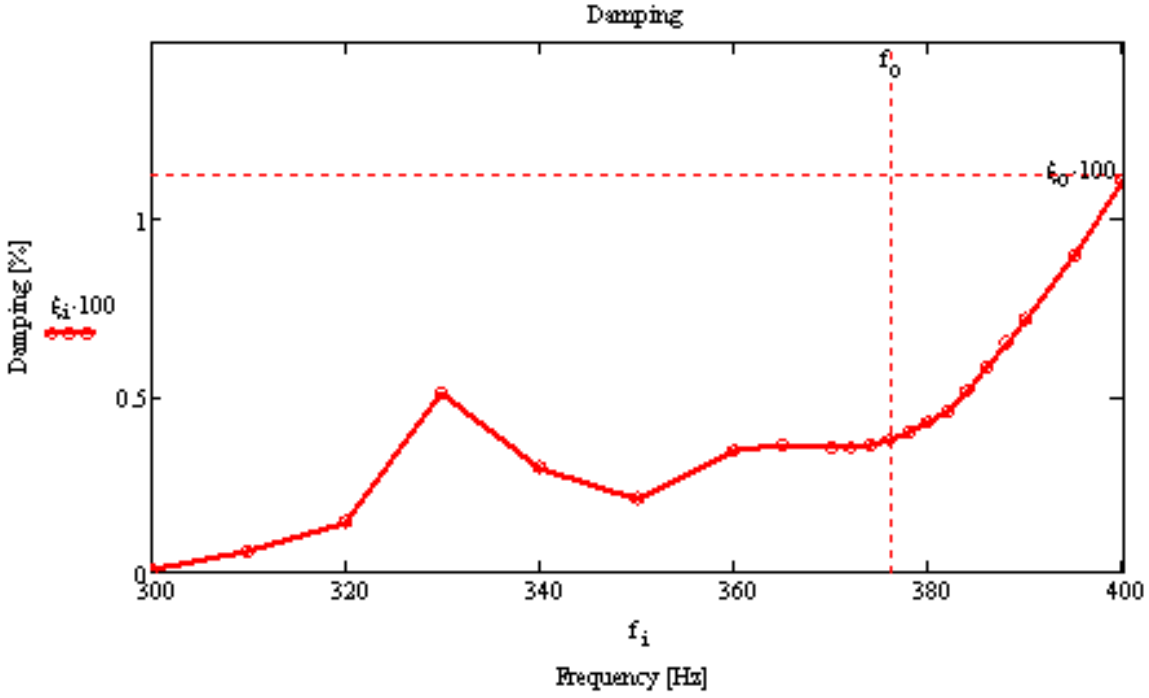
Damping
1
0.5
0
300
320
340
360
380
400
f_o
$\xi_o \cdot 100$
Damping [%]
$\xi_i \cdot 100$
f_i
Frequency [Hz]

APPENDIX D

Raw Data

D.1 NR Method Test Raw Data

The tables contained in this section provide the input data for the MathCAD worksheets given in Appendix C.

D.1.1 Specimen 2

Table D.1 - Specimen 2 partially saturated NR torsional raw data

Frequency **Hz**	**Transfer Function** **--**	**Phase** **deg.**	**$V_{pp,\ out}$** **mV**
10	0.0009	-155	5
15	0.0025	-171	11.25
20	0.005	-177	20
25	0.0088	180	31.2
30	0.0143	178	45
35	0.0219	178	61.2
40	0.0454	-176	80
45	0.0723	175	101.2
50	0.1358	171	125
52	0.2212	165	135.2
54	0.352	155	145.8
56	0.6823	128	156.8
58	0.6651	46.2	168.2
60	0.3801	24.7	179.9
62	0.2615	16	192.1
64	0.1992	11.2	204.7
66	0.1658	8.92	217.7
68	0.1428	7.25	231
70	0.1301	6.47	245
74	0.1087	4.86	274
80	0.0901	3.44	320
90	0.0743	2.54	405

D.1.2 Specimen 3

Table D.2 - Specimen 3 dry NR torsional raw data

Frequency Hz	Transfer Function --	Phase deg.	$V_{pp,\ out}$ mV
45	0.65	179.1	945
50	0.968	177.4	1167
55	1.803	175.5	1412
60	5.035	169.5	1680
65	16	28.73	1972
70	3.779	5.294	2287
75	2.37	2.866	2626
80	1.825	1.799	2988
85	1.542	1.309	3373
90	1.381	1.068	3781
95	1.257	0.678	4213
100	1.162	0.425	4668

Table D.3 - Specimen 3 dry NR axial raw data

Frequency Hz	Transfer Function --	Phase deg.	$V_{pp,\ out}$ mV
300	0.739	179.9	1168
310	0.794	178.9	1248
320	0.89	177	1329
330	0.989	168.4	1414
340	1.22	171.7	1501
350	1.643	172.2	1590
360	3	156.2	1683
365	4.569	141	1730
370	7.33	101.3	1777
372	7.22	74.9	1797
374	5.823	52.68	1816
376	4.405	38.52	1835
378	3.406	30.48	1855
380	2.71	25.44	1875
382	2.211	22.27	1894
384	1.834	20.47	1914
386	1.561	19.46	1934
388	1.35	18.85	1954
390	1.19	18.17	1975
395	0.894	16.8	2026
400	0.69	15.72	2077

Table D.4 - Specimen 3 partially saturated NR torsional raw data

Frequency	**Transfer Function**	**Phase**	$\mathbf{V_{pp,\ out}}$
Hz	**--**	**deg.**	**mV**
40	0.833	175	1697
44	1.331	171.1	2054
46	1.832	167.6	2245
48	2.061	165.7	2444
50	2.959	160.8	2652
52	5.174	148.8	2869
54	10.03	108	3094
56	9.507	65.26	3327
58	5.92	31.4	3569
60	4.205	20.92	3819
62	3.32	15.32	4078
64	2.705	11.64	4346
66	2.425	10.76	4621
68	2.076	7.965	4906
70	1.884	7.122	5199
75	1.562	4.989	5968
80	1.364	3.836	6790
85	1.229	3.275	7665
90	1.164	3.68	8593

Table D.5 - Specimen 3 partially saturated NR axial raw data

Frequency	**Transfer Function**	**Phase**	$\mathbf{V_{pp,\ out}}$
Hz	**--**	**deg.**	**mV**
300	0.808	173.8	501
310	0.9	172.3	535
320	1.062	169.3	570
330	1.324	160	606
340	1.558	152.9	643
350	2.118	148.9	682
355	3.032	134.6	701
360	3.878	106.6	721
362	3.997	92.3	729
364	3.85	77.2	737
366	3.486	63.3	745
368	3.023	52.2	754
370	2.606	44	762
375	1.81	30.6	782
380	1.317	23.7	803
390	0.821	18.6	846
400	0.547	14.7	890

D.1.3 Specimen 4

Table D.6 - Specimen 4 dry NR torsional raw data

Frequency **Hz**	**Transfer Function** **--**	**Phase** **deg.**	**$V_{pp,\ out}$** **mV**
35	0.418	176.7	856
40	0.859	-179.8	1118
42	1.077	176.7	1233
44	1.405	175.5	1353
46	1.404	174.3	1479
48	2.742	172.2	1610
50	4.39	167.7	1747
52	9.838	153.6	1890
54	20.21	57.81	2038
56	7.489	15.91	2192
58	4.646	9.298	2351
60	3.411	6.147	2516
65	2.205	3.249	2953
70	1.723	2.129	3425
75	1.463	1.384	3932
80	1.302	0.907	4473
85	1.194	0.617	5050
90	1.125	1.069	5662

Table D.7 - Specimen 4 dry NR axial raw data

Frequency	**Transfer Function**	**Phase**	$\mathbf{V_{pp,\ out}}$
Hz	**--**	**deg.**	**mV**
300	1.102	178.1	1624
310	1.317	177.2	1734
320	1.641	173.1	1847
330	2.417	171.4	1965
335	3.429	166.3	2025
340	5.849	149.6	2086
342	7.618	134	2110
344	7.61	106.3	2135
346	8.89	101.1	2160
348	9.157	67.8	2185
350	6.825	44.2	2210
355	3.548	22.1	2274
360	2.137	14.7	2338
370	0.975	8.8	2470

Table D.8 - Specimen 4 partially saturated NR torsional raw data

Frequency	**Transfer Function**	**Phase**	$\mathbf{V_{pp,\ out}}$
Hz	**--**	**deg.**	**mV**
35	0.515	179.8	1300
40	1.148	173.3	1697
42	1.693	171.1	1871
44	2.52	167.9	2054
46	4.232	160.9	2245
48	8.237	140.3	2444
50	13.57	65.31	2652
52	6.247	21.03	2869
54	4.04	12.37	3094
56	3.045	8.632	3327
58	2.541	6.909	3569
60	2.159	5.194	3819
65	1.68	3.391	4482
70	1.421	2.272	5199
75	1.265	1.67	5968
80	1.161	1.3	6790

Table D.9 - Specimen 4 partially saturated NR axial raw data

Frequency	**Transfer Function**	**Phase**	$\mathbf{V_{pp,\ out}}$
Hz	**--**	**deg.**	**mV**
300	1.738	170.7	1624
305	2.094	167.4	1678
310	2.562	162	1734
315	3.245	151.7	1790
320	4.191	135.4	1847
322	4.656	124.2	1871
324	4.894	114.3	1894
326	5.218	103	1917
328	5.31	87	1941
330	4.751	71.6	1965
332	4.107	60.6	1989
334	3.583	52.1	2013
336	3.096	45.9	2037
338	2.731	40.5	2061
340	2.292	33.9	2086
350	1.679	23.2	2210
360	0.916	13.1	2338

D.1.4 Specimen 5

Table D.10 - Specimen 5 dry NR torsional raw data

Frequency **Hz**	**Transfer Function** **--**	**Phase** **deg.**	**$V_{pp,\ out}$** **mV**
20	0.38	177.2	386
24	0.697	176.6	555
26	0.968	176.2	652
28	1.41	175.1	756
30	2.294	173.2	868
32	4.563	167.1	987
34	18.31	128.2	1114
36	8.344	17.4	1249
38	4.2	7.33	1392
40	2.931	4.371	1542
45	1.821	1.924	1952
50	1.426	1.123	2410
55	1.232	0.676	2916
60	1.111	0.405	3470
65	1.032	0.279	4072
70	0.979	0.119	4723

Table D.11 - Specimen 5 partially saturated NR torsional raw data

Frequency	**Transfer Function**	**Phase**	$\mathbf{V_{pp,\ out}}$
Hz	**--**	**deg.**	**mV**
110	0.197	179.9	1149
120	0.339	180	1368
130	0.711	174.6	1605
140	0.651	179.5	1862
150	0.599	155.9	2137
160	0.851	-154	2432
170	1.796	175.7	2745
175	2.069	167.8	2909
180	2.685	163.6	3078
182	3.082	161.5	3147
184	3.535	158.4	3216
186	4.385	154	3287
188	5.442	148.2	3358
190	6.88	135.1	3429
192	9.413	116.2	3502
194	10.42	90.5	3575
196	9.563	63.72	3649
198	7.579	44.47	3724
200	5.873	32.99	3800
205	3.665	19.21	3992
210	2.602	12.91	4189
220	1.556	10.26	4598
230	1.133	11.13	5025

Table D.12 - Specimen 6 saturated NR torsional raw data

Frequency	**Transfer Function**	**Phase**	**$V_{pp,\ out}$**
Hz	**--**	**deg.**	**mV**
25	0.154	178	386
35	0.393	177	757
45	1.05	176	1251
50	2.126	173	1544
52	3.343	171	1670
54	6.262	163	1801
56	19.64	126	1937
58	11.05	23.7	2077
60	5.649	10.9	2223
62	3.893	6.9	2374
64	3.102	5.2	2529
66	2.602	4.2	2690
68	2.244	3.3	2856
70	2.034	3	3026
80	1.422	1.3	3952
90	1.182	0.8	5002
100	1.065	0.4	6176

Table D.13 - Specimen 6 saturated NR axial raw data

Frequency Hz	Transfer Function --	Phase deg.	$V_{pp,\ out}$ mV
325	0.13	179	22
335	0.147	178.4	24
345	0.082	177	25
355	0.31	175	27
365	0.892	171.9	28
367	0.968	154.5	28
369	0.918	129.8	29
371	0.881	118.8	29
373	0.833	110.4	29
375	0.833	103.3	30
377	0.879	95.4	30
379	0.927	83.6	30
381	0.925	69.5	31
383	0.877	58.8	31
385	0.879	47.6	31
395	0.388	14.6	33
405	0.185	12.4	35
415	0.118	8.2	36
425	0.115	1.9	38

Table D.14 - Specimen 6 partially saturated NR torsional raw data

Frequency	**Transfer Function**	**Phase**	$\mathbf{V_{pp,\ out}}$
Hz	**--**	**deg.**	**mV**
35	0.138	179	7
45	0.268	179	11
55	0.583	177	16
65	0.857	179	22
70	1.262	179	26
72	1.494	178	28
74	1.79	178	29
76	2.189	178	31
78	2.746	178	32
80	3.631	177	34
82	5.114	176	36
84	8.27	174	38
86	19.59	168	39
88	56.04	34.7	41
90	13.35	7.1	43
92	7.674	3.8	45
94	5.437	2.7	47
100	3.089	1.4	53
110	1.989	0.3	64
120	1.558	0	77
130	1.312	-0.1	90

Table D.15 - Specimen 6 partially saturated NR axial raw data

Frequency	**Transfer Function**	**Phase**	$\mathbf{V_{pp,\ out}}$
Hz	**--**	**deg.**	**mV**
330	0.047	179	25
340	0.055	179	27
350	0.118	179	27
360	0.162	178	30
370	0.421	178	32
375	0.824	178	32
380	1.706	177.5	33
382	2.117	177	34
384	2.784	176	34
386	3.544	175	34
388	3.761	174	35
390	3.872	170	35
392	4.255	166	35
394	5.048	139	36
396	5.157	98.4	36
398	3.476	62.8	36
400	2.162	44.7	37
410	0.644	24.4	39
420	0.354	7.7	41
430	0.219	0.7	43

Table D.16 - Specimen 7 saturated NR torsional raw data

Frequency **Hz**	**Transfer Function** **--**	**Phase** **deg.**	**$V_{pp,\ out}$** **mV**
25	0.12	179	305
35	0.295	178	598
45	0.916	177	989
55	1.835	175	1477
60	4.437	169	1758
62	24.58	130	1877
64	10.54	16	2000
66	5.343	7.4	2127
68	3.764	4.9	2258
70	2.966	3.5	2393
76	2.008	1.9	2821
80	1.674	1.3	3125
90	1.328	0.7	3956
100	1.148	0.4	4883

Table D.17 - Specimen 7 saturated NR axial raw data

Frequency	**Transfer Function**	**Phase**	$\mathbf{V_{pp,\ out}}$
Hz	**--**	**deg.**	**mV**
380	0.517	174.5	943
390	0.612	179	993
400	0.763	179	1045
410	1.474	168.1	1098
415	1.848	163.7	1124
420	3.004	154.7	1152
422	3.948	145.3	1163
424	5.444	125.6	1174
426	6.292	91.5	1185
428	5.088	60	1196
430	3.645	42	1207
432	2.711	32	1218
434	2.12	26	1230
436	1.719	22	1241
438	1.42	19	1253
440	1.198	17	1264
450	0.631	12	1322

Table D.18 - Specimen 7 partially saturated NR torsional raw data

Frequency	**Transfer Function**	**Phase**	$\mathbf{V_{pp,\ out}}$
Hz	**--**	**deg.**	**mV**
50	0.236	179	10
60	0.401	181	14
70	0.51	178	19
80	1.1	179	25
85	1.581	179	28
90	2.476	179	32
92	3.069	178	33
94	4.002	178	34
96	5.492	177	36
98	8.637	176	37
100	17.93	174	39
102	158.8	73.1	41
104	18.26	6.7	42
106	9.56	3.1	44
108	6.58	1.9	45
110	5.066	1.7	47
120	2.484	0.7	56
130	1.858	-0.1	66
140	1.527	-0.3	76
150	1.336	-0.4	88

Table D.19 - Specimen 7 partially saturated NR axial raw data

Frequency Hz	Transfer Function --	Phase deg.	$V_{pp,\ out}$ mV
400	0.396	179	32
410	0.655	178	33
420	0.877	177	35
430	0.933	174	37
435	1.198	173.4	38
440	1.676	168.1	38
442	1.985	164.1	39
444	2.471	158.5	39
446	3.305	148	40
448	4.542	126.9	40
450	5.287	97.1	40
452	4.3	61	41
454	3.075	42	41
456	2.178	32	41
458	1.646	26	42
460	1.327	23	42
470	0.644	13	44
480	0.356	8	46
490	0.268	7	48
500	0.15	6	50

D.2 Flow Test Raw Data

The tables contained in this section provide the raw data for the measured time interval and computed hydraulic conductivity plots contained in Section 5 of this thesis.

D.2.1 Specimen 1

Table D.20 - Specimen 1 flow test raw data

Series	**1**	**2**	**3**	**4**	**5**	**6**	**7**	**8**	**9**	**10**	**11**
Trial	17-Jan-08	18-Jan-08	21-Jan-08	21-Jan-08	21-Jan-08	22-Jan-08	22-Jan-08	22-Jan-08	24-Jan-08	24-Jan-08	28-Jan-08
1	35.13	40.20	59.02	82.52	51.67	25.04	41.70	54.32	40.92	39.96	35.93
2	33.29	43.15	61.94	91.75	94.31	35.30	39.84	60.34	42.59	44.81	34.80
3	31.05	51.29	61.93	52.61	90.57	41.50	41.81	40.10	34.14	48.87	35.06
4	32.84	40.72	48.41	82.25	91.32	30.71	32.83	47.52	36.58	61.01	35.88
5	32.14	53.38	59.63	90.03	65.08	44.44	41.71	64.02	41.49	35.72	35.29
6	29.09	44.82	62.75	56.34	106.88	41.18	56.68	50.32	41.39	55.32	36.41
7	32.61	36.38	62.48	90.26	99.75	46.81	51.66	40.43	42.34	50.09	36.66
8	32.20	55.20	51.40	57.70	105.72	55.00	43.27	56.32	45.64	51.70	36.57
9	29.51	53.62	63.57	85.17	97.86	39.06	53.52	71.19	39.84	60.02	37.34
10	34.16	42.68	69.07	90.42	106.22	38.03	54.49	73.21	46.65	44.30	38.06
11	37.77	57.84	67.15	59.21	76.55	37.90	26.51	60.36	43.13	14.64	38.29
12	40.54	50.46	53.00	94.32	99.04	49.81	38.86	33.71	51.24	33.34	38.59
13	35.60	41.90	70.74	93.38	98.74	29.65	53.68	43.17	28.41	58.43	38.88
14	34.84	61.99	74.00	94.42	92.19	43.08	57.39	60.11	46.77	52.71	34.82
15	40.94	54.34	75.19	82.54	102.16	41.02	37.14	57.81	50.53	53.45	41.11
16	41.30	43.49	53.95	62.58	86.57	49.36	39.88	51.38	50.54	55.26	41.11
17	38.15	58.56	72.91	90.24	105.62	41.82	56.30	27.59	51.49	39.60	45.54
18	53.44	55.35	77.67	95.24	83.41	19.95	56.56	43.71	53.60	56.77	43.39
19	42.41	58.82	57.60	63.30	100.97	32.37	24.13	58.16	42.02	59.04	42.74
20	36.84	45.56	83.94	80.65	96.01	47.11	34.17	52.21	28.95	60.45	38.38

D.2.2 Specimen 2

Table D.21 - Specimen 2 flow test raw data

Series	**1**	**2**	**3**	**4**	**5**	**6**	**7**	**8**	**9**	**10**	**11**	**12**
Trial	19-Feb-08	21-Feb-08	21-Feb-08	21-Feb-08	21-Feb-08	22-Feb-08	26-Feb-08	27-Feb-08	27-Feb-08	27-Feb-08	27-Feb-08	27-Feb-08
1	39.40	45.57	45.52	45.44	47.27	51.91	22.24	19.79	22.34	21.07	23.09	22.12
2	38.15	45.56	45.45	45.55	47.24	50.20	21.56	19.40	22.23	21.31	21.51	21.52
3	38.28	45.35	45.32	45.61	47.22	49.35	21.69	19.49	22.74	21.38	21.89	22.13
4	38.15	45.35	45.34	45.38	46.89	48.80	21.61	19.44	22.85	21.34	21.63	21.91
5	38.11	45.33	45.29	45.53	46.79	48.90	21.73	19.60	22.35	21.48	21.03	22.31
6	38.73	45.23	45.49	45.34	47.02	48.72	21.85	19.86	22.31	21.56	21.23	22.14
7	38.10	45.16	45.45	45.45	47.07	48.94	21.89	19.96	22.63	21.63	21.13	22.22
8	38.06	45.38	45.52	45.48	45.51	49.20	21.98	20.07	22.71	21.74	21.49	22.57
9	38.67	45.29	45.50	45.52	45.68	49.12	22.20	20.41	22.92	21.63	21.38	22.50
10	38.94	45.14	45.57	45.47	47.09	49.52	22.37	20.09	23.02	22.02	21.46	22.82
11	39.20	45.03	45.33	45.49	46.84	49.20	22.39	20.39	23.08	21.95	21.59	22.49
12	38.40	45.13	45.51	45.52	46.70	49.46	22.62	20.06	23.13	22.09	21.74	22.74
13	38.67	45.09	45.36	45.54	46.64	49.46	22.54	20.32	23.18	22.02	21.84	22.83
14	38.69	45.02	45.47	45.52	46.32	49.68	22.56	20.61	23.24	22.34	21.69	22.86
15	38.69	44.88	45.44	45.69	46.57	49.38	22.92	20.56	23.44	22.27	21.95	23.03
16	38.99	45.08	45.50	45.50	46.84	49.38	22.91	23.56	23.42	23.00	21.85	23.07
17	38.91	45.00	45.55	45.49	47.03	49.50	22.95	20.63	23.43	22.94	21.95	23.05
18	38.78	45.09	45.47	45.59	46.84	50.05	23.09	20.95	23.61	23.10	22.21	23.09
19	39.12	45.06	45.54	45.64	46.31	49.72	23.09	21.28	23.66	23.13	22.15	23.52
20	39.02	45.20	45.40	45.56	45.82	49.58	23.03	21.38	23.73	23.09	22.31	23.30

D.2.3 Specimen 3

Table D.22 - Specimen 3 flow test raw data

Series	**1**	**2**	**3**	**4**	**5**	**6**	**7**	**8**	**9**	**10**
Trial	23-May-08	23-May-08	23-May-08	26-May-08	26-May-08	26-May-08	26-May-08	26-May-08	26-May-08	26-May-08
1	24.52	25.97	22.52	25.33	24.21	30.88	28.95	24.72	25.03	32.99
2	23.63	26.77	26.66	25.48	23.84	30.30	28.25	25.20	25.04	25.27
3	23.42	26.72	25.22	25.19	23.65	29.19	27.95	25.03	27.69	28.75
4	23.27	26.45	24.52	25.49	22.99	28.99	27.88	25.08	27.03	29.29
5	23.52	26.89	23.84	23.79	22.50	28.21	27.66	24.98	31.20	28.87
6	23.79	26.32	23.35	24.92	22.05	27.90	27.47	24.99	27.71	27.39
7	24.01	27.59	23.05	23.72	21.63	27.56	27.11	25.08	31.74	29.82
8	24.21	27.60	22.52	24.24	21.56	27.21	26.99	24.95	28.03	28.19
9	24.99	27.70	22.50	23.62	21.33	26.83	26.71	24.81	31.16	30.74
10	24.41	28.13	21.86	25.56	19.91	26.82	26.71	24.90	28.83	27.57
11	24.52	27.00	21.99	25.78	19.79	26.74	26.61	24.90	29.46	51.60
12	24.70	27.84	21.72	26.41	19.74	26.52	26.20	24.80	32.53	29.45
13	24.77	28.08	21.55	26.16	19.70	26.30	26.08	24.83	28.56	30.79
14	24.74	26.79	21.33	26.14	19.63	26.33	25.86	24.70	26.95	31.75
15	24.33	27.09	20.77	26.57	19.46	26.14	25.97	24.70	36.75	29.74
16	23.97	26.80	21.08	26.59	19.49	26.06	26.08	24.84	28.39	37.25
17	25.88	27.18	21.03	26.51	19.31	26.06	25.99	24.99	29.38	29.22
18	25.37	27.31	20.95	26.43	19.42	25.83	25.65	24.98	28.56	34.42
19	25.14	27.20	20.85	26.96	19.40	25.76	25.66	24.91	30.48	28.13
20	25.20	27.20	21.00	27.04	19.42	25.88	25.62	24.92	29.06	28.81

Table D.22 - Specimen 3 flow test raw data (continued)

Series	**11**	**12**	**13**	**14**	**15**	**16**	**17**	**18**	**19**
Trial	27-May-08	27-May-08	27-May-08	27-May-08	27-May-08	27-May-08	27-May-08	27-May-08	27-May-08
1	25.09	22.14	26.09	26.85	26.48	26.13	26.84	27.26	23.74
2	23.74	24.27	25.87	27.26	29.04	24.81	25.55	26.74	32.12
3	23.57	22.49	25.96	26.58	27.30	24.08	24.41	26.16	27.14
4	23.31	22.69	25.79	26.56	26.90	23.22	23.70	25.88	27.54
5	21.96	22.16	25.81	24.86	26.66	22.89	23.10	28.09	26.69
6	21.88	22.70	25.59	23.49	26.76	22.51	22.75	32.22	26.76
7	21.73	22.12	25.70	23.01	26.88	22.53	22.27	32.00	26.41
8	21.43	22.25	25.49	22.88	26.91	22.52	22.21	31.74	25.34
9	21.37	22.09	25.66	22.71	27.06	22.45	21.95	31.63	25.39
10	21.34	22.00	25.70	22.40	27.03	22.38	21.70	32.80	25.38
11	21.18	21.28	25.87	22.57	27.32	22.34	20.34	32.34	25.53
12	21.27	22.11	25.98	22.53	27.38	22.09	20.23	30.69	25.59
13	21.31	22.14	25.96	22.57	27.54	20.70	20.00	33.33	25.09
14	21.37	22.26	25.95	22.62	27.49	22.18	19.95	29.07	25.26
15	22.66	22.30	25.94	22.66	27.52	21.78	20.05	33.32	25.47
16	22.73	22.31	26.19	22.73	27.77	21.77	19.73	30.44	25.71
17	23.07	22.26	26.13	22.50	27.72	21.57	19.74	33.43	25.92
18	23.15	22.42	26.16	22.70	27.74	21.39	19.70	32.24	26.09
19	23.31	22.45	26.38	22.70	28.00	21.31	19.56	28.59	26.18
20	23.30	22.45	26.40	22.97	27.96	21.16	19.52	31.06	26.36

D.2.4 Specimen 4

Table D.23 - Specimen 4 flow test raw data

Series	**1**	**2**	**3**	**4**	**5**	**6**	**7**	**8**	**9**
Trial	5-Jun-08	5-Jun-08	5-Jun-08	5-Jun-08	5-Jun-08	5-Jun-08	5-Jun-08	5-Jun-08	5-Jun-08
1	13.61	13.89	13.13	13.43	13.28	12.91	12.83	13.13	12.94
2	13.49	13.16	12.73	12.70	13.34	12.62	12.91	12.43	13.13
3	13.13	13.09	12.57	12.66	12.69	13.61	13.16	12.64	13.16
4	13.19	13.26	13.09	12.73	13.41	13.45	12.64	13.24	13.36
5	13.11	14.02	12.93	12.61	13.38	13.15	13.31	13.12	13.32
6	13.28	14.16	13.34	12.71	12.92	13.43	13.49	12.43	13.38
7	13.43	14.12	12.74	12.70	13.45	13.23	13.49	12.57	13.45
8	13.38	13.38	12.90	12.80	13.24	13.13	13.67	12.59	13.60
9	13.47	13.49	13.66	12.96	13.69	13.12	13.57	12.56	13.63
10	13.48	13.58	13.65	12.94	12.95	13.56	13.76	13.61	12.81
11	13.21	14.54	13.74	13.00	13.07	13.17	12.87	12.72	13.84
12	13.69	14.53	13.70	13.20	13.91	12.99	14.03	12.70	13.84
13	13.91	14.75	13.13	13.23	13.31	13.06	13.93	13.80	14.09
14	14.35	14.75	13.11	13.47	13.19	14.02	14.11	14.02	13.91
15	14.18	13.99	14.13	13.49	14.01	13.13	14.14	13.20	14.14
16	14.24	14.15	14.26	13.65	13.41	13.27	14.27	13.25	13.22
17	14.22	14.07	14.16	13.50	13.74	13.25	14.31	13.37	14.37
18	14.67	14.20	14.74	13.63	13.81	13.38	14.56	14.36	14.43
19	14.74	14.90	14.11	14.21	14.69	13.42	14.67	13.54	14.73
20	15.31	14.38	13.66	14.13	14.81	13.60	14.83	14.62	14.59

Table D.23 - Specimen 4 flow test raw data (continued)

Series	10	11	12	13	14	15	16	17	18
Trial	9-Jun-08	9-Jun-08	9-Jun-08	9-Jun-08	9-Jun-08	9-Jun-08	9-Jun-08	9-Jun-08	9-Jun-08
1	14.19	13.02	12.64	12.69	13.17	13.29	13.21	13.30	12.82
2	12.75	13.27	13.76	12.65	13.51	13.06	13.25	12.74	13.08
3	13.43	13.24	12.92	13.34	12.88	13.43	13.45	12.68	13.31
4	13.76	13.24	12.37	13.12	12.97	13.24	13.62	12.71	13.10
5	12.78	13.30	12.35	13.06	12.59	12.70	12.57	12.60	13.17
6	12.67	13.36	12.47	13.41	12.62	12.63	12.72	12.70	12.62
7	12.72	13.55	12.44	13.41	12.69	12.74	12.77	12.86	12.79
8	12.91	12.69	12.56	13.63	12.60	12.82	12.74	12.88	12.77
9	12.98	12.74	12.64	12.79	12.58	12.87	12.81	12.93	12.66
10	12.98	12.79	12.68	12.99	12.72	12.95	13.87	13.02	12.77
11	13.05	12.87	12.68	13.74	12.74	13.02	13.02	13.10	12.82
12	13.16	13.06	12.76	13.04	12.80	13.02	13.04	13.20	12.97
13	13.13	13.23	12.81	13.06	12.93	13.21	13.04	13.28	12.99
14	13.24	13.29	12.98	13.26	13.13	13.33	13.27	13.40	13.00
15	13.36	13.34	13.06	13.39	13.08	13.31	13.17	13.37	13.10
16	13.54	13.36	13.17	13.57	14.26	13.41	13.20	13.50	13.34
17	13.51	13.45	13.22	13.38	13.35	13.43	13.30	13.44	13.26
18	13.69	13.44	13.19	13.47	13.32	13.44	13.41	13.54	13.47
19	13.59	13.56	13.31	13.48	13.45	13.66	13.37	13.59	13.47
20	13.85	13.61	13.24	13.76	13.45	13.63	13.56	13.69	13.59

Table D.24 - Specimen 6 flow test raw data

Series	1	2	3	4	5	6	7	8
Trial	26-Sep-08	26-Sep-08	26-Sep-08	26-Sep-08	3-Oct-08	3-Oct-08	3-Oct-08	3-Oct-08
1	32.91	25.4	26.07	25.12	42.68	48.71	45.53	51.42
2	24.44	23.72	22.88	24.23	47.01	50.69	58.45	53.99
3	24.52	26.05	23.44	25.09	43.48	54.62	52.75	52.16
4	30.26	22.5	23.23	23.65	42.71	53.07	48.27	51.96
5	26.29	23.57	24.42	24.12	43.15	48.79	55.37	54.98
6	25.45	23.57	24.12	24.45	42.74	57.25	47.42	49.02
7	26.07	22.73	22.51	25.07	43.32	52.55	51.25	52.84
8	24.65	23.7	22.46	25.22	51.87	49.82	58.1	52.85
9	24.43	23.9	23.97	24.18	54.37	54.35	49.4	52.57
10	24.69	24.79	23.74	24.58	48.28	48.48	56.91	50.51

Table D.25 - Specimen 7 flow test raw data

Series	**1**	**2**	**3**	**4**	**5**	**6**	**7**	**8**
Trial	5-Oct-08	5-Oct-08	5-Oct-08	5-Oct-08	5-Oct-08	5-Oct-08	5-Oct-08	5-Oct-08
1	24.1	25.28	28.62	27.33	24.98	22.94	24.28	26.3
2	26.47	27.21	28.19	27.24	24.86	22.73	24.87	25.75
3	25.67	25.93	27.52	26.95	23.9	23.08	24.52	27.17
4	25.16	25.59	27.31	27.59	23.62	23.72	24.32	26.17
5	24.77	26.87	26.77	27.75	24.02	23.59	25.45	26.57
6	24.59	28.95	27.53	26.98	23.67	23.6	24.34	26.18
7	26.22	29.17	26.7	27.94	24.29	23.44	25.64	26.16
8	23.5	26.82	27.41	27.36	23.72	23.8	25.53	26.09
9	23.34	27.19	27.24	27.29	23.72	24.75	25.91	26.36
10	25.33	26.87	27.01	26.32	23.25	25.1	25.02	26.33

APPENDIX E

Driving Plate Axial Modes

E.1 Driving Plate Axial Modes

A complete analysis of driving plate axial modes is included in this section. A stainless steel probe is fixed to the resonant column base and driving plate. Five accelerometers are fixed to the driving plate at varying distance from the centre. A 1600 *Hz* bandwidth sweep is performed for all five accelerometers to determine resonant peaks of the driving plate and stainless steel probe and then 50 *Hz* bandwidth resonant method tests are performed at each peak for each accelerometer to determine the transfer function, phase and damping ratio. This procedure is used to identify the resonant peaks due to driving plate vibration, as well as the mode shape for each peak.

E.2 Equipment Setup

Figure E.1 shows the equipment setup and Figure E.2 shows a plan-view of the driving plate and accelerometer locations, including relevant dimensions.

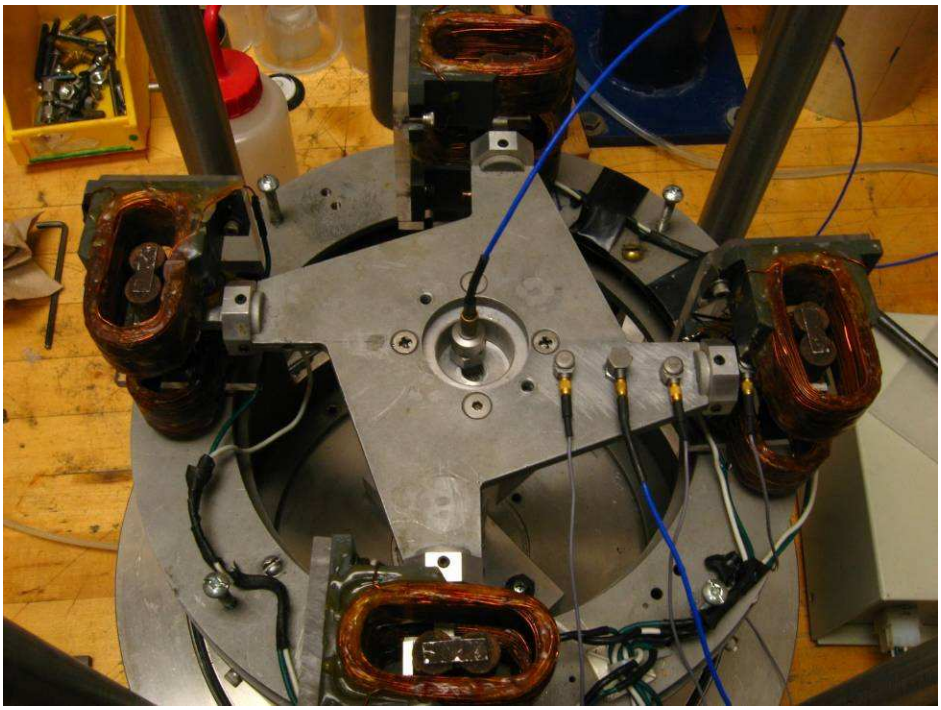

Figure E.1 - Physical equipment setup

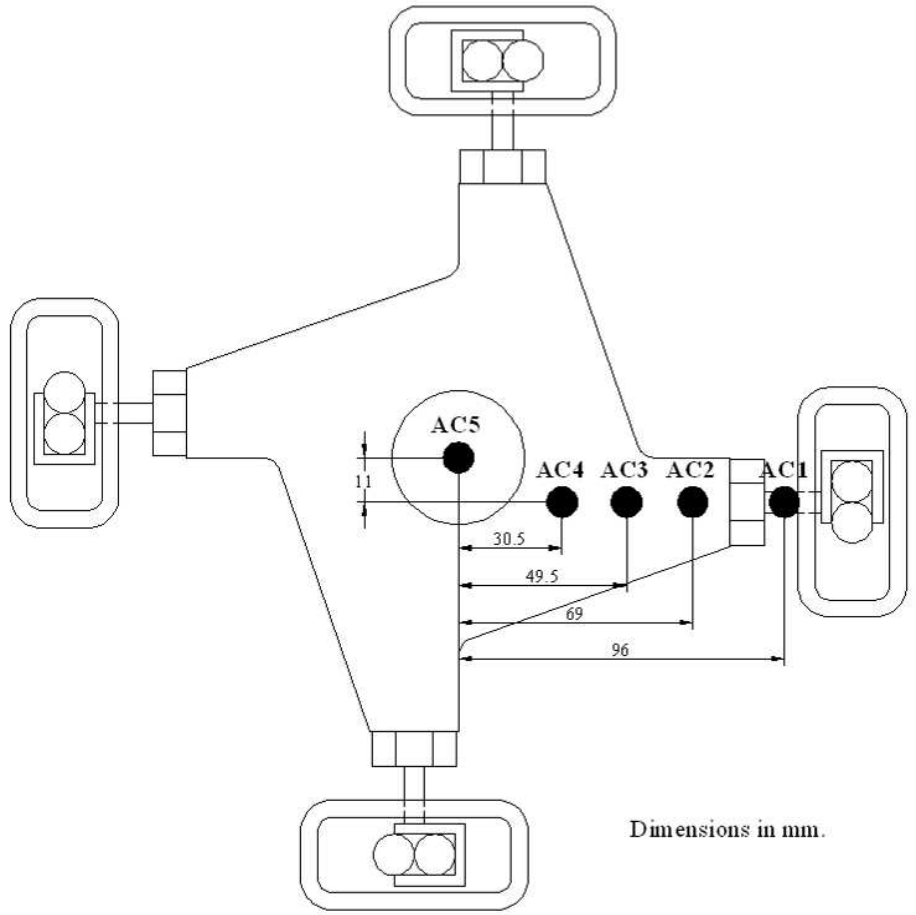

Figure E.2 - Plan view of driving plate and accelerometer locations

E.3 Wide-Bandwidth Sweeps

The 1600 *Hz* wide-bandwidth frequency sweep transfer functions are shown in Figure E.3. There are consistently five significant peaks on the transfer function for each accelerometer, at 93 *Hz*, 207 *Hz*, 501 *Hz*, 723 *Hz* and 1305 *Hz*. The transfer function for accelerometer 1 is normalized with respect to the peak at 207 *Hz*; all subsequent transfer functions are normalized with respect to this peak. Using Equations [3.39] and [3.40], the expected resonant peaks of the stainless steel rod are 264 *Hz* and 3668 *Hz*, respectively. Therefore, none of the peaks observed in the wide-bandwidth sweeps are caused by the calibration rod, but rather the driving plate itself.

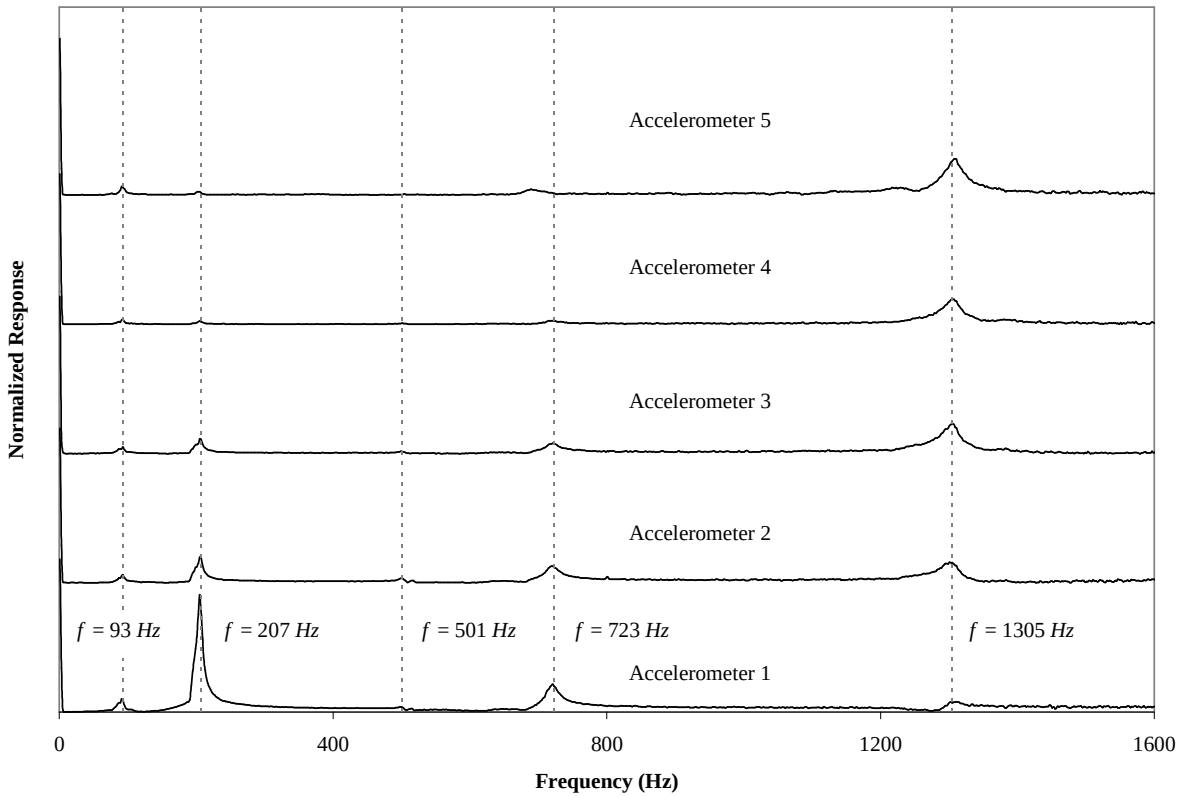

Figure E.3 - Wide-bandwidth frequency sweep

E.4 Resonant Method Tests

Transfer functions for the resonant tests performed at f = 207 Hz, 723 Hz and 1305 Hz are shown in Figures E.4, E.5 and E.6, respectively. The mode shape for each frequency (Figure E.7) is determined by the normalization factor and phase of the transfer functions for each accelerometer and the distance from centre.

The peak at 207 *Hz* appears to be caused by vibration of the magnets at the outer edge of the driving plate. The magnets are fixed to the plate with aluminum spacers that are less rigid than the plate itself. The mode shape shows that the largest deformation occurs at the magnet. The peak at 723 *Hz* appears to be the first mode of vibration of the plate itself, due to the linear nature of the mode shape. Finally, the peak at 1305 Hz appears to be a higher mode of vibration of the magnets since the mode shape is inverted compared to the 207 *Hz* mode.

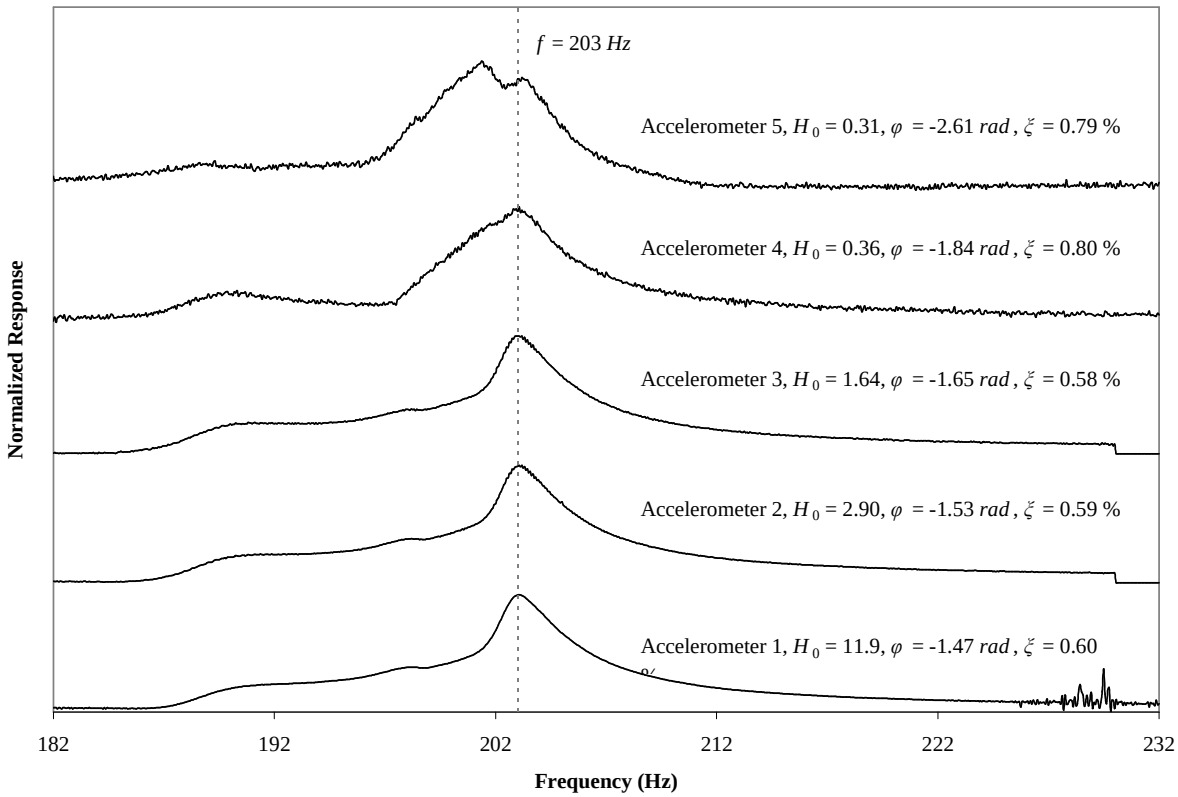

Figure E.4 - Resonant method for $f = 207\ Hz$

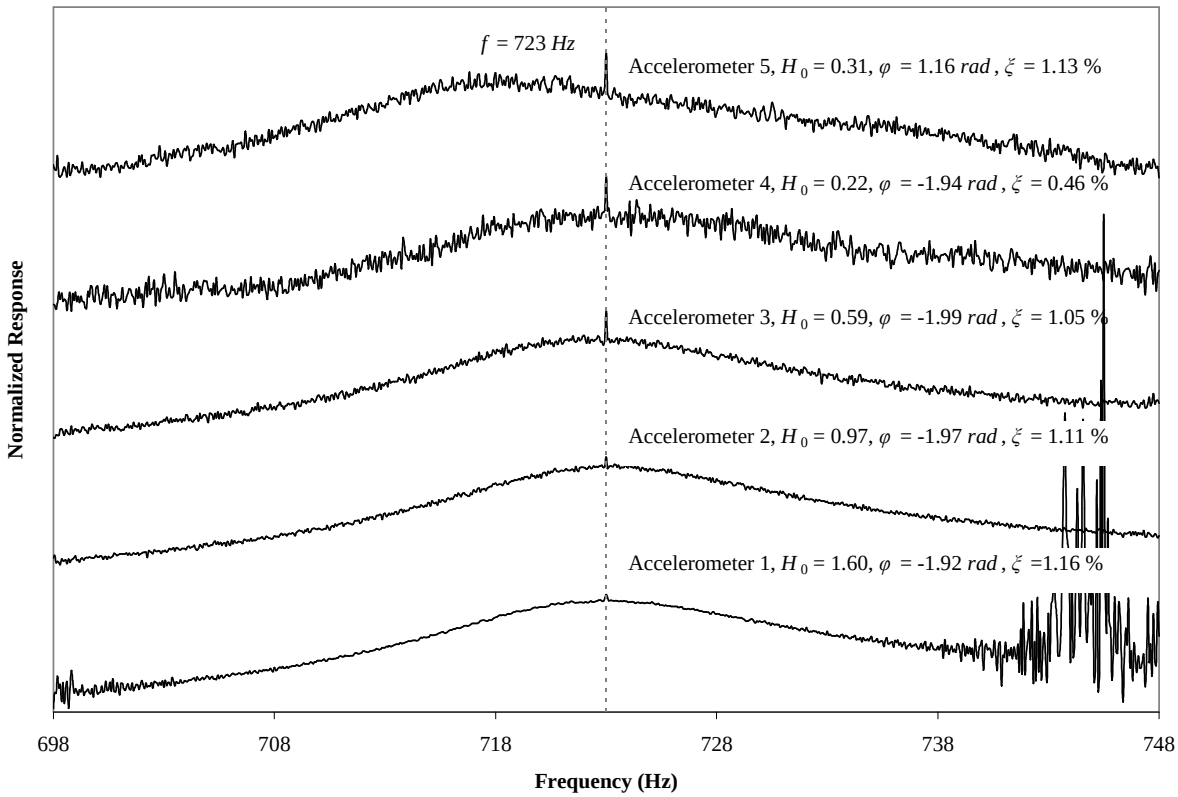

Figure E.5 - Resonant method for $f = 723\ Hz$

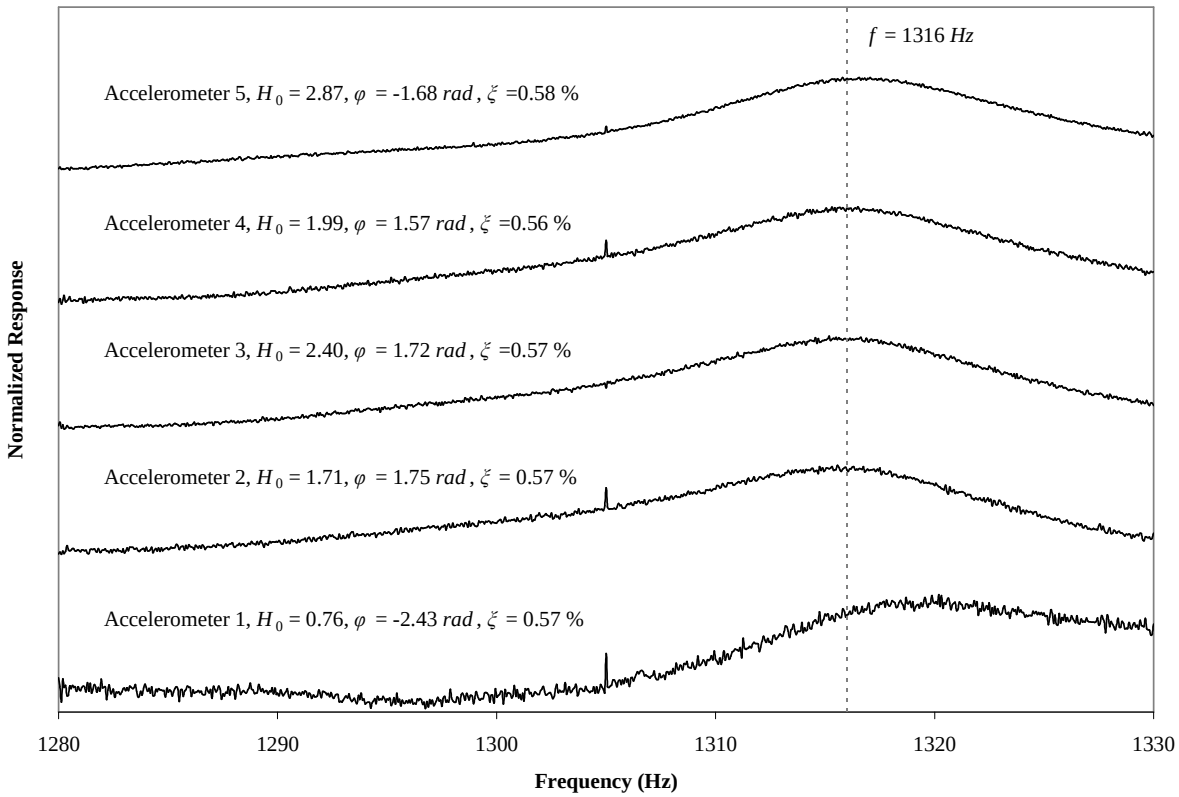

Figure E.6 - Resonant method for f = 1305 *Hz*

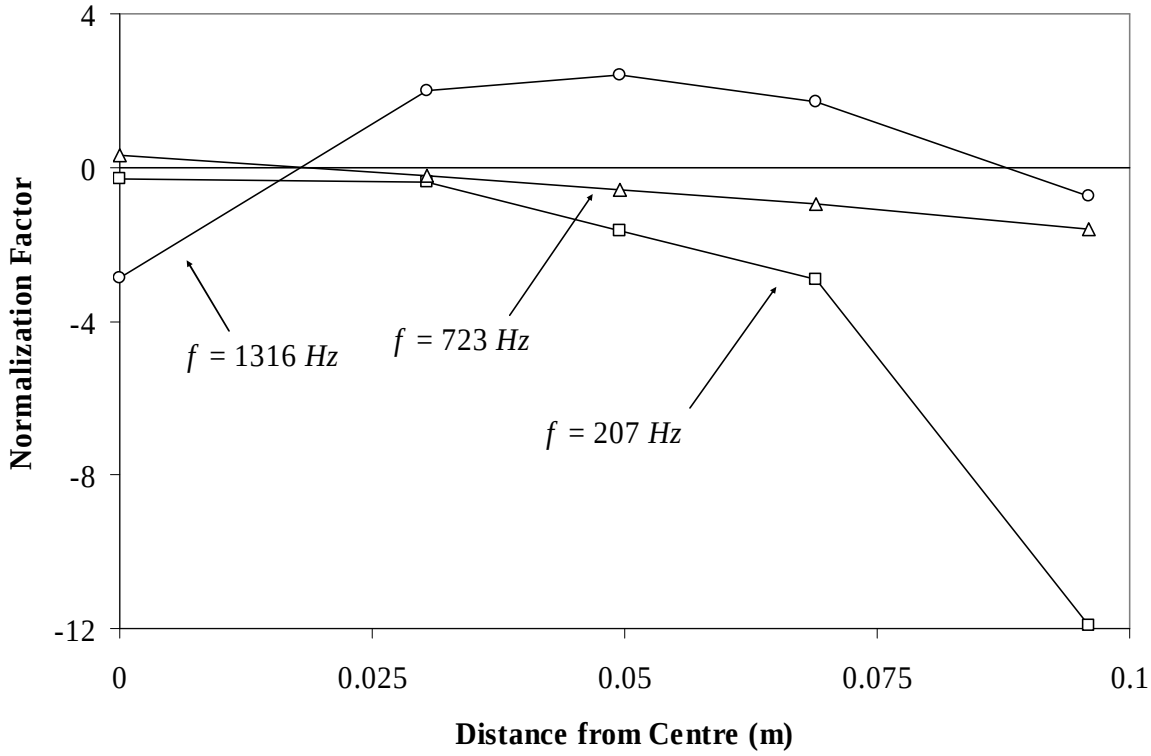

Figure E.7 - Mode shapes

APPENDIX F

Rayleigh Estimate of First Mode of Vibration

F.1 Rayleigh Estimate of First Torsional Mode

Assuming a linear mode shape, the angle of twist θ is defined as

$$\theta(x) = a_0 + a_1 x \quad \text{.....[F.1]}$$

where x is the distance along the length of the specimen. From the boundary condition,

$$\theta(0) = 0 \quad \text{.....[F.2]}$$

therefore,

$$\theta(x) = a_1 x \quad \text{.....[F.3]}$$

Potential energy of the system is given by

$$J_u = \frac{1}{2} G \cdot J_p \cdot \int_0^L \left(\frac{d\theta}{dx} \right)^2 dx \quad \text{.....[F.4]}$$

where G is the shear modulus of the specimen, J_p is the area polar moment of inertia and L is the height. Therefore,

$$J_u = \frac{1}{2} G \cdot J_p \cdot \left(\frac{a_1}{r} \right)^2 \cdot L \quad \text{.....[F.5]}$$

where r is the specimen radius. Kinetic energy of the system is given by

$$J_T = \frac{1}{2} \rho \cdot J_p \cdot \int_0^L \left(\frac{d\theta}{dt} \right)^2 dx + \frac{1}{2} I_0 \cdot \left(\frac{d\theta}{dt}(L) \right)^2 \quad \text{.....[F.6]}$$

which simplifies to

$$J_T = \frac{1}{6} I \cdot \left(\frac{a_1}{r} \right)^2 \cdot L^2 + \frac{1}{2} I_0 \cdot \left(\frac{a_1}{r} \right)^2 \cdot L^2 \quad \text{.....[F.7]}$$

By Rayleigh's principle,

$$\omega^2 = \frac{J_u}{J_T} = V_s^2 \frac{I}{L^2 \left(\frac{1}{3} I + I_0 \right)} \quad \text{.....[F.8]}$$

F.2 Rayleigh Estimate of First Axial Mode

Assuming a linear mode shape, the displacement *u* is defined as

$$u(x) = a_0 + a_1 x \quad \text{.....[F.9]}$$

where *x* is the distance along the length of the specimen. From the boundary condition,

$$u(0) = 0 \quad \text{.....[F.10]}$$

therefore,

$$u(x) = a_1 x \quad \text{.....[F.11]}$$

Potential energy of the system is given by

$$J_u = \frac{1}{2} E \cdot A \cdot \int_0^L \left(\frac{du}{dx} \right)^2 dx \quad \text{.....[F.12]}$$

where *E* is the Young's modulus of the specimen and *A* is the area. Therefore,

$$J_u = \frac{1}{2} E \cdot A \cdot (a_1)^2 \cdot L \quad \text{.....[F.13]}$$

Kinetic energy of the system is given by

$$J_T = \frac{1}{2} \rho \cdot A \cdot \int_0^L \left(\frac{du}{dt} \right)^2 dx + \frac{1}{2} m_0 \cdot \left(\frac{du}{dt}(L) \right)^2 \quad \text{.....[F.14]}$$

which simplifies to

$$J_T = \frac{1}{6} m \cdot (a_1)^2 \cdot L^2 + \frac{1}{2} m_0 \cdot (a_1)^2 \cdot L^2 \quad \text{.....[F.15]}$$

By Rayleigh's principle,

$$\omega^2 = \frac{J_u}{J_T} = V_L^2 \frac{m}{L^2 \left(\frac{1}{3} m + m_0 \right)} \quad \text{.....[F.16]}$$